The nature of the metal-insulator transition in 5d transition metal oxides

James George Vale

A thesis presented for the degree of

Doctor of Philosophy

Department of Physics and Astronomy

UCL

November 2016

I, James George Vale, confirm that the work presented in this thesis is my own. Where information has been derived from other sources, I confirm that this has been indicated in the thesis.

Signed

Date

"I'm a scientist and I know what constitutes proof. But the reason I call myself by my childhood name is to remind myself that a scientist must also be absolutely like a child. If he sees a thing, he must say that he sees it, whether it was what he was expecting to see or not. See first, think later, then test. But always see first. Otherwise you will only see what you're expecting. Most scientists forget that. [. . .] You can't possibly be a scientist if you mind people thinking that you're a fool."

Wonko The Sane
So long, and thanks for all the fish
Douglas Adams

Abstract

A number of 5d transition metal oxides (TMOs) either undergo, or lie proximate to, a metal-insulator transition (MIT). However these MITs frequently depart from a Mott-Hubbard picture, in which the interactions are dominated by the interplay between the on-site Coulomb repulsion and electronic bandwidth. In 5d TMOs the sizeable intrinsic spin-orbit coupling plays an important role, and gives rise to electronic and magnetic ground states – at both sides of the MIT – that cannot be adequately described within a purely L–S coupling scenario.

In this thesis the aim is to understand the role of spin-orbit coupling in determining the electronic and magnetic properties of 5d TMOs. There has been a large amount of recent interest within this field (both experimentally and theoretically), however thus far has mostly been limited to the $5d^5$, $j_{\text{eff}} = \frac{1}{2}$ limit. The perovskite iridates Sr_2IrO_4 and $Sr_3Ir_2O_7$ lie within this limit. Theoretical predictions suggest a significant easy-plane anisotropy is present for the single layer Sr_2IrO_4. I show that this anisotropy can be observed and quantified, using magnetic critical scattering and previously published resonant inelastic X-ray scattering (RIXS) data. This differs from previous results that suggest purely 2D Heisenberg behaviour. Meanwhile the critical fluctuations in bilayer $Sr_3Ir_2O_7$ have a three-dimensional nature, which can be directly related to the intra-bilayer coupling and significant anisotropy previously probed by RIXS.

I also demonstrate that resonant X-ray scattering techniques can be successfully applied to other 5d systems, especially the d^3 osmates. Both $NaOsO_3$ and $Cd_2Os_2O_7$ undergo MITs directly linked to the onset of antiferromagnetic order (Slater or Lifshitz mechanisms). The first ever high-resolution RIXS measurements at the Os L_3 absorption edge reveal that there is a correlated evolution of the electronic and magnetic excitations through the respective MITs. The behaviour is consistent with a scenario in which the effect of spin-orbit coupling and electron correlations are reduced with respect to the iridates, yet still manifests through a strong spin wave anisotropy.

Finally I show that the study of 5d TMOs can be extended into the time domain. Through the development of new instrumentation, the transient dynamics of photo-doped Sr_2IrO_4 were probed by time-resolved resonant (in)elastic X-ray scattering. The relevant time scales can be directly compared to the interaction strengths and anisotropies in the undoped state. Moreover, there seems to be an effective mapping of the transient behaviour in the photo-doped state to an equivalent level of bulk electron doping in $Sr_{2\text{-}x}La_xIrO_4$.

List of publications

1. S. Calder, **J. G. Vale**, N. Bogdanov, C. Donnerer, M. Moretti Sala, X. Liu, M. H. Upton, D. Casa, Y. G. Shi, Y. Tsujimoto, K. Yamaura, J. P. Hill, J. van den Brink, D. F. McMorrow, and A. D. Christianson, *Strongly gapped spin-wave excitation in the insulating phase of* $NaOsO_3$, Physical Review B **95**, 020413(R) (2017)
2. C. Donnerer, M. C. Rahn, M. Moretti Sala, **J. G. Vale**, D. Pincini, J. Strempfer, M. Krisch, D. Prabhakaran, A. T. Boothroyd, and D. F. McMorrow, *All-in all-out magnetic order and propagating spin-waves in* $Sm_2Ir_2O_7$, Phys. Rev. Lett. **117**, 037201 (2016)
3. S. Calder, **J. G. Vale**, N. A. Bogdanov, X. Liu, C. Donnerer, M. H. Upton, D. Casa, A. H. Said, M. D. Lumsden, Z. Zhao, J. -Q. Yan, D. Mandrus, S. Nishimoto, J. van den Brink, J. P. Hill, D. F. McMorrow, and A. D. Christianson, *Spin-orbit-driven magnetic structure and excitation in the 5d pyrochlore* $Cd_2Os_2O_7$, Nature Communications **7**, 11651 (2016).
4. M. P. M. Dean, Y. Cao, X. Liu, S. Wall, D. Zhu, R. Mankowsky, V. Thampy, X. M. Chen, **J. G. Vale**, D. Casa, Jungho Kim, A. H. Said, P. Juhas, R. Alonso-Mori, J. M. Glownia, A. Robert, J. Robinson, M. Sikorski, S. Song, M. Kozina, H. Lemke, L. Patthey, S. Owada, T. Katayama, M. Yabashi, Yoshikazu. Tanaka, T. Togashi, J. Liu, C. Rayan Serrao, B. J. Kim, L. Huber, C. -L. Chang, D. F. McMorrow, M. Först, and J. P. Hill, *Ultrafast energy- and momentum-resolved dynamics of magnetic correlations in the photo-doped Mott insulator* Sr_2IrO_4, Nature Materials **16**, 601 (2016).
5. C. Donnerer, Z. Feng, **J. G. Vale**, S. N. Andreev, I. V. Solovyev, E. C. Hunter, M. Hanfland, R. S. Perry, H. M. Rønnow, M. I. McMahon, V. V. Mazurenko, and D. F. McMorrow, *Pressure dependence of the structure and electronic properties of* $Sr_3Ir_2O_7$, Phys. Rev. B **93**, 174418 (2016).
6. M. Moretti Sala, V. Schnells, S. Boseggia, L. Simonelli, A. Al-Zein, **J. G. Vale**, L. Paolasini, E. C. Hunter, R. S. Perry, D. Prabhakaran, A. T. Boothroyd, M. Krisch, G. Monaco, H. M. Rønnow, D. F. McMorrow, and F. Mila, *Evidence of quantum dimer excitations in* $Sr_3Ir_2O_7$, Phys. Rev. B **92**, 024405 (2015).

7. **J. G. Vale**, S. Boseggia, H. C. Walker, R. Springell, Z. Feng, E. C. Hunter, R. S. Perry, D. Prabhakaran, A. T. Boothroyd, S. P. Collins, H. M. Rønnow, and D. F. McMorrow, *Importance of XY anisotropy in* Sr_2IrO_4 *revealed by magnetic critical scattering experiments*, Phys. Rev. B **92**, 020406(R) (2015).

8. S. Boseggia, H. C. Walker, **J. Vale**, R. Springell, Z. Feng, R. S. Perry, M. Moretti Sala, H. M. Rønnow, S. P. Collins, and D. F. McMorrow, *Locking of iridium magnetic moments to the correlated rotation of oxygen octahedra in* Sr_2IrO_4 *revealed by x-ray resonant scattering*, J. Phys.: Condens. Matter **25**, 422202 (2013).

Contents

Abstract **5**

List of publications **7**

List of figures **26**

List of tables **28**

Introduction **29**

1 Correlations and spin-orbit coupling in 5d transition metal oxides **36**

- 1.1 Metal-insulator transitions 36
  - 1.1.1 Mott-Hubbard transitions 37
  - 1.1.2 Charge-transfer MIT 39
  - 1.1.3 Lifshitz transition 40
  - 1.1.4 Slater transition 42
- 1.2 Crystalline environment 44
  - 1.2.1 Crystal field theory 45
  - 1.2.2 Molecular orbital theory 47
  - 1.2.3 Ligand field theory 47
- 1.3 Hund's coupling (J_H) 49
- 1.4 Spin-orbit coupling (SOC) 50
  - 1.4.1 Effect of SOC on electronic behaviour 51
  - 1.4.2 Effect of SOC on the magnetic Hamiltonian 52
- 1.5 Outlook 54

2 Resonant X-ray scattering **56**

- 2.1 Numerical treatment 58
- 2.2 Resonant elastic X-ray scattering 62
  - 2.2.1 A resonant elastic scattering beamline - I16 63
- 2.3 Resonant inelastic X-ray scattering (RIXS) 64
  - 2.3.1 Comparison with optical absorption spectroscopy 65
  - 2.3.2 Technical details 67

2.3.3 RIXS beamline - MERIX at the APS 68
2.4 Resonant X-ray scattering at XFELs 70

3 Magnetic correlations and the MIT in $Cd_2Os_2O_7$ studied with RIXS 72
3.1 Literature review 73
3.1.1 Structure and general aspects of pyrochlore physics 73
3.1.2 Synthesis 74
3.1.3 Bulk properties 74
3.1.4 Optical conductivity 75
3.1.5 X-ray and muon spin relaxation (μSR) measurements 76
3.1.6 Theoretical calculations 77
3.2 Low resolution measurements 80
3.2.1 Incident energy dependence 81
3.2.2 Intra-t_{2g} excitations 83
3.2.3 Excitations across Δ_O 83
3.2.4 Momentum dependence at 60 K 86
3.2.5 Temperature dependence 88
3.3 High resolution RIXS measurements 92
3.3.1 Origin of peak A 93
3.3.2 Temperature dependence 95
3.3.3 Dependence on momentum transfer 99
3.4 Summary 107
3.4.1 Proximity to Lifshitz transition 107

4 Excitations through the Slater MIT in $NaOsO_3$ 109
4.1 Introduction to physical properties of $NaOsO_3$ 110
4.2 Low resolution RIXS measurements 113
4.3 High resolution RIXS measurements 117
4.3.1 Momentum dependence 117
4.3.2 Magnon dispersion 117
4.3.3 Validity of Hamiltonian 121
4.3.4 Temperature dependence 124
4.3.5 Discussion 127
4.4 Summary and outlook 130

5 Magnetic critical scattering measurements on Sr_2IrO_4 and $Sr_3Ir_2O_7$ 132
5.1 Critical scattering theory 134
5.2 2D Heisenberg antiferromagnet on a square lattice (2DQHAFSL) 136
5.3 Critical scattering on Sr_2IrO_4 139

5.3.1 Introduction to physical properties 139
5.3.2 Experimental setup 142
5.3.3 Order parameter 142
5.3.4 Magnetic scattering above the Néel temperature 144
5.4 2D XYh_4 model 149
5.4.1 Correlation length and amplitude for 2D XY 151
5.4.2 Comparison to experimental data 152
5.5 2D anisotropic Heisenberg model (2DAH) 153
5.6 RIXS on Sr_2IrO_4 155
5.7 Critical scattering from $Sr_3Ir_2O_7$ 163
5.7.1 Synthesis and bulk properties 163
5.7.2 Critical scattering experiment 165
5.7.3 Summary 172

6 Time-resolved resonant X-ray scattering measurements on Sr_2IrO_4 173
6.1 X-ray free electron lasers (XFELs) 176
6.2 System dynamics 179
6.3 Time-resolved RXMS measurements on Sr_2IrO_4 180
6.3.1 Experimental procedure 181
6.3.2 Results 184
6.4 Time-resolved RIXS (tr-RIXS) 187
6.5 tr-RIXS measurements 187
6.5.1 Spectrometer calibration 188
6.5.2 Measurements at (π, π) 192
6.5.3 Measurements at $(\pi, 0)$ 194
6.5.4 Comparison with chemical doping 196
6.5.5 Summary 197

7 Conclusions and future perspectives 199
7.1 $Cd_2Os_2O_7$ 199
7.1.1 ARPES 199
7.1.2 Resistivity under pressure 200
7.2 $NaOsO_3$ 201
7.2.1 Resistivity/magnetisation measurements as a function of applied pressure 201
7.2.2 Non-resonant magnetic X-ray diffraction (nRXMS) 202
7.2.3 Probing the band structure 203
7.2.4 Itinerant model for magnetic excitations 203
7.3 Sr_2IrO_4 204
7.3.1 Crossover phenomena 204
7.3.2 Sample dependence of magnetic properties 204

7.3.3 Imaging the Griffiths phase 204
7.3.4 Effect of carrier doping 205
7.4 $Sr_3Ir_2O_7$ 205
7.5 Summary 205

Appendices 207
A Energy resolution of RIXS instruments 207
B Linear spin wave theory applied to $NaOsO_3$ 209

Bibliography 213

Acknowledgements 228

List of Figures

1 Schematic phase diagram for electronic materials as a function of the electron correlations U/t and the spin-orbit coupling λ/t, where t is the hopping amplitude. 5d transition metal oxides lie somewhere in the centre of the phase diagram, with approximate positions for the materials studied in this thesis highlighted in blue. Adapted from Ref. [5]. 30

2 (a): schematic of energy levels for Sr_2IrO_4 and $Sr_3Ir_2O_7$, assuming a strong field scenario $\Delta_{oct} > \lambda > U$. Spin-orbit coupling splits the t_{2g} manifold into $j_{eff} = \frac{3}{2}$ and $j_{eff} = \frac{1}{2}$ states, the latter of which is half-filled. A weak electron correlation U is sufficient to open up an insulating gap at the Fermi level. The real space representation of the corresponding wavefunctions is also shown, with red/blue reflecting spin up/down contributions to the wavefunctions respectively. (b): RXMS data (red circles) and fluorescence (black solid line) obtained by Kim *et al.* [26]. Reprinted with permission from AAAS. There is a significant resonant enhancement at the L_3 absorption edge compared to the L_2 edge. (c): Optical conductivity measurements by Moon *et al.* [27], which show transitions between the UHB and LHB (α) and from the $j_{eff} = \frac{1}{2} \rightarrow j_{eff} = \frac{3}{2}$ states (β). 32

1.1 Radial distribution functions for nd-orbitals, where a_0 is the Bohr radius. The orbitals become more diffuse as you move down the group, with the number of radial nodes equal to $n - (l + 1)$, where $l = 2$ for a d-orbital. 37

1.2 Schematic of a Mott-Hubbard transition for a system at half-filling within dynamical mean-field theory (DMFT). In the weak-coupling limit ($U/t \rightarrow 0$), there is the simple case of a metallic band, filled up to the Fermi level E_F. As U increases, spectral weight shifts towards two bands below and above E_F. These are the lower and upper Hubbard bands (LHB/UHB). A quasiparticle peak remains at E_F below some critical ratio U_c/t_c, with its width going to zero at the Mott-Hubbard transition. 39

1.3 Illustration of the two types of Lifshitz transition tuned by some external parameter g. The top row depicts an open Fermi surface changing to a closed surface by disruption of a 'neck' (neck-forming type), whereas the bottom row depicts splitting off of a new portion of Fermi surface (pocket forming/vanishing type). 41

1.4 Model band structure describing a Lifshitz MIT. The electronic bands are uniformly shifted apart from each other with decreasing temperature, leading to the formation of an insulating gap. Here Δ_D and Δ_C refer to the direct (optical) and charge gaps respectively. 42

1.5 Phase diagram of a general quantum phase transition (QPT). At $T = 0$, a Lifshitz transition falls under these auspices. Dashed lines indicate crossovers between phases, since singularities in the electronic density of states are only infinite at $T = 0$. Solid blue line indicates proximity of certain 5d TMOs to the quantum critical point at $g = g_c$ and $T = 0$. 43

1.6 Schematic of crystal field splittings obtained for various symmetry environments, in the absence of correlation effects or spin-orbit coupling. Tetragonal (D_{4h}) and trigonal (D_{3d}) distortions are assumed as weak perturbations from the octahedral case. The tetragonal and trigonal energy levels as drawn are appropriate for axial elongation along the z-axis or local three-fold symmetry axis respectively. The term γ arises from the contribution of off-diagonal parameters, and is defined [60] as $\gamma = 300\, Dq^2 - 20\, Dq(3D\sigma - 5D\tau) - 3(3D\sigma - 5D\tau)^2$. 46

1.7 Molecular orbital (MO) diagram of a 5d TMO cation octahedrally coordinated to six oxygen ligands. The MOs are hybridised, and have character arising both from the transition metal and ligand atomic orbitals. Adapted from Katukuri [61]. 48

2.1 Left panel – Resonant X-ray scattering process as illustrated for an Ir^{4+} ion. In the displayed scenario an electron has been excited from the $\mathrm{j} = \frac{3}{2}$ to the $\mathrm{j} = \frac{1}{2}$ manifold, and hence $\hbar\omega_{\mathbf{k}} \neq \hbar\omega_{\mathbf{k}'}$. Right panel – Iridium X-ray absorption edges along with their respective energies. 57

2.2 Rowland circle geometry. The distance between O and O′ is defined as $R/2$, where R is the radius of the Rowland circle. 68

2.3 Top panel: General schematic of the upstream optical elements used at a RIXS instrument. DCM stands for double crystal monochromator. Bottom panel: Picture of the MERIX spectrometer at 30-ID, Advanced Photon Source, USA. The spectrometer is in horizontal scattering geometry (π-polarized light incident), and important components of the spectrometer have been labelled. 69

3.1 (a): Temperature dependence of the magnetic susceptibility (green symbols, [95]), charge gap from resistivity data (solid: [94], dashed: [99]), and direct (optical) gap from optical conductivity data (solid circles: [98], open triangles: [99]) which show the link between the MIT and onset of AFM order. (b): Magnetic AIAO ground state of $\mathrm{Cd_2Os_2O_7}$. 75

3.2 Phase diagram adapted from Shinaoka [104]. The three phases are a non-magnetic metallic state (NMM), an antiferromagnetic metal (AFM), and an antiferromagnetic insulator (AFI). The Os moment (a), charge gap Δ_C and optical gap Δ_O (b) increase with increasing electron correlation $U_\text{eff} = U - J$. 78

3.3 (a): RIXS spectra for $Cd_2Os_2O_7$ as a function of incident energy collected at 300 K. Three features (B, C, D) can be observed, which correspond to intra-t_{2g}, $t_{2g} \rightarrow e_g$, and ligand-to-metal charge transfer (LMCT) excitations respectively. Solid line is the best fit to the data. The fitting model comprised a sum of Gaussian functions, each representing the elastic line and aforementioned inelastic features. (b): Example spectrum collected for an incident energy of 10.875 keV. Superimposed are the expected transitions based on the quantum chemistry (QC) calculations [106]. 81

3.4 Fits of the low energy RIXS spectra at 30 K for the L (a) and Γ (b) points. The quasi-elastic feature is fitted to a resolution limited Pearson VII function constrained to the width of the resolution function, whilst all other features are fitted by Gaussians. The energies of the intra-t_{2g} excitations comprising the broad peak at ca. 1 eV (peak B in Fig. 3.3) were fitted to $3J_\text{H}$ and $5J_\text{H}$ respectively, with J_H as a fitted parameter. 82

3.5 Brillouin zone for the Fd$\bar{3}$m space group, with high symmetry points highlighted. The points Δ and Σ – as referenced later – have been omitted from this diagram as they are not high symmetry points, but correspond to (0, $\frac{1}{4}$, 0) and ($\frac{1}{4}$, $\frac{1}{4}$, 0) respectively. 82

3.6 (a): Terms of a t_2^3 configuration in a first (strong field) approximation, including the effect of Coulomb repulsion. Spin-orbit coupling and distortions away from an ideal octahedral geometry are neglected. The Hund's coupling J_H is equivalent to $3B + C$, where B and C are Racah parameters. The terms ^2E and $^2T_1$ are accidentally degenerate. (b): Electronic terms when spin-orbit coupling is added as a weak perturbation. Terms are calculated by decomposition of the direct product $\Gamma \times D^{(3/2)}$. The separation between terms originating from ^2E and $^2T_1$ is exaggerated for clarity. (c): Addition of a weak trigonal perturbative field to the case presented in (b). Note that the $^4A_2$ ground state is only split (zero field splitting) by a combination of spin-orbit coupling and trigonal distortion, and even then third-order perturbations are required. 85

3.7 (a): Momentum dependence at 60 K in a low-resolution setup. Spectra have been offset for clarity. Δ and Σ correspond to points intersecting the $\Gamma - X$ and $\Gamma - K$ high symmetry directions respectively. The peak at 0.15 eV energy loss corresponds to peak A, with the high energy tail resulting from the intra-t_{2g} excitations. (b,c): Example fits to spectra collected at L (b) and Γ (c), with individual peak components superimposed. 87

3.8 Energy (a) and intensity (b) of the feature at 160 meV energy loss (peak A) as a function of momentum transfer. There is a weak variation of the peak energy and intensity across the Brillouin zone. 88

3.9 (a): Temperature dependence of RIXS spectra collected at (2.5, 8.8, 8.8). Spectra have been offset by a constant factor for clarity. (b): Comparison of spectra at 60 K and 300 K. Peak A weakens and broadens with increasing temperature. Solid line is the best fit to the data with the model given in the main text. (c): Fitted peak intensity as a function of temperature, with a fit to a power law $T_\mathrm{C} = 226$ K, $\beta = 0.17(2)$ added as a guide. Such behaviour is consistent with a magnetic excitation. 89

3.10 Exact diagonalization calculations performed by Satoshi Nishimoto on an 8-site cluster for $Cd_2Os_2O_7$. Markers correspond to experimental data points after background subtraction. Green, blue, and purple lines represent excitation spectra $I(\omega)$ for $\Delta S_z = 1,2,3$ respectively, multiplied by identical scale factors and broadened by the instrumental resolution. Inset shows similar calculations for a minimal 4-site cluster, along with the unbroadened excitation spectra. The energy scale compares well with peak A. Adapted from Ref. [118]. 91

3.11 Best fits to high-resolution RIXS data collected in the (6, 7, 7) Brillouin zone, using a symmetric Lorentzian (black dashed) or a phenomenological gap function (Eqn. 3.4, solid) functional form at 30 K (a,c) and 200 K (b,d) for momentum transfers Γ and L. The Lorentzian fails to adequately describe the region between the elastic line and peak A for all temperatures and momentum transfers **Q**. Dotted lines illustrate the functional form of the fitted and deconvoluted gap function, which has been offset and multiplied by a constant scale factor for clarity. 93

3.12 Temperature dependence of RIXS spectra in the (7, 7, 8) Brillouin zone. (a): Stack plot of data normalized to intensity of intra-t_{2g} excitations at 0.7 eV, plotted with best fit to gap function model. (b): RIXS intensity at 60 meV (open diamonds) and 150 meV (filled triangles), which at 30 K correspond to the intra-gap and peak regions respectively. The peak intensity is consistent with a power law ($\beta \sim 0.4$), whereas the intra-gap intensity follows Arrhenius-type behaviour. Both models have critical temperature T_MI. (c): Normalized data with elastic and intra-t_{2g} contributions subtracted. Dashed line indicates the location of the MIT. There is a clear evolution of the lineshape from 30 K (bottom) to 300 K (top) as the gap closes. 96

3.13 Fits of RIXS spectra obtained at (7, 7, 8) and 30 K (a), or 275 K, with peak A described by a gap function (Eqn. 3.4). 97

3.14 Fits of RIXS spectra obtained at (7, 7, 8) and 30 K (a), or 275 K (b), with peak A described by a Fano resonance (Eqn. 3.5). 98

3.15 Comparison of fitted parameters for peak A. (a,b): Fits of peak A to a Fano resonance. (a): Energy of uncoupled resonance ω_0 (filled squares) and maximum of peak (open diamonds). (b): Intensity I_0, a power law with critical exponent $\beta = 0.36$ and critical temperature $T = T_{\mathrm{N}}$ is added as a guide. Inset: spectral weight taken from integral of Fano resonance. (c,d): Fits of peak A to a gap function (Eqn. 3.4). (c): Extracted parameters from fitted gap function ω_{gap} (filled squares) and ω_{p} (open diamonds). Solid line: Best fit with BCS function, $T_{\mathrm{MI}} = 230(4)$ K, $\Delta_0 = 87(2)$ meV. (d): Peak intensity as a function of T. The solid line is a guide to the eye. Inset: Spectral weight of gap as a function of T. 99

3.16 (a): Momentum dependence of the RIXS spectra, along with best fits of the data (solid line). Unexplained feature at 0.3 eV energy loss indicated by asterisk, which has **not** explicitly been accounted for in the fit. (b): Extracted parameters from fitted gap function ω_{gap} (filled squares) and ω_p (open diamonds). (c): Peak intensity (filled squares) and spectral weight (open circles) as a function of momentum transfer. 100

3.17 Fitted parameters of peak A as a function of temperature for three different momentum transfers: $L = (6.5, 7.5, 7.5)$ [purple circles], $\Gamma = (6.5, 7.5, 7.5)$ [pink stars], and $X = (6.5, 7.5, 7.5)$ [green squares]. Note that this is a different Brillouin zone to the temperature dependence displayed in Fig. 3.15. (a): Peak intensity as a function of temperature. The dashed line is guide to the eye. (b): ω_{gap} [solid symbols] and ω_{p} [open symbols] as a function of temperature. The dashed line is identical to that given in Fig. 3.15c. 100

3.18 Same layout as for Fig. 3.16, except fits include a Gaussian to account for the feature at 300 meV energy loss, which has been highlighted in (a). Open circles in (b) indicate its energy as a function of momentum transfer. 102

3.19 (a): Fits of the low-temperature data in the (6, 7, 7) Brillouin zone to the model given in the main text as a function of momentum transfer. Right panels show the energy (b) and integrated spectral weight (c) of peak A as a function of momentum transfer. Solid line is the best fit to a representative Hamiltonian given by Eqn. 3.7. 104

3.20 Results from simulated annealing runs performed for different system sizes of $Cd_2Os_2O_7$. All data displayed occurs from the mean of five successive runs, with error bars reflecting the standard deviation about this mean. Parameters plotted (per magnetic moment) are the specific heat C (a), isothermal susceptibility χ (b), and mean internal energy $\langle U \rangle$ (c). Curves in (a) and (c) have been offset for clarity. In (d) the fitted maximum of the specific heat (squares) and susceptibility (diamonds) has been plotted. Dashed lines indicate the experimental Néel temperature T_{N}. There appears to be a convergence of the calculated T_{N} with the experimental one in the thermodynamic limit. 105

4.1 (a): Crystal structure of $NaOsO_3$. The magnetic moments lie along the c-axis. (b): Unit cell volume through the MIT. (c): Lattice parameters through the MIT normalised to the value at T_{MI}. Subfigures (b) and (c) adapted from Ref. [131]. (d): Coupling of the magnetic, electronic, structural, and phonon degrees of freedom in $NaOsO_3$. Adapted from Ref. [132]. (e): Optical gap (purple squares) and charge gap (green circles) extracted from data presented in Refs. [57] and [130] respectively. Solid line is a Slater model with $E_g(T = 0) = 102$ meV and $T_{\mathrm{MI}} = 410$ K. 111

4.2 RIXS spectra from $NaOsO_3$, collected at 300 K as a function of varying incident energy ($\Delta E = 275$ meV). (a): RIXS map presented as a contour plot. Three peaks are evident: peaks A, B, and C correspond to intra-t_{2g}, $t_{2g} \to e_g$, and ligand-to-metal charge transfer (LMCT) excitations respectively. (b): Single RIXS spectrum obtained for an incident energy of 10.879 keV. 115

4.3 Temperature dependence of the orbital excitations (offset for clarity). (a): RIXS spectra out to 8 eV energy loss. Inset shows the fitted energy of peak B as a function of temperature. (b): Spectra focussing on the low energy excitations through the MIT. No significant difference can be seen as a function of temperature. 116

4.4 (a): Momentum dependence of the RIXS spectra in the (5, 3, 4) Brillouin zone at 300 K. Error bars on individual data points have been omitted for reasons of clarity. There is a strongly momentum dependent feature at ca. 100 meV which corresponds to a spin wave excitation. Solid lines are best fits to the data using the model described in the main text. (b,c): Representative fits at Γ and Y respectively. 118

4.5 Fitted energy (a) and intensity (b) of dispersive feature, along with best fit to spin wave model described in text (solid line). Inset illustrates exchange pathways J_1 and J_2. 119

4.6 Schematic of energy levels in a $5d^3$ material. The octahedral crystal field Δ splits the d-electron manifold into states with t_{2g} and e_g symmetry. The t_{2g} manifold is at half-filling, consequently the orbital angular momentum L is quenched in the LS (Russell-Saunders) coupling limit. Strong spin-orbit coupling can split these levels further, leading to $j_{\mathrm{eff}} = \frac{3}{2}$ and $j_{\mathrm{eff}} = \frac{1}{2}$ states. The orbital angular momentum is no longer quenched. $Cd_2Os_2O_7$ and $NaOsO_3$ are likely intermediate between these coupling schemes. 123

4.7 RIXS spectra collected at the Γ (a), Γ–Y (b), and Y (c) points of the Brillouin zone for various temperatures (300 K – 450 K). All data has been normalised to the intensity of the d-d excitations at 1 eV energy loss. There is a progressive increase in intensity at 0.2 eV with increasing temperature. (d): Intensity at points A (solid symbols) and B (open symbols) as a function of temperature. A and B correspond to the magnon peak and feature at 0.2 eV energy loss respectively. Solid and dashed lines are guides to the eye. 125

4.8 Analysis of RIXS spectra collected at Γ. (a): Spectra with elastic line and $d-d$ contributions subtracted. Added are the best fit to the data (black solid line), and relative components of the magnon peak (purple) and particle-hole continuum (green). (b): Spectra from the second run normalised to the intensity of $d-d$ excitations at 1 eV. Fitted peak intensity (c), energy (d) and FWHM (e) of the two components as a function of temperature. The two sets of symbols correspond to the first (open) and second (filled) runs respectively. Dashed lines indicate the metal-insulator transition at 410 K. 126

4.9 Analysis of RIXS spectra collected at $\Gamma-Y$. (a): Spectra with elastic line and $d-d$ contributions subtracted. Added are the best fit to the data (black solid line), and relative components of the magnon peak (purple) and particle-hole continuum (green). (b): Spectra normalised to intensity of $d-d$ excitations at 1 eV. Fitted peak intensity (c), energy (d) and FWHM (e) of the two components as a function of temperature. Solid lines are guides to the eye. Dashed lines indicate the metal-insulator transition at 410 K. 127

4.10 Analysis of RIXS spectra collected at Y. (a): Spectra with elastic line and $d-d$ contributions subtracted. Added are the best fit to the data (black solid line), and relative components of the magnon peak (purple) and particle-hole continuum (green). (b): Spectra normalised to intensity of $d-d$ excitations at 1 eV. Fitted peak intensity (c), energy (d) and FWHM (e) of the two components as a function of temperature. Dashed lines indicate the metal-insulator transition at 410 K. 128

4.11 Top panels: Schematic of the orientation of antiferromagnetically (AFM) interacting magnetic moments on a square lattice for $T = 0$, and finite temperatures in the Heisenberg or Stoner limits. Bottom panels: Excitation spectra in the Heisenberg limit, for an itinerant AFM (with insulating gap 2Δ), and for a metal with weak AFM correlations. Dashed lines indicate damped excitations. 129

5.1 Schematic phase diagram of the quantum non-linear sigma model as a function of temperature T and coupling strength g. The renormalized classical phase exhibits Néel long range order (LRO) at $T = 0$. The dashed line represents the 2DQHAFSL. 135

5.2 (a): Crystal structure of Sr_2IrO_4. The IrO_6 octahedra are rotated by $\pm 12^\circ$ in the ab-plane with respect to the ideal $I4/mmm$ structure; alternate layers have the opposite sign of rotation. The magnetic moments rigidly follow this distortion, which is highlighted in (b). (c,d): Magnetization (c) and resistivity (d) measurements by Cao *et al.* [21] on a single crystal of Sr_2IrO_4, which show significant anisotropy in the respective bulk properties. 140

5.3 Magnetic critical scattering data previously obtained by Fujiyama *et al.* [38]. (a): Intensity map in hl-plane of $(1, 0, 22)$ magnetic Bragg peak at 229 K. (b): In-plane (red squares) and out-of-plane (black circles) correlation length ξ_{a} above $T_{\mathrm{N}} = 228.5(5)$ K. Overlaid are the theoretical models for the 2DHAFSQL [167] (red), 2D XY model (green), and 2D Ising model (blue). A 2D Heisenberg model with $J = 100(10)$ meV apparently seems to give the best description of the in-plane data, whilst the out-of-plane correlation length ξ_{c} is best described by a power law with critical exponent $\nu = 0.748$, consistent with 3D interactions. 141

5.4 (a): Energy scan of the $(1, 0, 24)$ magnetic Bragg peak with σ–π' polarisation (symbols). Overlaid is the total fluorescence yield (TFY) from the sample (solid line). (b)–(d): Reciprocal space scans of the $(1, 0, 24)$ peak at 180 K, which was used to represent the resolution function. Nearby structural peaks exhibited similar behaviour. Added are the best fit (solid lines) of the data to either an asymmetric Lorentzian squared function (b,d) or an asymmetric Gaussian (c). Bars indicate the FWHM of the peak. 143

5.5 (a): Temperature dependence of $(1, 0, 24)$ magnetic Bragg peak for Sr_2IrO_4. Plotted are the integrated intensities for the in-plane (squares) and out-of-plane (diamonds) directions normalised to the in-plane scattering at 180 K. (b): Variation of χ^2 (squares) as a function of fits to $I_{\mathrm{M}} \propto [(T_{\mathrm{N}} - T)/T_{\mathrm{N}}]^{2\beta}$ using fixed values of T_{N}. The minimum of the χ^2 surface occurs at $T_{\mathrm{N}} = 226.8(2)$ K and $\beta = 0.195(2)$.144

5.6 (a): Observation of two order parameters for Sr_2IrO_4 as determined from rocking curves (η scans). Red and grey curves are the primary [$T_{\mathrm{N}} = 226.8(2)$ K, $\beta = 0.195(4)$] and secondary [$T_{\mathrm{c}} = 232.3(1)$ K, $\beta = 0.32(1)$] order parameters respectively. (b): Same as (a), but plotted on logarithmic axes and as a function of reduced temperature $\tau = (T_{\mathrm{c}} - T)/T_{\mathrm{c}}$. Open diamonds are Lorentzian squared components of scattering from h-scans. (c): Variation of χ^2 as a function of T_{c} (squares), with corresponding values of β (circles). 145

5.7 Comparison of scattering in-plane [(a)–(d), purple] and out-of-plane [(e)–(h), green], along with best fits to the data using the model described in the main text (solid line). The separate Lorentzian and Lorentzian squared components to the scattering are indicated by dashed and dotted lines respectively. A logarithmic y-axis has been used to highlight the two components. 146

5.8 (a): Correlation length of Lorentzian component both in-plane (purple squares) and out-of-plane (green diamonds) given in terms of the Ir-Ir distance $a_0 = 3.9$ Å. (b): Amplitude of Lorentzian (filled symbols) and Lorentzian squared (open symbols) components to observed scattering. Dashed line is the same as presented in Figure 5.6. Solid line in (a) and (b) is the best fit to the 2DAH model at high temperatures as plotted in Fig. 5.13. 147

5.9 Selected in-plane scans of the $(1, 0, 24)$ magnetic Bragg peak above T_N. Superimposed are the best fits to a Lorentzian convoluted with the resolution function (full width at half maximum represented by solid bars). 148

5.10 Comparison of critical scattering in-plane (a,b) and out-of-plane (c) for the $(1, 0, 24)$ magnetic Bragg peak (filled squares) with that presented in Ref. [38] for $(1, 0, 22)$ (open circles). The data have been normalised to fit on the same axes and allow a direct comparison of the lineshapes and peak widths. Note that a sloping background has also been subtracted from the Fujiyama *et al.* [38] data. 149

5.11 Comparison of various models for the 2DQHAFSL to the experimental data. (a): In-plane correlation length ξ. (b): Structure factor S_0. All models are calculated assuming $J = 60$ meV, with the structure factor predictions scaled such that they pass through the data point at 300 K. None of the theoretical models for the 2DQHAFSL are a satisfactory fit to the data for the entire temperature range studied. 150

5.12 (a): Experimentally determined correlation lengths ξ (filled circles) and best fit to 2D XYh_4 model (solid red line). The data from Fujiyama *et al.* [38] (open squares) divided by a factor a_0 and the QMC result for the 2DQHAFSL [167] with $J = 60$ meV (dashed black line) have been added as a guide. (b): Experimentally obtained amplitudes S_0 (filled circles) and best fit to 2D XYh_4 (solid red line). 152

5.13 (a): Experimentally determined correlation lengths ξ (filled circles) and best fit to 2DAH model (solid red line). The data from Fujiyama *et al.* [38] (open squares) and the QMC result for the 2DQHAFSL [167] with $J = 60$ meV (dashed black line) have been added as a guide. (b): Experimentally obtained amplitudes S_0 (filled circles) and best fit to 2DAH model. Dashed line is 2DQHAFSL model ($J = 60$ meV) scaled to pass through data point at 300 K. 154

5.14 (a,b): Magnon dispersion and intensity measured by Kim and colleagues [37] on Sr_2IrO_4. Parameters were obtained from fits to medium resolution data ($\Delta E = 130$ meV). Solid line in (a) is the best fit of the dispersion to a J–J'–J'' model with $J = 60$ meV, $J' = -20$ meV and $J'' = 15$ meV. (c): High resolution ($\Delta E = 30$ meV) RIXS data for Sr_2IrO_4 measured by Kim *et al.* [192] at normal incidence. Dots at ca. 0.5 eV indicate the spin-orbit exciton feature. The dispersive feature between 0 and 0.2 eV is the magnon peak. There appears to be a magnon gap of ~ 30 meV at $(0, 0)$, which has been highlighted. 156

5.15 (a): Stack plot of the low energy RIXS data from Kim *et al.* [192] fitted to the model described in the text (solid black lines). The fitted position of the magnon peak is shown as the solid red line. (b),(c): Representative RIXS spectra at $(0, 0)$ and $(\pi, 0)$, along with best fits to data and their respective components. The dashed line represents the magnon peak. (d): Magnon dispersion as a function of in-plane momentum transfer. (e): Spectral weight as a function of momentum transfer. Dashed lines in (d,e) represents the fitted model presented in Ref. [37]. 157

5.16 (a): Raw RIXS spectra [192] overlaid with the fitted magnon peak energy (orange squares), gapped (solid) and gapless (dashed) modes of the 2D XYh_4 model. (b): Spin wave dispersion as simulated in SpinW, which highlights the two distinct magnon modes. The simulated data has been convoluted with a Gaussian of FWHM 10 meV. The colour scale reflects the real part of the spin-spin correlation function components $S^{xx}(\mathbf{Q}, \omega) + S^{yy}(\mathbf{Q}, \omega) + S^{zz}(\mathbf{Q}, \omega)$. 158

5.17 (a): Raw RIXS spectra overlaid with the fitted magnon peak energy (orange squares), gapped (solid) and gapless (dashed) modes of the 2DAH. (b): Spin wave dispersion as simulated in SpinW, which highlights the two distinct magnon modes. The simulated data has been convoluted with a Gaussian of FWHM 10 meV. The colour scale reflects the real part of the spin-spin correlation function components $S^{xx}(\mathbf{Q}, \omega) + S^{yy}(\mathbf{Q}, \omega) + S^{zz}(\mathbf{Q}, \omega)$. 160

5.18 (a): Crystal structure of $Sr_3Ir_2O_7$. The material is a G-type antiferromagnet below T_N, as shown by the arrows on each Ir site. (b): Relationship between the $I4/mmm$ space group used for $Sr_3Ir_2O_7$ compared to the $I4_1/acd$ space group used for Sr_2IrO_4. The $I4_1/acd$ unit cell is enlarged by $\sqrt{2}a \times \sqrt{2}b$ and rotated by 45° with respect to the $I4/mmm$ unit cell. (c): Intensity of the $\left(\frac{1}{2}, \frac{1}{2}, 24\right)$ magnetic Bragg peak obtained from XRMS, compared to magnetisation data obtained from a SQUID magnetometer. Adapted from Ref. [233]. (d): In-plane resistivity of Sr_2IrO_4 and $Sr_3Ir_2O_7$. Adapted from Ref. [234]. 164

5.19 (a): Energy scan of the $\left(\frac{1}{2}, \frac{1}{2}, 24\right)$ magnetic Bragg peak with σ–π' polarisation (symbols). Overlaid is the total fluorescence yield (TFY) from the sample (solid line). Peaks marked with asterisks result from multiple scattering. (b)–(d): Reciprocal space scans of the $\left(\frac{1}{2}, \frac{1}{2}, 24\right)$ peak at 200 K, which was used to represent the resolution function. Nearby structural peaks exhibited similar behaviour. Added are the best fit (solid lines) of the data to either a Gaussian function (b) or Lorentzian squared functions (c,d). 166

5.20 (a): Order parameter of $\left(\frac{1}{2}, \frac{1}{2}, 24\right)$ magnetic Bragg peak in terms of the reduced temperature $|t| = |T - T_N|/T_N$, as obtained from θ–2θ scans. Solid line: Best fit to power law convoluted with a Gaussian distribution of T_N with FWHM 2.7(1) K. Dashed line: Corresponding power law assuming single value of T_N. Inset focusses on region around T_N, highlighting the rounding of the transition. Dotted line: Distribution of T_N. (b): Variation of χ^2 (solid line) and β (diamonds) as a function of T_N. The minimum of the χ^2 surface occurs for $T_N = 283.4(2)$ K and $\beta = 0.361(8)$, which is consistent with the theoretical value for 3D Heisenberg interactions. 167

5.21 Evolution of the $\left(\frac{1}{2}, \frac{1}{2}, 24\right)$ magnetic Bragg peak above T_N in the k- and l-directions (left and right columns respectively). The critical scattering is nearly isotropic. Solid lines are best fit to a Lorentzian-squared function convoluted with the resolution function. 168

5.22 Lineshape comparison of fits to critical scattering for the in-plane (a,c) and out-of-plane (b,d) directions. Solid line: Fit to Lorentzian scattering function. Dashed line: Fit to Lorentzian squared scattering function. Results are displayed on a logarithmic scale to highlight differences in the peak tails. 169

5.23 Values of χ^2 obtained using either a Lorentzian (squares), or Lorentzian squared (circles) lineshape for the scattering function along $\Delta Q_\perp$ (a) or $\Delta Q_{||}$ (b). A Lorentzian squared function provides the best fit to the data over most of the temperature range. 169

5.24 Inverse correlation length (a) and intensity (b) of $\left(\frac{1}{2}, \frac{1}{2}, 24\right)$ magnetic Bragg peak as a function of reduced temperature $t = T/T_N - 1$. Solid and dashed purple lines are fits of the out-of-plane data to the relevant power law for two different temperature regions: $\nu_1 = 0.49(4), \gamma_1 = 1.86(3)$; $\nu_2 = 1.4(1), \gamma_2 = 8.2(3)$. Solid black lines are best fit to a power law convolved with a Gaussian distribution of T_N [FWHM 2.7(1) K]. Inset in (b) is the same as the main panel, only plotted on linear axes. 170

6.1 Phase diagram for the hole-doped cuprates. There are expected to be a number of similarities between this phase diagram and that for the electron-doped iridates. Crossovers are indicated by dashed lines. There is a quantum critical point (QCP) situated underneath the superconducting dome. 174

6.2 Formation of doublon-hole pairs upon excitation with some pump pulse. Left panel: An electron is excited across the charge gap and populates the valence band. Right panel: This excited electron hops to a neighbouring site, leading to the formation a doublon-hole pair. These doublon-hole pairs then recombine on some ultrafast timescale ($\sim$ picoseconds) which depends on their energy of formation and their separation. 175

6.3 Power gain $P(z)$ as a function of undulator distance z for a high-gain XFEL. Labelled are the startup, self-amplified spontaneous emission (SASE) and saturation regions. The SASE region is characterised by an exponential gain in the FEL power as a function of z. After a critical distance $\sim 18L_{g0}$, the FEL power saturates as the electron beam begins to take energy away from the generated light wave. 177
6.4 (a): Comparison of the spectra of a single FEL pulse using a SASE or a seeded mode. (b): Temporal profile of two FEL pulses (different shades of purple), along with average over 120 pulses (black). FEL parameters used were obtained from Huang [246]. 178
6.5 Schematic time evolution of a system in a pump-probe experiment, with various physical processes labelled. The time scale of the various phenomena are dictated by the electronic bandwidth W, with the actual time in femtoseconds given as a ballpark figure. Adapted from [251]. 180
6.6 (a): Sample mount as used at SACLA. Labelled are the GaAs, Bi $(1, 1, 1)$ single crystals, and Sr_2IrO_4 thin film. (b): Experimental setup. 182
6.7 Schematic of a single-stage optical parametric amplifier (OPA) as described in the main text. WL stands for white light generator, DF for dichroic filter. The greyed out or bold type font after the non-linear crystal represents the attenuation of the pump and amplification of the seed respectively. 183
6.8 Rocking curves of $(0, 0, 28)$ (a) and $(-2, -2, 24)$ (b) structural Bragg reflections collected at SACLA. Solid lines are fits to Lorentzian functions. Also plotted is the fluorescence obtained at the Ir L_3 edge (c). 184
6.9 (a,b): Rocking curves about the $(-3, -2, 28)$ magnetic Bragg peak for delay times of -1 ps (open circles) and 1 ps (filled squares) collected at SACLA. The best Lorentzian squared fits to the data are given by the solid and dashed lines respectively. The pump fluences used were (a): 0.4 mJ cm^{-2} and (b): 6.8 mJ cm^{-2} respectively. Long-ranged magnetic order has been melted within this timescale at high pump fluences. (c): Intensity of the magnetic Bragg peak as a function of pump fluence, normalised to the intensity with the pump laser off. 185
6.10 Intensity of the $(-3, -2, 28)$ magnetic Bragg peak as a function of time delay focussing on short (left panel) and long (right panel) timescales. Different symbols correspond to different incident pump fluences. Two recovery timescales are apparent from the data out to long time delays. 185
6.11 Fitted parameters for Eqn. 6.3 as a function of pump fluence. Symbols and colours correspond to those plotted in Fig. 6.10. 186

6.12 Photograph of RIXS spectrometer constructed at the LCLS. The photograph has been annotated with the locations of key components and X-ray beam path. The helium flight path is in fact a dry cleaning garment bag obtained nearby, with any holes taped up to prevent leakage of gas. 188

6.13 Determination of the instrumental resolution. (a): CCD image of elastic line obtained from scattering off transparent adhesive tape (after thresholding). White box indicates region of interest used for subsequent plots. (b): CCD image summed over the non-dispersive direction. Solid line is a fit to a Gaussian with FWHM 8.09(5) px, equivalent to an instrumental resolution of 66.4(4) meV. (c): Peak position extracted from fits of single cuts through the elastic peak. Neighbouring pixels have been binned together to ensure a reliable fit. (d): Width of elastic line (symbols), with width extracted from fit shown in (b) added as a comparison (solid line). 189

6.14 (a): Histograms of the entire CCD (purple), and a 310×150 px region of interest (green), each summed over 1800×20 shots and before thresholding. (b): Raw CCD image (within the aforementioned region of interest) and lineplot of the sum in the non-dispersive direction resulting from a single run of 1800×20 shots. (c): Same as for (b), but with dark image subtracted and lower threshold of 160 ADUs applied. In (b) and (c), the extremes of the colorscale reflect the 5% and 95% confidence limits. Additionally neighbouring pixels have been binned together in the in-plane direction for clarity. 191

6.15 (a,b) Pump-probe RIXS spectra at (π, π) along with difference spectra $I_{\text{on}} - I_{\text{off}}$ (open symbols) for different optical delays. (c): Overlay of difference spectra for optical delays of 2 ps and 10 ps. Error bars have been omitted for clarity. (d): Fitted intensity of magnon peak normalised to intensity with no pump laser (symbols). Overlaid are models comprising Equation 6.3 with parameters interpolated from the elastic data for a pump fluence of 6 mJ cm^{-2} and convoluted with a Gaussian of FWHM 300 fs. The two models are identical apart from the value of C: $C = 1$ (solid), $C = 0.35$ (dashed). 193

6.16 (a): RIXS spectra at $(\pi, 0)$ before (purple squares) and after (green diamonds) the pump, along with their difference $\mathrm{I_{on}} - \mathrm{I_{off}}$ (open circles). The solid grey line is the difference between the best fits to the two RIXS spectra. (b): Enlarged view of the difference spectra at (π, π) (blue stars, dashed) and $(\pi, 0)$ (green circles, solid), each normalised to the fitted maximum of the magnon peak at E_0. (c): Same as (b), except normalised to fitted maximum of SO-exciton at $E_0 \sim 0.6$ eV. Again the dashed (solid) lines in (b,c) reflect the normalised difference between the best fits to the RIXS spectra at (π, π) and $(\pi, 0)$ respectively. 195

6.17 (a): RIXS spectra of $(Sr_{1\text{-}x}La_x)_2IrO_4$ at $(\pi, 0)$, collected for three doping levels $x = 0$, 0.01, 0.035. Solid lines are the best fit to a sum of four Lorentzian squared functions. The spectra have been offset vertically to aid comparison. Right panels reflect the magnon peak position (b), FWHM (c) and intensity (d) relative to the value for $x = 0$. Squares: values extracted from fits to data in (a). Triangles: data extracted from Ref. [256]. The solid(dashed) line on each of the plots represents the fitted value from the tr-RIXS data with pump laser on(off). 197

7.1 Pressure dependence of structural parameters for $NaOsO_3$. (a): Lattice parameters normalised to the zero pressure values at 300 K (lines) and 450 K (symbols). (b): c/a ratio at 300, 420 and 450 K. (c): Equation of state at 300, 420 and 450 K show minimal volume change as a function of temperature, with no obvious anomalies characteristic of a first-order phase transition. (d): Above the MIT an additional peak appears above 40 GPa which is consistent with a continuous monoclinic distortion. 201

List of Tables

1.1 Approximate values (in electronvolts) for the typical energy scales found in transition metal oxides. From left to right these are the electron correlation (Hubbard U), the crystal field splitting in an octahedral environment Δ_O, the ferromagnetic Hund's coupling J_H and the single-electron spin-orbit coupling parameter ζ. 37

1.2 Symmetry of orbitals for a MO_6 octahedral complex as obtained from a group theoretical analysis. 47

1.3 Approximate scaling of various sources of anisotropy (Refs. [66] and [65]), assuming a d^3 electronic configuration and uniaxial anisotropy. The relative magnitudes for these sources have been estimated using suitable parameters for $NaOsO_3$: $\lambda = \zeta/3 = 0.172$ eV, $\delta E = 3.7$ eV, $J = 21$ meV (see Chapter 4). 53

3.1 MRCI and MRCI + SOC relative energies (eV) for the Os^{5+} $5d^3$ multiplet structure in $Cd_2Os_2O_7$, as obtained by Bogdanov [106]. As cubic symmetry is lifted, the triplet states are split even without SOC. Each MRCI + SOC value stands for a spin-orbit doublet; for the ^4T states, only the lowest and highest components are shown. 79

3.2 Crystal field parameters (as obtained by spectroscopic methods), M–O bond distances, and M–O–M bond angles for $Cd_2Os_2O_7$ [96], the double perovskite Sr_2ScOsO_6 with Os^{5+} [108, 109], and the pyrochlore iridates $(Y,Eu,Pr)_2Ir_2O_7$ [86, 88, 110, 111]. All bond distances are given for ambient temperature. 84

4.1 Summary of fitting parameters for $NaOsO_3$, and obtained mean field Néel temperature T_N^MF. Note that the fits to the data involved either A or Γ as a free parameter; the other parameter was set to zero. The uncertainties for the $S = 1.0(1)\ \mu_\mathrm{B}$ row include both the uncertainty in the moment size and the errors obtained from the least-squares routine. 120

4.2 Approximate scaling of various sources of anisotropy (Ref. [65]), assuming a d^3 electronic configuration and that they are the sole source of uniaxial anisotropy. The relative magnitudes for these sources have been estimated using suitable parameters for $NaOsO_3$: $\lambda = \zeta/3 = 0.172$ eV, $\delta E = 3.7$ eV, $J = 21$ meV. 121

5.1 Comparison of microscopic parameters used in theoretical studies of $\mathrm{Sr_2IrO_4}$. All parameters assume zero tetragonal distortion $\delta = 0$ unless otherwise stated. Definitions used in some of the parameters calculated in this table: $U' = U - 2J_\mathrm{H}$, $J = 4t^2/U$, $\delta J_{xy} = J_{xx} - J$, $\delta J_z = J_{zz} - J$. 161

5.2 Comparison of anisotropy parameter Δ_λ derived from different theoretical studies and the parameters given in Table 5.1. All models show some degree of weak anisotropy. For reference $\Delta_\lambda = 1 - (J_{zz}/J_{xx}) = (\delta J_{xy} - \delta J_z) / (\delta J_{xy} + J)$. 161

5.3 Values of critical exponents for 3D systems as given by Collins [154]. 167

5.4 Scaling relations. Expected values are calculated from experimental values. Theoretical values for 3D Heisenberg model are obtained from Holm and Janke [242]. 172

Introduction

Transition metal oxides (TMOs) are an important source of novel electronic and magnetic phenomena which are of significant interest to experimentalists, theoreticians and engineers alike. These phenomena lead to a diverse range of potential practical applications; from thermochromic window coatings which filter out sunlight above a certain temperature (VO_2), to high temperature superconductivity in the cuprates, colossal magnetoresistance (CMR) and multiferroicity in the manganites for use in memory storage for instance.

Competition between electron correlation (which acts to localise electrons) and the bandwidth gives rise to the range of effects observed. $3d$ transition metal oxides are typically strongly correlated (large U/t), as a consequence of localised valence orbitals. Progressing down the periodic table, one generally finds that materials become less correlated (more itinerant), as a consequence of diffuse and extended d orbitals due to increased screening of the nuclear charge from the core orbitals. However this increased nuclear charge also gives rise to increased spin-orbit coupling (SOC). This relativistic phenomenon has the effect of narrowing the electronic bands and acting as the source of significant anisotropy in the magnetic Hamiltonian for $5d$ TMOs.

This competing behaviour is illustrated in Figure 1. At the left hand side of the diagram (weak spin-orbit coupling) are Mott insulators, band insulators and simple metals. In this region the leading electronic behaviour is mainly governed either by the interaction between electrons for the case of Mott insulators (large U/t), or by the interaction of electrons with the periodic lattice potential for band insulators and simple metals (small U/t). The majority of $3d$ transition metal oxides broadly fall within one of these two regimes. With increasing atomic number Z comes increased spin-orbit coupling and reduced electron correlations. Consequently spin-orbit coupling plays more of a role in the electronic Hamiltonian for $5d$ TMOs as opposed to $3d$ TMOs. Spin-orbit coupling can enhance the splitting between degenerate or nearly degenerate bands. In the case of weak U/t, this can give rise to topological insulating or semi-metallic states. Topological insulators are characterised by bulk insulating behaviour, yet exhibit conducting surface states as a consequence of broken time-reversal symmetry. These surface states are topologically protected as a consequence of band crossing at the Fermi level. A great deal of experimental and theoretical work has been performed on these materials over the past ten years [1–4].

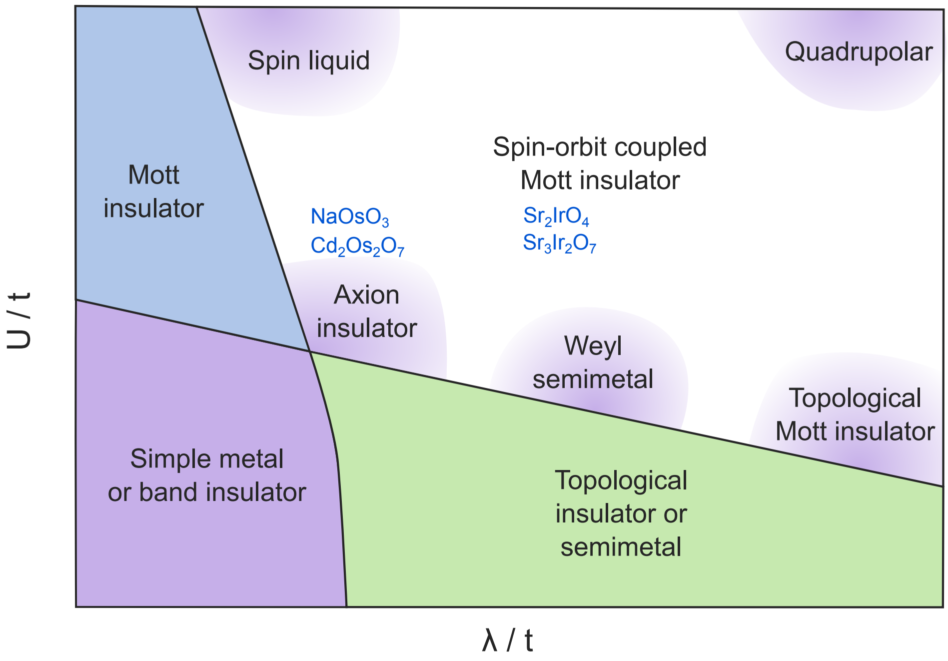

Figure 1: Schematic phase diagram for electronic materials as a function of the electron correlations U/t and the spin-orbit coupling λ/t, where t is the hopping amplitude. 5d transition metal oxides lie somewhere in the centre of the phase diagram, with approximate positions for the materials studied in this thesis highlighted in blue. Adapted from Ref. [5].

Upon increasing the electron correlation, further exotic electronic and magnetic phases become accessible. Notable examples include the Weyl semimetal (WSM) [6–11] and quantum spin liquid (QSL) phases [12–16], each celebrated in their own right and a continuing source of interest. In the middle of this phase diagram lie the spin-orbit coupled Mott insulators. Here the spin-orbit coupling and Coulomb repulsion compete to such an extent that there is evidence of a Mott-Hubbard insulating gap separating electronic states where spin-orbit coupling plays a leading role.

In truth Fig. 1 is a bit of an oversimplification; for 5*d* TMOs the local crystalline environment – with corresponding ligand field – and the Hund's coupling also play an important role. This means that 5*d* TMOs lie in a rich multidimensional phase space giving rise to a panoply of electronic and magnetic ground states. Seemingly weak perturbations to the Hamiltonian such as tetragonal or trigonal distortions of the crystal field can drive the system to a new paradigm within this phase space.

A prime example of this complex interplay of interactions is the electronic and magnetic behaviour of the perovskite iridates Sr_2IrO_4 and $Sr_3Ir_2O_7$. Remember that in a conventional band theory, one would expect these materials to be metallic as a consequence of the extended and diffuse valence orbitals. The 4*d* TMO Sr_2RhO_4 has Fermi liquid character [17–20], however bulk measurements on the isostructural Sr_2IrO_4 showed insulating behaviour all the way to 600 K [20–23]. This seemingly anomalous result is a direct manifestation of competition between the aforementioned energy scales, and in particular, the strong intrinsic spin-orbit coupling.

The theoretical framework behind this competition was built rather recently [24, 25]; in the meantime it has been used to explain the electronic and magnetic interactions in a number of iridates and other d^5 systems with significant spin-orbit coupling.

The $\mathbf{j_{\text{eff}} = 1/2}$ ground state

The starting point is the d-orbitals of a transition metal ion in a large octahedral crystal field. The role of this crystal field is to lift the orbital degeneracy such that two manifolds of t_{2g} and e_g symmetry are formed. If the crystal field is sufficiently large, then the five d-electrons only populate the three orbitals with t_{2g} symmetry. This leaves a single hole in the t_{2g} subspace, which has an effective angular momentum $L_{\text{eff}} = -1$: $|L_z = 0\rangle = |xy\rangle$, $|L_z = \pm 1\rangle = -\frac{1}{\sqrt{2}}(i\,|xz\rangle \pm |yz\rangle)$.

Now consider the effect of spin-orbit coupling on the t_{2g} states. In an intermediate coupling scheme, the degenerate t_{2g} manifold is separated into a $j_{\text{eff}} = \frac{3}{2}$ quartet and a $j_{\text{eff}} = \frac{1}{2}$ doublet.[1]. The $j_{\text{eff}} = \frac{3}{2}$ states are fully occupied with four electrons, whereas the j_{eff} states are half filled. In the hole representation, the $j_{\text{eff}} = \frac{1}{2}$ state is the ground state (Figure 2a)

Spin-orbit coupling entangles the spin and orbital components of the microscopic wavefunction. What this means is that the $j_{\text{eff}} = \frac{1}{2}$ ground state wavefunction is in fact a superposition of $|L_z = 0\rangle$ and $|L_z = \pm 1\rangle$ states. Furthermore, since the system has five d-electrons, Kramers theorem (a consequence of time reversal invariance) is realised and hence the $j_{\text{eff}} = \frac{1}{2}$ state is a Kramers doublet of states with mixed spin and orbital components. These can effectively be treated as spin-up and spin-down states $|j_{\text{eff}} = \frac{1}{2}, \pm\rangle$, also referred to as isospins. In the limit of ideal octahedral crystal symmetry, and for magnetic moments pointing along the local z-axis (in the octahedral reference frame), the wavefunction of the $j_{\text{eff}} = \frac{1}{2}$ state can be written [24] as:

$$|j_{\text{eff}} = \tfrac{1}{2}, \pm\rangle = \frac{\pm\,|xy, \pm\rangle + |yz, \mp\rangle + \mathrm{i}\,|xz, \mp\rangle}{\sqrt{3}}, \tag{1}$$

where ± indicates the spin polarisation, and the mixing of different spin and orbital components is readily apparent.

The fact that the ground state wavefunction is pseudo-cubic in real space, plus has mixed spin and orbital character, has important implications for the magnetic interactions in real systems. In particular, the role of anisotropic exchange is heavily dependent on the lattice geometry. Jackeli and Khaliullin [25] found that the exchange Hamiltonian for isospins situated on 180° TM–O–TM bonds contained both isotropic Heisenberg and weaker anisotropic pseudodipolar contributions, the latter arising purely from Hund's coupling. This contrasts with the case where spin-orbit coupling is a weak perturbation of the Hamiltonian, and anisotropy arises from expansion in powers of λ. Conversely, for isospins located on 90° TM–O–TM bonds, it was found that the isotropic Heisenberg part of the Hamiltonian exactly vanishes by symmetry, and only the anisotropic part remains. Furthermore the form of the remaining exchange interaction is dependent on the spatial orientation of the bond between the two isospins. For certain lattices

---

[1] From the Clebsch-Gordan series $j = |l - s|, |l - s| + 1, \ldots, l + s$.

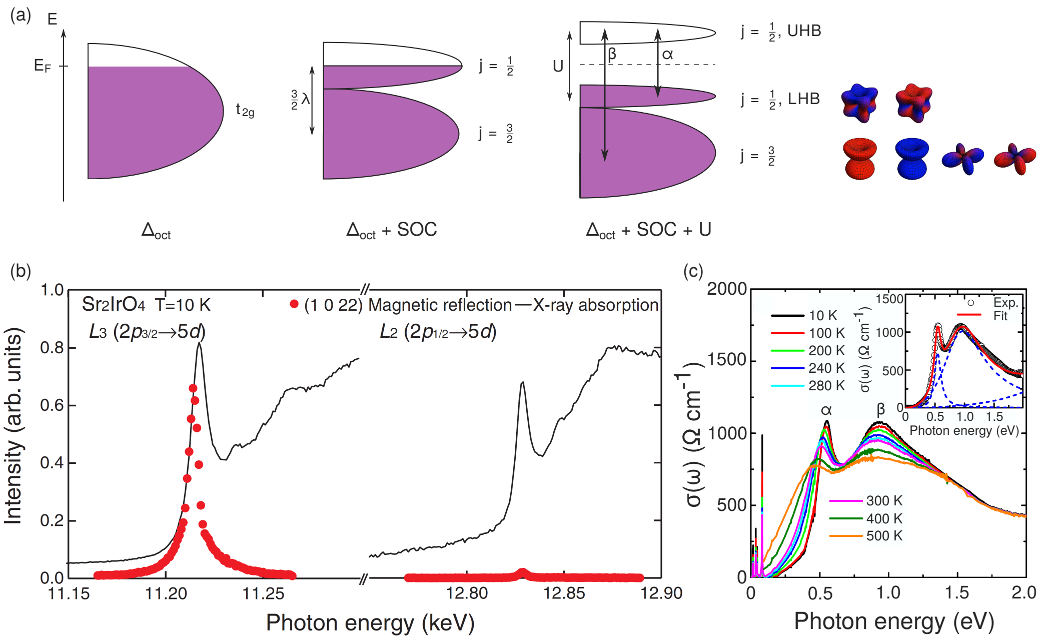

Figure 2: (a): schematic of energy levels for Sr_2IrO_4 and $Sr_3Ir_2O_7$, assuming a strong field scenario $\Delta_{oct} > \lambda > U$. Spin-orbit coupling splits the t_{2g} manifold into $j_{\mathrm{eff}} = \frac{3}{2}$ and $j_{\mathrm{eff}} = \frac{1}{2}$ states, the latter of which is half-filled. A weak electron correlation U is sufficient to open up an insulating gap at the Fermi level. The real space representation of the corresponding wavefunctions is also shown, with red/blue reflecting spin up/down contributions to the wavefunctions respectively. (b): RXMS data (red circles) and fluorescence (black solid line) obtained by Kim *et al.* [26]. Reprinted with permission from AAAS. There is a significant resonant enhancement at the L_3 absorption edge compared to the L_2 edge. (c): Optical conductivity measurements by Moon *et al.* [27], which show transitions between the UHB and LHB (α) and from the $j_{\mathrm{eff}} = \frac{1}{2} \to j_{\mathrm{eff}} = \frac{3}{2}$ states (β).

(honeycomb for example) this leads to extensive frustration, and can be directly mapped onto the Kitaev model, a theoretical model for a quantum spin liquid state [28–31].

There is significant experimental evidence for the $j_{\mathrm{eff}} = \frac{1}{2}$ state. Kim and colleagues [24], carried out angle-resolved photoelectron spectroscopy (ARPES) and X-ray absorption spectroscopy (XAS) measurements on Sr_2IrO_4, in order to measure the electronic band structure, and compared it with LDA+SO+U first-principles calculations. Their measurements revealed the opening of a gap of approximately 400 meV at the Fermi level, which they suggested was due a transition from a $j_{\mathrm{eff}} = 1/2$ lower Hubbard band (LHB) to an upper Hubbard band (UHB). This coincides with an optical transition at ca. 0.5 eV observed by Moon *et al.* [27, 32] (Figure 2c).

In a later work Kim *et al.* [26] examined the ratio of the scattering intensities for the (1 0 22) magnetic reflection at the iridium L_2 and L_3 edges using resonant magnetic X-ray scattering (RXMS). They found that there was a large resonant enhancement at the L_3 edge, but no appreciable enhancement at the L_2 edge (Fig. 2b). The magnetic signal from XRMS arises from the off-diagonal terms of the scattering matrix [33] and proposed that Sr_2IrO_4 was thus an example of a $j_{\mathrm{eff}} = \frac{1}{2}$ system, since the $L_3 : L_2$ ratio should be statistically equal to 2 if spin-orbit coupling is negligible.

However, Moretti Sala and colleagues [34] have recently suggested that the $L_3 : L_2$ ratio cannot be used as evidence for a $j_{\text{eff}} = \frac{1}{2}$ ground state in a system with arbitrary magnetic moment directions in the *ab*-plane. They determined that the RXMS intensity at the L_2 edge in the $\sigma - \pi'$ polarization channel is exactly zero, regardless of the tetragonal crystal field splitting of the t_{2g} states. Strictly speaking, the precise form of Equation 1 depends on the orientation of the magnetic moments in the octahedral reference frame. Moreover, the pure $j_{\text{eff}} = \frac{1}{2}$ state is only realised in the limit of an ideal octahedral environment. The addition of tetragonal or trigonal distortion Δ for instance changes the admixture of the orbital components and hence the ground state wavefunction. For $\Delta \gg \lambda$, the classical $S = \frac{1}{2}$ limit is recovered and there is no mixing in of the orbital component.

This competition between different energy scales is not limited to the case of $j_{\text{eff}} = \frac{1}{2}$ iridates, but occurs for the entire series of 5d TMOs. One of the most intriguing cases is that of the $d^3, S = \frac{3}{2}$ osmates. These materials have a half-filled t_{2g} manifold, which should nominally result in insulating behaviour as a consequence of the large Hund's coupling term and quenched orbital component to the magnetisation. However a number of osmates, including $Cd_2Os_2O_7$ and $NaOsO_3$ undergo metal-insulator transitions (MITs) concomitant with the onset of antiferromagnetic order. This is, at least in part, due to competition between Hund's coupling and the intrinsic spin-orbit coupling.

In $Cd_2Os_2O_7$, the onset of antiferromagnetic order likely results in a change in topology of the Fermi surface, also known as a Lifshitz transition. Such a transition is normally limited to metals, but the intrinsic spin-orbit coupling plays a direct role in the formation of the insulating state below $T_{\text{MI}} = T_{\text{N}}$. For $NaOsO_3$, the magnetic, electronic and structural degrees of freedom are coupled to such an extent that a 3D Slater MIT has been proposed by multiple authors. The Slater MIT mechanism requires that the onset of antiferromagnetic order itself drives the formation of an insulating gap below the Néel temperature.

The key concept that links all of the compounds studied in this thesis is the proximity of the MIT, and its influence upon the observed antiferromagnetic ground state and spin wave excitations. Furthermore these materials undergo MITs which depart significantly from a conventional Mott-Heisenberg picture as a direct result of competition between a number of energy scales.

However there remain a number of outstanding questions. The first of these refers to the precise nature of the MITs in $Cd_2Os_2O_7$ and $NaOsO_3$, which remain somewhat controversial. This includes the role of spin-orbit coupling, and the effect that antiferromagnetic correlations have within the respective MITs. The Slater transition is driven by the onset of antiferromagnetic order, yet implicitly assumes a weak coupling scenario. This is somewhat at odds with a situation where spin-orbit coupling is a relevant parameter in the electronic Hamiltonian.

The second is the dimensionality of the magnetic interactions in the perovskite iridates. It has been shown [35, 36] that the spin wave dispersion is strongly anisotropic in $Sr_3Ir_2O_7$, yet the behaviour in Sr_2IrO_4 has been claimed [37, 38] to be isotropic. This contrasts with the prediction by Jackeli and Khaliullin [25] of a pseudodipolar anisotropic term $\Gamma/J \approx 0.04$ for Sr_2IrO_4, which would give rise to a spin gap.

In this thesis, I attempt to answer these questions through resonant X-ray scattering techniques. Resonant X-ray scattering techniques lend themselves naturally to studies of $5d$ TMOs. Reasons for this include typically small samples which make neutron scattering measurements difficult, absorption edges that are sensitive to magnetic phenomena at easily accessible energies, and element and orbital specificity.

This thesis is divided into seven chapters. The first chapter introduces some theoretical background behind different mechanisms of metal-insulator transition, in particular those which are directly influenced by the onset of antiferromagnetism. Examples of these are the eponymous Slater and Lifshitz transitions. The effect of spin-orbit coupling on the magnetic and electronic degrees of freedom of the Hamiltonian shall also be discussed.

In the first part of chapter 2 I present a brief introduction into the X-ray resonant scattering formalism. In the second part, the characteristics of resonant (in)elastic X-ray scattering instruments will be discussed, focussing on two instruments at Diamond Light Source and the Advanced Photon Source (APS) where some of the work presented in this thesis was carried out. This concludes the theoretical aspects of the thesis.

Chapter 3–6 contain the main experimental results. These are in turn split into two sections: studies of osmates and studies of perovskite iridates. In Chapter 3, I present results of two sets of resonant inelastic X-ray scattering (RIXS) measurements on $Cd_2Os_2O_7$ at the Os L_3 edge. Low resolution RIXS measurements at the APS, combined with theoretical calculations from collaborators, reveal a non-dispersive feature consistent with an unusual type of magnetic excitation, which reflects an admixture of $\Delta S = 1,2,3$ spin-flip excitations. High-resolution RIXS measurements at the European Synchrotron Radiation Facility (ESRF) suggest however that the feature is more indicative of the optical gap and the Lifshitz metal-insulator transition, albeit with some evidence of more conventional $\Delta S = 1$ magnons.

Chapter 4 explores the magnetic and orbital excitations in $NaOsO_3$, which is proposed to undergo a Slater transition. RIXS measurements well below the Néel temperature reveal well-defined spin wave excitations, which have been modelled within a linear spin wave theory interpretation. These measurements reveal a large anisotropy, which manifests due to the interplay of single-ion, Dzyaloshinskii-Moriya and symmetric anisotropic exchange terms in the Hamiltonian. The temperature dependence of the RIXS spectra show an increase of high-energy spectral weight with increasing temperature, which is directly related to the onset of metallic and itinerant magnetic behaviour through the MIT. A potential model linking the behaviour in the antiferromagnetic insulating phase and paramagnetic metallic phase is briefly outlined.

Chapters 5 and 6 look at perovskite iridates. Chapter 5 contains magnetic critical scattering measurements on Sr_2IrO_4 and $Sr_3Ir_2O_7$ as probed by resonant magnetic X-ray scattering (RXMS). For Sr_2IrO_4, significant magnetic in-plane correlations are observed well above the

Néel temperature, which agree with previous measurements that imply isotropic 2D Heisenberg behaviour. However an extension to higher temperatures, coupled with a more rigorous treatment of the data, shows that the observed behaviour is in fact characteristic of a system with weak easy-plane anisotropy. Such an interpretation is quantitatively consistent with high-resolution RIXS measurements and a number of theoretical studies, and differs strongly from previous experimental conclusions. The magnetic critical scattering from the bilayer $Sr_3Ir_2O_7$ is more isotropic. Whilst the analysis is complicated somewhat by obvious rounding of the transition from antiferromagnetic to paramagnetic order, the magnetic interactions appear consistent with three-dimensional behaviour. This highlights the impact of the significant interlayer interactions present in $Sr_3Ir_2O_7$ compared to Sr_2IrO_4.

The final experimental chapter 6 focuses on time-resolved resonant scattering performed at X-ray free electron lasers (XFELs). These experiments include the first ever time-resolved RIXS (tr-RIXS) measurements ever performed in the hard X-ray regime. Using a 620 meV mid-infrared pump, it was possible to photo-dope a thin film of Sr_2IrO_4, induce a metal-insulator transition, melt the long-ranged magnetic order and probe the recovery dynamics as a function of optical delay and pump fluence. The two recovery timescales observed are characteristic of the magnitude of the in-plane and out-of-plane magnetic correlations, with an upper limit of the decay timescale set by the jitter of the XFEL. Furthermore there seems to be an effective mapping of the transient behaviour in the photo-doped state to an equivalent level of bulk electron doping in $Sr_{2-x}La_xIrO_4$.

The final chapter 7 briefly summarises the conclusions presented in this thesis and suggests future developments in this field.

Chapter 1

Correlations and spin-orbit coupling in 5d transition metal oxides

The electronic and magnetic properties of transition metal oxides (TMOs) are principally governed by five competing energy scales: the electron correlation U, the electronic bandwidth W, the crystal field environment (generalised as Δ), ferromagnetic Hund's coupling J_{H}, and the spin-orbit coupling ζ. The relative magnitudes of some of these interactions are summarised in Table 1.1.

As you go down the periodic table, the d-orbitals become more extended and diffuse (Fig. 1.1). This is a consequence of the increased screening that the orbital experiences due to the core electrons. As a result, there is increased probability that an electron can be found on a neighbouring site, so the kinetic energy term of the Hamiltonian increases, and hence the bandwidth W increases. Furthermore, since the orbitals are more diffuse, the correlation between different electrons decreases, so the electron correlation U decreases. Thus the ratio U/t decreases, and systems are expected to be more metallic as you move down the periodic table.

1.1 Metal-insulator transitions

Normally one thinks of materials as either insulators, semiconductors, or metals, depending on their electrical conductivity. Yet a number of materials undergo transitions between these seemingly discrete states as a function of temperature, carrier doping, pressure, or other intensive thermodynamic variables. These are collectively known as metal-insulator transitions (MITs), and are a prominent feature of TMOs. A few types of MITs are detailed below.

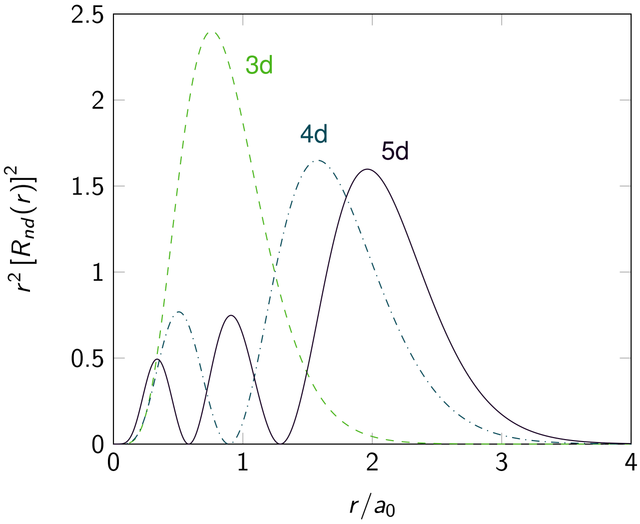

Figure 1.1: Radial distribution functions for nd-orbitals, where a_0 is the Bohr radius. The orbitals become more diffuse as you move down the group, with the number of radial nodes equal to $n-(l+1)$, where $l=2$ for a d-orbital.

	U	Δ_{O}	J_{H}	ζ
3d	6–7	1–1.5	0.8–0.9	0.05–0.1
4d	3–4	1.5–2	0.6-0.7	0.15–0.25
5d	1–2	2.5–3	0.5	0.4–0.5

Table 1.1: Approximate values (in electronvolts) for the typical energy scales found in transition metal oxides. From left to right these are the electron correlation (Hubbard U), the crystal field splitting in an octahedral environment Δ_{O}, the ferromagnetic Hund's coupling J_{H} and the single-electron spin-orbit coupling parameter ζ.

1.1.1 Mott-Hubbard transitions

The electronic and magnetic properties of transition metal oxides (TMOs) are not described adequately by an elementary tight-binding model; interactions between electrons must also be considered. A model that has been successfully used to model 3d TMOs is the eponymous single-band Hubbard model:[1]

$$\mathcal{H} = t\sum_{\langle ij\rangle,\sigma}\left(c^{\dagger}_{i\sigma}c_{j\sigma}+h.c.\right)+U\sum_{i}n_{i\uparrow}n_{i\downarrow}, \tag{1.1}$$

where the number operator $n_{i\sigma}=c^{\dagger}_{i\sigma}c_{i\sigma}$, t is the hopping integral, and U indicates the energy cost required to put two electrons on the same lattice site (a so-called doublon-hole pair). This model describes the competition between the two terms of the Hamiltonian: the kinetic (first) term wants to delocalise the electrons and create a conductor, whereas the interaction (second) term wants to force electrons to remain on a given site, and hence create an insulator. The conduction behaviour of a given system is partly determined by the relative strength of these

---

[1] Note that an exact solution for this Hamiltonian only exists in the one-dimensional case and at half-filling.

two interactions, and the band filling n. At some given ratio of U/t, and at half-filling ($n = 1$), we would expect a transition between metallic and insulating behaviour. This is indeed the case, and a Mott-Hubbard metal-insulator transition (MIT) is observed when $U/t \sim 1$. This can also be understood in terms of the bandwidth W. The bandwidth is proportional to t and the lattice coordination number z ($W = 2zt$ at half-filling). Increasing the kinetic energy (and hence the likelihood that electrons will hop to adjacent sites) increases the bandwidth, and at some critical point the individual bands will start to overlap with each other and form a metallic state. In the insulating state, antiferromagnetism arises naturally in the strong coupling limit ($U \gg t$) by treating the hopping term as a perturbation to second order. This leads to an effective Hamiltonian:

$$\mathcal{H}_{\text{eff}} = \text{const.} + \frac{4t^2}{U} \sum_{\langle nn \rangle} \mathbf{S}_i \cdot \mathbf{S}_j, \tag{1.2}$$

with the second term clearly reminiscent of a Heisenberg nearest-neighbour exchange Hamiltonian with exchange constant $J = 4t^2/U$. This is the basis for understanding the phenomenology of $3d$ TMOs, where the spin-orbit interaction can be treated as a weak perturbation, and often, neglected all together.

The MIT can often be tuned experimentally by varying either the ratio U/t, or the band filling n. Applying pressure for instance will compress the lattice and hence move ions closer to each other. Consequently the hopping probability will increase, and the ratio U/t will decrease. This implies a tendency to metallic behaviour at high pressure, and is an example of a bandwidth-controlled MIT. Conversely varying the filling number n through carrier doping for example can also induce an MIT. This is what is known as a band-filling controlled MIT.

The former case is illustrated in Figure 1.2 for a system at half filling ($n = 1$). For non-interacting electrons ($U/t = 0$) there is the simple case of a metallic band, filled up to the Fermi level, which in the case of $n = 1$, lies in the middle of the band. As the correlations increase, there is a change in the shape of the quasiparticle peak close to the Fermi level; spectral weight is transferred to incoherent features at $\pm U/2$. These will become the upper and lower Hubbard bands. A coherent portion of the density of states remains at the Fermi level consisting of well-defined quasiparticles. The width of the quasiparticle peak continues to decrease with increasing U/t, until some critical correlation strength U_c. At this point no states remain at the Fermi level and the system is insulating (Mott insulator).

In an ideal Hubbard model, the MIT is expected to be continuous. However in real materials the MIT is often sharply discontinuous (first-order), and often accompanied by some form of lattice distortion or the onset of antiferromagnetic order at the MIT. This can be explained, at least in part, by the fact that the ideal Hubbard model neglects coupling of the correlated electrons to the lattice. In this sense, it is frequently unclear whether the structural distortion is driven by the MIT, or vice versa.

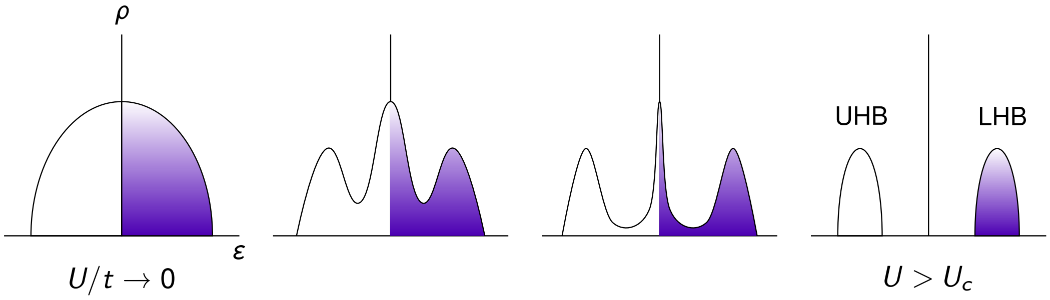

Figure 1.2: Schematic of a Mott-Hubbard transition for a system at half-filling within dynamical mean-field theory (DMFT). In the weak-coupling limit ($U/t \to 0$), there is the simple case of a metallic band, filled up to the Fermi level E_F. As U increases, spectral weight shifts towards two bands below and above E_F. These are the lower and upper Hubbard bands (LHB/UHB). A quasiparticle peak remains at E_F below some critical ratio U_c/t_c, with its width going to zero at the Mott-Hubbard transition.

1.1.2 Charge-transfer MIT

In the Mott insulator case presented in the previous section, only interactions between d electrons have been considered. Yet in real materials the transition metal cations are coordinated to intermediate ligands, whose valence p-orbitals have a finite interaction with the metal d-orbitals. Instead of considering a hopping from one d-orbital to another, consider what happens when an electron is transferred from the filled p-shell of the ligand to the metal site. This costs a *charge-transfer energy* Δ, defined as $\Delta = \epsilon_d - \epsilon_p + U_{dd}$, where $\epsilon_{p(d)}$ is the energy of the $p(d)$ electron levels, and U_{dd} is the correlation energy for the d-orbitals on the metal site. It can also be defined [39] as the energy required to go from the initial configuration $d^n p^6$ to the excited configuration $d^{n+1} p^5$. Such a model can also be formulated in terms of p and d holes, which has proved useful for the cuprates.

The character of any insulator [40] is governed by the smallest electronic energy scale in the system. In a Mott insulator, the Fermi level lies between the two Hubbard bands separated by U_{dd}, with the ligand p-levels well below the Fermi level. This case corresponds to the limit $U_{dd} < \Delta$. Consider instead what happens when $U_{dd} > \Delta$, that is, the ligand p-levels lie above the lower Hubbard band. In this case the most relevant excitation process involves the removal of a p-electron from the ligand, which is then transferred to the upper Hubbard band. This process creates a d-like quasiparticle and a p-hole, which are then free to propagate through the lattice. A substance which exhibits such behaviour is known as a *charge-transfer insulator*.

In a broad sense Mott insulator behaviour is most prevalent for early period TMOs, whereas charge-transfer insulator behaviour dominates for late period TMOs. For late period TMOs, the attractive potential is larger due to the increased nuclear charge. This leads to a large electron removal energy and hence reduced screening. There is relatively little difference in terms of the magnetic properties, in that the predominant behaviour tends to be antiferromagnetic superexchange, albeit with a slightly different mechanism where two holes are situated on the same ligand site in the intermediate state. The differences between the two become most apparent however upon hole doping. In the Mott-Hubbard regime, these holes would move to the metal site. However in the charge-transfer case, it is more favourable for the holes to be situated on a ligand site, which has ramifications for the electronic and magnetic properties. Just as for a Mott insulator, a metal-insulator transition can be induced through bandwidth or band-filling control. An example is the charge-transfer MIT undergone by $NdNiO_3$ as a function of applied pressure [41].

The metal-insulator transitions discussed thus far explicitly consider strong electron correlations U. The following examples of MITs are more relevant in the weak-coupling limit $U \to 0$.

1.1.3 Lifshitz transition

Prelude

A Lifshitz transition [42–44] is also known as an electronic topological transition (ETT), and is associated with a change of topology of the Fermi surface. Consider some arbitrary band structure with a bandwidth $W = \varepsilon_{\text{max}} - \varepsilon_{\text{min}}$. This band structure can be conveniently explained in terms of so-called equienergy surfaces: $\varepsilon^{(n)}(\mathbf{p}) = \varepsilon$, where $\mathbf{p}$ refers to crystal momentum and n indexes the band number. For real materials, there is significant variation in the topology and connectivity of equienergy surfaces as a function of ε as a consequence of electron repulsion and local electronic environment.

A change in topology occurs when ε coincides with a maximum or minimum of the equienergy surface $\varepsilon(\mathbf{p})$ at $\mathbf{p} = p_c$. If the longitudinal and two transverse effective masses m_i are all positive (electron carriers), then p_c corresponds to a local minimum. The resulting equienergy surface is ellipsoidal, and hence an electron pocket is formed (bottom row of Fig. 1.3). Conversely if the three effective masses are all negative (hole carriers), then p_c is a local maximum, and a hole pocket is formed. If however one of the effective masses differs in sign from the other two, then equienergy surfaces exist for $\varepsilon < \varepsilon_c$ and $\varepsilon > \varepsilon_c$. At one side of ε_c, a 'neck' is formed near p_c which has the shape of a hyperboloid with two sheets (top row of Fig. 1.3).

These maxima or minima are associated with a singularity in the electron density of states (DOS) per unit energy range $\nu(\epsilon)$ (Van Hove singularities). In the case of a free electron gas, $\nu(\epsilon)$ is proportional to $\sqrt{\epsilon}$:

$$\nu(\epsilon) = \frac{\sqrt{2}}{\pi^2}\frac{V}{\hbar^3} m^{3/2}\sqrt{\epsilon}, \tag{1.3}$$

where $m = m_1 = m_2 = m_3$ since the Fermi surface is isotropic. This can be extended to ellipsoidal constant energy surfaces in the vicinity of minima ($\epsilon > \epsilon_0$) or maxima ($\epsilon < \epsilon_1$):

$$\nu(\epsilon) = \begin{cases} \frac{\sqrt{2}}{\pi^2}\frac{V}{\hbar^3}\sqrt{m_1 m_2 m_3}\,(\epsilon - \epsilon_0)^{1/2}, & \epsilon > \epsilon_0 \\ \frac{\sqrt{2}}{\pi^2}\frac{V}{\hbar^3}\sqrt{m_1' m_2' m_3'}\,(\epsilon_1 - \epsilon)^{1/2}, & \epsilon < \epsilon_1. \end{cases} \tag{1.4}$$

It is clear this leads to a singularity of the type $\sqrt{\epsilon - \epsilon_k}$ near to ϵ_0, ϵ_1. What this means is that a new sheet of the constant energy surface (dis)appears for minima(maxima) above the critical

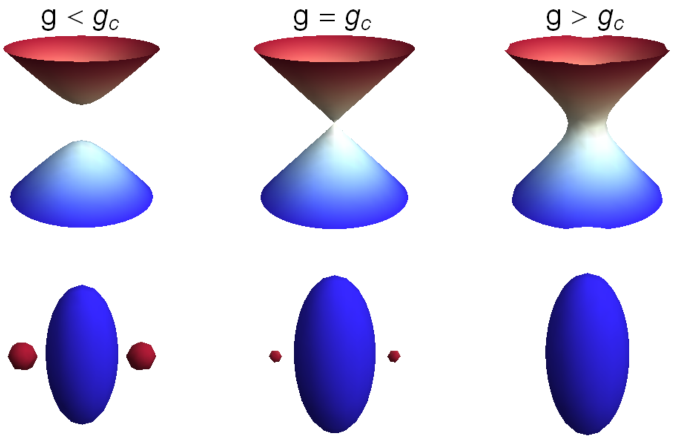

Figure 1.3: Illustration of the two types of Lifshitz transition tuned by some external parameter g. The top row depicts an open Fermi surface changing to a closed surface by disruption of a 'neck' (neck-forming type), whereas the bottom row depicts splitting off of a new portion of Fermi surface (pocket forming/vanishing type).

value ϵ_k. Such an analysis can also be extended to the 'neck disruption' case presented earlier with equivalent results.

Formation of Lifshitz transition

Now these singularities can occur anywhere within the band, and often they play little to no role in the bulk electronic properties of the material. However if ϵ_k lies close to the Fermi energy ϵ_F, then it may be possible to observe the change in band topology through the tuning of some suitable parameter g. Experimentally one can do this via a number of techniques, which include: application of external pressure [45], carrier doping [46], application of an external magnetic field [47], and temperature [48]. A simple schematic of a temperature-induced Lifshitz transition is given in Figure 1.4. At the point where $\epsilon_k = \epsilon_F$ one can observe anomalies in the thermodynamic and kinetic properties of the metal, as a consequence of the singularities in the density of states $\nu(\epsilon)$. Thermodynamic parameters which have been shown to be particularly sensitive to a change in the topology of the Fermi surface include the resistivity, thermoelectric power, thermal expansion coefficient and electronic specific heat.

It should be stressed at this point that the singularities in the DOS are defined precisely at $T = 0$; at finite temperature they are smeared out as a consequence of the Fermi-Dirac distribution of electrons. What this means is that a transition at finite temperature which shows Lifshitz-like behaviour cannot be considered as a transition in the classical sense within Landau theory[2]; it is more of a crossover between the two phases. Consequently the thermodynamic anomalies which are well defined at $T = 0$ are less apparent at finite temperatures.

---

[2] However within the Ehrenfest terminology it can be considered as a "$2\frac{1}{2}$ order" phase transition. This notation arises because the second derivatives of the thermodynamic potentials have a vertical kink at $\epsilon_F - \epsilon_k = 0$, and the third derivatives have a singularity $\sim (\epsilon_F - \epsilon_k)^{-1/2}$ [42].

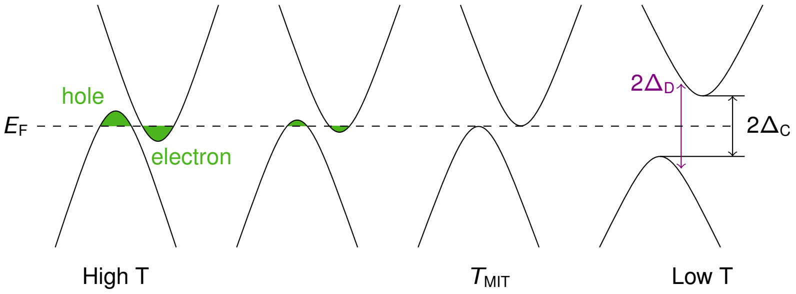

Figure 1.4: Model band structure describing a Lifshitz MIT. The electronic bands are uniformly shifted apart from each other with decreasing temperature, leading to the formation of an insulating gap. Here Δ_D and Δ_C refer to the direct (optical) and charge gaps respectively.

A true Lifshitz transition is an example of a quantum phase transition (QPT), with a quantum critical point at $T = 0$ and $g = g_c$ (Fig. 1.5). For $g > g_c$ the system is in a so-called quantum disordered regime, where well characterised quasiparticle excitations can be observed [49]. The majority of Lifshitz transitions observed experimentally are metal-metal transitions; this makes sense given that the original theory considers the case of non-interacting fermions. The presence of interactions, such as a Coulomb interaction U or spin-orbit coupling, would likely induce some form of semi-metallic, or even insulating, behaviour. It has been shown [50–53] that the Lifshitz transition can be driven weakly first order (at least in two dimensions) by the presence of interactions V at zero temperature, with a corresponding discontinuity observable in the electronic specific heat for Na_xCoO_2 as a function of doping x. The first order jump is predicted to decrease continuously with increasing temperature, eventually vanishing at some second-order critical point (T_c, V_c).

As an aside, rather than by tuning some external parameter, it is intriguing whether a Fermi surface reconstruction can be driven by the variation of some interaction strength. There are two possibilities: symmetry breaking transitions such as Pomeranchuk instabilities, and non-symmetry breaking transitions. The latter case includes continuous Mott transitions, which Yanagi [54] argues are simply Lifshitz transitions driven by the on-site Coulomb repulsion U for the two-dimensional Hubbard model.

The key points to remember are that a true Lifshitz transition is a continuous change in topology of the Fermi surface, and does not require any symmetry breaking. However it is strictly defined at $T = 0$ for the non-interacting case; transitions at finite temperature exhibit crossover behaviour, and may even be driven weakly first-order by the presence of interactions.

1.1.4 Slater transition

In contrast to a Mott transition, where variation of the bandwidth or filling parameter drives the MIT, Slater [55] argued that in certain cases, the onset of antiferromagnetic order may be sufficient to open up an insulating gap. The argument goes as follows. Imagine a one-dimensional system which can be divided into two interpenetrating sublattices. It is assumed that each site

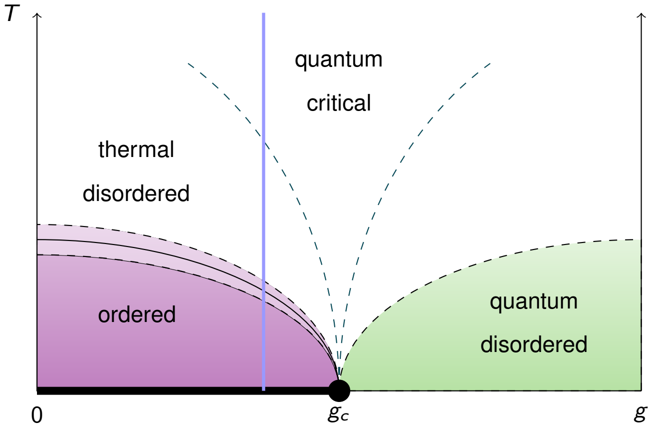

Figure 1.5: Phase diagram of a general quantum phase transition (QPT). At $T = 0$, a Lifshitz transition falls under these auspices. Dashed lines indicate crossovers between phases, since singularities in the electronic density of states are only infinite at $T = 0$. Solid blue line indicates proximity of certain 5d TMOs to the quantum critical point at $g = g_c$ and $T = 0$.

is at half-filling, and the sites are sufficiently far apart such that there is minimal interaction between sites ($U \to 0$). This latter point is the main distinction from the model examined earlier for the Mott transition. The spin-orbit interaction is also neglected in the first instance. Since spin-up and spin-down electrons mutually repel due to the Coulomb interaction, the two species of electrons arrange themselves on alternating lattice sites in order to minimize their interaction energy. Thus they form a spin-density wave (SDW) commensurate with the lattice. As a consequence the volume of the Brillouin zone is reduced by a factor of two, and the initial band is separated into two sub-bands at the zone boundary by the periodic potential between neighbouring ions. This results in insulating behaviour.

At finite temperatures (but still below the Néel temperature T_N), the two sublattices are partially disordered, but importantly, the electrons remain localised on each site. Consequently the charge gap decreases due to the reduction of the periodic potential. At the Néel temperature, long-ranged magnetic order disappears, and hence so does the periodic potential driving the insulating state. The system is now metallic and paramagnetic. Des Cloizeaux [56] derived an expression for the magnitude of the charge gap ϵ_g as a function of temperature which mirrors that obtained from the BCS theory of superconductivity:

$$\int_0^{\epsilon_c} \frac{\tanh\left(\frac{\beta}{2}\sqrt{\epsilon^2+\epsilon_g^2}\right)}{\sqrt{\epsilon^2+\epsilon_g^2}}\,\mathrm{d}\epsilon = \frac{\epsilon_c}{g}.$$

The variables ϵ_c and g are related to the bandwidth and Coulomb interaction between electrons respectively, and $\beta = 1/kT$. If one assumes that the charge gap goes to zero at the metal-insulator transition temperature T_MI, and that the system lies within the weak coupling regime, then the temperature dependence of the charge gap is given by [57]:

$$\frac{\epsilon_g(T)}{\epsilon_g(0)} = \tanh\left[\frac{T_\mathrm{MI}}{T}\frac{\epsilon_g(T)}{\epsilon_g(0)}\right]. \tag{1.5}$$

This model for a 1D Slater insulator contrasts with that required for a Peierls transition in that there is no structural distortion required for the MIT to occur.[3] Furthermore the Slater transition is continuous, as a consequence of the charge gap depending on the degree of magnetic order. The interpretation for the 1D Slater insulator can readily be extended to three dimensions, however Fermi surface nesting – which is a requirement for the MIT to occur – is much less prevalent [40]. Consequently there are few examples of these materials experimentally. However it shall be shown later in this thesis that there are some $5d$ TMOs which exhibit behaviour reminiscent of a Slater MIT.

1.2 Crystalline environment

The electronic and magnetic behaviour of transition metal oxides is directly linked to the local chemical environment of the transition metal ion. Thus far the discussion has been restricted to the electron repulsion U and the bandwidth $W \propto t$, and their role for a MIT. However there are other contributions to the electronic Hamiltonian which play a considerable role for $5d$ TMOs, starting with the crystal field interaction.

In a free atom, the five d orbitals are degenerate since the energy of these orbitals is directly related to the effective nuclear charge Z_{eff} that they experience: $E_{n,l} = -hcR_{\infty}Z_{\text{eff}}^2/n^2$. The shape of any particular d-orbital ($l = 2$) is related to a linear combination of spherical harmonics, along with $(n-3)$ radial nodes, where n is the principal quantum number. Ionising said atom and placing it in a spherically symmetric Coulomb potential raises the energy of all of the d-orbitals equally due to Coulomb repulsion.

Now consider what happens when that ion is placed in a molecular complex with non-spherical symmetry, for instance the octahedral MO_6 (symmetry O_h). For simplicity a Cartesian coordinate system is assumed. The d-orbitals on the metal site have a finite overlap with the valence $2p$ orbitals on the oxygen sites. The ligand p-orbitals point along the Cartesian axes $p_{\text{x,y,z}}$. Consequently p–d overlap (and therefore repulsion) is highest for those d-orbitals with lobes which also point along the Cartesian axes. These are the $d_{\text{x}^2-\text{y}^2}$ and d_{z^2} orbitals, which results in these orbitals having a higher energy compared to the spherical case. On the other hand, the lobes of the other three d orbitals (d_{xy}, d_{yz}, d_{xz}) point between the metal-ligand bonds. This leads to a reduced overlap, and effective stabilisation of the orbital compared to the spherical case.

What this means is that there is a splitting of the d-levels with respect to the free ion: a triply degenerate level and a doubly degenerate level higher in energy. From group theoretical arguments these levels are indexed as t_{2g} and e_g respectively, with the separation between them known as the octahedral crystal field splitting parameter. Qualitatively this analysis can be extended to any arbitrary symmetry by considering the irreducible representations of the metal d-orbitals for the relevant point group.

---

[3] In a Peierls transition, insulating behaviour is driven by dimerization of the lattice due to electron-lattice interactions.

1.2.1 Crystal field theory

Quantitative estimates of the orbital energies can also be made by making various approximations. The simplest treats the central metal ion and the surrounding ligands as point charges, and assumes purely Coulombic interactions. A detailed derivation is given in Hutchings [58], however briefly the argument goes as follows.[4] One can construct matrix elements of the form $\langle lm|V_{\mathrm{CF}}|lm'\rangle$, where V_{CF} is the crystal field potential operating on some state $|lm\rangle$. If these states are quantised along the fourfold symmetry axis, then the octahedral crystal field matrix is given by:

$$\mathcal{H}_{\mathrm{oct}} = \begin{bmatrix} Dq & 0 & 0 & 0 & 5\,Dq \\ 0 & -4\,Dq & 0 & 0 & 0 \\ 0 & 0 & 6\,Dq & 0 & 0 \\ 0 & 0 & 0 & -4\,Dq & 0 \\ 5\,Dq & 0 & 0 & 0 & Dq \end{bmatrix} \tag{1.6}$$

Diagonalising this matrix[5] one finds two sets of eigenvalues and eigenvectors: a triply degenerate set with energy $-4\,Dq$, and a doubly degenerate set with energy $6\,Dq$. These are equivalent to the t_{2g} and e_g states referred to earlier. Hence the separation between the t_{2g} and e_g levels in an octahedral crystal field is given by $\Delta_{\mathrm{CF}} = 10\,Dq$.

This treatment can be extended to any arbitrary symmetry, however the most applicable in this thesis are weak tetragonal (D_{4h}) and trigonal (D_{3d}) distortions away from an ideal octahedral environment. It should be emphasised at this point that we are considering weak perturbations; this will become especially apparent in the trigonal case. The reader is referred to the discussion by Perumareddi [59].

Tetragonal (D_{4h}) distortions

Consider the effect of an axial distortion along the z-axis for an octahedral complex. In our case the apical M–O bonds are elongated with respect to the equatorial bonds. Due to the increased M–O distance, the overlap (and therefore repulsion) in the z-direction is reduced compared to that in the basal plane. What this means is that those orbitals with components in the z-direction are stabilised, and hence have a lower energy. The distortion can be parametrised by two additional terms:

$$Ds = \frac{2}{7} Ze^2 \left\langle r^2 \right\rangle \left[\frac{1}{a^3} - \frac{1}{b^3}\right] \tag{1.8}$$

$$Dt = \frac{2}{7} Ze^2 \left\langle r^4 \right\rangle \left[\frac{1}{a^5} - \frac{1}{b^5}\right]. \tag{1.9}$$

---

[4] Note that the Russell-Saunders L–S limit is implicitly assumed.

[5] The widespread notation Dq is in fact a product of D and q:

$$* \; E(e_g) - E(t_{2g}) = 10\,Dq = \frac{35Ze^2}{4a^5}\frac{2}{105}\left\langle r^4 \right\rangle_{nd}. \tag{1.7}$$

The parameter D refers to the strength of the main component of the crystal field, while q arises from the ratio of certain matrix elements. In the above expression, $\langle r^\alpha \rangle_{nd} = \int r^\alpha r^2 \left|R_{nd}(r)\right|^2 \mathrm{d}r$ is the mean distance of the d-electron from the nucleus to the α^{th} power. The parameter a is the metal-ligand distance.

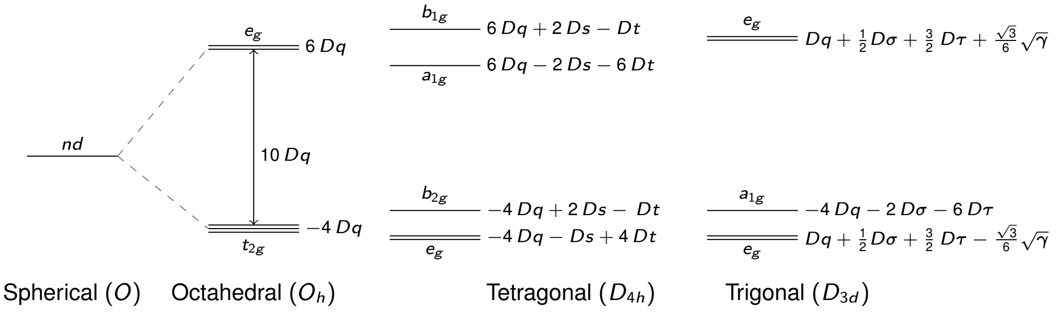

Figure 1.6: Schematic of crystal field splittings obtained for various symmetry environments, in the absence of correlation effects or spin-orbit coupling. Tetragonal (D_{4h}) and trigonal (D_{3d}) distortions are assumed as weak perturbations from the octahedral case. The tetragonal and trigonal energy levels as drawn are appropriate for axial elongation along the z-axis or local three-fold symmetry axis respectively. The term γ arises from the contribution of off-diagonal parameters, and is defined [60] as $\gamma = 300\,Dq^2 - 20\,Dq(3D\sigma - 5D\tau) - 3(3D\sigma - 5D\tau)^2$.

Here a is the in-plane metal-ligand distance, and b is the metal-ligand distance along the axial z-direction. Notably Ds and Dt are positive for an elongated octahedron, and negative for a compressed octahedron. One can then construct the crystal field matrix analogously to the cubic case, simply by summing the octahedral and tetragonal matrix elements:

$$\mathcal{H}_{\text{tet}} = \begin{bmatrix} Dq+2\,Ds-Dt & 0 & 0 & 0 & 5\,Dq \\ 0 & -4\,Dq-Ds+4\,Dt & 0 & 0 & 0 \\ 0 & 0 & 6\,Dq-2\,Ds-6\,Dt & 0 & 0 \\ 0 & 0 & 0 & -4\,Dq-Ds+4\,Dt & 0 \\ 5\,Dq & 0 & 0 & 0 & Dq+2\,Ds-Dt \end{bmatrix} \tag{1.10}$$

Trigonal (D_{3d}) distortions

In a similar fashion, one can perform a distortion along the local three-fold symmetry axis. This is known as a trigonal distortion. Consider the weak-field case, in which the trigonal distortion is much smaller than the octahedral distortion ($\Delta_{\text{O}} \gg \Delta_{\text{trig}}$). If the trigonal axis is chosen as the axis of quantisation, then:

$$\mathcal{H}_{\text{trig}} = \begin{bmatrix} -\frac{2}{3}Dq+2\,D\sigma-D\tau & 0 & 0 & -\frac{10\sqrt{2}}{3}\,Dq & 0 \\ 0 & \frac{8}{3}Dq-D\sigma+4\,D\tau & 0 & 0 & \frac{10\sqrt{2}}{3}\,Dq \\ 0 & 0 & -4\,Dq-2\,D\sigma-6\,D\tau & 0 & 0 \\ -\frac{10\sqrt{2}}{3}\,Dq & 0 & 0 & \frac{8}{3}Dq-D\sigma+4\,D\tau & 0 \\ 0 & \frac{10\sqrt{2}}{3}\,Dq & 0 & 0 & -\frac{2}{3}Dq+2\,D\sigma-D\tau \end{bmatrix} \tag{1.11}$$

The parameters $D\sigma$ and $D\tau$ are defined analogously to the tetragonal parameters Ds and Dt.

A summary of all the energy levels obtained upon diagonalising these crystal field matrices is plotted in Fig. 1.6.

1.2.2 Molecular orbital theory

However crystal field theory considers both the TM ion and the coordinating ligands as point charges – the ionic limit. In reality the atomic orbitals (AOs) of the transition metal ion and the ligand interact with each other and mix. This can be described within a *molecular orbital theory*.

Consider a perfect octahedral ligand environment (O_h point group). Within the O_h point group, certain orbitals transform as the representations listed in Table 1.2. Orbitals with the same symmetry mix and repel each other. Two sets of molecular orbitals (MOs) are formed: bonding MOs when the AOs overlap in phase, and anti-bonding MOs, where the AOs overlap out of phase. If the overlapping AOs are oriented parallel to the metal-ligand bond, then this is known as σ-bonding, whereas if the overlapping AOs are oriented perpendicular to the metal-ligand bond, then this is known as π-bonding.

TM orbital	Γ_i	Ligand orbital	Γ_i
5d	$t_{2g} \oplus e_g$	O 2p (σ-bonding)	$a_{1g} \oplus e_g \oplus t_{1u}$
6s	a_{1g}	O 2p (π-bonding)	$t_{2g} \oplus t_{1u}$
6p	t_{1u}	O 2p (non-bonding)	$t_{1g} \oplus t_{2u}$

Table 1.2: Symmetry of orbitals for a MO_6 octahedral complex as obtained from a group theoretical analysis.

Since the 5d orbitals with e_g symmetry on the TM cation ($d_{x^2-y^2}$ and d_{z^2}) point directly at the ligands, there is a strong overlap – and hence hybridisation – with the ligand 2p-orbitals. This leads to the occupied bonding (predominantly O 2p character) MO being pushed downwards in energy, and unoccupied anti-bonding (predominantly TM 5d character) MO pushed upwards in energy relative to the respective AO. There is a similar effect for orbitals with t_{2g} symmetry (d_{xy}, d_{yz} and d_{xz}); however since these orbitals point between the O 2p ligands, there is reduced overlap and hence reduced hybridisation. What this means is the effective octahedral crystal field splitting Δ_O is increased within a molecular orbital picture compared to crystal field theory as a result of electron repulsion.

1.2.3 Ligand field theory

Whilst crystal field theory does reproduce a number of the features observed in ultraviolet-visible spectroscopy of $3d^1$ TMO complexes for example, the method does not work as well for many-electron ions. This is because orbital overlap between the metal and ligand ions is neglected, as is the effect of electron-electron repulsion. Similarly molecular orbital theory is frequently unsatisfactory due to its complexity, and the fact that it is more suited to neutral molecules – the covalent limit.

Real TMOs are intermediate between these two extremes. Consequently *ligand field theory* has been developed, which is predominantly based on crystal field theory, but takes electron-

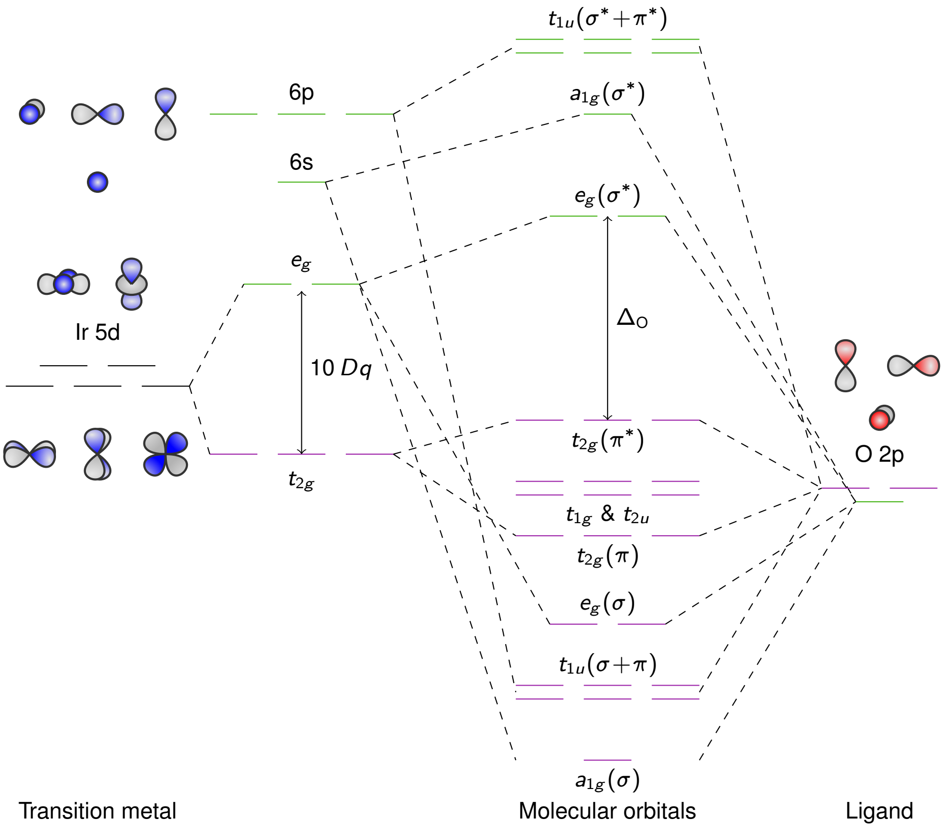

Figure 1.7: Molecular orbital (MO) diagram of a 5d TMO cation octahedrally coordinated to six oxygen ligands. The MOs are hybridised, and have character arising both from the transition metal and ligand atomic orbitals. Adapted from Katukuri [61].

electron repulsion into account. Such a theory has worked very well for 3d TMOs in particular. A concise description follows.

Consider a d^2 complex in a strong octahedral crystal field. We already know that the d-electron manifold is split into two sets of levels with t_{2g} and e_g symmetry. It follows that the d-electrons be configured as: t_{2g}^2, $t_{2g}e_g$ or e_g^2, each separated in energy by 10 Dq. However the Pauli exclusion principle forbids two electrons with the same spin state to occupy the same orbital. To first order in a perturbation theory, electron-electron repulsion splits the t_{2g}^2 level into four terms. Group theory predicts that the nine-dimensional representation $t_{2g} \otimes t_{2g}$ can be reduced[6] into four irreducible representations: $t_{2g} \otimes t_{2g} = {}^1a_{1g} \oplus {}^1e_g \oplus {}^3t_{1g} \oplus {}^1t_{2g}$. Each term is associated with an appropriate many-electron wavefunction. Consequently to calculate the effect of Coulomb repulsion, one calculates matrix elements such as $\langle t_{2g}^2\,{}^1a_{1g}|\mathcal{H}|t_{2g}^2\,{}^1a_{1g}\rangle$ for each of the symmetry-allowed terms. These simplify into combinations of the Coulomb and exchange two-electron integrals, and the process can be extended to the $t_{2g}e_g$ and e_g^2 levels.

By making the approximation that the t_{2g} and e_g many-electron wavefunctions have pure d-character – or in other words, weak hybridisation – then the two-electron integrals can be

---

[6] The direct product of the representations Γ_1 and Γ_2 is a representation whose basis consists of the products $\varphi(\Gamma_1\gamma_1)\,\varphi(\Gamma_2\gamma_2)$ [62].

reduced into three semi-empirical parameters. Depending on the notation used, these can be given as combinations of the related Slater-Condon parameters F_0, F_2, F_4 or Racah parameters A, B, and C. In this thesis, the Racah parameters shall be used as they are more frequently used in spectroscopy. The parameter A is an average of the total interelectronic repulsion; it can be neglected if we are only interested in the separation between levels.

One complication is that terms with the same symmetry can mix and mutually repel one another. This is known as *configuration mixing*, and results in a shift of the energy levels compared to the case with non-repeating terms. Hence in order to accurately calculate the energy levels for a given term, one has to solve the complete set of secular equations containing the interaction between the different states.

A key assumption has been made in the simplification of the two-electron integrals into Racah (Slater-Condon) parameters: that the t_{2g} and e_g many-electron wavefunctions have pure d-character, i. e. weak hybridisation. Whilst this assumption works well for the localised d-orbitals in $3d$ TMOs, it is likely not as successful for more itinerant $5d$ TMOs. This is a limitation of the model.

1.3 Hund's coupling (J_H)

In the limit of weak spin-orbit coupling, the electronic ground state of a system can be conveniently determined through the use of Hund's rules. These three simple rules have in fact been utilised previously in this chapter, yet not explicitly referred to. The first of these states that for a given shell, those electronic configurations which maximise the total spin S lie lowest in energy, provided that they are consistent with the Pauli exclusion principle. This can be understood simply in terms of Coulomb repulsion: electrons with parallel spins will want to be situated in different orbitals, hence minimising Coulomb repulsion and lowering the overall energy of the system. An alternative way of phrasing this is that there an energy cost associated with putting two electrons in the same orbital, which is parameterised by the Hund's coupling J_{H}. Assuming a spherically symmetric interaction, and $t_{2\mathrm{g}}$ wavefunctions obtained from crystal field theory, then J_{H} can be expressed[7] in terms of the Racah parameters: $J_{\mathrm{H}} = 3B + C$.

Consider two isolated transition metal atoms, and in particular, what happens when one electron is transferred from one to the other. Assume that the ground state has the maximum value of S^z, as required by Hund's rules. Furthermore assume all electrons are located in the t_{2g} manifold, with large separation from the empty e_g manifold. This corresponds to a low-spin electronic configuration applicable for $5d$ transition metal oxides. For systems at less than half filling, the ground state energy only involves the pairwise interactions between parallel spins. Filling all the orbitals with parallel spins lowers the total energy of the system. Consequently the

---

[7] There is a technicality which should be addressed [63]. There is a difference in definition of the Hund's coupling depending on whether a single t_{2g} manifold or the entire d-shell is considered [64]. For an entire d-shell, it is customary to define the Hund's coupling $J_{\mathrm{H}}^d = \frac{1}{10}(35B + 14C)$, along with an additional parameter $C_d = 9B/2$. The two definitions for the Hund's coupling are related by the expression $J_{\mathrm{H}} = 5J_{\mathrm{H}}^d/7 + C_d/9$.

effective Hubbard interaction $U_{\text{eff}} = U - 3J_{\text{H}}$ is reduced compared to the case of zero Hund's coupling. Similar behaviour occurs for systems at more than half filling as a consequence of particle-hole symmetry.

The situation is quite different for the case of exactly half filling $\left(t_{2g}^{3}\right)$. The excited state $\left(t_{2g}^{4}\right)$ involves one doubly-occupied orbital; hence its energy is pushed up with respect to the ground state. The conclusion is that for systems at half filling, $U_{\text{eff}} = U + 2J_{\text{H}}$ is *enhanced* with the inclusion of a finite Hund's term. In practice this means that only a small Hubbard U term is necessary to open up an insulating gap in t_{2g}^{3} transition metal oxides (in the absence of spin-orbit coupling).

1.4 Spin-orbit coupling (SOC)

Spin-orbit coupling is another important energy scale for $5d$ TMOs. For a single-electron atom, the effect of spin-orbit coupling is to couple the spin and angular momenta ($\vec{\mathbf{s}}$ and $\vec{\mathbf{l}}$ respectively) of a given electron into a total angular momentum $\vec{\mathbf{j}} = \vec{\mathbf{l}} + \vec{\mathbf{s}}$. The relativistic spin-orbit interaction is governed by the Hamiltonian $\mathcal{H}_{\text{SO}} = \sum_i \zeta_i \vec{\mathbf{l}_i} \cdot \vec{\mathbf{s}_i}$, where the sum runs over all electrons.

For a many-electron atom one obtains the total angular momentum $\vec{\mathbf{J}}$, not $\vec{\mathbf{j}}$. There are two limiting coupling schemes: Russell-Saunders (L–S) coupling, and jj coupling. Within Russell-Saunders coupling, the total spin $\vec{\mathbf{S}}$ and total orbital momentum $\vec{\mathbf{L}}$ are determined from the sum of the individual spin and orbital momenta: $\vec{\mathbf{S}} = \sum_i \vec{\mathbf{s}_i}$ and $\vec{\mathbf{L}} = \sum_i \vec{\mathbf{l}_i}$. These are then summed together to form $\vec{\mathbf{J}} = \vec{\mathbf{L}} + \vec{\mathbf{S}}$. For jj coupling, the spin-orbit interaction is deemed to be stronger than spin-spin or orbital-orbital couplings. Consequently for a single electron $\vec{\mathbf{j}_i} = \vec{\mathbf{l}_i} + \vec{\mathbf{s}_i}$. These total angular momenta $\vec{\mathbf{j}_i}$ are then summed to obtain the atomic total angular momentum $\vec{\mathbf{J}} = \sum_i \vec{\mathbf{j}_i}$.

Generally speaking Russell-Saunders coupling is appropriate for systems with weak spin-orbit coupling, whereas jj-coupling is more applicable for systems with large spin-orbit coupling.[8] An oft-quoted statement is that the spin-orbit coupling scales with Z^4, where Z is the nuclear charge:

$$\zeta_{nl} = \frac{\alpha^2 R_\infty Z^4}{n^3 l \left(l + \frac{1}{2}\right)(l+1)}, \tag{1.12}$$

where α is the fine structure constant, R_∞ is the Rydberg constant, n is the principal quantum number, and l the orbital angular momentum quantum number. Strictly speaking this is only the case for a single-electron atom of nuclear charge Z with hydrogenic orbitals. For many-electron atoms the appropriate spin-orbit operator in the Russell-Saunders scheme is given by $\mathcal{H}_{\text{SO}} = \lambda \vec{\mathbf{L}} \cdot \vec{\mathbf{S}}$. The two spin-orbit coupling parameters are related by the expression $\lambda = \pm\zeta_{nl}/2S$, with λ positive if the valence shell is less than half-full, and negative if the valence

---

[8] The crossover between the schemes is approximately when the spin-orbit coupling is of similar magnitude to the interelectronic repulsion. The electronic behaviour of a number of materials however can be explained in terms of an *intermediate coupling* scheme, which has characteristics of both Russell-Saunders and jj-coupling. This is somewhat complex, so the present discussion is limited to the two limiting cases.

shell is more than half full (Hund's third rule). Consequently atoms of the same type, but in different valence states, will have different values of λ. The role of SOC both for the electronic and magnetic behaviour of $5d$ TMOs shall now be examined.

1.4.1 Effect of SOC on electronic behaviour

As previously discussed, the role of spin-orbit coupling is to entangle the spin and orbital components of the angular momentum of an electron. Depending on the strength of this interaction compared to the inter-electronic repulsion (parameterised by Racah parameters), SOC acts either as a perturbation of the electronic energy levels – leading to fine structure – or is a leading contribution to the electronic Hamiltonian.

Russell-Saunders limit

It is instructive to start with the case of zero SOC for an isolated atom.[9] For a free-ion (SO_3 symmetry), the d-orbitals are degenerate. Electron-electron repulsion breaks the degeneracy of the d-orbitals, and leads to the formation of free-ion terms ^{2S+1}L characterised by the angular momenta of the electrons within that term. The ordering and ground state of the free-ion terms are determined by Hund's rules. Each term has a total degeneracy of $L \times S$. Inclusion of SOC breaks this degeneracy such that they are split into levels $^{2S+1}L_J$, with their order again determined by Hund's rules.

Incorporation into a crystalline lattice gives rise to a crystal field interaction as discussed earlier. It is assumed that the crystal field interaction is stronger than the spin-orbit coupling, which holds true for the materials studied in this thesis. In the weak field limit $E_{\mathrm{ee}} > E_{\mathrm{CF}} > E_{\mathrm{SO}}$, where E_{ee} refers to the inter-electronic repulsion. The effect of the crystal field is to branch the free-ion terms with SO_3 symmetry into the corresponding irreducible representations of the point group for the crystal field. These new terms are then split by the spin-orbit interaction. Although the discussion thus far has focussed on the weak field limit, it is equally applicable to the strong field limit where $E_{\mathrm{CF}} > E_{\mathrm{ee}}$. Spin-orbit coupling simply acts as a perturbation to the symmetry-adapted terms.

jj-coupling

In the jj-coupling limit however, the inter-electron repulsion is weaker than spin-orbit coupling. The energy levels of the free-ion are not described by term symbols $^{2S+1}L_J$, but instead by levels $(j_1, j_2, \ldots j_{\mathrm{n}})_J$, where j_{n} is the total angular momentum of one of the electrons. Each of these levels can be directly related to states in the Russell-Saunders limit $\left(^{2S+1}L_J\right)$, since the number of available states is independent of the coupling scheme used.

Assuming that the crystal field is smaller than the spin-orbit coupling, then one can treat it using the eponymous Stevens parameters O_l^m. Within this treatment the crystal field (operator

---

[9] This corresponds to the weak crystal field limit.

equivalent) Hamiltonian is given by $\mathcal{H}_{\text{CF}} = \sum_{lm} B_l^m O_l^m$, with B_l^m parameters either obtained from experiment or determined within a point-charge model. Fortunately the number of these parameters is strongly restricted by symmetry arguments.[10]

5*d* TMOs

However for iridates and osmates, the crystal field ($\sim$ 4 eV) is much stronger than both the spin orbit coupling ($\zeta \sim$ 0.5 eV) and the electron-electron repulsion (B, $C \sim$ 0.1–0.2 eV). Consequently neither Russell-Saunders or jj-coupling is strictly correct. A more appropriate model is to start from the t_{2g} and e_g states of the d-electron manifold. Depending on the magnitude of $\lambda = \pm\zeta/2S$, then one either applies spin-orbit coupling or electron-electron repulsion as the next perturbation to the Hamiltonian. The remaining interaction then acts as a further perturbation.

Take the t_{2g} manifold as an example. If $\lambda > B$ and C, then to first order the t_{2g} states are split into a $j_{\text{eff}} = \frac{1}{2}$ doublet and $j_{\text{eff}} = \frac{3}{2}$ quartet. Electron repulsion then acts to perturb these levels. If electron-electron repulsion is dominant instead, then the t_{2g} states are split into a series of terms ${}^{2S+1}\Gamma$, which depend on the electron occupation of the manifold. Spin-orbit coupling then either splits, mixes, or perturbs these states depending on how the direct product of the term and the spin-orbit operator transforms.

1.4.2 Effect of SOC on the magnetic Hamiltonian

Spin-orbit coupling also has an important effect on the magnetic Hamiltonian. Magnetic interactions in 5d transition metal oxides are mainly governed by superexchange between transition metal cations mediated by the 2p orbitals on a mutually neighbouring oxygen atom. The mechanism is similar to that relevant for 3d TMOs. Anisotropy of these interactions arises as a result of spin-orbit coupling. The reason for this is as follows [65]. In a purely Heisenberg interaction picture, the interactions are isotropic ($\mathcal{H} = J \sum \mathbf{S}_i \cdot \mathbf{S}_j$). The local spin directions have nothing to do with the orientation of the spins within the lattice. Only through coupling to the orbital moment $\mathbf{L}$ does the spin orientation align with the lattice.

There are two microscopic methods of magnetic anisotropy: single-ion anisotropy (SIA), and exchange anisotropy. The latter is divided into symmetric and antisymmetric contributions, frequently known as symmetric anisotropic exchange and the Dzyaloshinskii-Moriya (DM) interaction respectively. These methods shall be discussed in turn, with their relative magnitudes outlined in Table 1.3.

Exchange anisotropy

In the absence of spin-orbit coupling the Heisenberg exchange term $J \sum \mathbf{S}_i \cdot \mathbf{S}_j$ is the scalar product of two vectors. However in general the interaction parameter J is not a scalar, but in fact

---

[10] As an example, the cubic crystal field Hamiltonian is given by $\mathcal{H}_c = B_4^0 \left[O_4^0 + 5O_4^4\right] + B_6^0 \left[O_6^0 - 21O_6^4\right]$, with the Stevens operators and B_l^m parameters tabulated in [58].

Source	Scaling	$NaOsO_3$ (meV)
Single-ion anisotropy	$K \sim \frac{\lambda^2}{\delta E}$	8.0
Dzyaloshinskii-Moriya (DM)	$D \sim \frac{\lambda}{\delta E} J$	1.0
Exchange anisotropy	$\delta J \sim \left(\frac{\lambda}{\delta E}\right)^2 J$	0.05

Table 1.3: Approximate scaling of various sources of anisotropy (Refs. [66] and [65]), assuming a d^3 electronic configuration and uniaxial anisotropy. The relative magnitudes for these sources have been estimated using suitable parameters for $NaOsO_3$: $\lambda = \zeta/3 = 0.172$ eV, $\delta E = 3.7$ eV, $J = 21$ meV (see Chapter 4).

a 3×3 tensor $\bar{J}_{\alpha\beta}$, where the indices $\alpha, \beta = \{x, y, z\}$. If this tensor is diagonal and $J_{\alpha\beta} = J\delta_{\alpha\beta}$, then one returns to the Heisenberg exchange interaction. In general however it may contain both symmetric and antisymmetric exchange terms off the leading diagonal.

Symmetric exchange anisotropy

The symmetric exchange[11] terms are given by $J^{(s)}_{\alpha\beta} = J^{(s)}_{\beta\alpha}$, and can always be diagonalised. The precise form of the diagonal components is dependent on the crystal symmetry, but as an example consider the tetragonal case, with a distortion along the local z-axis: $\mathcal{H}_{ij} = \sum_{ij} J_{\parallel} S^z_i S^z_j + J_{\perp}\left(S^x_i S^x_j + S^y_i S^y_j\right)$. The two parameters $J_{\parallel}$ and $J_{\perp}$ reflect exchange coupling along or perpendicular to the distortion direction respectively. In the case of an orbital singlet, the difference between $J_{\parallel}$ and $J_{\perp}$ can be estimated as $\delta J \sim J\left(\lambda/\delta E\right)^2 \sim J\left(\delta g/g\right)^2$. For partially occupied t_{2g} orbitals, the non-zero orbital component to the magnetisation increases results in increased spin-orbit coupling and hence increased anisotropy. For the case that $\lambda \sim \delta E$, perturbation theory breaks down and the anisotropy is directly governed by λ.

Dzyaloshinskii-Moriya interaction

The antisymmetric exchange contribution can be written as $\mathcal{H}_{ij} = \mathbf{D}_{ij} \cdot \mathbf{S}_i \times \mathbf{S}_j$, where $\mathbf{D}_{ij}$ is known as the Dzyaloshinskii-Moriya (DM) vector. In contrast to Heisenberg exchange, which favours collinear spins (as demonstrated by the dot product), the antisymmetric exchange term prefers spin canting parallel with the DM vector $\mathbf{D}_{ij}$.

Moriya [66] formulated a set of rules which govern the direction of the DM vector – and whether it is non-zero – for a given bond. These rules are derived from a symmetry analysis, however they do not tell us about the magnitude, or more importantly, the sign of the DM vector. One example which shall be shown to be relevant later is the case of a nearest-neighbour Heisenberg antiferromagnet on the pyrochlore lattice with DM interaction. Different antiferromagnetic ground states arise for different signs of the DM vector. Expansion within a perturbation theory leads to the estimate that $|\mathbf{d}| \sim J\left(\lambda/\delta E\right) \sim J\left(\delta g/g\right)$, which indicates that it should be significantly stronger than the symmetric exchange anisotropy (when present).

---

[11] Symmetric exchange is also known as a pseudodipolar interaction [66, 67], and the two notations are used interchangeably in the literature.

Single-ion anisotropy

One more important source of anisotropy remains, which is single-ion anisotropy. Single-ion anisotropy is characteristic of the local crystal field environment of the metal cation. The single-ion anisotropy term $\mathcal{H}_{\mathrm{SIA}}$ in the Hamiltonian is given by $\mathcal{H}_{\mathrm{SIA}} = \sum_i \mathbf{S}_i \cdot \bar{\mathrm{D}} \cdot \mathbf{S}_i$, where

$$\bar{\mathrm{D}} = \begin{pmatrix} D_{\mathrm{xx}} & D_{\mathrm{xy}} & D_{\mathrm{xz}} \\ D_{\mathrm{xy}} & D_{\mathrm{yy}} & D_{\mathrm{yz}} \\ D_{\mathrm{xz}} & D_{\mathrm{yz}} & D_{\mathrm{zz}} \end{pmatrix} \tag{1.13}$$

is a second-rank tensor. The coordinate system that diagonalises $\bar{\mathrm{D}}$ is called the magnetic axis frame [68]. Transforming the initial coordinates into this new reference frame gives the transformation matrix and zero-field splitting (ZFS) components:

$$\bar{\mathrm{D}}_{mag} = \begin{pmatrix} D_{\mathrm{XX}} & 0 & 0 \\ 0 & D_{\mathrm{YY}} & 0 \\ 0 & 0 & D_{\mathrm{ZZ}}. \end{pmatrix} \tag{1.14}$$

In this reference frame z is defined as the highest symmetry axis. Consequently $\mathcal{H}_{\mathrm{SIA}}$ becomes

$$\mathcal{H}_{\mathrm{SIA}} = \sum_i D\mathbf{S}_{\mathrm{z}}^2 + E\left(\mathbf{S}_{\mathrm{x}}^2 - \mathbf{S}_{\mathrm{y}}^2\right), \tag{1.15}$$

where D and E are the axial and rhombic components to the zero field splitting respectively, and defined by: $D = D_{\mathrm{ZZ}} - \frac{1}{2}\left(D_{\mathrm{XX}} + D_{\mathrm{YY}}\right)$, $E = \frac{1}{2}\left(D_{\mathrm{XX}} - D_{\mathrm{YY}}\right)$. E is known as the rhombic splitting parameter because it vanishes for systems where the highest symmetry axis is threefold or higher. If D is negative, then it corresponds to the easy axis of magnetisation. However the single-ion anisotropy vanishes[12] for $S = \frac{1}{2}$ materials. This conclusion arises simply by consideration of the spin operators $\mathbf{S}_\alpha$ in terms of the Pauli matrices: $\mathbf{S}_\alpha = S\sigma_\alpha$, where $\alpha = \{x, y, z\}$.

Now given that single-ion anisotropy involves – as its name suggests – one site rather than two, that it would have a larger magnitude than exchange anisotropy (symmetric and antisymmetric). This is indeed the case. Assuming uniaxial anisotropy and an orbital singlet ground state (and hence $E = 0$), then D scales approximately as $D \sim \lambda^2/\delta E \sim (\delta g/g)^2\,\delta E$.

1.5 Outlook

What the present discussion has shown is that the electronic and magnetic interactions in 5d TMOs are reliant on the interplay of a series of energy scales, including spin-orbit coupling. Two sets of materials shall be studied within this thesis: the d^5, $j_{\mathrm{eff}} = \frac{1}{2}$ iridates, and the d^3, $S = \frac{3}{2}$ osmates. In both sets of materials, the octahedral crystal field splitting $10\,Dq$ is expected to be the dominant energy scale. The differences in behaviour between the iridates and osmates is

---

[12] There is some debate whether this is indeed the case; DFT calculations suggest that for most $S = \frac{1}{2}$ materials, there should be some degree of single-ion anisotropy [69]. The original assumption that the magnetic ions are treated as spin-only moments, with the unquenched orbital moments included in anisotropic g-factors may not be entirely valid. Only in the ideal octahedral case does single-ion anisotropy completely vanish.

primarily governed by the relative magnitudes of the other microscopic parameters discussed thus far.

The iridates Sr_2IrO_4 and $Sr_3Ir_2O_7$ are characterised by strong spin-orbit coupling in the electronic ground state, with insulating behaviour resulting from the perturbative effect of a weak Coulomb term. These insulating states are relatively robust, with metal-insulator transitions driven by carrier doping in both cases. The entangled nature of the $j_{\mathrm{eff}} = \frac{1}{2}$ state leads to intrinsic anisotropic exchange terms in the Hamiltonian, which in the case of 180° Ir–O–Ir bonds, arise purely from Hund's coupling [25]. This contrasts with the conventional situation where anisotropy results from the spin-orbit coupling.

The osmates $Cd_2Os_2O_7$ and $NaOsO_3$ on the other hand are nominally orbital singlets; spin-orbit coupling is thus expected to play a reduced role in the electronic and magnetic Hamiltonian compared to the iridates. The osmates lie in an intermediate regime where the spin-orbit interaction competes with the Hund's coupling; this has important ramifications for the mechanism of the MIT. Bulk measurements have shown that these materials undergo continuous MITs concomitant with the onset of long-ranged antiferromagnetic order.

The aim is to understand the role of spin-orbit coupling in determining the electronic and magnetic interactions within these materials. Resonant X-ray scattering techniques are especially sensitive microscopic probes of the collective behaviour of transition metal oxides. The following chapter shall examine some characteristics of resonant X-ray scattering, along with some details pertaining to its implementation.

Chapter 2

Resonant X-ray scattering

This chapter details the use and characteristics of resonant X-ray scattering techniques, both elastic and inelastic. Resonant X-ray scattering has proven itself as a unrivalled tool for the study of electronic and magnetic correlations in 5d TMOs. The present treatment includes a brief numerical description of the relevant interactions, along with a focus of its application at two specific instruments. These instruments were used for a subset of the work presented in this thesis. The final part of this chapter discusses the extension of resonant X-ray scattering to X-ray free-electron lasers.

The advent of third- and fourth-generation synchrotron sources provides a tunable, intense probe for the study of condensed matter systems. Depending on the precise setup, measurements can be performed across a wide range of the electromagnetic spectrum, ranging from the far infrared, all the way to gamma radiation. Electromagnetic radiation comprises perpendicular electric and magnetic fields; one or both of these can couple to the electronic and magnetic degrees of freedom of a system. In the X-ray regime, the wavelength of radiation is comparable to the inter-atomic spacing, permitting studies of the structure and interactions of materials at the atomic scale. X-ray diffraction, scattering and absorption are therefore complementary to other analysis methods, such as neutron scattering or optical spectroscopy.

However conventional X-ray scattering does suffer from a couple of limitations. The first of these is that the observed scattering is dominated by the heaviest elements present in a system. This is because the atomic form factor $f_0(\mathbf{Q})$ scales with the atomic number Z, and hence the observed intensity $|f_0(\mathbf{Q})|^2 \sim Z^2$. For some circumstances it can lead to obscuring of the desired behaviour.

The second limitation is the magnitude of coupling to the magnetic degrees of freedom. The interaction between the magnetic field of the electromagnetic wave and the magnetic moment generated by the unpaired electrons in the material is due to perturbative relativistic effects [70]. Unfortunately this process is significantly weaker (10^6–10^8 times) than normal Thomson charge scattering measured in a typical X-ray scattering experiment, and thus requires a high-intensity X-ray source (such as a synchrotron) to observe.

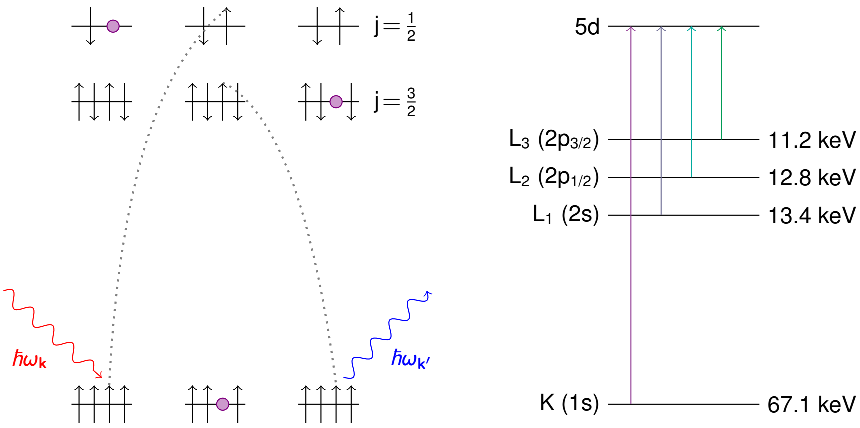

Initial Intermediate Final

Ir absorption edges

Figure 2.1: Left panel – Resonant X-ray scattering process as illustrated for an Ir^{4+} ion. In the displayed scenario an electron has been excited from the j$=\frac{3}{2}$ to the j$=\frac{1}{2}$ manifold, and hence $\hbar\omega_{\mathbf{k}} \neq \hbar\omega_{\mathbf{k}'}$. Right panel – Iridium X-ray absorption edges along with their respective energies.

There is however a partial solution to these problems. Strictly speaking the scattering amplitude of an atom $f(\mathbf{Q},\omega)$ is only equal to the atomic form factor for the free-electron case. Electrons in atoms are bound to the nucleus. One assumption is that these electrons respond to the driving field of the X-ray as classical damped harmonic oscillators. It follows [71] that the scattering amplitude can be written in the form:

$$f(\mathbf{Q},\omega) = f_0(\mathbf{Q}) + f'(\omega) + if''(\omega), \tag{2.1}$$

where f' and f'' are the real and imaginary parts of the dispersion corrections. These parameters reach their extremal values at an atomic absorption edge. Consequently the scattering amplitude differs significantly from the free-electron case close to an absorption edge, the energy of which is specific to a particular element and orbital configuration. This is termed resonant scattering.

From a quantum mechanical perspective, resonant scattering is a second-order process involving the creation of some short-lived intermediate state. A schematic of the resonant process is shown in Fig. 2.1. A photon with energy $h\omega_{\mathbf{k}}$ excites a core electron to an unoccupied intermediate state. This leaves a hole in a core orbital, which is inherently unstable. After a short period of time (typically $\sim$fs), a valence electron decays to fill the core-hole, and emits a photon with energy $h\omega_{\mathbf{k}'}$ in the process. If $h\omega_{\mathbf{k}} \neq h\omega_{\mathbf{k}'}$, then one has resonant *inelastic* X-ray scattering, else it is termed resonant *elastic* X-ray scattering.

Since the resonant process involves a specific combination of core and valence states (which may be split by spin-orbit coupling), the process is spin and orbital specific. Consequently it is especially sensitive to magnetic and charge ordering of a material. It was discovered by Gibbs *et al.* [72] and Hannon *et al.* [73] that the magnetic cross-section can be dramatically enhanced close to an X-ray absorption edge. In the case of the 5d L edges, the resonant enhancement is around 100-fold compared to the non-resonant case. Whilst this is still considerably weaker than charge scattering, it does mean that magnetic phenomena can be readily observed in 5d TMOs with careful choice of experimental setup.

The advantages of resonant X-ray scattering also extend to the inelastic case (Chapter 2.3). Due to the resonant process, there is increased sensitivity towards electronic and magnetic excitations (spin waves) as compared to inelastic X-ray scattering (IXS). Furthermore unlike X-ray absorption spectroscopy (XAS) – which is a single-photon technique – the spectra are only broadened by the core hole potential of the intermediate state. This gives rise to increased spectral resolution, and has been put to use in a series of chemical applications. Recent developments in instrumental resolution have enabled the observation – and successful modelling – of spin waves in a number of materials, including 5d TMOs. RIXS is thus unique in this regard as a simultaneous probe of charge neutral electronic and magnetic excitations.

2.1 Numerical treatment

What follows is a brief numerical treatment of the resonant scattering process. This section mostly follows the formalism presented by Blume and Gibbs [33], Paolasini [74], and Ament *et al.* [75].

In general incident X-ray photons interact with the electron density of an atom. X-rays (like all electromagnetic waves) have perpendicular electric and magnetic fields, and these couple with the electronic charge to absorb or scatter a photon. The coherent elastic scattering cross-section for a crystal can be written as follows:

$$\frac{d\sigma}{d\Omega} = r_0^2 \left| \sum_n e^{i\mathbf{Q}\cdot\mathbf{R}_n} f_n\left(\mathbf{k}, \mathbf{k}', \boldsymbol{\epsilon}, \boldsymbol{\epsilon}', \hbar\omega_k\right) \right|^2 ,$$

where $f_n\left(\mathbf{k}, \mathbf{k}', \boldsymbol{\epsilon}, \boldsymbol{\epsilon}', \hbar\omega_k\right)$ is the scattering amplitude of the electrons at site n for given incident wavevector $\mathbf{k}$, outgoing wavevector $\mathbf{k}'$, incident and outgoing polarizations $\boldsymbol{\epsilon}$ and $\boldsymbol{\epsilon}'$ respectively, and photon energy $\hbar\omega_k$. The quantity r_0 in this case is the classical Thomson radius for an electron. The scattering amplitude generally contains four terms: $f = f_0 + f_{mag} + f' + if''$.

f_0 is the Thomson scattering amplitude and corresponds to the Fourier transform of the electron density in the atom, normalised to Z at $\mathbf{Q} = 0$. The magnetic scattering amplitude f_{mag} shall be discussed later. The anomalous terms f' and f'' are energy dependent, and typically f' and f'' have local minima at an absorption edge. These absorption edges correspond to transitions of core electrons into available electronic states above the Fermi level.

Theory of electron-photon interaction

The incident X-rays are defined by an electromagnetic (EM) field with vector potential $\mathbf{A}(\mathbf{r}, t)$. Consider an ensemble of N electrons which interact with such an EM field. There are three terms in the subsequent electron-photon interaction Hamiltonian: one which relates to non-interacting photons ($\mathcal{H}_{ph}$), another relating to non-interacting electrons ($\mathcal{H}_{el}$), and a final term describing the interaction between them ($\mathcal{H}'$). In the non-relativistic limit, and assuming a small photon potential, the total Hamiltonian $\mathcal{H}$ is given by:

$$\begin{aligned}
\mathcal{H} &= \mathcal{H}_{ph} + \mathcal{H}_{el} + \mathcal{H}' \\
\mathcal{H}_{el} &= \sum_j \frac{1}{2m}\mathbf{p}_j^2 + \sum_{ij} V(\mathbf{r}_{ij}) + \frac{e\hbar}{2(mc)^2}\sum_j \boldsymbol{\sigma}_j \cdot \left(\nabla\phi_j \times \mathbf{p}_j\right), \\
\mathcal{H}_{ph} &= \sum_{\kappa,\epsilon} \hbar\omega_\kappa \left(a^\dagger_{\boldsymbol{\kappa\epsilon}} a_{\boldsymbol{\kappa\epsilon}} + \frac{1}{2}\right), \\
\mathcal{H}' &= \sum_{i=1}^{N} \left[\frac{e}{m}\mathbf{A}(\mathbf{r}_i)\cdot\mathbf{p}_i + \frac{e^2}{2m}\mathbf{A}(\mathbf{r}_i)^2 + \frac{e\hbar}{2m}\boldsymbol{\sigma}_i \cdot \nabla \times \mathbf{A}(\mathbf{r}_i) \right. \\
&\quad \left. - \frac{e^2\hbar}{(2mc)^2}\boldsymbol{\sigma}_i \cdot \left(\frac{\partial\mathbf{A}(\mathbf{r}_i)}{\partial t} \times \mathbf{A}(\mathbf{r}_i)\right)\right], \qquad (2.2)
\end{aligned}$$

where $\mathbf{p}_i$, $\mathbf{r}_i$, and $\boldsymbol{\sigma}_i$ are, respectively, the momentum and position operators, and the Pauli matrices operating on an electron i. The operators $a^{(\dagger)}_{\boldsymbol{\kappa\varepsilon}}$ annihilate (create) a photon with wavevector $\boldsymbol{\kappa}$ and polarisation $\boldsymbol{\epsilon}$. At this point it is convenient to expand the vector potential into linearly polarised plane waves:

$$\mathbf{A}(\mathbf{r}) = \sum_{\kappa,\boldsymbol{\varepsilon}} \sqrt{\frac{\hbar}{2V\varepsilon_0\omega_\kappa}} \left(\boldsymbol{\varepsilon} a_{\kappa\varepsilon}\, e^{i\kappa\cdot\mathbf{r}} + \boldsymbol{\varepsilon}^* a^\dagger_{\kappa\varepsilon}\, e^{-i\kappa\cdot\mathbf{r}}\right). \qquad (2.3)$$

However we are predominantly interested in the resonant scattering cross-section, which is governed by the term $\mathcal{H}'$, and is considerably smaller than the other terms. Consequently one can treat $\mathcal{H}'$ as a weak perturbation to the Hamiltonian. For weak potentials this is a valid assumption. In this scheme the incident photon is defined by the initial state $|\mathbf{k}, \boldsymbol{\varepsilon}\rangle$ with energy $\hbar\omega$. The electron is initially in a state $|\alpha\rangle$, which is an eigenstate of the electronic Hamiltonian $\mathcal{H}_{el}$ and energy E_α. The interaction between electrons and photons creates a new eigenstate of the Hamiltonian $|\beta\rangle$ for the electrons with energy E_β, and a photon is scattered in the state $|\mathbf{k}', \boldsymbol{\varepsilon}'\rangle$ with final energy $\hbar\omega'$. This transition has a associated probability which can be calculated by Fermi's Golden Rule. Using second-order perturbation theory, the transition probability for N incident photons is written as follows:

$$W = \frac{2\pi}{\hbar}\left|\langle f|\mathcal{H}'|i\rangle + \sum_n \frac{\langle f|\mathcal{H}'|n\rangle\,\langle n|\mathcal{H}'|i\rangle}{E_i - E_f}\right|^2 \delta(E_i - E_f), \qquad (2.4)$$

where the initial state $|i\rangle = |\alpha, \mathbf{k}, \boldsymbol{\epsilon}\rangle$, the final state $|f\rangle = |\beta, \mathbf{k}', \varepsilon'\rangle$, $E_i = E_\alpha + \hbar\omega_k$ and $E_f = E_\beta + \hbar\omega'_k$. (There are two cases: elastic and inelastic scattering. In elastic scattering $E_\alpha = E_\beta$, and for inelastic scattering $E_\alpha \neq E_\beta$. For now we shall only consider elastic scattering, but we shall come back to the inelastic case later.) In general the first order amplitude dominates the second order one, however the second term in W becomes large when the incident photon energy corresponds to an atomic transition in the material. In this case a resonant process occurs: a core electron is excited into an orbital above the Fermi energy. This produces a hole in the core electron orbital. A valence electron decays and fills the core hole, with a photon being emitted with energy E_f, wavevector $\mathbf{k}'$ and polarization $\boldsymbol{\varepsilon}'$. Hence the two terms in the scattering probability correspond to non-resonant and resonant processes respectively.

Compare Equation 2.4 with the expression of the interaction Hamiltonian $\mathcal{H}'$, which is repeated here for convenience:

$$\begin{aligned}\mathcal{H}' &= \sum_{i=1}^{N}\left[\frac{e}{m}\mathbf{A}(\mathbf{r}_i)\cdot\mathbf{p}_i + \frac{e^2}{2m}\mathbf{A}(\mathbf{r}_i)^2 + \frac{e\hbar}{2m}\boldsymbol{\sigma}_i\cdot\nabla\times\mathbf{A}(\mathbf{r}_i) - \frac{e^2\hbar}{(2mc)^2}\boldsymbol{\sigma}_i\cdot\left(\frac{\partial\mathbf{A}(\mathbf{r}_i)}{\partial t}\times\mathbf{A}(\mathbf{r}_i)\right)\right]\\ &= \mathcal{H}'_1+\mathcal{H}'_2+\mathcal{H}'_3+\mathcal{H}'_4\end{aligned}$$

Terms that are quadratic in $\mathbf{A}(\mathbf{r}_i)$ contribute to the non-resonant scattering amplitude $(\mathcal{H}'_2, \mathcal{H}'_4)$, whereas terms linear in $\mathbf{A}(\mathbf{r}_i)$ contribute to the resonant scattering amplitude $(\mathcal{H}'_1, \mathcal{H}'_3)$. This is because we are interested in processes which contain both the creation and annihilation of a photon. The vector potential $\mathbf{A}(\mathbf{r}_i)$ is linear in photon annihilation and creation, so conservation of the number of photons only occurs for even degrees of $\mathbf{A}$.

One can thus write the transition probability as:

$$\begin{aligned}W = \frac{2\pi}{\hbar}\,\Bigg|\langle\beta,\mathbf{k}',\boldsymbol{\varepsilon}'|\,\mathcal{H}'_2+\mathcal{H}'_4\,|\alpha,\mathbf{k},\boldsymbol{\varepsilon}\rangle\\ + \sum_n \frac{\langle\beta,\mathbf{k}',\boldsymbol{\varepsilon}'|\,\mathcal{H}'_1+\mathcal{H}'_3\,|n\rangle\,\langle n|\,\mathcal{H}'_1+\mathcal{H}'_3\,|\alpha,\mathbf{k},\boldsymbol{\varepsilon}\rangle}{E_i-E_f+\hbar\omega_{\mathbf{k}'}-\hbar\omega_{\mathbf{k}}}\Bigg|^2, \qquad (2.5)\end{aligned}$$

Experimentally one measures the double differential cross-section, $\frac{d^2\sigma}{d\Omega dE}$, which is proportional to the number of incident probe particles scattered within an energy range ΔE and momentum variation into a solid angle $\Delta\Omega$. It is possible to derive a theoretical expression for $\frac{d^2\sigma}{d\Omega dE}$ from the transition probability W, if one makes the assumptions that the unperturbed radiation is monochromatic and that the intermediate states have a finite lifetime Γ_c. After some algebra, one can rewrite the double differential cross-section as

$$\frac{d^2\sigma}{d\Omega dE} = \left(\frac{e^2}{mc^2}\right)^2\frac{\omega_{\mathbf{k}'}}{\omega_{\mathbf{k}}}|A_0+A_{\mathrm{NRXMS}}+A_{\mathrm{res}}|^2\,\delta(E_i-E_f+\hbar\omega_{\mathbf{k}}-\hbar\omega_{\mathbf{k}'})\,, \qquad (2.6)$$

where A_0, A_{NRXMS} and A_{res} represent the Thomson, non-resonant magnetic and resonant scattering amplitudes respectively. It is clear that there are three main contributions in this expression, which shall be discussed in turn.

Thomson scattering

The first, A_0, is given by:

$$A_0 = \left\langle\beta,\mathbf{k}',\boldsymbol{\varepsilon}'\left|\sum_j e^{i\mathbf{Q}\cdot\mathbf{r}_j}\right|\alpha,\mathbf{k},\boldsymbol{\varepsilon}\right\rangle\boldsymbol{\varepsilon}'\cdot\boldsymbol{\varepsilon}, \qquad (2.7)$$

where $\mathbf{Q} = \mathbf{k}' - \mathbf{k}$. In the case that $|\alpha\rangle = |\beta\rangle$ and $\omega_{\mathbf{k}} = \omega_{\mathbf{k}'}$, then A_0 represents Thomson (charge) scattering $\propto Zr_0$, where r_0 is the classical electron radius. Thomson scattering is directly related to the Fourier transform of the electron density. If the periodicity of the crystal is considered (as applicable for the $\sum_j e^{i\mathbf{Q}\cdot\mathbf{r}_j}$ term), then Bragg scattering occurs. Finally if $|\alpha\rangle \neq |\beta\rangle$ and $\omega_{\mathbf{k}} \neq \omega_{\mathbf{k}'}$, then this gives rise to non-resonant inelastic X-ray scattering (IXS). This can in turn be related to the dynamic structure factor $S(\mathbf{Q}, E)$ which can be obtained from neutron scattering, allowing a direct comparison between the two techniques.

Non-resonant magnetic scattering

The second component A_{NXRMS} is a purely non-resonant magnetic scattering term, which far from any absorption edge reads:

$$\begin{aligned} A_{\mathrm{NXRMS}} &= -i\frac{\hbar\omega}{mc^2}\left\langle f \left| \sum_j e^{i\mathbf{Q}\cdot\mathbf{r}_j}\left(\frac{i\mathbf{Q}\times\mathbf{P}_j}{\hbar Q^2}\cdot\mathbf{A}' + \mathbf{s}_j\cdot\mathbf{B}'\right)\right| i \right\rangle \\ &= -i\frac{\hbar\omega}{mc^2}\left(\frac{1}{2}\mathbf{L}(\mathbf{Q})\cdot\mathbf{A}'' + \mathbf{S}(\mathbf{Q})\cdot\mathbf{B}'\right). \end{aligned} \tag{2.8}$$

In the above expressions, $\mathbf{A}'$, $\mathbf{A}''$ and $\mathbf{B}'$ are vectors which describe the polarisation dependence of the magnetic scattering [76, 77]:

$$\begin{aligned} \mathbf{A}' &= \hat{\boldsymbol{\varepsilon}}' \times \hat{\boldsymbol{\varepsilon}}, \\ \mathbf{A}'' &= -2(1 - \hat{\mathbf{k}}\cdot\hat{\mathbf{k}}')(\hat{\boldsymbol{\varepsilon}}' \times \hat{\boldsymbol{\varepsilon}}) + (\hat{\mathbf{k}} - \hat{\mathbf{k}}')\cdot(\hat{\boldsymbol{\varepsilon}}' \times \hat{\boldsymbol{\varepsilon}})(\hat{\mathbf{k}} - \hat{\mathbf{k}}'), \\ \mathbf{B}'' &= \hat{\boldsymbol{\varepsilon}}' \times \hat{\boldsymbol{\varepsilon}} + (\hat{\mathbf{k}}' \times \hat{\boldsymbol{\varepsilon}}')(\hat{\mathbf{k}}' \cdot \hat{\boldsymbol{\varepsilon}}) - (\hat{\mathbf{k}} \times \hat{\boldsymbol{\varepsilon}})(\hat{\mathbf{k}} \cdot \hat{\boldsymbol{\varepsilon}}') - (\hat{\mathbf{k}}' \times \hat{\boldsymbol{\varepsilon}}') \times (\hat{\mathbf{k}} \times \hat{\boldsymbol{\varepsilon}}), \end{aligned} \tag{2.9}$$

whilst $\mathbf{S}(\mathbf{Q})$ and $\mathbf{L}(\mathbf{Q})$ refer to the Fourier transforms of the spin and orbital components to the magnetisation respectively.

Compared to classical charge scattering, the pure non-resonant magnetic scattering amplitude is reduced by a factor of $\hbar\omega/mc^2$. Given that the topic of this thesis is resonant scattering, the non-resonant magnetic component shall not be considered further. However the key point to take home is that the orbital and spin components to the magnetisation can be discriminated in non-resonant magnetic X-ray scattering (NRXMS). This contrasts with susceptibility and neutron measurements for example, which are sensitive only to the total magnetic moment.

Resonant scattering amplitude

Finally we come to the resonant scattering amplitude. The derivation is rather complex, and the author refers the reader to Ament's review [75] for a full discussion. However it can be shown that the pure resonant scattering amplitude can be written as the *Kramers-Heisenberg* formula:

$$\mathcal{A}_{\mathrm{res}} \approx -\frac{1}{m}\sum_n\sum_{ij}\frac{E_g - E_n}{\hbar\omega_k}\frac{\left\langle f \left| e^{-i\mathbf{k}'\cdot\mathbf{r}_i}\ (\boldsymbol{\varepsilon}'\cdot\mathbf{p}_i)\right| n\right\rangle \langle n \,|\, e^{i\mathbf{k}\cdot\mathbf{r}_j}\ (\boldsymbol{\varepsilon}\cdot\mathbf{p}_j)\,|\, g\rangle}{E_g - E_n + \hbar\omega_k - i\Gamma_n/2}.$$

This equation gives the amplitude for both elastic ($|f\rangle = |g\rangle$) and inelastic ($|f\rangle \neq |g\rangle$) scattering.[1] Recall that the primes refer to photon emission events. Assuming that dipole-dipole contributions are dominant in the scattering,[2] then the Kramers-Heisenberg equation can be rewritten as:

$$\mathcal{A}_{\mathrm{res}}^{\mathrm{E1\text{-}E1}} = m\sum_n\sum_{ij}\frac{(E_n - E_g)^3}{\hbar^3\omega_k}\left[\frac{\langle f \,|\, (\boldsymbol{\varepsilon}'\cdot\mathbf{r}_i)\,|\, n\rangle \langle n \,|\, (\boldsymbol{\varepsilon}\cdot\mathbf{r}_j)\,|\, g\rangle}{E_g - E_n + \hbar\omega_k - i\Gamma_n/2}\right] \tag{2.10}$$

---

[1] Note that the notation for the initial state has been changed from i to g to avoid confusion with the summation indices, and is consistent with the notation given in Ref. [75].

[2] In general the term $e^{i\mathbf{k}\cdot\mathbf{r}}$ can be Taylor expanded as $e^{i\mathbf{k}\cdot\mathbf{r}} \sim 1 + \mathbf{k}\cdot\mathbf{r} + \ldots$ Truncating this at first-order gives the dipole-dipole only terms.

This can be conveniently rewritten (by taking care of some pre-factors) in terms of the dipole operator $\mathcal{D} = \varepsilon \cdot \mathbf{r}_i$:

$$\mathcal{A}_{\text{res}}^{\text{E1-E1}} = \sum_n \frac{\langle f \,|\, \mathcal{D}'^{\dagger} \,|\, n \rangle \langle n \,|\, \mathcal{D} \,|\, g \rangle}{E_g - E_n + \hbar\omega_k - i\Gamma_n/2} \tag{2.11}$$

The matrix elements contain information about the unoccupied electronic states. In particular, since the resonant scattering amplitude is so strongly dependent on the incident photon energy, then it becomes possible to discriminate between elements and even different orbitals, depending on what absorption edge is chosen. One key point is the resonant scattering amplitude is dependent on the lifetime of the intermediate states, as shown by the factor of Γ_c in the denominator.

In Equation 2.11, it is not immediately apparent where the sensitivity to magnetism lies. However the sensitivity to magnetism arises from symmetry breaking of the spin states. Unlike the non-resonant case, resonant scattering is insensitive to the individual spin and orbital magnetisation components as spin-orbit coupling entangles the two.

2.2 Resonant elastic X-ray scattering

Solving the Kramers-Heisenberg equation (Equation 2.11) is generally not required for resonant elastic X-ray scattering. The scattering amplitude for magnetic systems in particular is strongly dependent on the incident polarization and the magnetic moment orientation. Hannon [73] derived an expression for the scattering amplitude per magnetic site, which Hill and McMorrow developed further [78]. Using the notation of Hill and McMorrow, the scattering amplitude can be written as:

$$\mathcal{A}_{\text{XRES}}^{\text{E1}} = \left[(\boldsymbol{\varepsilon}' \cdot \boldsymbol{\varepsilon})F^{(0)} - i\,(\boldsymbol{\varepsilon}' \times \boldsymbol{\varepsilon}) \cdot \hat{\mathbf{z}}_n F^{(1)} + (\boldsymbol{\varepsilon}' \cdot \hat{\mathbf{z}}_n)\,(\boldsymbol{\varepsilon} \cdot \hat{\mathbf{z}}_n)F^{(2)}\right] \tag{2.12}$$

with

$$\begin{aligned} F^{(0)} &= (3/4k)\,[F_{11} + F_{1-1}] \\ F^{(1)} &= (3/4k)\,[F_{11} - F_{1-1}] \\ F^{(2)} &= (3/4k)\,[2F_{10} - F_{11} - F_{1-1}]\,. \end{aligned}$$

The terms F_{LM} are determined by atomic properties and correspond to the strength of the resonance, and $\hat{\mathbf{z}}_\mathbf{n}$ is a unit vector corresponding to the direction of the magnetic moment. Let's return to the electric dipole-dipole (E1-E1) resonant scattering amplitude given in Equation 2.12. The first term corresponds to the charge Bragg peak, the second term is linear in the magnetization direction and hence produces a resonant magnetic contribution, and the third term produces second order magnetic satellites in antiferromagnets. This third term shall be neglected for now.

One point to focus on from Equation 2.12 is the polarization dependence of the scattering for both the charge and first-order magnetic terms. The charge term is dependent on the scalar product of the incident and outgoing photon polarizations, whereas the magnetic term is dependent on the cross product. This implies that for magnetic scattering, the polarization of the outgoing photon is rotated with respect to the incident photon. Typically a basis is defined such that the σ direction is perpendicular to the scattering plane, and the π direction is parallel to the scattering plane. Hence it is possible to define the polarization dependence of the scattering amplitude in terms of a 2×2 Jones matrix:

$$(\boldsymbol{\varepsilon}', \boldsymbol{\varepsilon}) = \begin{pmatrix} (\boldsymbol{\varepsilon}'_\sigma, \boldsymbol{\varepsilon}_\sigma) & (\boldsymbol{\varepsilon}'_\sigma, \boldsymbol{\varepsilon}_\pi) \\ (\boldsymbol{\varepsilon}'_\pi, \boldsymbol{\varepsilon}_\sigma) & (\boldsymbol{\varepsilon}'_\pi, \boldsymbol{\varepsilon}_\pi) \end{pmatrix}$$

Applying this Jones matrix to the first two terms in the scattering amplitude gives the following result:

$$(\boldsymbol{\varepsilon}' \cdot \boldsymbol{\varepsilon}) = \begin{pmatrix} 1 & 0 \\ 0 & \hat{\mathbf{k}}' \cdot \hat{\mathbf{k}} \end{pmatrix}, \quad (\boldsymbol{\varepsilon}' \times \boldsymbol{\varepsilon}) \cdot \hat{\mathbf{z}}_n = \begin{pmatrix} 0 & \hat{\mathbf{k}} \\ -\hat{\mathbf{k}}' & \hat{\mathbf{k}}' \times \hat{\mathbf{k}} \end{pmatrix}, \tag{2.13}$$

where $\hat{\mathbf{k}}' \cdot \hat{\mathbf{k}} = \cos 2\theta$. The key points to note are that a non-zero amplitude for charge scattering is only observed when the incident and outgoing polarizations are the same ($\sigma - \sigma'$ and $\pi - \pi'$ scattering). On the other hand, resonant magnetic scattering can be observed when the outgoing polarization is rotated with respect to the incident polarization, however scattering in the $\sigma - \sigma'$ channel is forbidden.[3] This suggests that through the careful consideration of experimental setup, it may be possible to discriminate between charge and magnetic contributions to the resonant scattering. This is indeed the case, and a number of instruments around the world have been built to do exactly this.

2.2.1 A resonant elastic scattering beamline - I16

Resonant X-ray scattering is a complementary technique to neutron scattering, and as discussed above, it has a number of advantages, including the ability to measure small samples, polarization analysis, high **Q** resolution, and element and orbital specificity. For these reasons, a RXS instrument should exploit each of these advantages. However the scattering cross-section is still relatively low, making it prohibitive to perform in a laboratory setting. Synchrotron radiation sources provide an incredibly luminous source of X-rays with a small beam divergence, almost perfect in-plane polarization (on an undulator insertion device at least) and tunable incident energies. One RXS instrument at a synchrotron source is I16 (Materials and Magnetism) at Diamond Light Source, which shall be briefly discussed.

TThe beamline consists of a number of different components. The first of these is the in-vacuum undulator, which provides a continuous spectrum of X-rays with energies from 3–15 keV. The energy can be varied by varying the gap between the undulator poles. However the bandwidth of the undulator is typically on the order of 1%, so a channel cut Si (1, 1, 1) monochromator is used to further select a particular incident energy with a typical bandwidth of 1.5 eV. Slits and mirrors are used to focus the beam, improve the beam profile, and reject higher undulator harmonics that may contaminate the X-ray spectrum. If the incident energy is sufficiently

---

[3] Remember that the assumption is that dipole-dipole (E1-E1) processes are dominant. In reality, there may be higher-order terms which contribute to the magnetic scattering in the $\sigma - \sigma'$ channel, and give a non-zero intensity.

low ($E \leq 7$ keV), then a diamond quarter-wave phase retarder can be employed to circularly polarize the beam. This type of setup has proved useful for the study of magnetic domains in multiferroics [79–81].

A Newport six-circle kappa diffractometer enables the sample environment to be oriented in a number of different configurations. The advantage of a kappa diffractometer over one based on Eulerian cradles is that the geometry is much more open, which means that a number of different sample environments can be accommodated, such as applied magnetic fields and cryostats. However the circle rotations themselves are non-intuitive, since they correspond to combinations of the traditional Eulerian rotations.

Finally the detector arm includes a number of different detectors, all suited for different purposes. These include an avalanche photodiode (APD) and Pilatus 100k position-sensitive detector, which is useful for sample alignment and imaging a large region of reciprocal space. A linear polarization analyser crystal can also be fitted to the detector arm, which enables the outgoing photon polarization to be determined. This crystal is chosen such that for a given incident energy, there is a strong Bragg reflection which is as close to $2\theta_P = 90^\circ$ as possible. The reasoning for this follows from the polarization dependence for the charge scattering given in Equation 2.13. If $2\theta_P = 90^\circ$, then it becomes possible to completely separate out the scattering component perpendicular to the scattering plane of the analyzer. Rotating the analyzer crystal about its principal axis enables individual components of the polarization vector to be selected. However since the resonant X-ray scattering process requires a specific incident energy, $2\theta_P$ will never be precisely equal to 90°. There will always be some ‘leakage’ from one polarization channel to another, which approximately scales as $\cos^2(2\theta_P)$. Imagine that we are looking at a reflection in the $\sigma - \pi'$ polarization channel. So for example, if $2\theta_P = 89^\circ$ for a particular photon energy, then the leakage will be approximately 0.03%. This does not seem large, but remember that the intensity of charge reflections can be orders of magnitude more than for magnetic reflections. There is a further advantage in that fluorescent background is also subtracted by this method, which is useful when looking at particularly weak signals. This shall be demonstrated in Chapter 5.

2.3 Resonant inelastic X-ray scattering (RIXS)

Thus far only elastic scattering has been discussed, whereby the final state of the system is at the same energy as the initial state ($\mathbf{k_i} = \mathbf{k_f}$). With inelastic scattering, the final state is at a different energy to the initial state, i.e $\mathbf{k_i} \neq \mathbf{k_f}$. The interaction Hamiltonian $\mathcal{H}'$ is given once more by Eqn. 2.2, with the corresponding double-differential cross-section by Eqn. 2.6. As mentioned previously, the non-resonant IXS scattering amplitude derives from Thomson scattering. Terms linear in $\mathbf{p} \cdot \mathbf{A}$ (the resonant terms $\mathcal{H}'_1$ and $\mathcal{H}'_3$) dominate the scattering amplitude close to an absorption edge; thus it shall be assumed that the non-resonant IXS contribution is negligible.

The resonant scattering amplitude A_{res} is given by the Kramers-Heisenberg equation (Eqn. 2.11), which is repeated here for convenience:

$$\mathcal{A}_{\text{res}}^{\text{E1-E1}} = \sum_n \frac{\langle f|\mathcal{D}'^{\dagger}|n\rangle \langle n|\mathcal{D}|g\rangle}{E_g + \hbar\omega_{\mathbf{k}} - E_n + i\Gamma_n}.$$

Note that the scattering amplitude is dependent on the polarisation vectors $\boldsymbol{\varepsilon}$ and $\boldsymbol{\varepsilon}'$, just as for the elastic case. Consequently any determination of the scattering cross-section has to take this into account.[4]

2.3.1 Comparison with optical absorption spectroscopy

RIXS allows for the study of charge neutral excitations. Consequently RIXS can be directly compared to ultraviolet-visible (UV-vis) absorption spectroscopy, an optical probe which is commonly used by chemists to examine the coordination environment and electronic excitations in transition metal oxide complexes. UV-vis spectroscopy measures the attenuation of light when the light passes through a sample or is reflected from a sample surface. This attenuation can result from absorption, scattering, reflection or interference. The majority of UV-vis experiments are carried out in transmission geometry. A solution of the desired complex is placed in a cuvette and light of a given wavelength shines through it. This light is generally generated from a continuous source (usually a lamp) and dispersed by a diffraction grating. Rotation of the grating changes the wavelength of incident light. Assuming a weak concentration of the absorbing species, then the intensity of light incident on the detector is related to the Beer-Lambert law. In a reflection geometry, light is incident on a clean, polished sample. The diffuse reflectance spectra are recorded by an integrating sphere.

In optical spectroscopy, only transitions which satisfy the condition $\Delta S = 0$ are allowed (in the Russell-Saunders limit).[5] Furthermore transitions which conserve parity are forbidden (Laporte selection rule). However transitions that are forbidden by the Laporte selection rule (such as d–d transitions) may be allowed if the centre of symmetry of the absorbing species is disrupted. In practice this occurs at finite temperature even for centrosymmetric species as the actual transitions are coupled to antisymmetric vibrations which have the same symmetry as the dipole moment operator (T_{1u} in O_h symmetry). For transition metal complexes, spin-forbidden d–d transitions (such as $t_{2g}^3 \rightarrow t_{2g}^3$) are the weakest, with spin-allowed d–d transitions ($t_{2g}^3 \rightarrow t_{2g}^2 e_g$) stronger, and spin-allowed charge transfer excitations stronger still.

There are a number of issues with using conventional optical spectroscopy to study magnetic 5d TMOs. The first is that the observed spectrum is an average of all the different processes going on within the system; this can prove especially problematic when there are multiple transition metal species present. Secondly only bimagnon excitations which satisfy $\Delta S = 0$ can be

---

[4] See the review by Ament and colleagues [75] for a discussion of the decoupling of the experimental geometry from the intrinsic RIXS cross-section.

[5] Finite spin-orbit coupling relaxes this selection rule; “spin-forbidden” transitions can still occur, albeit with a lower transition probability than those where $\Delta S \neq 0$. In the jj-coupling limit, the appropriate selection rule is $\Delta J = 0, \pm 1$, however $j = 0 \rightarrow j = 0$ transitions are forbidden.

observed. Furthermore only the area around $\mathbf{k} \to 0$ can be probed, as a consequence of the low photon energy limiting the available energy-momentum phase space for scattering events. Finally since the photon energy is so low, exceptionally clean surfaces are required when performing UV-vis measurements in a reflection geometry, or very thin/dilute samples used in a transmission geometry. This is a consequence of the limited optical penetration depth.

RIXS on the other hand is a bulk sensitive technique (at least in the hard X-ray regime); the penetration depth at 11 keV is on the order of 10 μm. Because an X-ray photon is much more energetic than a visible or ultraviolet photon (or a neutron for that matter), then the scattering phase space is that much larger. In the hard X-ray regime the entirety of multiple Brillouin zones can be mapped as a function of momentum transfer. Secondly the resonant process leads to element and orbital specificity as it requires tuning of the incident energy to a particular elemental absorption edge. When the incoming photon energy is tuned to a L absorption edge,[6] an electron with spin s is excited from a core p-level to a valence d-shell. However the strong spin-orbit coupling in the core p state means that the resultant core hole can flip its spin from s to $-s$. Consequently a d-electron with spin $-s$ can decay from the valence shell to fill the core hole, emitting an X-ray in the process. This effectively corresponds to a spin-flip excitation in the valence state, which is not only allowed, but strong. This means that RIXS lends itself naturally as a technique for studying d–d transitions.

Recent developments have vastly improved the energy resolution of RIXS spectrometers around the world, permitting the characterisation of dispersive spin waves as a function of momentum transfer, which was formerly the reserve of inelastic neutron scattering (INS). One further advantage of RIXS over INS is that much smaller sample volumes are required for RIXS; the more intense undulator source, and stronger probe-matter interaction, permits the use of a smaller beam. The incident beam size at a RIXS instrument has dimensions $\sim$10 μm $\times$ 10 μm, whereas at a neutron triple-axis spectrometer it is on the order of centimetres across.

However there are two main drawbacks with RIXS. The first is that even though the photon-matter interaction is stronger than the neutron-matter interaction, the technique still remains ‘photon-hungry’ since only a small number of photons are scattered with a given final energy. This leads to long counting times, especially using high-resolution setups. Furthermore the energy resolution is only sufficient to resolve magnetic features at a small subset of absorption edges. This is a consequence of technical constraints, primarily finding a suitable choice of crystal analyser and secondary monochromator reflections.

---

[6] Single spin-flip scattering at a K absorption edge is generally forbidden. This is because spin-orbit coupling is absent in the isotropic $1s$ core state. However, single magnon excitations can be observed at the oxygen K edge if there is spin orbit coupling in the transition metal d shell, and if inversion symmetry is broken at the oxygen site. This has been demonstrated both experimentally [82, 83] and theoretically [84].

2.3.2 Technical details

The general principle of performing a hard X-ray RIXS[7] experiment is as follows. Just as for resonant elastic X-ray scattering (REXS), X-rays are produced by an undulator source and are monochromated to the desired energy (with some intrinsic bandwidth governed by the Darwin width of the monochromator), which corresponds to an atomic transition in the material to be studied. However there is a trade-off: monochromators with a low bandwidth have a large Bragg angle θ_M, which corresponds to a small Darwin width and hence good energy resolution. However higher order reflections are less intense, so the diffraction intensity is lower. The incident energy resolution is one component to the overall energy resolution (and hence which features can be measured), more detail is given in Appendix A. These pseudo-monochromatic X-rays are focussed by mirrors – often Kirkpatrick-Baez type – so that small samples can be measured and improve the incident energy resolution further. The incident X-rays scatter off the sample and those which satisfy the Bragg condition for the sample are diffracted towards the spectrometer. Note that due to inelastic processes these photons are no longer monochromatic.

The spectrometer itself usually comprises a diced analyser crystal and a position-sensitive detector (PSD). The diced analyser crystal is made up of blocks of a material with a small Darwin width (typically Si or Ge) and a specific crystal orientation, chosen that the Bragg angle of the analyser 2θ is close[8] to 90°, and is placed on the Rowland circle with radius $R/2$ (Fig. 2.2). Photons which satisfy the Bragg condition for the analyser are diffracted and focussed towards the PSD. A diced spherical analyser is used since bent spherical analysers have historically suffered from elastic distortions. However diced analysers add a geometrical broadening term to the energy resolution, which is due to the individual crystals comprising the analyser each focussing onto a slightly different spot on the detector. Spectral analysis is performed by simultaneously varying the analyser angle $2\theta_A$ and detector angle, such that the focussed spot remains approximately in the same position on the PSD. There is a well-defined relationship between the position of the spot on the detector surface x (in the dispersive direction), and the photon energy E:

$$\frac{\mathrm{d}E}{\mathrm{d}x} = \frac{E}{2R} \cot\theta_B \tag{2.14}$$

Here R is the analyser-to-detector distance. As an example the dispersion at the Ir L_3 edge is about 210 meV mm^{-1} for a analyser of radius 2 m. The resulting spectrum is then the binned intensity from each channel summed over the non-dispersive direction.

The RIXS cross-section derived from the Kramers-Heisenberg formula contains geometrical terms which are suppressed when the spectrometer angle $2\theta = 90^\circ$. Operating close to

---

[7] RIXS in the soft X-ray regime is somewhat different due to the requirement of ultra high vacuum (UHV) conditions and the lack of suitable crystal reflections in this energy window. In this thesis only hard X-ray RIXS shall be discussed in detail.

[8] The crystal analyser has an energy acceptance window, where photons with an energy corresponding to this window are diffracted by the analyser. If the geometry is perfectly backscattering, then only elastic photons will be diffracted, which defeats the purpose of an inelastic measurement! However if 2θ is too far from 90°, then it adds negative contributions to the spectrometer energy resolution, as detailed in Appendix A.

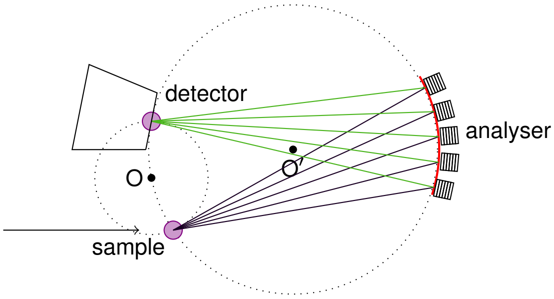

Figure 2.2: Rowland circle geometry. The distance between O and O′ is defined as $R/2$, where R is the radius of the Rowland circle.

90° has the added advantage of suppressing the elastic component to the inelastic spectrum – which fundamentally derives from $\boldsymbol{\varepsilon}' \cdot \boldsymbol{\varepsilon}$ – since its intensity typically scales as $\cos^2(2\theta)$. RIXS measurements are also usually performed at low temperature for two main reasons. Firstly one purpose for performing RIXS measurements is to measure the magnon dispersion for a particular system. Since the magnetic excitations can mostly only be observed below the magnetic transition temperature, then performing these measurements below this temperature is required. Secondly the energy resolution of a RIXS spectrometer is typically not good enough to resolve phonons. Thus contributions from phonons (especially acoustic phonons) are usually absorbed into the elastic line. Since the population of phonons follows the Bose-Einstein distribution, then there a greater number of phonons at high temperatures, and hence a greater probability of scattering from them, which means a larger elastic line. A lower phonon population also minimises broadening of electronic features due to electron-phonon coupling.

2.3.3 RIXS beamline - MERIX at the APS

As an example, the MERIX spectrometer at the Advanced Photon Source (APS), Chicago, shall be examined. An overview of the spectrometer is given in Fig. 2.3, and further details are given in the report by Shvyd'ko *et al.* [85].

The MERIX spectrometer is situated at the undulator beamline, 27-ID, which comprises two planar in-vacuum undulators (3.0 cm period), situated in tandem in order to maximise the number of photons produced (3×10^{13} ph/sec at 9 keV). MERIX is a medium-resolution instrument: it uses a double bounce Si $(1, 1, 1)$ liquid nitrogen cooled monochromator, followed by a four-bounce secondary monochromator in order to reduce the bandpass to the tens of meV range. The precise secondary monochromator used is dependent on the system to be measured, and the degree of resolution required. The incident X-ray beam is focussed to dimensions of 6 μm (V) $\times$ 45 μm (H) by planar mirrors in the horizontal direction, and Kirkpatrick-Baez mirrors in the vertical (energy dispersive) direction. This arrangement was chosen primarily for improved energy resolution, but has the added advantage that small samples can be measured. A series of slits help to define the beam profile.

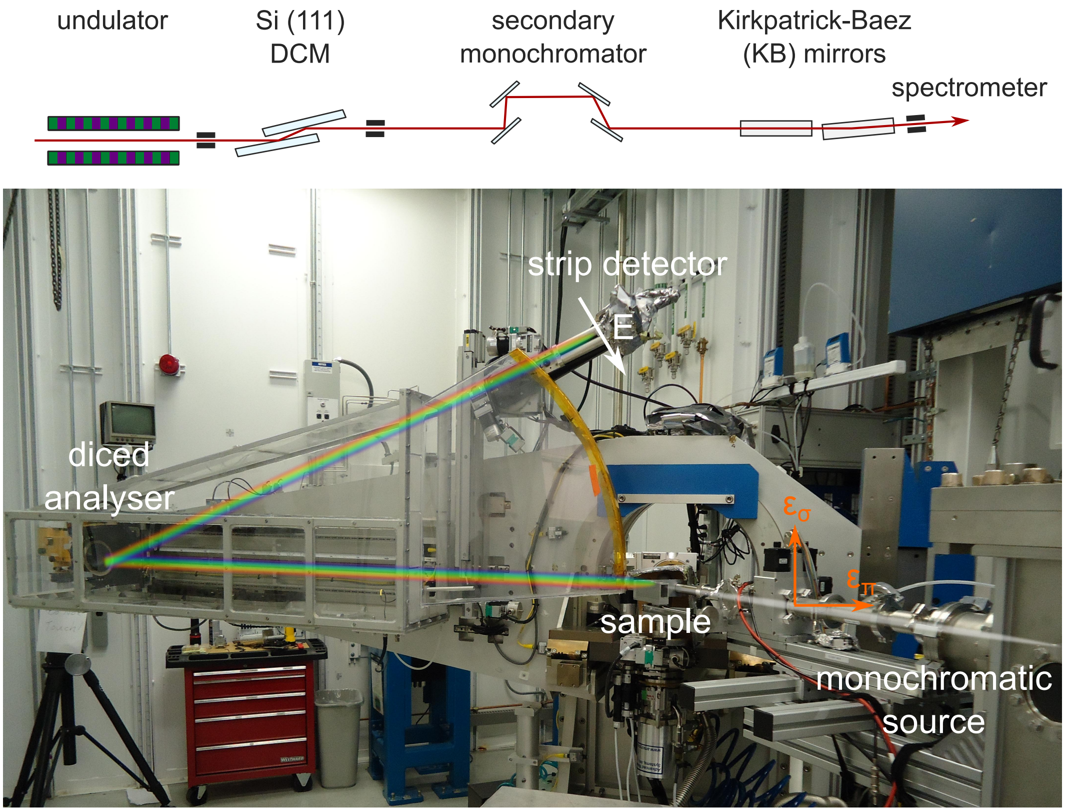

Figure 2.3: Top panel: General schematic of the upstream optical elements used at a RIXS instrument. DCM stands for double crystal monochromator. Bottom panel: Picture of the MERIX spectrometer at 30-ID, Advanced Photon Source, USA. The spectrometer is in horizontal scattering geometry (π-polarized light incident), and important components of the spectrometer have been labelled.

The spectrometer itself is situated on a Huber four-circle diffractometer in an Eulerian geometry. MERIX can operate in either horizontal or vertical scattering geometry, however horizontal geometry is generally used for RIXS (π-incident polarisation) since this minimises elastic terms which have a $(\boldsymbol{\varepsilon} \cdot \boldsymbol{\varepsilon}')$ polarisation dependence. This means that the 2θ arm rotates in the horizontal plane. A diced spherical analyser crystal of 100 mm diameter is typically mounted on a Rowland circle at a distance $R_A = 2\,\text{m}$ away from the sample position (put into the centre of rotation of the spectrometer) and detector; however one usually varies this distance slightly in order to focus the diffracted spot on the detector surface. Consequently the angular acceptance of the analyser is approximately ± 2.86 degrees. The detector currently used on MERIX is a Mythen micro-strip detector with pixel size 50 μm. Finally the analyser and majority of the flightpath is situated within a Perspex tank filled with helium gas. The reason for this is to minimise absorption and the background from air-scattering, since helium is lighter than air, and evacuating the whole chamber would be prohibitive.

Variations on spectrometer setup

Different RIXS beamlines have come up with slightly alternative setups, however the general principle remains the same. The first of these is the use of a 2-dimensional CCD instead of a 1D strip detector. This has the advantage of a larger collection area (and thus theoretically speaking higher count-rates), however some post-processing is required to extract the RIXS spectra. The second is the use of lead masks to reduce the usable area of the crystal analyser. This has the benefit of improved momentum resolution, since the angular acceptance is reduced;[9] however this also reduces the collected intensity as a consequence of Liouville's theorem.

2.4 Resonant X-ray scattering at XFELs

The radiation emitted from an undulator at a third-generation synchrotron is one of the most brilliant light sources known to mankind. However users are pushing towards experiments that require shorter length-scales and performed on shorter timescales. Additionally there is an increasing requirement for high transverse coherence of the incident beam, for example in coherent diffractive imaging (CDI) where the phase problem can be solved through phase reconstruction of a speckle pattern. The typical electron bunch duration in a synchrotron is typically on the order of 100 ps; this is a considerably longer timescale than many electronic and magnetic phenomena.[10] The transverse coherence of the incident beam in a synchrotron is limited because whilst each individual electron radiates coherently, the electrons in each bunch radiate incoherently with each other. Ideally what one would want is a scenario where all of the electrons in a bunch radiate coherently with each other. This scenario is an X-ray free electron laser (XFEL).

This topic shall be explored in more detail later (Chapter 6), but a few comments are noteworthy at this point. From a practical point of view resonant X-ray scattering experiments at XFELs are rather similar to those performed at synchrotrons. The incident photon energy is tuned to a suitable absorption edge for the material to be studied. Depending on the operation mode (SASE or self-seeded), a monochromator may or may not be used to limit the incident bandwidth. Plane or circularly polarised X-rays are incident on the sample and scatter (in)elastically, with the scattered X-rays collected by a two-dimensional detector. The main difference is that at an XFEL, incredibly intense, short (~100 fs) X-ray pulses are incident on the sample, each separated by 1–100 ms. Contrast this with a synchrotron, where pulses of 100 ps duration are separated by 1–10 ns. The short pulses generated at an XFEL allow pump-probe experiments to be carried out, whereby the system to be measured is excited by an external perturbation (such as an optical pulse), then probed with the XFEL pulse. These types of experiments have

---

[9] The in-plane momentum resolution ΔQ is given by $\Delta|\mathbf{Q}| = \frac{4\pi}{\lambda}\sin\delta\theta$, where $\delta\theta$ is the angular acceptance of the analyser.

[10] Synchrotron slicing sources, for example FEMTO at the Swiss Light Source, can push this down to the femtosecond regime. However this comes at a cost of six orders of magnitude lower incident flux.

already been used to shed insight into the mechanism of high-temperature superconductivity for example, and have been extended towards 5d transition metal oxides.

Summary

The theory behind resonant elastic and inelastic X-ray scattering has been briefly discussed, as well as detailing instruments where it is possible to perform these techniques. One reason for using these techniques is to probe the electronic and magnetic dynamics of a given material. As detailed above, 5d TMOs are an ideal case for the use of resonant X-rays.

Chapter 3

Magnetic correlations and the MIT in $Cd_2Os_2O_7$ studied with RIXS

One of the unique aspects of resonant inelastic X-ray scattering (RIXS) is the ability to follow both electronic and magnetic correlations through the MIT. The pyrochlore osmate $Cd_2Os_2O_7$ *undergoes a continuous Lifshitz MIT concomitant with the onset of long-ranged Néel order at 227 K. RIXS was used to determine the role of spin-orbit coupling and magnetic interactions upon the MIT. These measurements show broad orbital excitations consistent with a scenario wherein electron correlations and spin-orbit coupling appear to play a reduced role in the electronic Hamiltonian. Furthermore a weakly dispersive feature at 150 meV energy loss shows evidence of both the continuous closing of the charge gap and strong magnetic anisotropy. This provides further indication that the electronic and magnetic interactions are intimately linked for* $Cd_2Os_2O_7$*.*

The metal-insulator transition is of continuing interest in condensed matter physics. A number of transition metal oxides (TMOs) undergo MITs, either by bandwidth control, filling control, temperature, or the onset of magnetic order. In the insulating phase one would expect localised magnetic and electronic excitations, which become more itinerant in the metallic phase. However, there is a dearth of literature in which these excitations are systematically characterised through the MIT. This is especially the case for 5d TMOs where, as previously alluded to, the onset of magnetic order and MIT are directly linked for a number of materials. This appears to manifest as some degree of Slater character. Fortunately RIXS is uniquely placed as a method with which to simultaneously probe the spin and electronic degrees of freedom that govern the Hamiltonian.

One prime example where RIXS has proven to be a useful tool is the set of pyrochlore iridates, which have been predicted to exhibit a variety of non-trivial topological states such as the in vogue Weyl semimetallic phase. Pyrochlore iridates $Ln_2Ir_2O_7$, where Ln^{3+} is a rare-earth ion, and Ir^{4+} has 5 *d*-electrons ($S = \frac{1}{2}$), undergo an MIT through bandwidth control. The ionic radius of the rare earth site decreases moving across the period,[1] which leads to insulating behaviour for early-period rare-earths, and metallic behaviour for late-period rare-earth ions. Those in the centre of the period (Eu, Sm, Nd) undergo finite-temperature MITs concomitant with the onset of long-ranged antiferromagnetic order.

RIXS measurements on these materials [86–89] surprisingly reveal little change through the MIT; the only significant difference between the spectra in the insulating antiferromagnetic phase and metallic paramagnetic phase is the intensity of the magnon peak. This demonstrated that structural distortions were not responsible for the MIT. Furthermore the presence of well-defined spin wave excitations in the insulating phase for $Sm_2Ir_2O_7$ – albeit somewhat damped – indicated that significant electronic correlations were present [90]. This suggests a departure from the ideal Weyl semimetal scenario.

The isostructural osmate $Cd_2Os_2O_7$ ($S = \frac{3}{2}$, d^3) also undergoes a metal-insulator transition concomitant with the onset of antiferromagnetic order. The mechanism of this MIT has been much debated, and in particular, the role of magnetic correlations and spin-orbit coupling. Furthermore the proposed “all-in, all-out” (AIAO) magnetic structure is somewhat tentative. Fortunately RIXS provides information about the electronic and magnetic interactions throughout the Brillouin zone, which allows characterisation of the MIT from a microscopic perspective.

3.1 Literature review

3.1.1 Structure and general aspects of pyrochlore physics

$Cd_2Os_2O_7$ is an example of a osmate on the pyrochlore lattice. The general formula of a pyrochlore is $A_2B_2O_6O'$, with the A [Wyckoff position 16d, lattice coordinates $(\frac{1}{2}, \frac{1}{2}, \frac{1}{2})$] and B [16c, (0,0,0)] sites usually A^{3+} and B^{4+} respectively; however A^{2+} and B^{5+} examples exist where the ionic radius of the A site is especially large. The two sites form interpenetrating FCC sublattices, with a network of corner-sharing tetrahedra. Each A and B site is coordinated to 8 and 6 oxygen atoms respectively $\left[\text{O at } (x, \frac{1}{8}, \frac{1}{8}), \text{O}' \text{ at } (\frac{3}{8}, \frac{3}{8}, \frac{3}{8})\right]$ The pyrochlore structure is consequently a member of the cubic $Fd\bar{3}m$ space group, with the only variable parameters the lattice constant a and the O x-coordinate. For an ideal pyrochlore $x = \frac{5}{16} = 0.3125$, which gives a perfect octahedron about the B sites, however real systems typically exhibit weak trigonal distortions give $x \sim 0.320$–0.345 [91].

Notably the lattice topology plays a key role for the magnetic ground state. Consider a single set of A or B sites, which form a network of corner-sharing tetrahedra. These sites are assumed to be magnetic, and interact to first order via isotropic Heisenberg exchange $\mathcal{H} = J \sum \mathbf{S}_i \cdot \mathbf{S}_j$. If these interactions are ferromagnetic, then the result is long-ranged collinear magnetic order. However if the interactions are antiferromagnetic, then the lattice geometry means that the system is unable to satisfy all of its pairwise interactions simultaneously. This is known as *geometric*

---

[1] This is the so-called *lanthanide contraction*.

frustration. As a compromise the system is forced to adopt a non-collinear spin arrangement, which leads to a ground state without long-ranged magnetic order. The distinguishing feature of this ground state is that it is highly degenerate, leading to an extensive ground state entropy. In the ideal case, this leads to a spin-liquid phase [92], in which the spins are strongly correlated yet remain dynamic to $T = 0$. Additional contributions including single-ion anisotropy, dipolar and further-neighbour exchange interactions can lift this degeneracy and result in the formation of an ordered ground state. This is what occurs for the pyrochlore iridates; the intrinsic geometric frustration is lifted by the presence of anisotropy. In general competition between a number of magnetic interactions is a defining feature of systems on the pyrochlore lattice.

3.1.2 Synthesis

Sleight *et al.* [93] report the initial synthesis of $Cd_2Os_2O_7$ by sealing ‘appropriate quantities’ of CdO, Os metal, and OsO_4 in a quartz tube and heating to 800°C. Upon cooling octahedral crystals ca. 1 mm across were formed. However the use of OsO_4 is extremely hazardous due to its high toxicity and volatility, and hence is discouraged. Current synthesis methods [94, 95] oxidise elemental osmium in situ, by using $KClO_3$ or AgO as an oxygen source.

Mandrus and colleagues [94] were the first to perform a thorough structural characterisation of $Cd_2Os_2O_7$. Using laboratory X-ray diffraction they found $a = 10.16$ Å, which was in good agreement with the initial study in [93], and varied very little as a function of temperature. This implied no structural distortion occurred between 180 K and 295 K. Refinement of the O(1) x-position gave $x = 0.319(2)$, indicative of a weak distortion from the ideal cubic case. These observations were corroborated by neutron diffraction measurements by Reading and Weller [96]. Neutron diffraction has the advantage of greater sensitivity to the oxygen positions compared to X-ray scattering. However in the case of $Cd_2Os_2O_7$, naturally occurring cadmium is strongly neutron absorbing (it is frequently used as shielding for inelastic neutron scattering measurements). This would strongly affect Rietveld refinements; consequently powder samples were enriched with ^{114}Cd. The only significant observations were a point of inflexion in the lattice constant around 225 K, and the absence of magnetic Bragg reflections which would be indicative of magnetic long-ranged order.

3.1.3 Bulk properties

Resistivity measurements by Sleight *et al.* [93] demonstrated that $Cd_2Os_2O_7$ undergoes a continuous metal-semiconductor transition around $T_{\mathrm{MI}} = 225$ K, with an increase in resistivity of three orders of magnitude at low temperature compared to room temperature. This is consistent with the point of inflexion observed in the lattice constant. Magnetic susceptibility and specific heat measurements also observed a transition at the same temperature (Fig. 3.1a), however the authors argued that the transition was entirely electronic in origin. Later measurements by Mandrus *et al.* [94], and Hiroi *et al.*, [97] found the same observations.

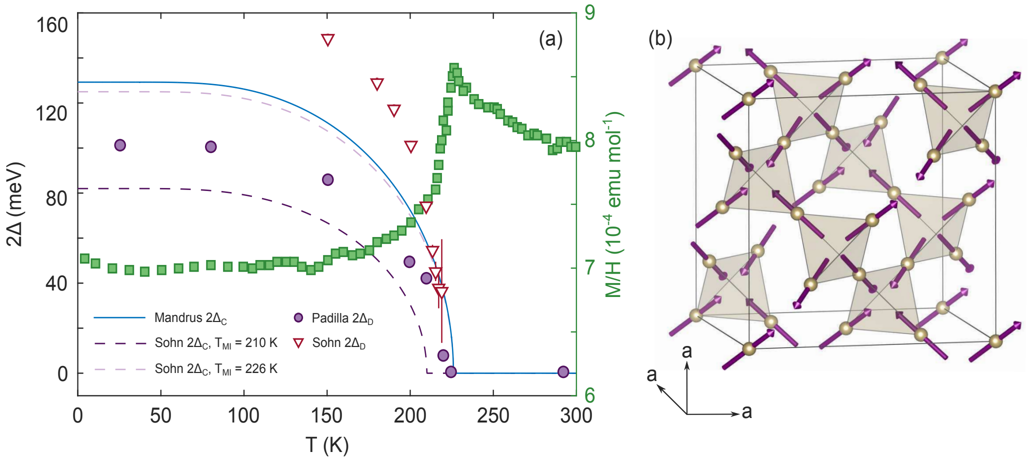

Figure 3.1: (a): Temperature dependence of the magnetic susceptibility (green symbols, [95]), charge gap from resistivity data (solid: [94], dashed: [99]), and direct (optical) gap from optical conductivity data (solid circles: [98], open triangles: [99]) which show the link between the MIT and onset of AFM order. (b): Magnetic AIAO ground state of $Cd_2Os_2O_7$.

The lack of structural distortion implies an unconventional mechanism for the MIT. It was proposed by Mandrus *et al.* that $Cd_2Os_2O_7$ undergoes a continuous Slater-type transition, in which the resistivity varies exponentially with temperature: $\Delta = T\ln(\rho/\rho_0)$. Calculation of the activation energy found that it was consistent with a BCS-type function for $T/T_{\rm MI} > 0.8$, and implied the zero temperature charge gap $\Delta = 750$ K $\equiv 63$ meV. For $T/T_{\rm MI} < 0.8$ there was significant suppression of the charge gap, which was assumed to be due to extrinsic conduction mechanisms. Application of an external pressure of 20 kbar weakly suppressed the metal-insulator transition. Susceptibility measurements indicated that the interactions below $T_{\rm MI}$ were antiferromagnetic, albeit with a small parasitic ferromagnetic component induced by defects. Thermopower measurements in polycrystalline samples showed a change in sign of the Seebeck coefficient S, which is typical of a gap opening up at the Fermi energy and the corresponding metal-insulator transition.

3.1.4 Optical conductivity

Infrared reflectance measurements were performed by Padilla and colleagues [98] as a function of temperature. At room temperature metallic behaviour could be observed, with a gradual transition to insulating behaviour at room temperature. The real part of the optical conductivity was extracted via Kramers-Kronig analysis, and showed a continuous development of a gap as the temperature was reduced. Spectral weight within the intra-gap region was transferred to higher energies. The temperature dependence of the gap could be fit to a BCS-type function, with the magnitude at zero temperature $2\Delta_0 = 100$ meV, which is broadly consistent[2] with the value obtained from bulk resistivity data. The fact that $\sigma(\omega) \sim \omega^{1/2}$ above the gap edge, and not

---

[2] There is a subtle distinction between the charge and optical gaps, see Section 3.3.2 for more details.

$\sim \omega^{3/2}$ as observed in the Hubbard limit, was suggested by the authors as proof that $Cd_2Os_2O_7$ is indeed an example of a Slater insulator.

This proposition is, however, refuted by Sohn *et al.* [99], who instead claim that $Cd_2Os_2O_7$ undergoes a Lifshitz transition at T_{MI}. The temperature dependence of the square of the absorption coefficient $\alpha^2(\omega)$ revealed a linear shift to lower energy with increasing temperature, whilst the gradient of $\alpha^2(\omega)$ remained constant. The authors argue that as $\frac{\mathrm{d}\alpha^2(\omega)}{\mathrm{d}\omega} \propto m_r^3$, where m_r is the reduced mass of the conduction and valence bands, then the constant gradient of $\alpha^2(\omega)$ as a function of temperature implies a rigid shift of the valence and conduction bands with minimal change in band dispersion. Furthermore the square of the plasma frequency ω_p^2 was found to be inconsistent with thermally excited carriers, as would be expected for a Slater insulator. Interestingly however, bulk measurements [93, 94, 97] determined that $T_{\mathrm{N}} = T_{\mathrm{MI}} = 227$ K, whereas Sohn [99] suggests the presence of a antiferromagnetic metallic phase between 210 K and 227 K. The latter fact suggests that the onset of magnetic order is not a driving force for the MIT. On the other hand, it may also be evidence of differences between the surface and bulk electronic phenomena, since optical spectroscopy – in the energy range used – is a surface-sensitive technique.

3.1.5 X-ray and muon spin relaxation (μSR) measurements

X-ray resonant magnetic scattering (XRMS) measurements by Yamaura and colleagues [95] showed the existence of forbidden Bragg reflections present at (0, 0, 4n+2) positions, which could only be observed in the π-σ' polarisation channel. This latter point indicates that they cannot arise from Bragg scattering from a structural peak, since these will only be observed in the π-π' polarisation channel. Moreover the temperature dependence of these reflections was consistent with a second-order transition at 227 K, which implied that the origin of these reflections was magnetic and reflected commensurate $\mathbf{q} = 0$ antiferromagnetic order below T_{N}. Representational analysis, coupled with the lack of a significant ferromagnetic component, indicated that the magnetic structure below T_{MI} was the "all-in, all-out" structure.[3] In this structure the local Os spins point into/out of an Os tetrahedron, with the spins pointing along the local [1 1 1] axes (Fig. 3.1b). The frustration arising from the pyrochlore lattice is lifted as a result of the strong magnetic anisotropy from the intrinsic spin-orbit coupling. The fact that the magnetic structure and crystal structure are commensurate with other was argued as proof that $Cd_2Os_2O_7$ is not an example of a Slater insulator, since in a *simple* Slater picture, unit cell doubling magnetic order is expected in the insulating regime.[4]

X-ray circular magnetic dichroism (XMCD) measurements by Matsuda *et al.* [100] revealed that the induced orbital component to the magnetization was non-negligible [$m_L/m_S = 0.16(2)$].

---

[3] Strictly speaking such an analysis utilising one family of forbidden reflections is insufficient to determine the magnetic structure *a priori*; see [89].

[4] In Chapter 4, I discuss how this condition can be relaxed for three-dimensional systems.

This contrasts with the expected behaviour for a d^3 ion in the Russell-Saunders L-S limit:

$$M_j = \sum_j m_j = 1 + 0 - 1 = 0$$

$$S_j = \sum_j s_j = \tfrac{1}{2} + \tfrac{1}{2} + \tfrac{1}{2} = \tfrac{3}{2},$$

that is, the orbital angular momentum is quenched. However in 5d TMOs spin-orbit coupling cannot be neglected; the spin and orbital components of the magnetisation are mixed and hence the orbital angular momentum can no longer be considered as quenched for $Cd_2Os_2O_7$. The positive sign of the ratio indicates that the two angular momentum components are parallel; a result that seems counter-intuitive considering the fact that the osmium ions have the d^3 electron configuration, and the t_{2g} manifold is at half-filling. One possibility for the observed result is that the spin and orbital angular momenta are aligned at an angle to one another, but the applied magnetic field cants the angular momenta to align with themselves.

Longitudinal muon spin relaxation (μSR) measurements by Koda and colleagues [101] suggested the presence of strong spin fluctuation between 150 K and T_N, based on the decay of the muon spin precession frequency above 150 K, and the external field dependence of the muon relaxation rate. Fitting the muon relaxation rate with the Redfield model (a Lorentzian-like dependence) gave the fluctuation rate of the local field $\nu \geq 5.2(2) \times 10^8$ Hz. Koda initially determined the long-ranged order to be spin density wave-like, but subsequent measurements [102] disproved this hypothesis.

3.1.6 Theoretical calculations

Density functional theory (DFT)

The first theoretical calculations were performed by Mandrus and colleagues [94]. In this study the full-potential linearised augmented plane-wave method (LAPW) was used, which is a variation on density functional theory (DFT). Within the local density approximation (LDA), $Cd_2Os_2O_7$ was found to be metallic. The authors argued that this was further proof of a Slater mechanism for the MIT, since a metallic state would be expected in the absence of magnetism. Inclusion of spin-orbit coupling merely shifted the bands upwards by 80 meV.

Subsequent calculations by Singh *et al.* [103] (LDA and generalised gradient approximation [GGA] within LAPW) found that the inclusion of spin-orbit coupling in fact substantially changed the electronic structure close to the Fermi energy, with two electron-like Fermi surfaces leading to a semimetallic ground state. Singh proposed, at least conceptually, that $Cd_2Os_2O_7$ could be made insulating by increasing the gap between the two bands crossing the Fermi level. The centres of mass of the t_{2g} and e_g manifolds were separated by approximately 4 eV, giving a first estimate for the crystal field splitting $10\,Dq$. It was found that $Cd_2Os_2O_7$ was close to an antiferromagnetic state within GGA, but not within the local spin density approximation (LSDA).

Shinaoka *et al.* [104] also used the local spin density approximation (LSDA), however also included the effect of the electron correlation U and Hund's coupling J through an empirical

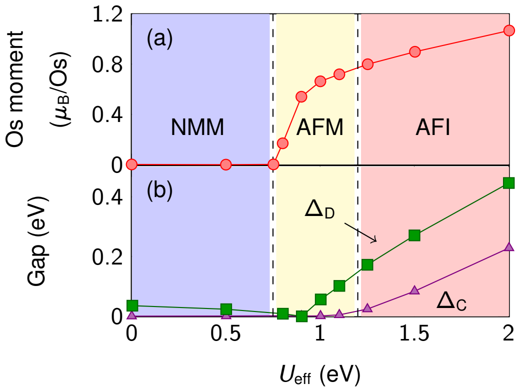

Figure 3.2: Phase diagram adapted from Shinaoka [104]. The three phases are a non-magnetic metallic state (NMM), an antiferromagnetic metal (AFM), and an antiferromagnetic insulator (AFI). The Os moment (a), charge gap Δ_C and optical gap Δ_O (b) increase with increasing electron correlation $U_{eff} = U - J$.

parameter $U_{eff} = U - J$. Through increasing U_{eff} (Fig. 3.2), they found a progression from a non-magnetic metallic state (NMM), to an antiferromagnetic metal (AFM), and finally an antiferromagnetic insulator (AFI). A continuous MIT occurred at $U_{eff} = 1.2$ eV, characterised by vanishing electron and hole surfaces, as appropriate for a Lifshitz transition. The magnetic moments in the AFI phase were found to be most stable for an all-in, all-out (AIAO) configuration, in agreement with the previous XRMS study [95]. Furthermore Shinaoka *et al.* predicted a significant single-ion anisotropy comparable to the nearest neighbour exchange, which stabilises the AIAO order and leads to a magnon gap of "several tens of meV".

Based on the relativistic LDA bandstructure, Uehara and colleagues [105] constructed the multiband tight-binding model for the Os 5d orbitals with t_{2g} symmetry. From this they could estimate tight-binding parameters using maximally-localised Wannier function (MLWF) analysis: the spin-orbit interaction $\lambda = 2\langle d_{xy}, \uparrow | \mathcal{H}^{\mathrm{LDA}} | d_{yz}, \downarrow \rangle = 332$ meV, nearest-neighbour hopping $|t| = 178$ meV, and trigonal crystal field splitting $\Delta = \langle d_{xy}, \uparrow | \mathcal{H}^{\mathrm{LDA}} | d_{yz}, \uparrow \rangle = 96.6$ meV. Inclusion of the electron correlation ($U = 0.7$ eV) and Hund's coupling ($J_H/U = 0.2$) led to significant spin fluctuations along the local $\langle 1\,1\,1 \rangle$ moment axes, consistent with all-in, all-out order.

Quantum chemistry

Bogdanov *et al.* [106] performed many-body quantum chemistry calculations on a small cluster of $Cd_2Os_2O_7$. These differ from DFT calculations in the following ways. In DFT, the assumption is that the atomic wavefunctions can be expressed as a set of plane waves. Consequently the translational symmetry can be exploited through the use of periodic boundary conditions, and the ground state problem solved in momentum space. Various properties can then be calculated from the ground state charge density. However, the formulations of DFT which are typically used (LDA and GGA for instance) treat electron-electron interactions on a mean-field level, where an individual electron is assumed to be moving in an effective field of the other electrons. In strongly correlated TMOs for instance, the underlying physics is dominated by the

$5d^3$ splittings	MRCI	MRCI + SOC ($\times$ 2)
$^4A_2$ (t_{2g}^3)	0.00	0.00; 0.014
^2E (t_{2g}^3)	1.51; 1.51	1.40; 1.53
$^2T_1$ (t_{2g}^3)	1.61; 1.61; 1.62	1.63; 1.66; 1.76
$^2T_2$ (t_{2g}^3)	2.46; 2.49; 2.49	2.63; 2.76; 2.87
$^4T_2$ ($t_{2g}^2e_g^1$)	5.08; 5.20; 5.20	5.14; . . . ; 5.45
$^4T_1$ ($t_{2g}^2e_g^1$)	5.89; 6.01; 6.01	6.02; . . . ; 6.33
$^4T_2$ ($t_{2g}^1e_g^2$)	10.29; 10.63; 10.63	10.41; . . . ; 11.00

Table 3.1: MRCI and MRCI + SOC relative energies (eV) for the Os^{5+} $5d^3$ multiplet structure in $Cd_2Os_2O_7$, as obtained by Bogdanov [106]. As cubic symmetry is lifted, the triplet states are split even without SOC. Each MRCI + SOC value stands for a spin-orbit doublet; for the ^4T states, only the lowest and highest components are shown.

mutual Coulomb repulsive interactions, which are rather local in nature. This leads to systematic discrepancies in calculated properties between theory and experiment.

Ab initio calculations on the other hand aim to solve the many-body wavefunction Ψ $(\mathbf{r}_1, \mathbf{r}_2, \ldots \mathbf{r}_n)$ directly. In the simplest approximation (Hartree-Fock), $\Psi(\mathbf{r}_1, \mathbf{r}_2, \ldots \mathbf{r}_n)$ is approximated as a Slater determinant of spin-orbitals situated at $\mathbf{r}_n$, which is obtained via minimisation of the energy in accordance with the variation theorem. Through the use of post Hartree-Fock methods, such as the configuration interaction (CI), and a suitable choice of basis set, it is possible to go beyond the single determinant approximation and include the effect of correlations between electrons. Unfortunately, the complexity of this approach means that is typically restricted to small clusters, especially for large Z elements where there are a large number of core electrons which have to be treated relativistically. The behaviour of the extended solid is recovered by embedding the cluster in an external Madelung potential formed by an array of point charges at the lattice positions, and subtracting the contribution from the cluster ions.

The electronic structure of the Os $5d$ atomic orbitals was determined for a cluster of seven OsO_6 octahedra surrounded by six Cd^{2+} ions. The results of these calculations are summarised in Table 3.1. What is apparent is the large octahedral crystal field splitting $t_{2g}^3 \rightarrow t_{2g}^2 e_g$ of $10\,Dq = 5.2$ eV. The *ab initio* results were then mapped onto a single site magnetic Hamiltonian with single-ion anisotropy (SIA) $\mathcal{H}_{\mathrm{SIA}} = \mathbf{S} \cdot \bar{\mathrm{D}} \cdot \mathbf{S}$, which gave the axial component $D = -6.774$ meV, and the rhombic component $E = 0$. In general the diagonalisation of the single-ion anisotropy tensor requires that the axial component points along the highest symmetry axis, which in this case is along the $\langle 1\,1\,1 \rangle$ direction. The negative sign of D indicates that this axis is an easy axis. Interestingly similar calculations on a cluster without trigonal distortions found $D = 2.50$ meV, which gives rise to easy-plane anisotropy.

Calculations of the inter-site magnetic couplings were performed on a ten octahedra cluster, which included two active Os $5d^3$ sites. This was mapped onto a nearest-neighbour Heisenberg Hamiltonian with antisymmetric (Dzyaloshinskii-Moriya, DM) exchange: $\mathcal{H} = J\,\mathbf{S}_1 \cdot \mathbf{S}_2 + \mathbf{d} \cdot \mathbf{S}_1 \times \mathbf{S}_2$, where $\mathbf{d}$ is the DM vector with components $(d_\mathrm{x}, d_\mathrm{y}, d_\mathrm{z})$. It was found that the nearest neighbour exchange parameter $J = 6.43$ meV, indicating antiferromagnetic interactions in agreement with experiment, and $\mathbf{d} = (1.17, -1.17, 0)$, which implies $|\mathbf{d}| = 1.65$ meV. The fact that J is similar in magnitude to D was proposed as the origin of the AIAO ground state observed in RXMS measurements [95].

This concludes the brief literature survey. The quantum chemistry calculations have estimated the electronic energy levels and local exchange parameters for $Cd_2Os_2O_7$. However an experimental study of the electronic and magnetic excitations is still lacking. To this end resonant inelastic X-ray scattering (RIXS) measurements were performed by the author to characterise the dynamics of this material.

3.2 Low resolution measurements

This section has been partly published as S. Calder *et al.*, Nature Comms. **7**, 11651 (2016).

Choosing the correct energy resolution is critical for any spectroscopic measurement. There is generally a trade-off between the bandpass of the spectroscopic probe and its resultant intensity, which, in the end, all boils down to Liouville's theorem of phase space. A increase in energy resolution (reduced $\Delta E/E$) leads to a corresponding decrease in the probe intensity. Lower resolution RIXS measurements allow fast characterisation of the orbital excitations out to large energy loss. This includes the determination of crystal field parameters such as $10\ Dq$. Since the orbital excitations tend to be relatively broad (especially at high energy), then energy resolution is not a limiting factor. Moreover, as each individual spectrum is collected relatively quickly in this setup, spectra can be collected at various incident energies and compared to determine which one results in the maximum intensity of the desired feature.

Single crystals of $Cd_2Os_2O_7$ were measured with RIXS at the Os L_3-edge on Sector 30 at the Advanced Photon Source (APS) using the MERIX spectrometer. All measurements were performed in a horizontal scattering geometry, that is π-incident polarisation.[5] The sample was mounted such that the [1 1 1] direction was normal to the sample surface, and placed in a closed-cycle refrigerator. The incident energy was determined through two monochromators: a primary Si (1, 1, 1) and a secondary Si (4, 4, 4) four-bounce, for a total bandpass of $\Delta E = 120$ meV. The beam was focussed by Rh plated mirrors down to $\sim 20 \times 10\,\mu\mathrm{m}^2$. The energy of the X-rays scattered from the sample was discriminated via a Si (4, 6, 6) 2 m diced analyzer situated on the Rowland circle, and detected by a MYTHEN strip detector (pixel size $50 \times 50\ \mu\mathrm{m}^2$). The combined RIXS energy resolution was 130 meV at FWHM, as calculated from fitting non-resonant scattering off a piece of adhesive tape.

---

[5] An undulator source at a synchrotron provides a highly plane-polarised (polarisation factor $P \simeq 1$) and collimated X-ray beam. It is henceforth assumed that the incident beam is entirely π-polarised, that is, parallel to the scattering plane defined by $\mathbf{k}_i$ and $\mathbf{k}_f$. This notation is the same as described in Chapter 2.

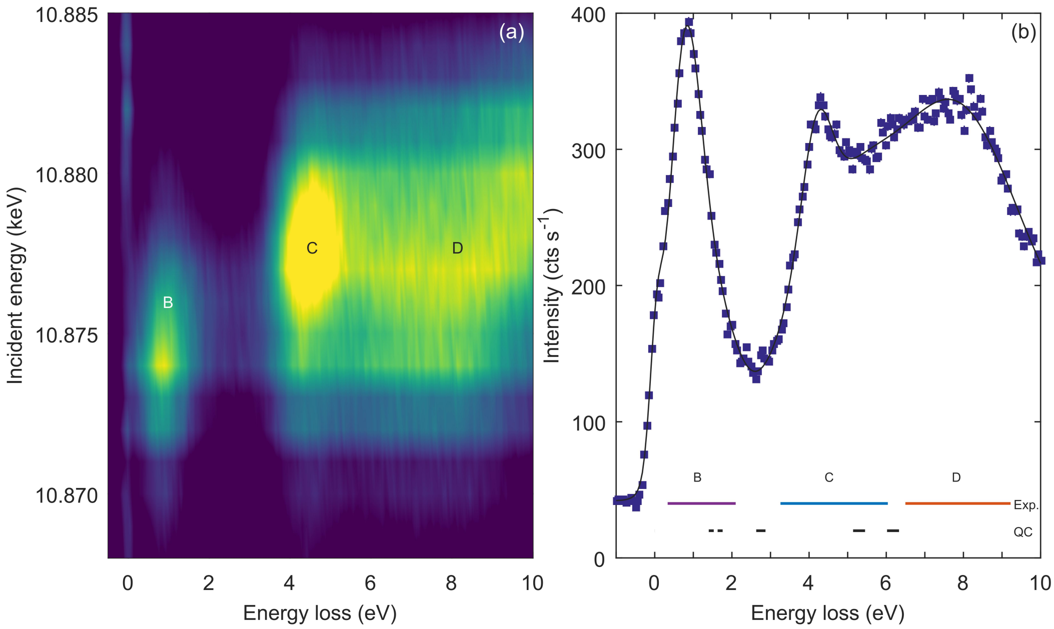

Figure 3.3: (a): RIXS spectra for $Cd_2Os_2O_7$ as a function of incident energy collected at 300 K. Three features (B, C, D) can be observed, which correspond to intra-t_{2g}, $t_{2g} \to e_g$, and ligand-to-metal charge transfer (LMCT) excitations respectively. Solid line is the best fit to the data. The fitting model comprised a sum of Gaussian functions, each representing the elastic line and aforementioned inelastic features. (b): Example spectrum collected for an incident energy of 10.875 keV. Superimposed are the expected transitions based on the quantum chemistry (QC) calculations [106].

3.2.1 Incident energy dependence

RIXS spectra were collected as a function of incident photon energy out to 10 eV energy loss. These are plotted in Figure 3.3. Three features are apparent at 1 eV, 4 eV and 7 eV, henceforth labelled as B, C, and D respectively (the reason for this notation shall become clear later). Peaks B and C are localised at a fixed energy loss, whereas peak D appears to increase with increasing incident energy. The fact that B and C resonate at different energies reflects the fact that they result from different processes. Based on comparison with the QC calculations, B and C can be associated with intra-t_{2g} and $t_{2g} \to e_g$ excitations respectively. Feature D on the other hand is more reminiscent of ligand-to-metal charge transfer (LMCT). Note that there is a constant offset between the experimental peak energies and the calculated values (see bottom of Figure 3.3b and Table 3.1), which may be due to some itinerant effects which are not taken into account within the cluster model used in QC. Nevertheless, the salient features are separated sufficiently in energy such that their present assignment is reasonable. Since the main aim was to study modes which involved transitions between t_{2g} states, the incident energy was fixed to maximise the RIXS intensity for peak B. Consequently the incident energy was kept fixed at 10.875 keV. Discussion of the different features in the RIXS spectra follows, starting with the intra-t_{2g} excitation peak.

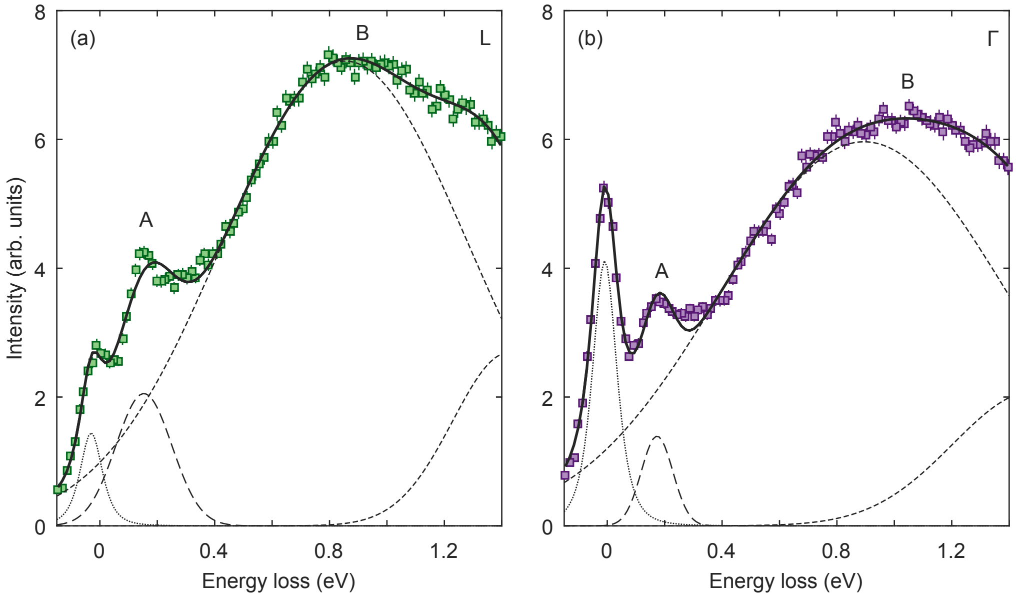

Figure 3.4: Fits of the low energy RIXS spectra at 30 K for the L (a) and Γ (b) points. The quasi-elastic feature is fitted to a resolution limited Pearson VII function constrained to the width of the resolution function, whilst all other features are fitted by Gaussians. The energies of the intra-t_{2g} excitations comprising the broad peak at ca. 1 eV (peak B in Fig. 3.3) were fitted to $3J_\text{H}$ and $5J_\text{H}$ respectively, with J_H as a fitted parameter.

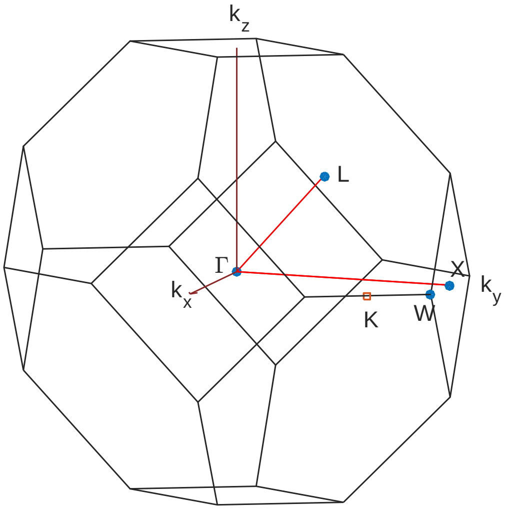

Figure 3.5: Brillouin zone for the Fd$\bar{3}$m space group, with high symmetry points highlighted. The points Δ and Σ – as referenced later – have been omitted from this diagram as they are not high symmetry points, but correspond to $(0, \frac{1}{4}, 0)$ and $(\frac{1}{4}, \frac{1}{4}, 0)$ respectively.

3.2.2 Intra-t_{2g} excitations

Representative RIXS spectra are plotted in Figure 3.4, which were collected at Γ (3, 9, 9) and L (2.5, 8.5, 8.5). These points correspond to the Brillouin zone centre and zone boundary respectively (Figure 3.5).

Calculation of Hund's coupling J_H

The starting point is a localised Os^{5+} (d^3) ion in the Russell-Saunders limit. To first order,[6] one can estimate the $\Delta S = 1$ intra-t_{2g} excitations as transitions from a $^4A_2$ ground state to either: (a) an accidentally degenerate state with $(^2E, ^2T_1)$ symmetry, or (b) a state with $^2T_2$ symmetry. These terms arise as a result of Coulomb repulsion. Such an excitation is not a pure spin-flip transition, as the excited state wavefunction includes a linear combination of atomic d-orbitals. In the atomic limit the two states (a) and (b) are separated from the ground state by $3J_\mathrm{H}$ and $5J_\mathrm{H}$ respectively, where J_H parameterises the Hund's coupling [107]. Alternatively from an atomic physics perspective, one can express $J_\mathrm{H} = 3B + C$, where B and C are Racah parameters.[7] A schematic of the various energy levels is displayed in Fig. 3.6a.

It is possible to estimate J_H by fitting the intra-t_{2g} excitations observed in the RIXS spectra with two Gaussians centered at $3J_\mathrm{H}$ and $5J_\mathrm{H}$ respectively. If one does this, one obtains $J_\mathrm{H} = 0.29(4)$ eV. This differs slightly from estimates for $J_\mathrm{H} = 0.16$ eV used in DFT calculations for instance [105]. It should be stressed at this point that the estimate given above applies in the atomic limit, and only to first order.

3.2.3 Excitations across Δ_O

Peak C corresponds to a $t_{2g} \rightarrow e_g$ excitation. The energy of this peak is, to first order,[8] an estimate of the octahedral ligand field splitting Δ_O (10 Dq in the crystal field approximation). In the utilised low resolution setup ($\Delta E = 275$ meV), $10\,Dq = 4.2(1)$ eV, which is significantly larger than for the isostructural pyrochlore iridates $(Y,Eu,Pr)_2Ir_2O_7$, and the isoelectronic double perovskite Sr_2FeOsO_6 (Table 3.2). The difference can mainly be attributed to the reduced bond distance for $Cd_2Os_2O_7$, increased effective charge for the osmium site compared to the iridium site (Os^{5+} vs. Ir^{4+}), and larger Os 5d – O 2p hybridisation. What this means is that there is very little mixing between the e_g and t_{2g} states for $Cd_2Os_2O_7$. Consequently in the case that SOC is treated as a perturbation to the Hamiltonian (close to the Russell-Saunders limit), it would have the effect of splitting the electronic terms into levels Γ_i, but the centre of mass of those levels would remain almost constant.

---

[6] The validity of this assumption shall be discussed later.

[7] These in turn can be related to the Slater integrals: $B = F_2 - 5F_4$, $C = 35F_4$.

[8] As mentioned earlier, electron-electron repulsion splits the e_g levels into a series of multiplets, the energy of which each contain 10 Dq as a prefactor.

	$Cd_2Os_2O_7$	Sr_2ScOsO_6	$Y_2Ir_2O_7$	$Eu_2Ir_2O_7$	$Pr_2Ir_2O_7$
$10\,Dq$ (eV)	4.2(1)	3.6(2)	3.90(5)	3.68(2)	3.40(2)
M–O (Å)	1.9344(4)	1.968(6), 1.957(6)	1.991	2.033(12)	2.013(8)
M–O–M (°)	86.95(5)	87.4(2)	81.471	80.3(9)	83.7(7)

Table 3.2: Crystal field parameters (as obtained by spectroscopic methods), M–O bond distances, and M–O–M bond angles for $Cd_2Os_2O_7$ [96], the double perovskite Sr_2ScOsO_6 with Os^{5+} [108, 109], and the pyrochlore iridates $(Y,Eu,Pr)_2Ir_2O_7$ [86, 88, 110, 111]. All bond distances are given for ambient temperature.

Discussion

In the atomic limit these transitions would be expected to be sharp, however even at 30 K the observed features are intrinsically broad. For example the peak centered at $3J_H$ has a width of 0.43(3) eV, significantly larger than the resolution of 0.13 eV. There are a number of reasons for this. One is that the excited state has a finite lifetime, and hence through the Heisenberg uncertainty principle, a finite bandwidth. For electronic transitions this is expected to be very short ($\sim$ fs), which is equivalent to an energy scale on the order of 0.1 eV. Another consideration is that the t_{2g} manifold is relatively broad in $Cd_2Os_2O_7$. This occurs as a direct consequence of weak to moderate electron correlations U and significant hybridisation between Os 5d and O 2p states.

However, these are not the only factors which contribute to the observed broad peaks in the RIXS spectra. These contributions include the effects of spin-orbit coupling and distortions away from an ideal cubic symmetry. Spin-orbit coupling has three main effects on the electronic terms within an L-S coupling scheme. The dominant effect is that it splits terms for which the direct product $D^{(S)} \times \Gamma$ is reducible. According to the Wigner theorem, each resulting irreducible representation corresponds to a certain energy level. Thus spin-orbit coupling results in so-called *fine structure* levels. Secondly mixing of many electron terms can occur if the direct product $\Gamma_1 \times \Gamma_2$ contains representations which transform in the same manner as those of the orbital angular momentum operators $\hat{l}_{x,y,z}$. This leads to a mutual ‘repulsion’ of the corresponding terms. Finally those terms for which $D^{(S)} \times \Gamma$ is irreducible (and hence not split by the spin-orbit interaction) are perturbed in accordance with second-order perturbation theory.

Distortions of the cubic environment result in a reduction of symmetry and a corresponding point group with fewer irreducible representations. Doubly or triply degenerate levels can be split by this low symmetry field. A canonical example is a tetragonal axial field with D_{4h} symmetry acting on a set of degenerate t_{2g} orbitals. The field acts along the local z-axis to stabilise the d_{xz} and d_{yz} orbitals, whilst simultaneously raising the energy of the d_{xy} orbital relative to the undistorted complex.

For a d^3 ion, quantitative calculations of the energy levels, whilst including both spin-orbit coupling and trigonal distortion, are rather complex. The procedure applied also depends on the relative magnitudes of the perturbations relative to the cubic splitting and electronic repulsion

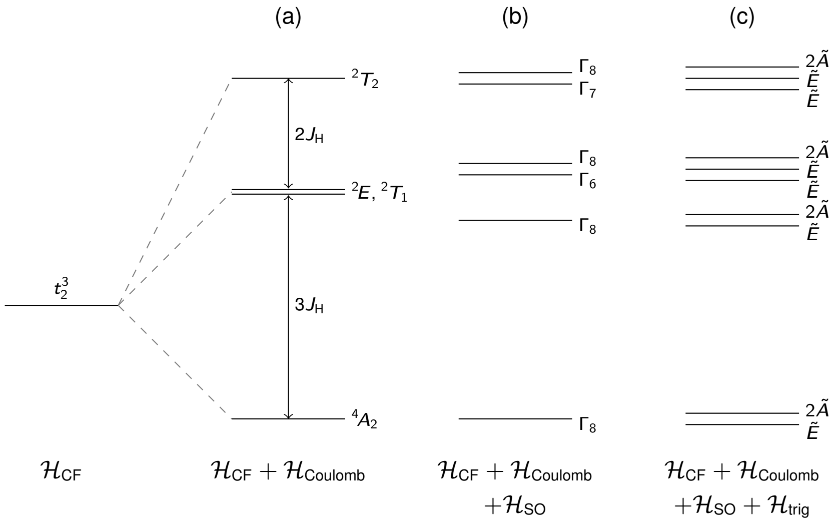

Figure 3.6: (a): Terms of a t_2^3 configuration in a first (strong field) approximation, including the effect of Coulomb repulsion. Spin-orbit coupling and distortions away from an ideal octahedral geometry are neglected. The Hund's coupling J_H is equivalent to $3B + C$, where B and C are Racah parameters. The terms ^2E and $^2T_1$ are accidentally degenerate. (b): Electronic terms when spin-orbit coupling is added as a weak perturbation. Terms are calculated by decomposition of the direct product $\Gamma \times D^{(3/2)}$. The separation between terms originating from ^2E and $^2T_1$ is exaggerated for clarity. (c): Addition of a weak trigonal perturbative field to the case presented in (b). Note that the $^4A_2$ ground state is only split (zero field splitting) by a combination of spin-orbit coupling and trigonal distortion, and even then third-order perturbations are required.

terms (strong or weak-field cases). From now on it is assumed that $10\,Dq > B, C > \zeta > \Delta_{\text{trig}}$, that is, the strong field limit. In this case the trigonal distortion is applied after the spin-orbit interaction. The assumption that $\zeta > \Delta_{\text{trig}}$ is reasonable given the expected magnitude of the spin-orbit coupling ($\zeta \sim 0.5$ eV) and near-cubic symmetry for $Cd_2Os_2O_7$. The assumption that $B, C > \zeta$ however is less convincing; this approach was chosen as it allows previously published analytical expressions to be used, and highlights the potential deficiencies of these calculations in the Russell-Saunders limit.

Practically what one has to do is solve the secular equation in which all $nS\Gamma$ terms are involved [62]:

$$|\langle \alpha_i S_i \Gamma_i | \hat{\mathcal{H}}_{SO} | \alpha_j S_j \Gamma_j \rangle - \epsilon \sigma_{ij}| = 0$$

Symmetry arguments simplify this equation somewhat, in that only the states belonging to the same irreducible representations Γ' contained within $D^{(S_i)} \times \Gamma_i$ are mixed by $\hat{\mathcal{H}}_{SO}$.

Example calculations were performed for a model Os^{5+} system including a strong octahedral crystal field, Coulomb repulsion terms and spin-orbit coupling. The trigonal distortion was neglected to a first approximation for the reasons given above. Energy matrices used were the same as those presented in the manuscripts by Tanabe and Sugano [112], and Runciman and Schroeder [113]. The four variable parameters were $10\,Dq$, the Racah parameters B and C, and the spin-orbit coupling ζ. In the first instance, $B = 35$ meV, $C = 165$ meV, and $\zeta = 330$ meV, were fixed to values determined[9] from spectroscopy on a Os^{5+} complex [114]. The values of the Racah parameters are consistent with $J_H = 3B + C = 0.29(4)$ eV as obtained from fitting of the RIXS spectra.

If spin-orbit coupling is included in addition to the octahedral crystal field and Coulomb repulsion, then to first order one finds that the $^2T_1$ and $^2T_2$ terms are split by approximately 20 and 80 meV respectively, whilst the $^4A_2$ and ^2E states are not. This is somewhat smaller than the values predicted within the MRCI+SOC quantum chemistry calculations by Bogdanov for an ideal octahedral environment. Furthermore the quantum chemistry calculations predict a small splitting of the $^4A_2$ and ^2E states. Both effects can be understood however in terms of a single-ion anisotropy contribution which was added in the prior theoretical study, but is not considered here.

It is somewhat surprising that the electronic transitions appear, at least to first order, to be consistent with a model in which spin-orbit coupling acts as a perturbation to the Hamiltonian. This is especially the case when comparing to RIXS data on the iridates for example, which show transitions between the $j_{\mathrm{eff}} = \frac{1}{2}$ and $j_{\mathrm{eff}} = \frac{3}{2}$ bands. Recall that these bands arise as a result of the strong intrinsic spin orbit coupling $\lambda \approx 0.5$ eV. However the difference can at least be partly explained simply by considering the difference between the single-electron and many-electron spin-orbit coupling parameters ζ and $\lambda = \zeta/2S$. Iridium and osmium have similar nuclear charges, so ζ_{5d} should be similar for the two atoms ($\zeta \sim Z^4$). For the iridates (d^5, $S = \frac{1}{2}$), $\lambda = \zeta_{5d} \approx 0.5$ eV so the effect of spin-orbit coupling is strong. However for the osmates $\left(d^3,\ S = \frac{3}{2}\right)$, $\lambda = \zeta_{5d}/3 \approx 0.17$ eV [115], which means that the role of SOC on the electronic states is effectively reduced compared to the iridates.

3.2.4 Momentum dependence at 60 K

Issues with the sample environment meant that it was not possible to cool below 60 K. Ideally one would want to perform RIXS measurements at as low a temperature as possible for a number of reasons. The predominant ones are to minimise the elastic line intensity, and maximise any intrinsic magnetic contribution to the inelastic spectra. Nevertheless a temperature of 60 K puts $Cd_2Os_2O_7$ well in the antiferromagnetic insulator phase, as determined by bulk measurements. The $Cd_2Os_2O_7$ single crystal was oriented in the (H, K, K) scattering plane in order to access high symmetry directions in the (3, 9, 9) Brillouin zone. This zone was chosen such that the scattering angle was within a few degrees of $2\theta = 90^\circ$ for all high symmetry points.

The momentum dependence of the RIXS spectra at 60 K is displayed in Fig. 3.7. All spectra displayed are the result of collecting for 25 seconds per point. Three peaks can be observed: a quasi-elastic feature, a peak at 150 meV, and a high-energy Gaussian tail. The intensity variation of the quasi-elastic feature is caused predominantly by RIXS matrix element effects as one goes away from the ideal $2\theta = 90^\circ$ scattering condition. The high-energy tail is due to the intra-

---

[9] Note that B, C, ζ are reduced from the free ion values as a consequence of covalency effects (nephelauxetic effect).

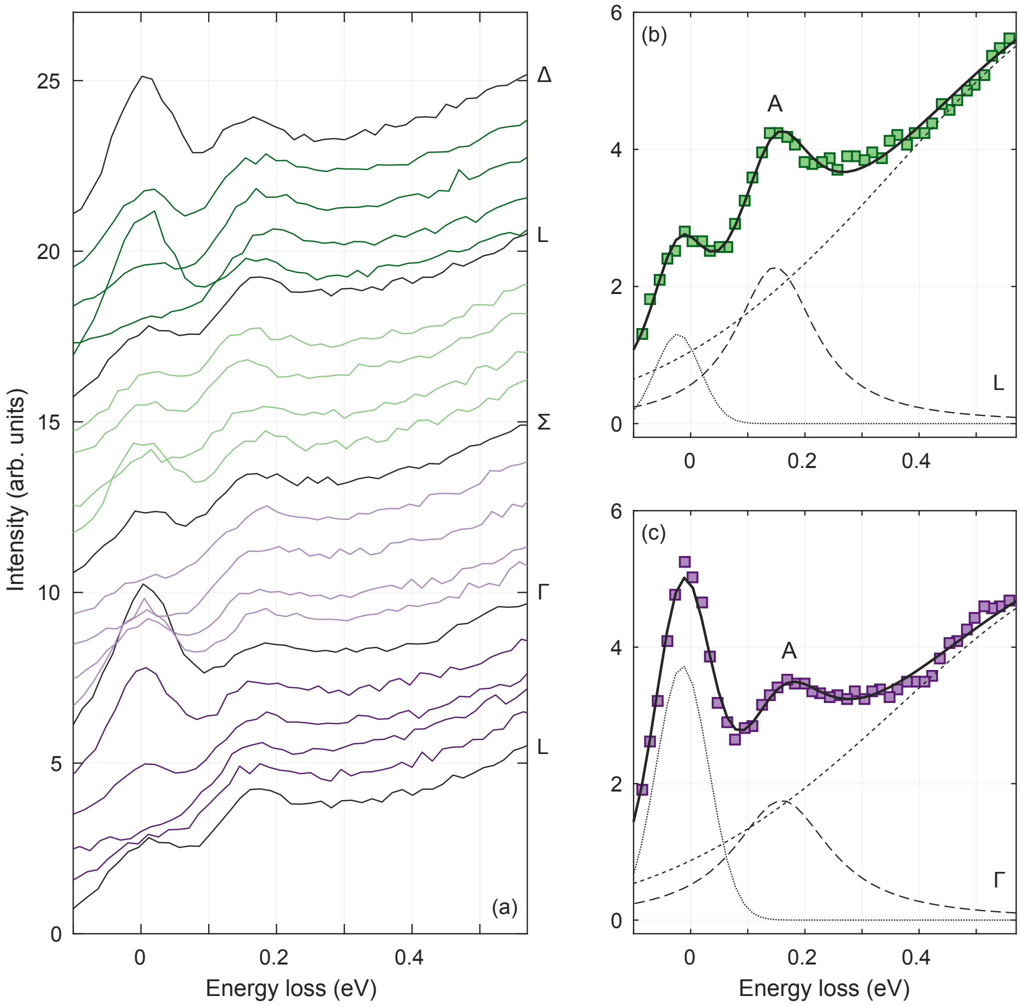

Figure 3.7: (a): Momentum dependence at 60 K in a low-resolution setup. Spectra have been offset for clarity. Δ and Σ correspond to points intersecting the $\Gamma - X$ and $\Gamma - K$ high symmetry directions respectively. The peak at 0.15 eV energy loss corresponds to peak A, with the high energy tail resulting from the intra-t_{2g} excitations. (b,c): Example fits to spectra collected at L (b) and Γ (c), with individual peak components superimposed.

t_{2g} excitations seen previously for the incident energy dependence. The feature at 150 meV energy loss however is the most unusual (henceforth referred to as peak A). Qualitatively it appears to have little dispersion or intensity variation as a function of momentum transfer. In order to parametrise these observations, the RIXS spectra were fitted with a functional form comprising the sum of a Lorentzian representing the quasi-elastic line, and two Gaussians for peak A and the intra-t_{2g} excitations respectively. The position and width of the intra-t_{2g} excitation was constrained to values obtained from the longer scans presented earlier.

Selected fits of the RIXS spectra are presented in Figures 3.7b and 3.7c, with the energy and intensity of peak A displayed in Figure 3.8. The energy of the feature indeed shows little variation as a function of momentum transfer, and could even be considered as dispersionless within error [$E = 170(10)$ meV]. The intensity on the other hand varies by around 50% through

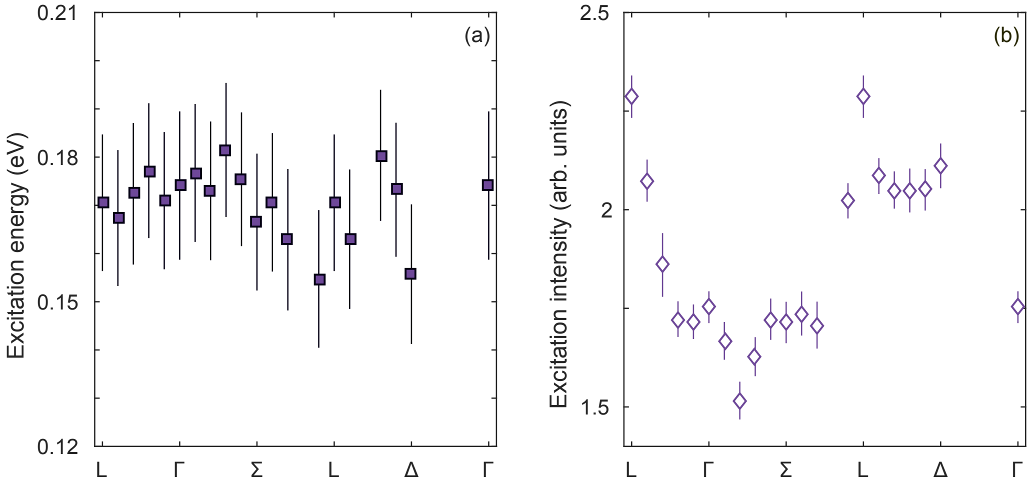

Figure 3.8: Energy (a) and intensity (b) of the feature at 160 meV energy loss (peak A) as a function of momentum transfer. There is a weak variation of the peak energy and intensity across the Brillouin zone.

the Brillouin zone. This observation can in part be explained by differences in the attenuation of the scattered beam as a function of sample orientation, but this is likely to be a rather small effect.

3.2.5 Temperature dependence

Further insight into the origin of peak A can be gathered by considering its dependence on temperature. Spectra were collected at (2.5, 8.8, 8.8); this point was chosen as it gave reasonable intensities of both the quasi-elastic line and peak A, which would aid in fitting. The resulting spectra are plotted in Figure 3.9. Peak A appears to weaken and broaden with increasing temperature, whereas the intra-t_{2g} excitations remain approximately constant. The variation of the quasi-elastic feature is likely due to the increased population of phonons present at high temperature in accordance with the Bose-Einstein distribution. These would be indistinguishable from the elastic line for an energy resolution of 130 meV.

In order to quantify these observations, the data were fitted with the model presented in Section 3.2.4. As displayed in Figure 3.9c, the intensity of peak A decreases continuously with increasing temperature, reaching a minimum around 225 K. This coincides with the metal-insulator transition (MIT) and the onset of antiferromagnetic order. Based on the power law-like dependence of the peak intensity [$\beta = 0.17(2)$] it is suggested that the feature is magnetic in origin.[10] Residual intensity above T_N may be indicative of short-ranged magnetic correlations in the paramagnetic phase.

---

[10] The value of the critical exponent is consistent with that expected for an all-in, all-out magnetic structure [116, 117]. However caution should be taken with this result, since the power law dependence is only strictly valid close to T_N, and there is insufficient data close to the transition to fully characterise the dimensionality of the critical fluctuations.

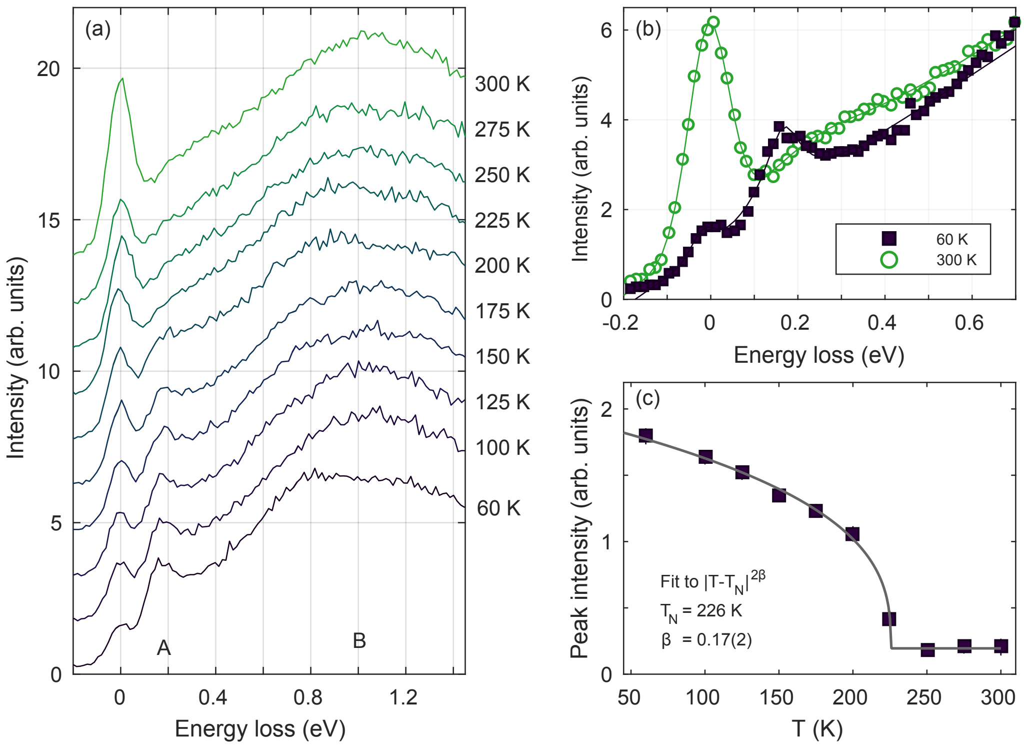

Figure 3.9: (a): Temperature dependence of RIXS spectra collected at (2.5, 8.8, 8.8). Spectra have been offset by a constant factor for clarity. (b): Comparison of spectra at 60 K and 300 K. Peak A weakens and broadens with increasing temperature. Solid line is the best fit to the data with the model given in the main text. (c): Fitted peak intensity as a function of temperature, with a fit to a power law $T_C = 226$ K, $\beta = 0.17(2)$ added as a guide. Such behaviour is consistent with a magnetic excitation.

The non-dispersive nature of peak A however is somewhat puzzling. Conventionally one would expect dispersive spin wave excitations, which for an antiferromagnet would have a bandwidth $\sim 4J$. Furthermore quantum chemistry calculations [106] predict $J = 6.4$ meV, albeit with a significant uniaxial anisotropy $D = -6.8$ meV which stabilises all-in, all-out magnetic order. This energy scale is considerably lower than seen here.

One suggestion proposed by theoretical collaborators in Dresden (Jeroen van den Brink, Satoshi Nishimoto and Nikolai Bogdanov) is that the proposed mode is in fact an unconventional magnetic excitation driven by spin-orbit coupling from an all-in, all-out ground state. The argument goes as follows. In $Cd_2Os_2O_7$ the interactions can be considered Ising-like to first order, as a direct result of the strong uniaxial single-ion anisotropy as predicted by quantum chemistry (QC) calculations. Consequently the dominant contribution to fluctuations are ΔS_z terms, with $S = \frac{3}{2}$ for a d^3 system. It is assumed that there is no orbital component to the magnetization. The non-collinear spin arrangement for an all-in, all-out magnetic structure requires that the local Dzyaloshinskii-Moriya (DM) vector $\mathbf{d}$ is non-zero. In the classical limit, three types of local spin excitations would thus be expected: $S = \frac{3}{2} \rightarrow \frac{1}{2}, -\frac{1}{2}, -\frac{3}{2}$ ($\Delta S_z = 1, 2, 3$ respectively).

These excitations would have the following discrete energies:

$$\begin{aligned}
\Delta S_z = 1: &\quad \Delta E = \left(\sqrt{2}d + \frac{1}{2}J\right) N - D \\
\Delta S_z = 2: &\quad \Delta E = \left(2\sqrt{2}d + J\right) N - D \\
\Delta S_z = 3: &\quad \Delta E = \left(3\sqrt{2}d + \frac{3}{2}J\right) N,
\end{aligned} \tag{3.1}$$

where $J = 6.4$ meV, $D = -6.8$ meV, and $d = |\mathbf{d}| = 1.6$ meV, are the same as determined from the QC calculations.

However this classical model does not take into account the quantum nature of the states and the interactions between them, so exact diagonalization (ED) calculations were performed using the following Hamiltonian:

$$\mathcal{H} = J \sum_{\langle i,j \rangle} \mathbf{S}_i \cdot \mathbf{S}_j + D \sum_i \left(\mathbf{S}_i \cdot \mathbf{A}_i\right)^2 + d \sum_{\langle i,j \rangle} \mathbf{e}_{ij} \left[\mathbf{S}_i \times \mathbf{S}_j\right], \tag{3.2}$$

with the unitary vectors $\mathbf{A}_i \in \langle 111 \rangle$, and $\mathbf{e}_{ij} \in \langle 110 \rangle$. The ground state and all possible excited states were obtained for a 4-site and an 8-site cluster; the former is the minimum required to fully describe the all-in, all-out magnetic ground state. All parameters used were identical to those determined from the QC calculations. The corresponding excitation spectrum for a given ΔS transition is evaluated as follows:

$$I(\omega) = \sum_n \left|\langle \psi_n | \hat{\mathcal{O}} | \psi_0 \rangle\right|^2 \delta(\omega - E_n - E_0), \tag{3.3}$$

where ψ_n and E_n are the n$^{\text{th}}$ eigenstate and eigenenergy ($n = 0$ corresponds to the ground state). Here the operator $\hat{\mathcal{O}}$ refers to $\hat{\mathcal{O}} = S_+$, $(S_+)^2$, and $(S_+)^3$ for $\Delta S_z = 1,2,3$ respectively. It is important to note that this spectrum is in fact equal to the density of states, and not the RIXS cross-section.

The results are displayed in Figure 3.10. The excitation spectra $I(\omega)$ have been broadened by the instrumental resolution and compared to background subtracted data points. Clearly the ED calculations reproduce the energy of peak A very well using the same parameter set as that used for the quantum chemistry calculations.

What is surprising however is that the largest contribution to the density of states (and the best fit to the experimental date) appears to be the $\Delta S_z = 3$ transition. Such a transition is forbidden within the RIXS spin-only selection rules, which limit $\Delta S_z = 1,2$. However spin-orbit coupling has two main effects which mean that contributions from $\Delta S_z = 3$ can indeed be seen with RIXS in this scenario.

In the classical limit, the excitation energies as calculated by Equations 3.1 are discrete. However within the ED calculations the ΔS_z excitations are mixed. This gives rise to the broad central peak in $I(\omega)$. The mixing occurs due to quantum fluctuations which leads to a superposition of spin states. This superposition is a direct result of the sizeable Dzyaloshinskii-Moriya interaction calculated for $Cd_2Os_2O_7$ which is directly linked to the intrinsic spin-orbit coupling. The DM term mixes states with different spin projection S_z into both the ground and excited states.

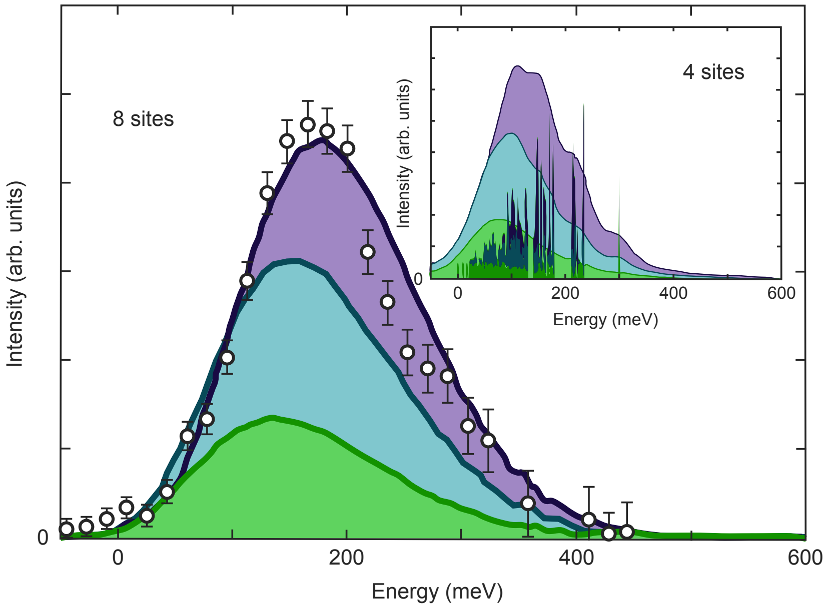

Figure 3.10: Exact diagonalization calculations performed by Satoshi Nishimoto on an 8-site cluster for $Cd_2Os_2O_7$. Markers correspond to experimental data points after background subtraction. Green, blue, and purple lines represent excitation spectra $I(\omega)$ for $\Delta S_z = 1,2,3$ respectively, multiplied by identical scale factors and broadened by the instrumental resolution. Inset shows similar calculations for a minimal 4-site cluster, along with the unbroadened excitation spectra. The energy scale compares well with peak A. Adapted from Ref. [118].

Furthermore remember that the RIXS process is a virtual transition involving an intermediate state. In this intermediate state, the electronic configuration of an osmium ion is $2p^5 5d^4$, which has a non-zero orbital component. Consequently spin-orbit coupling is increased due to the finite orbital component, and S is no longer a good quantum number in the intermediate state. The spin-only selection rules are thus invalid, and hence $\Delta S_z = 3$ transitions become allowed. However the fact that they become allowed does not necessarily imply that they are the dominant excitation mechanism. Equation 3.3 does not take the finite lifetime of the core hole onto account and the interaction with the intermediate state. One would still expect a single magnon process to be the dominant term in the RIXS cross-section, followed by $\Delta S = 2$ and $\Delta S = 3$ terms.

3.3 High resolution RIXS measurements

The observed magnetic feature occurs at an energy comparable to the energy resolution. Furthermore no significant dispersion could be observed. High resolution RIXS measurements were thus performed at the ESRF in order to determine whether the proposed magnetic mode is purely local in nature, or whether it shows dispersion which would be indicative of a propagating collective excitation.

Experimental setup

RIXS measurements at the Os L_3 edge (10.871 keV) were performed on a single crystal of $Cd_2Os_2O_7$ (ca. 0.5 mm across) on the ID20 spectrometer at the ESRF, Grenoble. The sample was oriented such that the [1, 1, 1] direction was perpendicular to a copper sample mount, fixed with GE varnish and placed in a closed-flow He cryostat. The scattering plane and incident photon polarisation were both horizontal, i. e. π-incident polarization, with the incident beam focussed to a size of 20×10 μm^2 (H$\times$V) at the sample position.

A Si (6, 6, 4) four-bounce secondary monochromator was used to define the incident energy, with a Si (6, 6, 4) diced spherical analyser (2 m radius) used to reflect the scattered photons towards a Medipix CCD detector (pixel size 55 μm). Total energy resolution was determined to be $\Delta E = 48$ meV based on scattering from a charge peak. This compares well with the theoretical energy resolution.

Initial findings

A qualitative comparison (Fig. 3.11) of the RIXS spectra in the (6, 7, 7) Brillouin zone at 30 K and 200 K reveals the same non-dispersive feature (peak A) as seen within the lower resolution data presented earlier, which weakens and broadens with increasing temperature. The energy scale of the peak is also rather similar. The main distinctions of the higher-resolution data however are an intrinsic asymmetry of peak A, combined with a suppression of spectral weight between the elastic line and the peak.

In order to quantify these observations, the salient features in the RIXS spectra were represented by a Gaussian for the quasi-elastic excitations, a Gaussian for the intra-t_{2g} excitations (position and width fixed based on selected scans which were performed out to large energy loss), and various functional forms for the asymmetric peak A, which are described below. All of these features were convoluted with the resolution function (Pearson VII function with width 48 meV, profile parameter $\mu = 1.6$) and fitted to the data via a non-linear least-squares approach.

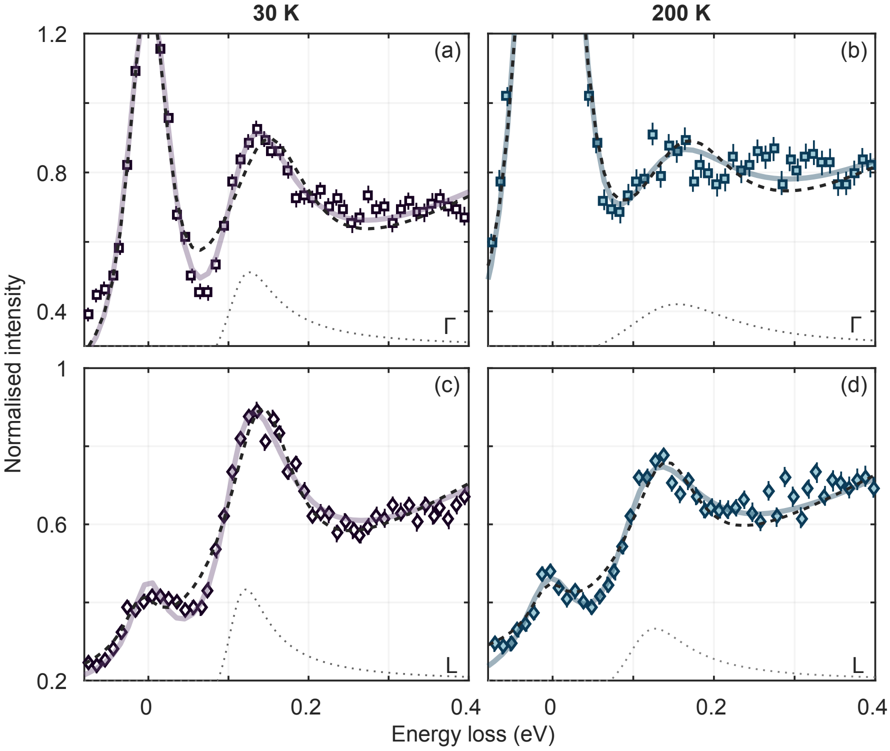

Figure 3.11: Best fits to high-resolution RIXS data collected in the (6, 7, 7) Brillouin zone, using a symmetric Lorentzian (black dashed) or a phenomenological gap function (Eqn. 3.4, solid) functional form at 30 K (a,c) and 200 K (b,d) for momentum transfers Γ and L. The Lorentzian fails to adequately describe the region between the elastic line and peak A for all temperatures and momentum transfers **Q**. Dotted lines illustrate the functional form of the fitted and deconvoluted gap function, which has been offset and multiplied by a constant scale factor for clarity.

3.3.1 Origin of peak A

A number of possible scenarios for the inherent asymmetry of peak A were explored. These are discussed in turn below.

I. Excitonic mode

The first scenario is a discrete exciton mode and associated electron-hole continuum arising from an excitation across the direct charge gap, as seen for example in Na_2IrO_3 and other iridates [119]. There are three main problems with this interpretation. The first is that fitting the peak to a Lorentzian (or a Lorentzian plus Gaussian, not displayed) as appropriate for such a mode fails to describe the low-energy suppression of spectral weight adequately (Fig. 3.11). The second is that the intensity of peak A is practically momentum independent, which is at odds with the band structure calculations by Shinaoka *et al.* [104] for $Cd_2Os_2O_7$, and previous studies on iridates [119], the latter of which shows a distinct localization of spectral weight at the zone centre. One would expect a large intensity for a Q-point with a high density of states. Finally if peak A were indicative of a simple excitation across the charge gap, then its energy would decrease concurrently with the gap energy. This proposition is not supported by the data. Consequently an excitonic model was disregarded from future analysis.

II. Gap opening

One of the main failures of the excitonic model was the poor fitting of the low-energy suppression of spectral weight. The second interpretation thus considered is somewhat related to the first, in that peak A has an electronic origin. Rather than an excitonic process however, the hypothesis was that the low-energy suppression of spectral weight was evidence of an electronic gap below the MIT. The reasoning is as follows.

Above the MIT $Cd_2Os_2O_7$ is metallic, and hence states cross the Fermi level over the entire Brillouin zone. Below the MIT the charge gap opens up continuously, as demonstrated by optical conductivity and resistivity measurements. Those states which previously crossed the Fermi level are continuously transferred to lower energies, and spectral weight builds up either side of the gap. This spectral weight gives rise to peak A.

At first glance, the proposed gap appears to continuously shift to lower energy loss with increasing temperature (Fig. 3.11). The transfer of spectral weight can be described by a modified damped Lorentzian functional form, given by:

$$S(Q,\omega) = H(\omega_{\text{gap}})\,\text{Im}\left[\frac{A(Q)^2}{\omega_{\text{p}}^2 - \omega^2 - i\gamma(\omega - \omega_{\text{gap}})}\right], \tag{3.4}$$

where $H(\omega_{\text{gap}})$ is the Heaviside step function, $A(Q)$ is a scale factor, ω_{p} (corresponds to the mid-point of the spectral weight), γ is the damping factor,[11] and ω_{gap} is the energy where the function goes to zero. A similar function has been used to describe the optical spectra of superconducting cuprates [120]. In the underdamped limit ($\gamma \to 0$), ω_{p} tends to ω_0, where ω_0 is the peak maximum; while in the overdamped limit ($\gamma \to \infty$), ω_{gap} tends to ω_0.

III. Fano resonance

The final scenario is that peak A arises as a result of interference between a discrete resonant process and a continuum spectrum [121, 122]. This interference results in a shift from the original peak position and a characteristic asymmetry of the observed peak. This process is known as a Fano resonance and is well known for Raman spectra; for instance it has been observed in the hyperkagome 5d TMO $Na_4Ir_3O_8$ [123], and for Sr_2IrO_4 [124]. The resonance is described by the Breit-Wigner-Fano (BWF) formula:

$$I(\omega) = I_0\left[\frac{1+q\epsilon}{1+\epsilon}\right]^2, \tag{3.5}$$

with $\epsilon = (\omega - \omega_0)/\Gamma$, where ω_0 is the uncoupled resonance energy, Γ is the spectral width, and $|1/q|$ is a parameter which is proportional to the coupling between the resonant mode and the

---

[11] This is a variable, however γ was fixed to $\gamma = 0.3$ for all future analysis in order to minimise the number of parameters in the fitting procedure.

continuum.[12] In the limit $|q| \rightarrow \infty$ this formula simplifies to a Lorentzian. Particularly for small $|q|$, there is a reduction in intensity at the low energy side of the peak which appears similar to that observed for $Cd_2Os_2O_7$. In order to discriminate between scenarios II and III, a detailed examination of the dependence of the RIXS spectra on both temperature and momentum transfer was performed.

3.3.2 Temperature dependence

RIXS spectra were collected as a function of temperature at the (7, 7, 8) Brillouin zone centre, which for the experimental geometry was the closest to the ideal case of $2\theta = 90^\circ$ ($2\theta = 91.1^\circ$). These spectra are plotted in Figure 3.12a, and were fitted using either a gap function (Eqn 3.4) or a Fano resonance (Eqn. 3.5) to describe peak A. It should be noted that for the fits to a Fano resonance, it was found that the width Γ and $|q|$ were strongly correlated as a consequence of insufficient data at low energy loss, since the reduction of spectral weight in that region is highly dependent on $|q|$. Henceforth all data presented has been obtained using a fixed value of $|q| = 7$, which was found to give an adequate description of the data across all temperatures. This value of $|q|$ indicates moderate coupling between the resonant mode and the electronic continuum. Figures 3.13 and 3.14 show the results of fits to a Fano resonance or a gap function respectively at 30 K and 275 K. Both the Fano resonance and gap function models provided a good fit to the data across all temperatures, ($\chi^2 < 2$), with only slight differences in the χ^2 values obtained for a given temperature. On this basis alone, it is difficult to discriminate between the two scenarios.

Extracted parameters from the fits are displayed in Figure 3.15 as a function of temperature. Previous measurements [118] observed a order parameter-like decay of peak A, with a critical temperature coincident with T_{MI}. Indeed the data show a continuous decay in the peak intensity and an associated spectral broadening with increasing temperature, both of which appear to saturate above T_{MI} and are independent of the model considered. The spectral weight is also approximately conserved through the MIT for both models. Quantitative analysis of the observed behaviour for both models shall be compared in turn.

Electronic gap

Within an electronic gap interpretation, the hypothesis is that the weakening and broadening of peak A with increasing temperature occurs as a result of the gap closing at the MIT. This gap closing explains two main features in the RIXS spectra: a continuous increase of spectral weight in the region between the elastic line and peak A, coupled with a shift of spectral weight to higher energies. The latter is shown by the increasing value of ω_p with increasing temperature.

One point of note is that a distinction has to be made between the optical gap and the charge gap: the direct optical gap is the $\Delta k = 0$ transition between two bands separated by the Fermi

---

[12] Strictly speaking q may be complex in the antiferromagnetic phase since time-reversal symmetry is broken [125]. In the paramagnetic phase, q is real since time-reversal symmetry is preserved.

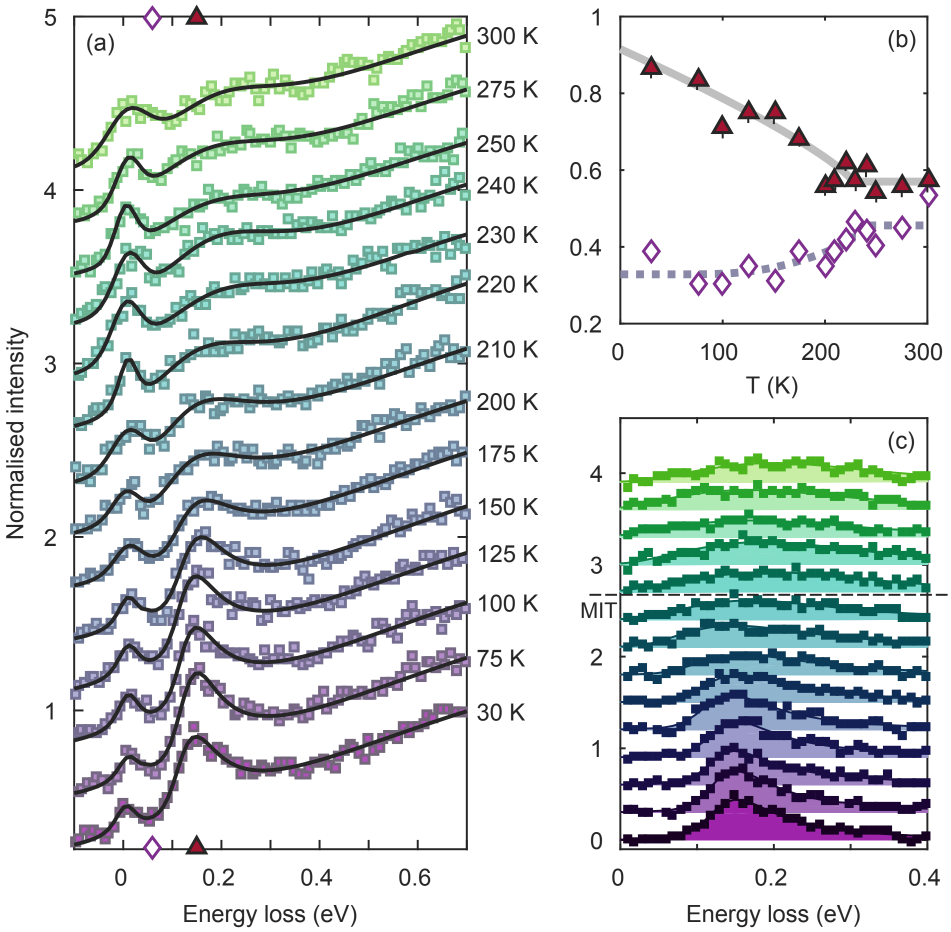

Figure 3.12: Temperature dependence of RIXS spectra in the (7, 7, 8) Brillouin zone. (a): Stack plot of data normalized to intensity of intra-t_{2g} excitations at 0.7 eV, plotted with best fit to gap function model. (b): RIXS intensity at 60 meV (open diamonds) and 150 meV (filled triangles), which at 30 K correspond to the intra-gap and peak regions respectively. The peak intensity is consistent with a power law ($\beta \sim 0.4$), whereas the intra-gap intensity follows Arrhenius-type behaviour. Both models have critical temperature T_{MI}. (c): Normalized data with elastic and intra-t_{2g} contributions subtracted. Dashed line indicates the location of the MIT. There is a clear evolution of the lineshape from 30 K (bottom) to 300 K (top) as the gap closes.

level, whilst the indirect charge gap is the minimum between the conduction and valence bands and governs the MIT. This distinction is illustrated in Fig. 1.4. If ω_{gap} is representative of an electronic gap, then it is expected to follow a BCS-like dependence. By fitting their data to a BCS-type gap function,

$$\frac{\Delta(T)}{\Delta_0} = \tanh \frac{\Delta(T)\, T_{\mathrm{MIT}}}{\Delta_0\, T}, \tag{3.6}$$

Padilla and colleagues [98] determined the zero temperature optical gap to be $2\Delta_{\mathrm{D}} = 100$ meV, whilst Mandrus *et al.* [94] determined the charge gap $2\Delta_{\mathrm{C}} = 130$ meV. However Mandrus *et al.* observe a clear suppression of the activation energy at low temperatures due to extrinsic conduction mechanisms, and only fits data close to the MIT with the BCS function. In the present study there is insufficient data close to the MIT to do this adequately. Thus fitting ω_{gap} to

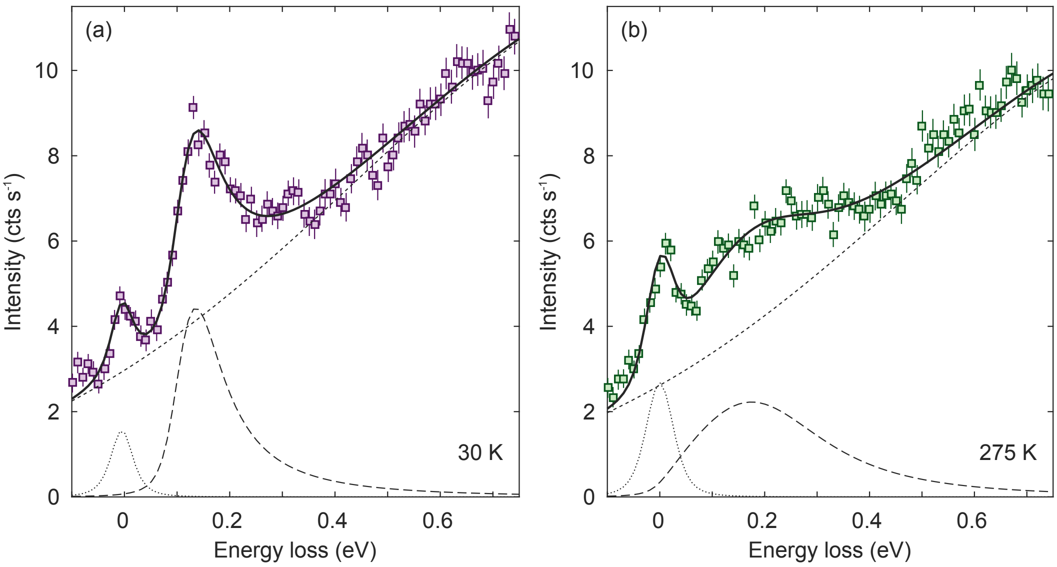

Figure 3.13: Fits of RIXS spectra obtained at (7, 7, 8) and 30 K (a), or 275 K, with peak A described by a gap function (Eqn. 3.4).

a BCS function over the whole temperature range measured gives $T_{\mathrm{MI}} = 230(4)$ K, $\Delta_0 = 87(2)$ meV and $\Delta_0/k_{\mathrm{B}}T_{\mathrm{MI}} = 4.4(2)$. The transition temperature and value for Δ_0 compare well with parameters extracted from optical conductivity measurements by Sohn *et al.* [99], who finds $2\Delta_{\mathrm{D}} \sim 160$ meV, where Δ_{D} is the direct optical gap. Hiroi *et al.* [97] note that whilst the value of T_{MI} is fairly consistent between samples and batches, 2Δ (as extracted from resistivity measurements) varies significantly even within samples from the same batch. Their supposition is that the $T = 0$ charge gap is actually fairly constant between samples, but very small deviations in oxygen stoichiometry ($\sim 10^{-4}$ f .u.) or impurity states within the gap causes the observed behaviour. Given this information (along with the instrumental energy resolution), the results presented are believed to be consistent with the previous studies. The value of $2\Delta_0/kT_{\mathrm{MI}}$ is significantly larger than the theoretical value for a BCS model with weak coupling ($2\Delta_0/kT_{\mathrm{MI}} = 3.5$) and implies that spin-orbit coupling may play some role in the electronic behaviour.

The fact that the spectral weight of the gap feature extends to ca. 0.6 eV agrees with observations in optical conductivity measurements by Padilla and colleagues [98], where they see a significant reduction of spectral weight in the intra-gap region. This spectral weight is transferred to the region above 3Δ, which in their study is surprisingly not exhausted until almost $40\Delta \approx 2$ eV. The full extent of the spectral weight transfer in the RIXS data is masked somewhat by the intra-t_{2g} excitations. Furthermore band structure calculations by Shinaoka *et al.* [104] reveal a pseudogap in the density of states originating in the metallic phase close to the MIT, which they argue originates from the modification of the band structure near the Fermi level with the magnetic order. The data presented here is consistent with their interpretation. These conclusions suggest that the gap parameterised by Δ_0 is indeed electronic in origin, and is likely to be the direct optical gap (which according to Sohn *et al.* [99] can be directly related to the charge gap magnitude for any given temperature).

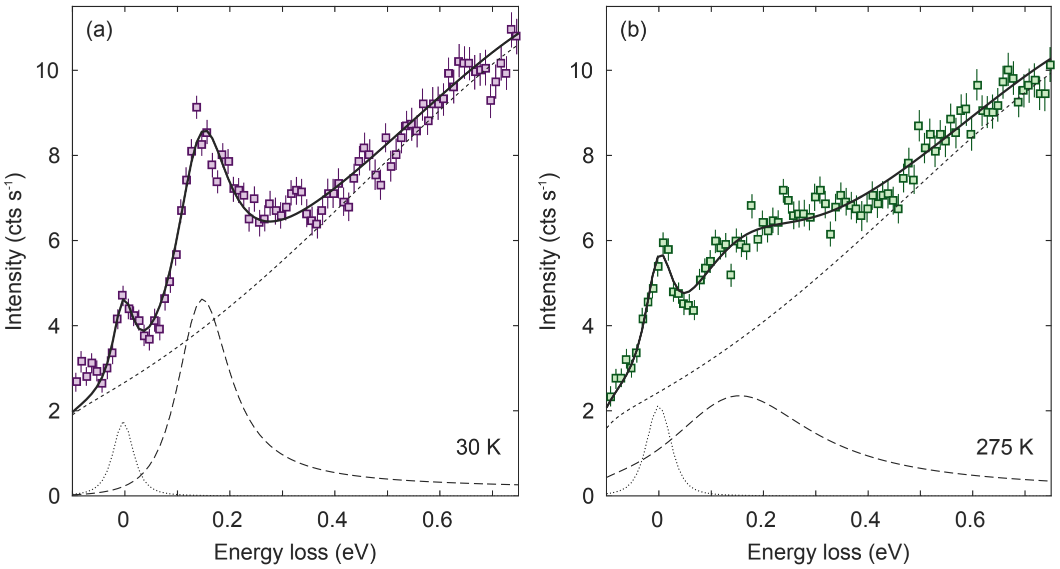

Figure 3.14: Fits of RIXS spectra obtained at (7, 7, 8) and 30 K (a), or 275 K (b), with peak A described by a Fano resonance (Eqn. 3.5).

Fano resonance

Within a Fano resonance interpretation the feature also weakens and broadens with increasing temperature, but the broadening occurs as a result of increased damping (with the caveat that $|q|$ is fixed as a function of temperature, which may not be a valid assumption). The Fano lineshape itself occurs as a result of interference between a resonant mode and a continuum of states. The two most plausible options for the identity of the resonant mode are a Raman-active phonon or a magnetic excitation. However the former is unlikely for the following reasons. Yamaura and colleagues [95] identified the highest energy $T_{2g}(4)$ phonon mode at 760 cm^{-1} (95 meV). This is significantly lower than ω_0 at 30 K, which suggests that this mode is not responsible for the resonance unless a magnon or another phonon is also involved. The cross-section for this type of interaction is likely to be very small. Furthermore the uncoupled resonance energy is practically independent of temperature, whereas the $T_{2g}(4)$ phonon undergoes a slight hardening with increasing temperature.

It is thus proposed that this resonance is in fact magnetic in origin. Such an interpretation of the data is supported by the following observations. Firstly the intensity of peak A as a function of temperature can be reasonably[13] described by a power law with a critical temperature equal to T_N, and $\beta = 0.4(1)$. This critical exponent is consistent with a 3D magnetic ordering scenario. Secondly the increased damping at high temperatures would be appropriate for any model involving a harmonic oscillator of some form.

The temperature dependence alone is insufficient to distinguish between an electronic or magnetic origin for peak A. Fortunately one of the main advantages of RIXS over other optical techniques is the ability to measure as a function of momentum transfer.

---

[13] Within the limitations of fitting thermodynamic parameters with a power law far from the critical temperature.

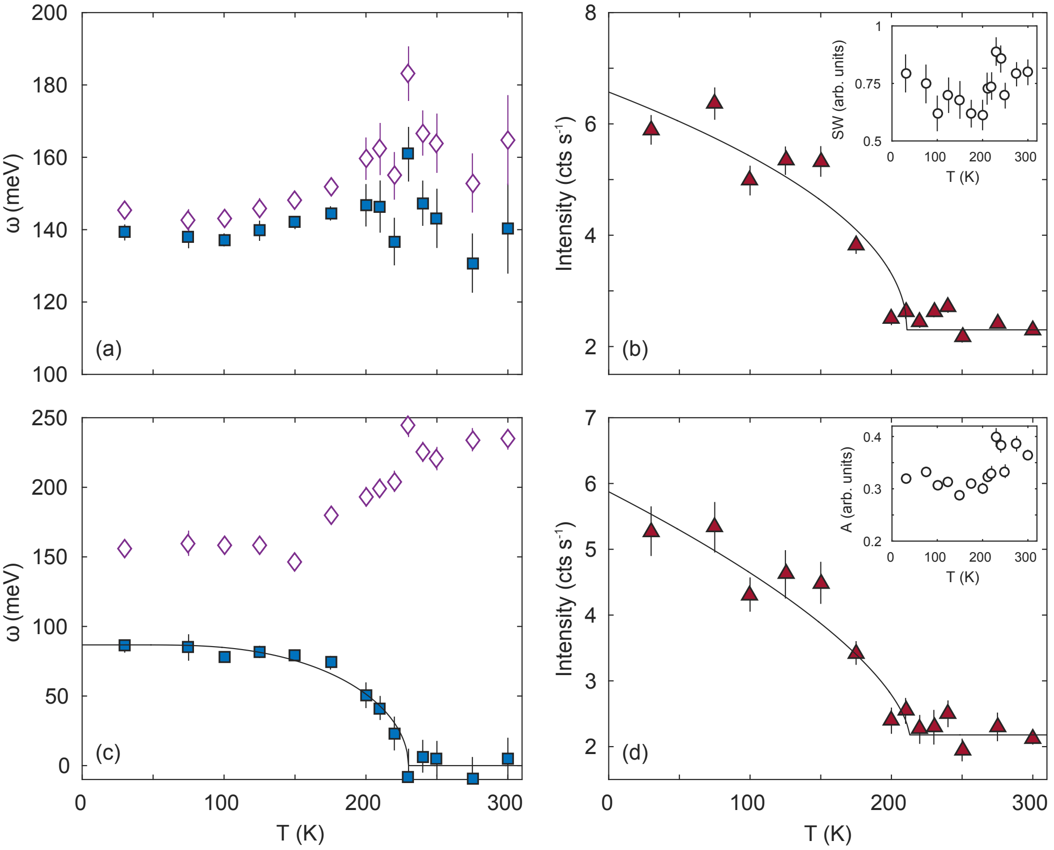

Figure 3.15: Comparison of fitted parameters for peak A. (a,b): Fits of peak A to a Fano resonance. (a): Energy of uncoupled resonance ω_0 (filled squares) and maximum of peak (open diamonds). (b): Intensity I_0, a power law with critical exponent $\beta = 0.36$ and critical temperature $T = T_N$ is added as a guide. Inset: spectral weight taken from integral of Fano resonance. (c,d): Fits of peak A to a gap function (Eqn. 3.4). (c): Extracted parameters from fitted gap function ω_{gap} (filled squares) and ω_p (open diamonds). Solid line: Best fit with BCS function, $T_{MI} = 230(4)$ K, $\Delta_0 = 87(2)$ meV. (d): Peak intensity as a function of T. The solid line is a guide to the eye. Inset: Spectral weight of gap as a function of T.

3.3.3 Dependence on momentum transfer

The momentum dependence of the RIXS spectra was measured[14] in the Brillouin zone around (6, 7, 7) at 30 K, with the results plotted in Fig. 3.16. In agreement with lower resolution RIXS (Chapter 3.2), there is little to no dispersion in peak A (Fig. 3.16b), and near constant intensity across the Brillouin zone (Fig. 3.16c). At first glance the only significant variation with momentum transfer is the intensity of the elastic line, which as before is almost entirely due to RIXS matrix element effects.

The data were fitted with the same model as used in the previous section, along with the same functional forms for peak A. Quantitative comparisons of the two models will now be made, starting with the optical gap.

---

[14] Measuring in the (7, 7, 8) Brillouin zone would have resulted in very large elastic line intensities at the zone boundaries, and made determination of the gap energy difficult.

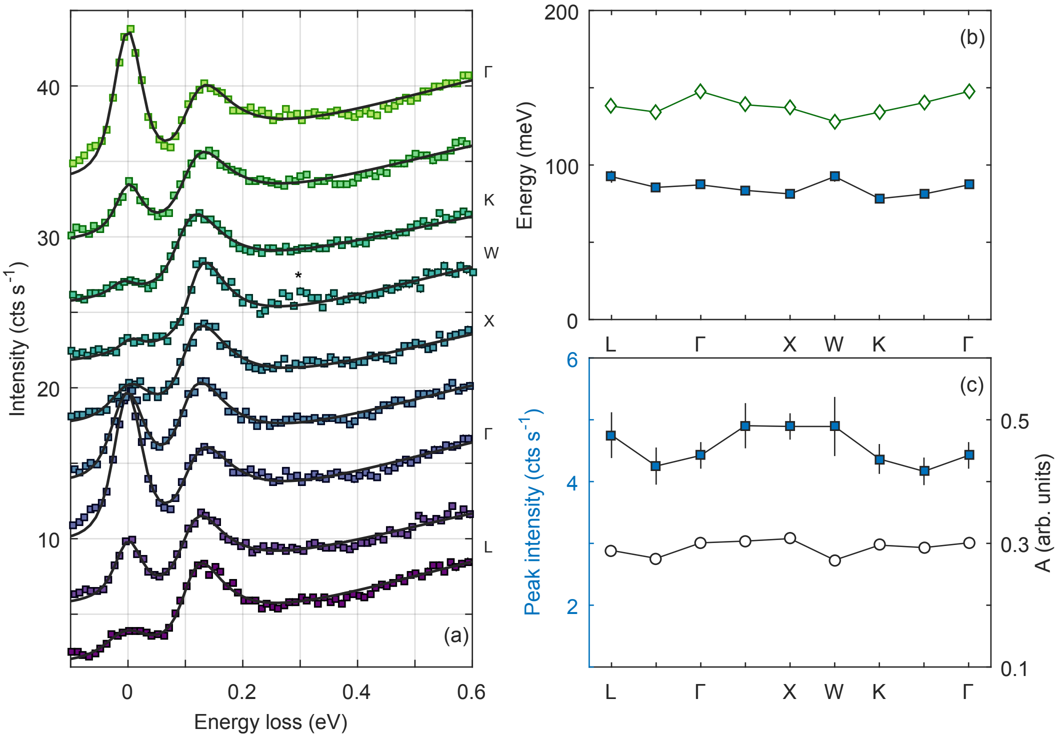

Figure 3.16: (a): Momentum dependence of the RIXS spectra, along with best fits of the data (solid line). Unexplained feature at 0.3 eV energy loss indicated by asterisk, which has **not** explicitly been accounted for in the fit. (b): Extracted parameters from fitted gap function ω_{gap} (filled squares) and ω_p (open diamonds). (c): Peak intensity (filled squares) and spectral weight (open circles) as a function of momentum transfer.

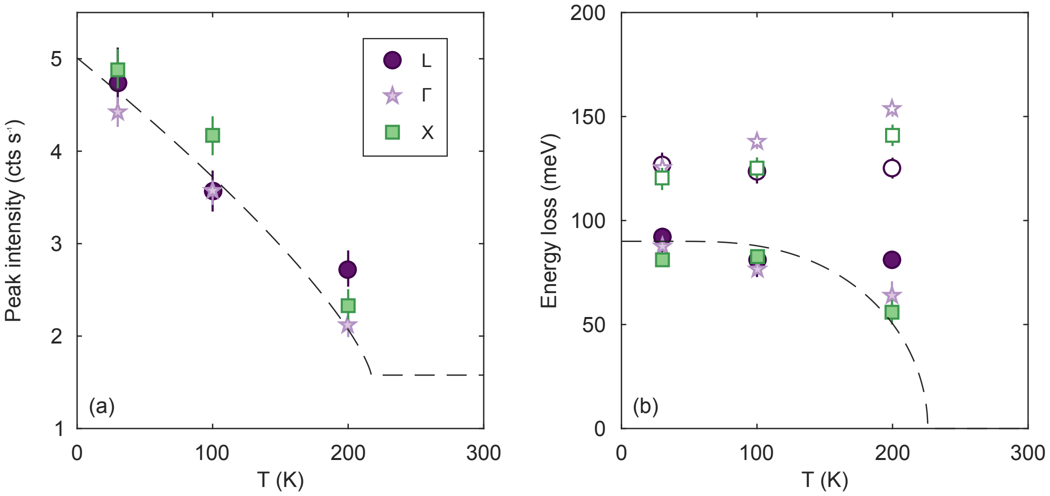

Figure 3.17: Fitted parameters of peak A as a function of temperature for three different momentum transfers: L = (6.5, 7.5, 7.5) [purple circles], Γ = (6.5, 7.5, 7.5) [pink stars], and X = (6.5, 7.5, 7.5) [green squares]. Note that this is a different Brillouin zone to the temperature dependence displayed in Fig. 3.15. (a): Peak intensity as a function of temperature. The dashed line is guide to the eye. (b): ω_{gap} [solid symbols] and ω_{p} [open symbols] as a function of temperature. The dashed line is identical to that given in Fig. 3.15c.

Optical gap

Fitting peak A with the functional form as appropriate for an optical gap provides a good fit to the data across all momentum transfers (Fig. 3.16), albeit with some discrepancy between 0.3–0.4 eV which seems to be consistent given the choice of damping parameters. This shall be discussed later in this section. The parameter ω_{gap} appears to show some weak dispersion of around 20 meV, however considering the intrinsic energy resolution of 45 meV it is unclear if this is significant. Nevertheless this dispersion is significantly smaller than that predicted by band structure calculations by Shinaoka *et al.* [104] and others for plausible values of U, and an all-in, all-out magnetic structure. Such an observation suggests that the electronic bands close to the Fermi level are flatter than previously considered. This is supported by the weak variation of the spectral weight as a function of momentum transfer indicative of a near constant density of states.

A similar temperature dependence is observed as a function of momentum transfer (Figure 3.17). This suggests a collective excitation involving electrons and holes at all locations in the Brillouin zone. The momentum independence is a signature of the ‘relativistic’ Lifshitz transition; at the MIT the occupied bands are uniformly pulled downward and the unoccupied ones are pushed up.

One observation discussed briefly earlier is that there is an additional weak feature at 0.3 eV energy loss which cannot be explained in terms of this gap or a *d*-*d* excitation (henceforth referred to as peak B). Interestingly it is particularly localised at the W point, which corresponds to a vertex of the Brillouin zone. Peak B proved difficult to fit across the Brillouin zone, given that its width and intensity vary significantly with momentum transfer. The constraint $\gamma = 0.2$ was required to give sensible fits to the experimental data, with the results summarised in Figure 3.18. Nevertheless the values for ω_{gap} and ω_p are broadly consistent with those shown in Figure 3.16, along with the associated peak intensity and spectral weight (albeit with increased uncertainty). Furthermore the quality of the fits improve consistently when fits to peak B are considered.

In contrast to peak A, peak B appears to be much more dispersive in energy, with minima at the zone centre and maxima at the zone boundaries. This feature is proposed to be electronic in origin for the following reasons. Recent LDA + U band structure calculations by Uehara *et al.* [105] provide further insight into the possible nature of peak B. These DFT calculations utilised $U = 0.8$ eV; the presence of electron and hole pockets indicate that $Cd_2Os_2O_7$ is metallic for this value of U. Sohn *et al.* [99] find that the effect of increasing U from 0.8 eV to 1.5 eV is to separate the valence and conduction bands by around 0.2 eV (and thus inducing a Lifshitz-type MIT), with only a slight variation in the band dispersion.[15] If one applies this shift to the data close to the Fermi energy as presented in Ref. [105], then semi-quantitative agreement is found between the dispersion of peak B and the LDA + U calculations at the zone boundaries.

---

[15] Only the band structure between $W - L - \Gamma$ was presented in the manuscript, however, hence the motivation for shifting the $U = 0.8$ eV data as presented in Ref. [105].

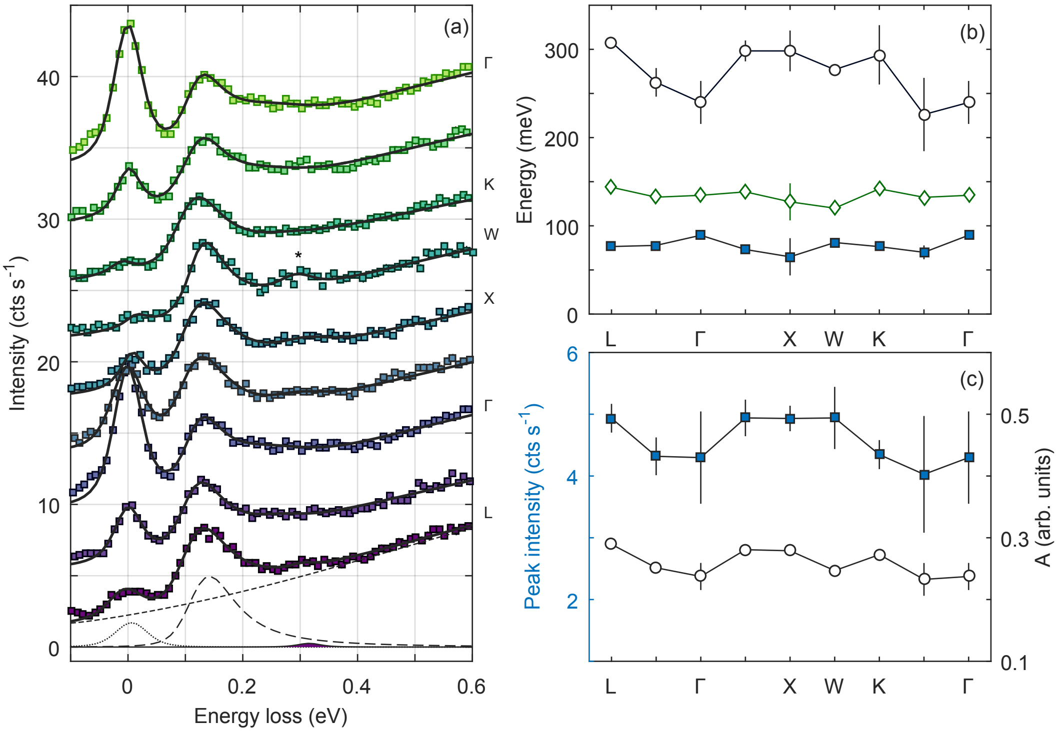

Figure 3.18: Same layout as for Fig. 3.16, except fits include a Gaussian to account for the feature at 300 meV energy loss, which has been highlighted in (a). Open circles in (b) indicate its energy as a function of momentum transfer.

The momentum dependence of the RIXS spectra at low temperature are thus supportive of peak A having an electronic origin. The weak dispersion of ω_{gap} is indicative of relatively flat bands close to the Fermi energy. Complementary information could be gathered from angle-resolved photo-electron spectroscopy (ARPES) measurements, which unlike RIXS probes the occupied valence states.

Magnetic excitation

The alternative is that peak A is magnetic can also be confirmed or disproved via consideration of its dependence upon momentum transfer. Fits of the low temperature RIXS spectra to the Fano resonance model given earlier are displayed in Fig. 3.19. At this point it should be noted that it proved difficult to reliably fit peak B across the Brillouin zone, so the analysis presented does not take it into account.

As with fitting to an electronic model, a magnetic description is also compatible with the low-temperature data. However, in common with Ref. [118], simple antiferromagnetic Heisenberg interactions are insufficient to describe the excitation spectra. Evidence is given by the very large gap ($\sim$120 meV) and relatively weak dispersion as a function of momentum transfer.

This conclusion naturally arises simply by considering the AIAO non-collinear magnetic ground state as proposed from the XRMS measurements by Yamaura *et al.* [95]. Elhajal and colleagues [126] argue that a 'direct' Dzyaloshinskii-Moriya (DM) interaction lifts the geometric frustration intrinsic to the pyrochlore lattice, and helps to stabilise the AIAO state; whereas an 'indirect' DM interaction results in a preferred XY ground state.[16] Specifically for $Cd_2Os_2O_7$, *ab initio* quantum chemistry calculations [106] determined that trigonal distortions away from an ideal pyrochlore structure (along with SOC) induce an easy-axis anisotropy ($D = 6.8$ meV) which is comparable to the nearest-neighbour antiferromagnetic exchange ($J = 6.4$ meV). This easy-axis anisotropy applies along the local $\langle 1\,1\,1 \rangle$ crystal directions, and thus also helps to stabilise the AIAO ground state in tandem with a direct DM interaction ($|\mathbf{d}| = 1.65$ meV).

The sizeable anisotropy has two main effects on the magnetic ground state and resulting spin wave dispersion. The first is to break the spin rotation symmetry (which leads to a Goldstone mode in the isotropic case) and lift the magnon energy away from zero at the magnetic zone centre. The spin wave spectrum is now gapped. The second effect is to effectively flatten the magnon dispersion.

The energy and dispersion of peak A appears compatible with a strongly anisotropic model. In order to investigate this, the dispersion was fit within a linear spin-wave theory (LSWT) to the following nearest neighbour Hamiltonian:

$$\mathcal{H} = J \sum_{ij} \mathbf{S}_i \cdot \mathbf{S}_j + \mathbf{d} \sum_{ij} \mathbf{S}_i \times \mathbf{S}_j + \sum_{i} \mathbf{S}_i \cdot \mathrm{D} \cdot \mathbf{S}_i, \tag{3.7}$$

where the three terms on the right-hand side of the equation represent nearest-neighbour antiferromagnetic exchange, an antisymmetric DM interaction, and single-ion anisotropy respectively. This Hamiltonian is identical to that given in [106]. Linear spin wave theory is expected to be a reasonable approximation for $Cd_2Os_2O_7$ in the low-temperature, localised limit given that $S = \frac{3}{2}$ for a d^3 ion. Calculations were done within the SpinW package [129] available for MATLAB, which has advantages in that the magnetic ground state and interactions can be easily visualised.

The experimental dispersion and spectral weight were fitted simultaneously to a model derived from Equation 3.7 within SpinW, with the resulting best fit to the data plotted in Fig. 3.19. As can be seen, the data is well described by such a Hamiltonian, with the resultant fitted parameters[17] given by $J = 6.5(4)$ meV, $D = -6.6(6)$ meV, and $|\mathbf{d}| = 3.5(2)$ meV. These values are in surprisingly good agreement with those derived from the earlier quantum chemistry calculations, with the exception of the DM term which is a factor of 2 larger than previously calculated. However since the error bars in the fitted parameters have been derived without consideration of the experimental energy resolution (45 meV), then such a discrepancy is not unreasonable. In any case, the significant gap observed for peak A across all momentum transfers is indicative of a strong anisotropy and consistent with a magnetic interpretation. The anisotropy arises as a direct result of spin-orbit coupling acting as a perturbation within the magnetic Hamiltonian.

---

[16] Since rotational symmetry is still preserved, one can still see a Goldstone mode. This type of interaction is exemplified by $Er_2Ti_2O_7$ [127, 128], with a small spin gap of 15 μeV occurring as a result of 'order-by-disorder'.

[17] It should be noted that the values obtained within SpinW itself are a factor of 2 larger than those given here; with the discrepancy arising from a difference in the definition of J between SpinW and the quantum chemistry calculations.

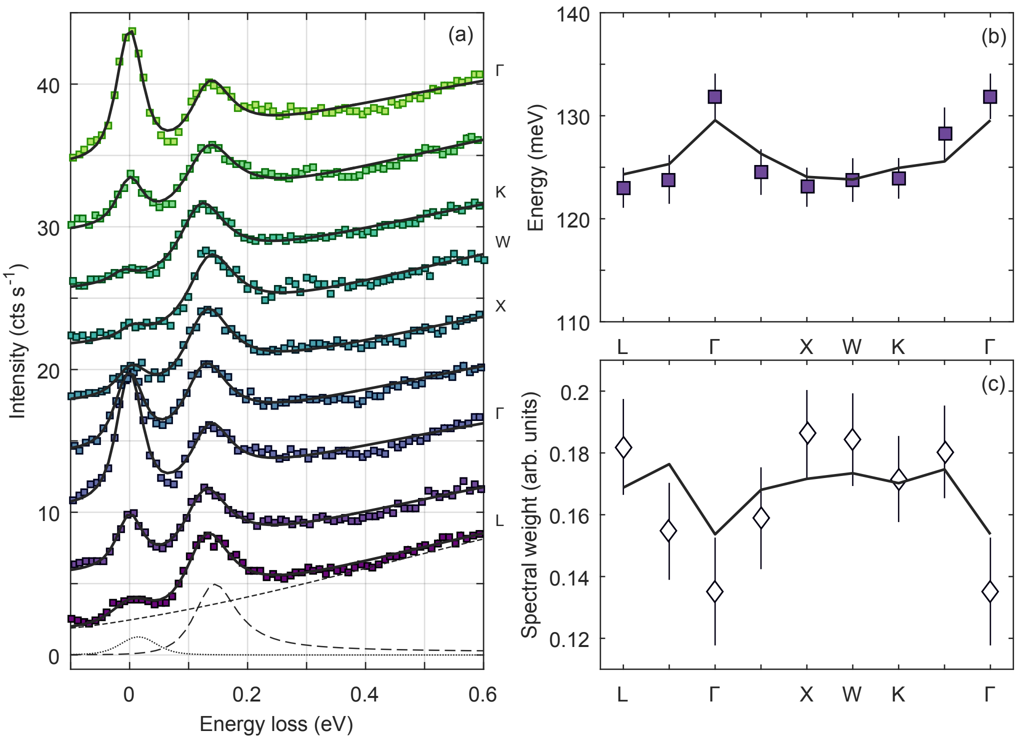

Figure 3.19: (a): Fits of the low-temperature data in the (6, 7, 7) Brillouin zone to the model given in the main text as a function of momentum transfer. Right panels show the energy (b) and integrated spectral weight (c) of peak A as a function of momentum transfer. Solid line is the best fit to a representative Hamiltonian given by Eqn. 3.7.

As mentioned earlier, it proved difficult to fit peak B within the current approach. Its energy and bandwidth as fitted within the electronic model could also be consistent with a double magnon process or bimagnon continuum.

In Ref. [118], it is argued that $\Delta S = 1$,2,3 excitations are mixed as a result of spin-orbit coupling, with the greatest density of states for the $\Delta S = 3$ process. The alternative interpretation presented here is not incompatible with the previous theory. Remember that the density of states as calculated via exact diagonalization is not equivalent to the RIXS cross-section. For this particular experimental geometry, it is found that $\Delta S = 1$ processes are the greatest contribution to the RIXS cross-section. There may indeed be contributions from $\Delta S = 2$ or $\Delta S = 3$ processes, but they seem to contribute only weakly to the cross-section. This is not unsurprising.

The present analysis does not preclude the presence of longer-ranged exchange interactions. Indeed this would be expected given the extended 5d valence orbitals on Os. However given the large Os–O–O–Os distance, this is likely to be weak and can be neglected to first order.

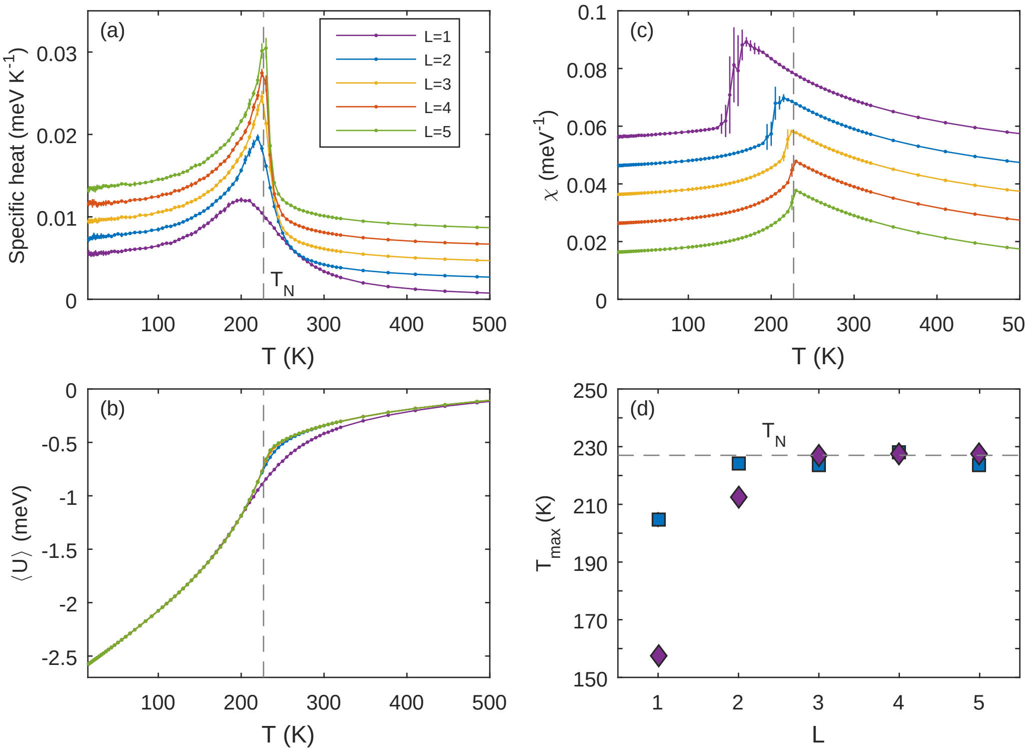

Figure 3.20: Results from simulated annealing runs performed for different system sizes of $Cd_2Os_2O_7$. All data displayed occurs from the mean of five successive runs, with error bars reflecting the standard deviation about this mean. Parameters plotted (per magnetic moment) are the specific heat C (a), isothermal susceptibility χ (b), and mean internal energy $\langle U \rangle$ (c). Curves in (a) and (c) have been offset for clarity. In (d) the fitted maximum of the specific heat (squares) and susceptibility (diamonds) has been plotted. Dashed lines indicate the experimental Néel temperature T_N. There appears to be a convergence of the calculated T_N with the experimental one in the thermodynamic limit.

Monte Carlo simulations

Further support for a magnetic interpretation for peak A can be garnered from results of simulated annealing runs. These simulations, whilst rather rudimentary, do seem to accurately reproduce the observed AIAO ground state and Néel temperature for the parameters derived from the fits to the spin wave dispersion. The classical Monte Carlo code was written by the author in MATLAB.

Simulated annealing runs were performed on system sizes of $L \times L \times L$ unit cells, where L ranges from 1 to 5 (16 – 2000 spins in total). The energy of the system and its interactions were determined via the Hamiltonian given by Equation 3.7, with the microscopic parameters used identical to those obtained from the spin-wave dispersion. The simulated annealing was performed with a standard Metropolis spin-flip algorithm, with 5×10^4 Monte Carlo steps (MCS) per spin to equilibrate the system for a given temperature, followed by a further 5×10^4 MCS per spin to evaluate thermodynamic parameters.

The thermodynamic parameters which were evaluated were the mean system energy $\langle U \rangle$, the specific heat C, and the isothermal susceptibility $\chi = \frac{1}{3}(\chi_{xx} + \chi_{yy} + \chi_{zz})$. The latter two quantities are determined via the following expressions:

$$C = \frac{\beta}{T}\left[\langle U^2\rangle - \langle U\rangle^2\right], \quad \chi_{\alpha\alpha} = \beta\left[\langle M_\alpha^2\rangle - \langle M_\alpha\rangle^2\right], \tag{3.8}$$

with $\beta = 1/k_B T$, and M_α referring to the component of the classical magnetic moment along the respective Cartesian direction. All parameters are given per magnetic moment. In practice the numerators in Eqns. 3.8 are identical to the variance of the mean energy and magnetisation respectively as a function of Monte Carlo time.

Two sets of runs were performed for each system size: one with a relatively coarse temperature step ($T_{\text{new}} = 0.92\,T$) initialised at 2000 K ($T/J \approx 25$) with the spins oriented randomly, and a dataset focussing on the critical region. The latter was initialised at 320 K (experimentally $T_{\text{N}} + 93$ K) with the state obtained from the coarse dataset at the same temperature, and run with a step-size of 5 K. This procedure was performed five times for each system size.

The results from the average of these five runs are plotted in Figure 3.20, with the error bars reflecting the standard deviation. The specific heat and magnetisation both show evidence of a continuous second-order transition in the vicinity of the Néel temperature $T_{\text{N}} = 227$ K, with the transition becoming sharper for larger system sizes. This would be expected as one progresses towards the thermodynamic limit. Furthermore the energy minimized magnetic structure coincides with that for an AIAO system at $T/J \sim 0$.

There are however a number of limitations with the simulations performed thus far. Most importantly, the number of equilibration and averaging steps per spin is relatively low. Ideally, one would want to perform the simulations with a large number of steps after equilibration ($\tau_{\text{av}} \sim 100\,\tau_{\text{eq}}$), in order to gain reliable information about the fluctuations of the system energy and magnetisation as a function of Monte Carlo time. As previously mentioned, these fluctuations parametrise the specific heat and susceptibility respectively. Moreover, the thermodynamic parameters can be accurately determined with appropriate statistical error bars by averaging over multiple runs, and performing a full autocorrelation analysis. The initial number of MCS performed per spin was sufficient to ensure equilibration for each temperature and lattice size, as determined from the temporal dependence of the internal energy. However, close to T_{N}, $\tau_{\text{av}} = 5 \times 10^4$ MCS per spin is only a couple of times larger than τ_{eq}.

This is linked to the second point. The Metropolis spin-flip algorithm suffers badly from the fundamental problem of ‘critical slowing-down’. In the vicinity of the critical point, equilibration is slow as both the length and time-scales involved diverge. Thus there are frequently issues with accurate determination of transition temperatures and critical exponents within this approach. This effect can be seen in Fig. 3.20c, where the statistical error in the susceptibility is large for $L = 1$ and $L = 2$ close to the critical point. Improvements could be made by utilising a cluster-flipping algorithm where critical slowing down is dramatically reduced.

Thirdly sharp fluctuations can be observed in the internal energy $\langle U\rangle$ and magnetisation at low temperature. These fluctuations occur over a single temperature step, and may be due to some long time-scale behaviour which has been incorrectly compensated for in the averaging procedure. Performing a full autocorrelation analysis is likely to improve this.

Finally a full finite-size scaling analysis has not been performed. Transition temperatures determined from the magnetisation for example for a given lattice size frequently do not represent the true behaviour of the system in the thermodynamic limit. This is partly the reason why the maximum of the specific heat and susceptibility curves plotted in Figure 3.20d diverge from one another slightly. Practically what one would do within a finite-size scaling analysis is to calculate the Binder cumulant for each temperature and lattice size, and determine their crossing point via a data collapse. Such an analysis is somewhat subjective however, since it requires some fine-tuning of the critical temperature and critical exponents to obtain the correct crossing-point.

Despite these limitations, the simulations appear to reproduce the correct magnetic ground state and transition temperature, at least to first order. This validates the choice of Hamiltonian and values of the parameters used to fit the spin-wave dispersion. More accurate simulations addressing the limitations given above, whilst instructive, are beyond the scope of this thesis.

3.4 Summary

Resonant inelastic X-ray scattering (RIXS) measurements have been performed on the pyrochlore osmate $Cd_2Os_2O_7$. The electronic excitations are, at least to first order, consistent with a d^3 multiplet model in which the spin orbit coupling (SOC) is a weak perturbation to the Hamiltonian. This seems at odds with the measurements performed on the iridates for example, which show transitions between $j_{\text{eff}} = \frac{1}{2}$ and $j_{\text{eff}} = \frac{3}{2}$ states as a result of the strong intrinsic SOC. However the effective role of spin-orbit coupling is reduced in d^3 osmates as a consequence of increased S (recall $\lambda = \zeta/2S$) and the large Os-O hybridisation, giving rise to a large bandwidth of the t_{2g} states ($W \sim 3$ eV).

Meanwhile a feature at ca. 150 meV energy loss appears to exhibit signatures of both electronic and magnetic behaviour, however it is difficult to disentangle the effects of one from the other within the experimental resolution. In a purely electronic model, this peak arises as a result of a continuous transfer of spectral weight from states close to the Fermi energy as the insulating gap is formed at the MIT. Such a transfer is associated with the Lifshitz transition proposed within previous studies [95, 97, 99]. On the other hand, it can also be described by a predominantly single magnon mode with microscopic parameters in good agreement with quantum chemistry calculations, and supported by Monte Carlo simulations. The significant anisotropy occurs as a direct result of spin-orbit coupling. Such behaviour is hence a further signature that the electronic and magnetic properties are indeed intimately linked for $Cd_2Os_2O_7$.

3.4.1 Proximity to Lifshitz transition

This leads to the question: To what extent does the MIT in $Cd_2Os_2O_7$ resemble a Lifshitz transition? It has already been stated that a true Lifshitz transition can only occur at zero temperature, and that any finite temperature transition with Lifshitz-like phenomena is in fact a crossover between the two regions.

There are a number of experimental features which seem to indicate that $Cd_2Os_2O_7$ exhibits such behaviour. The first is that the metal-insulator transition is continuous, with no observed symmetry breaking through the MIT. The second is that $q = 0$ magnetic order arises in the insulating phase without Brillouin zone folding. These are the more obvious ones, but subtle variations in thermodynamic parameters are also suggestive of a Lifshitz crossover. A point of inflexion can be observed in the lattice constant a as a function of temperature [96], which can be linked to a washed out discontinuity in the thermal expansion coefficient: $\alpha = V^{-1}\left(\mathrm{d}V/\mathrm{d}T\right)_p$. Further synchrotron powder diffraction measurements – which are more sensitive to unit cell parameters – are proposed to examine this further. The concurrent observation of spin and charge excitation phenomena within the RIXS spectra implies that the two are inextricably linked for $Cd_2Os_2O_7$. This supports the notion that $Cd_2Os_2O_7$ undergoes a Lifshitz transition driven by the onset of antiferromagnetic order.

DFT calculations by Shinaoka *et al.* [104] and Sohn *et al.* [99] are also suggestive of a Lifshitz mechanism for the MIT. An enhancement of U (argued to be similar to the onset of AIAO order) separates the valence and conduction bands without any significant band dispersion change. All of these factors lead to the conclusion that the MIT for $Cd_2Os_2O_7$ is indeed Lifshitz-like.

There are however some outstanding questions. These include the possibility that interactions – such as spin-orbit coupling – drive the transition weakly first order. A discontinuity in the electronic specific heat (as observed for Na_xCoO_2 for instance) would be a distinct telling point. There does appear to be a small jump in the electronic specific heat data given in Ref. [94] ($\sim$ 2 J mol^{-1} K^{-1}), however this may also be an artefact from the subtraction from the lattice contribution to the specific heat. It may be the case that the first order perturbation due to interactions is simply too weak to observe in the thermodynamic parameters, partly due to the departure from the $T = 0$ limit.

Summary of contributions

The low resolution RIXS measurements were carried out by the author in collaboration with Stuart Calder and Andy Christianson from Oak Ridge National Laboratory, and Christian Donnerer from UCL. Analysis of the RIXS data was carried out in tandem between the author and Oak Ridge, with converging results. Exact diagonalisation and quantum chemistry calculations are from Jeroen van den Brink's group in Dresden. High resolution RIXS measurements were carried out by the author, assisted by Christian Donnerer and Davide Pincini from UCL. All analysis and interpretation of the data, along with the supplementary Monte Carlo simulations, was performed by the author.

Chapter 4

Excitations through the Slater MIT in $NaOsO_3$

The perovskite osmate $NaOsO_3$ is a candidate Slater insulator, in that the onset of antiferromagnetic order directly drives a continuous metal-insulator transition (MIT) at 410 K. RIXS was used to characterise the electronic and magnetic excitations through the MIT. Broad orbital excitations similar to those observed for $Cd_2Os_2O_7$ imply that electron correlations and spin-orbit coupling play a weak role in governing the electronic ground state. Well-defined spin wave excitations are evident deep in the antiferromagnetic insulating phase ($T < T_{MI}$), which can be successfully modelled by a minimal nearest-neighbour Hamiltonian with sizeable anisotropy. With increasing temperature, these excitations damp into a particle-hole (Stoner) continuum, which is a signature of an itinerant system. A spin-fluctuation model is proposed to explain the magnetic interactions through the MIT.

The Slater transition is one of the more experimentally elusive concepts in condensed matter physics. It is characterised by a continuous metal-insulator transition (MIT) concomitant with the onset of antiferromagnetic order. The theoretical basis is that the onset of antiferromagnetic order itself drives the formation of the insulating gap, without a corresponding distortion of the lattice. Until relatively recently, the most concrete example of a Slater insulator in three dimensions was the pyrochlore osmate $Cd_2Os_2O_7$. In the previous chapter it was shown however that the metal-insulator transition in $Cd_2Os_2O_7$ has characteristics consistent with a Lifshitz transition. In this picture a rigid shift of the bands close to the Fermi energy gradually annihilates the Fermi surface. Optical conductivity measurements by Sohn *et al.* [99] suggest that there may be a substantial region (210–227 K) where antiferromagnetic metallic behaviour can be observed, at least on the surface. Consequently it can be argued that magnetic order cannot be the driving force for the MIT in $Cd_2Os_2O_7$, contrary to previous reports [94, 95, 98, 103]. The perovskite osmate $NaOsO_3$ (d^3, $S = \frac{3}{2}$) remains the most robust example of a 3D Slater insulator. Whilst a number of properties of this material have been well characterised, the nature of the magnetic

Hamiltonian and its effect on the MIT has not. This is the basis of the present chapter.

4.1 Introduction to physical properties of $NaOsO_3$

What follows is a brief survey of the literature published thus far on $NaOsO_3$. This will prove useful in the discussion of the true nature of the MIT.

Crystal structure

The general formula of a perovskite is ABO_3, which in the undistorted case, has cubic $Pm\bar{3}m$ symmetry. In this structure, the A cation sit on the corners of the cube, the smaller B cation sits at the centre of the cube, and is octahedrally coordinated to oxygen ions located at the face centres. $NaOsO_3$ (Figure 4.1a) exists in the orthorhombic $Pnma$ space group [130], with lattice parameters $a = 5.384$ Å, $b = 7.580$ Å, $c = 5.328$ Å. The orthorhombic distortion ($GdFeO_3$ distortion, $a^-a^-c^+$ in Glazer notation) arises as a result of a concerted rotation of the OsO_6 octahedra in the a-c plane, coupled with a tilting about the b-axis. Both of these distortions are of magnitude $\sim 10^\circ$, with a weak dependence on temperature (Figure 4.1b,c). This latter point shall be discussed in more detail later.

Bulk properties

Shi *et al.* [130] observed a MIT at 410 K, concomitant with the onset of antiferromagnetic long-ranged order. The charge gap appears to open continuously in the insulating phase, reaching a zero temperature value $2\Delta_C \approx 100$ meV. Laboratory X-ray diffraction and electron diffraction measurements showed that there was no significant structural symmetry change through the MIT. These observations indicate that the MIT is second-order in $NaOsO_3$, and deviates somewhat from the Mott-Hubbard paradigm.

Optical conductivity

Optical conductivity measurements by Lo Vecchio *et al.* [57] show a clear continuous transition from metallic to insulating behaviour through the MIT. The temperature dependence of the band gap $2\Delta_O$, as extracted from the intersection of a linear conductivity term ($\omega < 2\Delta_O$) and a $\omega^{1/2}$ ($\omega > 2\Delta_O$) term, resembled that of a BCS function. Fitting determined a zero temperature optical gap of $2\Delta_O = 102(3)$ meV, comparable to that observed for $Cd_2Os_2O_7$, and agrees with the charge gap obtained from the resistivity data [130] (Figure 4.1e) Moreover the ratio $2\Delta_O/kT_{MIT} = 3.0(1)$, which is indicative of a weak coupling BCS-like regime.[1]

---

[1] Compare this to $2\Delta_O/kT_{MIT} \sim 5$ for $Cd_2Os_2O_7$.

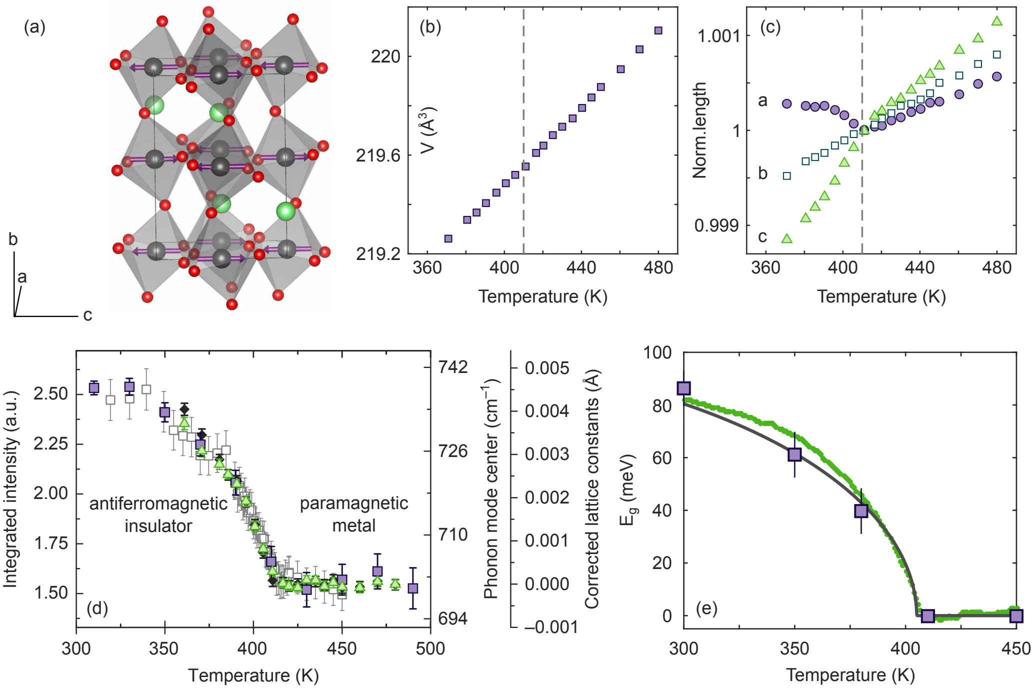

Figure 4.1: (a): Crystal structure of NaOsO$_3$. The magnetic moments lie along the c-axis. (b): Unit cell volume through the MIT. (c): Lattice parameters through the MIT normalised to the value at T_{MI}. Subfigures (b) and (c) adapted from Ref. [131]. (d): Coupling of the magnetic, electronic, structural, and phonon degrees of freedom in NaOsO$_3$. Adapted from Ref. [132]. (e): Optical gap (purple squares) and charge gap (green circles) extracted from data presented in Refs. [57] and [130] respectively. Solid line is a Slater model with $E_g(T = 0) = 102$ meV and $T_{\mathrm{MI}} = 410$ K.

Neutron and X-ray measurements

Calder *et al.* [131] performed powder neutron diffraction, polarized elastic neutron scattering and resonant X-ray scattering measurements, in order to determine the magnetic structure and the effect of spin-orbit coupling upon the ground-state electronic structure. Powder neutron diffraction revealed the presence of additional reflections below T_{N}, which were consistent with a $\mathbf{k} = 0$ magnetic propagation vector. Polarized neutron scattering confirmed that these reflections were indeed magnetic – since the reflections were only present in the spin-flip scattering channel – and not due to a structural symmetry change. Neutron pair distribution measurements [132] confirmed no structural symmetry change through the MIT on any length scale. Refinement of the powder neutron diffraction data, coupled with representation analysis, revealed a G-type antiferromagnetic structure. The local moment was determined from the magnetic refinement and found to be equal to 1.0(1) μ_{B}, significantly reduced from the nominal spin-only value of 2.67 μ_{B} for a $S = \frac{3}{2}$ d^3 system. The temperature dependence of the lattice parameters (Figure 4.1b,c) showed an anomaly in a and c at the MIT; however this was attributed to a cooperative rotation of the OsO$_6$ octahedra such that the octahedra better align with the unit cell axes. Below the MIT the Os ions are sufficiently close together such that they interact and form the long-ranged ordered phase.

Later neutron measurements by Calder and colleagues [132] found a significant spin-phonon coupling in $NaOsO_3$, with a large shift of 40 cm^{-1} of the B_{2g} breathing mode as a function of temperature. This cooperation between magnetic order and the lattice drives octahedral isotropy, which in turn promotes the breathing distortion and the insulating gap below the MIT. Notably the spin-phonon coupling was considerably larger than that observed for $Cd_2Os_2O_7$ ($\Delta\omega$ = 4 cm^{-1}), which further highlights the differences in the mechanisms of the MIT for the two compounds.

Resonant X-ray diffraction and simulations with FDMNES [133] showed that the observed L_3 / L_2 intensity ratio of 1.14 could only be realized if spin-orbit coupling did not break the degeneracy of the t_{2g} manifold. The integrated intensity of the white lines at the two absorption edges follows a similar trend, with the branching ratio $BR = 2.6(1)$ similar to those obtained for $Cd_2Os_2O_7$ [100] and Sr_2FeOsO_6 [134], but somewhat larger than the statistical branching ratio of 2. A branching ratio of 2.6 implies $\langle \mathbf{L} \cdot \mathbf{S} \rangle \sim \hbar^2$ (assuming the number of holes in the d-manifold $n_h = 7$), considerably lower than that expected if SOC were dominant $\left[\langle \mathbf{L} \cdot \mathbf{S} \rangle = 2.66\hbar^2\right]$. This can be compared with the iridates Sr_2IrO_4 and $Sr_3Ir_2O_7$ [24, 26], where spin-orbit coupling splits the t_{2g} states into the $j_{\mathrm{eff}} = \frac{3}{2}$ and $j_{\mathrm{eff}} = \frac{1}{2}$ bands, and the intensity ratio $L_3 / L_2 > 50$. Such a result for $NaOsO_3$ suggests an intermediate regime where there is competition between the SO coupling and Hund's coupling, probably leading to some orbital component to the magnetization and magnetic anisotropy. It was also argued that the correlation U is small for $NaOsO_3$ since the calculated lineshape for the L_2 resonance gave a poorer fit to the data for larger U. These observations are consistent with a weak coupling scenario for $NaOsO_3$, which is required for a Slater transition to occur.

Theoretical studies

First-principles calculations with LDA + U suggested [130] that antiferromagnetic correlations were key to opening up the electronic gap, whilst the spin-orbit coupling played only a minor role. This was the first theoretical evidence that $NaOsO_3$ is an example of a Slater insulator. Du *et al.* [135] performed further calculations with a local spin density approximation (LSDA) approach, and also determined that inclusion of the spin-orbit coupling only perturbed the band structure slightly. The calculated total density of states close to the Fermi energy was dominated by hybridisation between the Os 5d and O 2p orbitals, indicating an itinerant nature to the magnetic moment. They compared the effects of various magnetic structures on the band structure, and determined that G-type antiferromagnetic order had the lowest energy and was the only one that formed an insulating gap at the Fermi energy. This agrees with the experimental observations.

Jung *et al.* [136] found that spin-orbit coupling doubles the effective coupling strength U_{eff}, but has no effect on reducing the local moment. The local moment is reduced from the $S = \frac{3}{2}$ value of 3 μ_{B} to ~ 1 μ_{B} as a result of the itinerant conduction electrons and p-d hybridisation. The obtained value of the local moment is consistent with that obtained from neutron scattering

[131]. An additional notable feature was that each Os effectively had 4.3 d-electrons, which is a significant departure from the formal value of 3 for Os^{5+}, and is a further signature for itinerancy. This also gives rise to a significant orbital component to the local moment ($\boldsymbol{\mu}_O/\boldsymbol{\mu}_S \sim -0.1$), which would not be expected for a pure orbital singlet.

Middey and colleagues [137] focussed on the magnetic properties of NaOsO$_3$. They found that a modest correlation energy $U = 0.8$ eV was sufficient to stabilise the G-type AFM ground state, considerably less than the t_{2g} bandwidth of around 3 eV. Furthermore an estimate of the spin-wave dispersion was obtained by considering various spin spiral configurations, parameterised by a vector $\mathbf{q}$. They estimated the total magnon bandwidth $6J_1 + 12J_2 \approx 0.8$ eV.

Summary

The bulk, optical spectroscopy, neutron scattering, and X-ray measurements, combined with first-principles calculations, all point towards NaOsO$_3$ undergoing a MIT driven by magnetic order. In particular there are a number of characteristics of the eponymous Slater transition [55]. The situation of a Slater transition occurring for NaOsO$_3$ is complicated somewhat by the magnetic propagation vector being zero. This contrasts with the expected non-zero vector generally required for Fermi surface nesting. However, Slater's proposition in his original paper [55] did not require finite-**q**, so long as the charge gap opened up at the newly formed zone boundaries [136].

Apart from the aforementioned DFT study [137], there has been no examination of the magnetic excitations in NaOsO$_3$. Resonant inelastic X-ray scattering (RIXS) has previously been shown to successfully model the unconventional magnetic excitations present for Cd$_2$Os$_2$O$_7$. The remainder of this chapter pertains to RIXS measurements performed by the author on NaOsO$_3$. In summary, these measurements reveal well-defined spin wave excitations at 300 K consistent with an anisotropic Heisenberg model. At higher temperatures, there is evidence of a transition to more itinerant behaviour.

4.2 Low resolution RIXS measurements

Preliminary measurements were performed at 9-ID, Advanced Photon Source, with additional low-resolution data collected at ID20, ESRF. The two experiments differed somewhat in their setup, but had similar energy resolution. As mentioned previously in Chapter 3, low-resolution measurements permit fast collection of the orbital excitations out to large energy loss, including determination of the crystal field strength. Furthermore it allows a direct comparison with the results already obtained for Cd$_2$Os$_2$O$_7$.

APS experimental setup

A single crystal of $NaOsO_3$ (approx. 0.5×0.5×0.3 mm^3) was mounted in a high-temperature Displex cryostat (temperature range 10–800 K) on a Huber six-circle diffractometer equipped with an xyz translation stage to allow full orientation of the sample. The sample was mounted with the (5, 0, 5) direction approximately parallel to the direction of the incident beam. This direction was chosen as analysis using FullProf showed that (h, 0, h) reflections would have a non-zero magnetic structure factor. Additionally this was the only suitable reflection in the range $95^\circ \leq 2\theta \leq 105^\circ$; a criterion that was partly imposed to minimise the intensity of the elastic line, and partly due to the restrictive setup of the spectrometer. However, the direction can only be given as approximate as it was not possible to observe a Bragg peak in the limited region of reciprocal space that was accessible. Due to the setup of the spectrometer, rotations of no larger than about 10° were possible. This essentially means that the sample has to be pre-aligned before mounting in the cryostat. Without access to a Laue diffractometer on site, it was not possible to orient the sample such that the (5, 0, 5) direction was parallel to the incident beam.

The incident X-ray energy was selected by a Si (4, 4, 4) secondary monochromator, chosen to optimise the intensity at the expense of energy resolution. Rhodium plated mirrors focussed the incident beam to dimensions of 300×300 μm. The flight path of the X-ray beam between the sample and the detector was shrouded in a Perspex container filled with He gas, with the entrance and exit protected by kapton tape. A spherical Si (5, 5, 6) diced analyser was mounted at a distance of 1 m from the sample in horizontal scattering geometry. The diffracted X-rays were collected by a MYTHEN strip detector with pixel size 50 μm. The energy of the incident X-rays was matched to the Os L_3 absorption edge (10.875 keV). This energy corresponded to the maximum in intensity of a feature present at 1.1 eV. The total energy resolution obtained ($\Delta E = 300$ meV) was considerably worse than the theoretical resolution of $\approx$150 meV. The main reason for this is the large spot size of the incident X-ray beam, which was due to degradation of the Rh coating on the mirror.

ESRF data

Low resolution RIXS measurements were performed at the Os L_3 edge on the ID20 spectrometer at the ESRF, Grenoble. A single crystal of $NaOsO_3$ (approx. dimensions 0.3×0.3×0.3 mm^3) was oriented such that the (1, 0, 1) direction was normal to the sample surface. The sample was mounted with epoxy resin and placed in a custom-made heater setup filled with helium exchange gas. Temperature stability was better than ±0.5 K. The scattering plane and incident photon polarisation were both horizontal, i.e. π incident polarization, with the incident beam focussed to a size of 20×10 μm^2 (H×V) at the sample position.

The incident energy was selected with a Si (3, 1, 1) channel-cut secondary monochromator. A Si (6, 6, 4) diced spherical analyser (2 m radius) was used to reflect the scattered photons to-

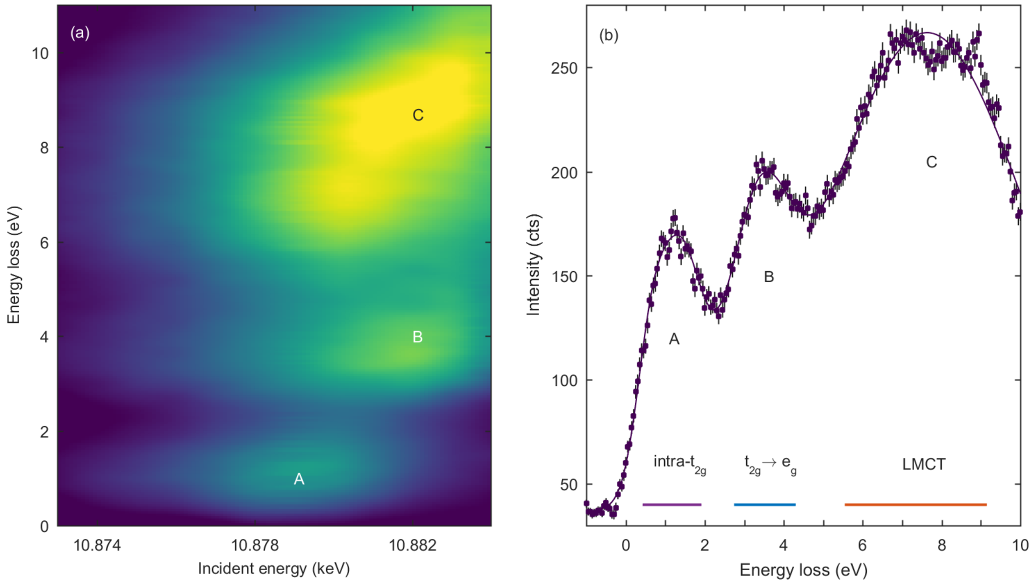

Figure 4.2: RIXS spectra from NaOsO$_3$, collected at 300 K as a function of varying incident energy (ΔE = 275 meV). (a): RIXS map presented as a contour plot. Three peaks are evident: peaks A, B, and C correspond to intra-t_{2g}, $t_{2g} \rightarrow e_g$, and ligand-to-metal charge transfer (LMCT) excitations respectively. (b): Single RIXS spectrum obtained for an incident energy of 10.879 keV.

wards a Maxipix CCD detector (pixel size 55 μm) and discriminate the scattered photon energy. The total energy resolution was determined to be ΔE = 275 meV, based on scattering from a charge peak. This compares well to the theoretical energy resolution of 305 meV.

The energy loss dependence of the RIXS intensity as a function of incident energy (RIXS map) provides an insight into the relevant excitation processes for that material. Such a RIXS map has been performed for NaOsO$_3$, with the results plotted in Fig. 4.2. Three peaks are evident (A, B and C), which correspond to $\Delta S = 1$ excitations within the t_{2g} manifold, between the t_{2g} and e_g orbitals, and ligand-to-metal charge transfer (LMCT) respectively. This assignment is based on the quantum chemistry calculations [106] and RIXS measurements performed for Cd$_2$Os$_2$O$_7$ (Chapter 3).

Given the similar local coordination environment and valence state for both NaOsO$_3$ and Cd$_2$Os$_2$O$_7$, one would expect the orbital excitations to occur at similar energies for the two compounds. Fitting the intra-t_{2g} peak (peak A) to two excitations at 3J_H and 5J_H respectively, one finds that J_H = 0.31(4) eV, which is identical to the value obtained for Cd$_2$Os$_2$O$_7$ [J_H = 0.29(4) eV]. This is unsurprising given that Os is nominally in the same oxidation state, and surrounded by the same ligands, for the two materials. Furthermore it also suggests that NaOsO$_3$ is in a similarly weak-to-intermediate spin-orbit coupling regime, wherein the effect of SOC is insufficient to noticeably split the t_{2g} manifold into $j_\mathrm{eff} = \frac{3}{2}, \frac{1}{2}$ bands.

However the energy of peak B (3.7 eV) is considerably lower than that observed for Cd$_2$Os$_2$O$_7$ (4.3 eV). From a purely crystal field perspective, the subtle differences in coordination environment are not sufficient to explain these differences. The trigonal distortion is

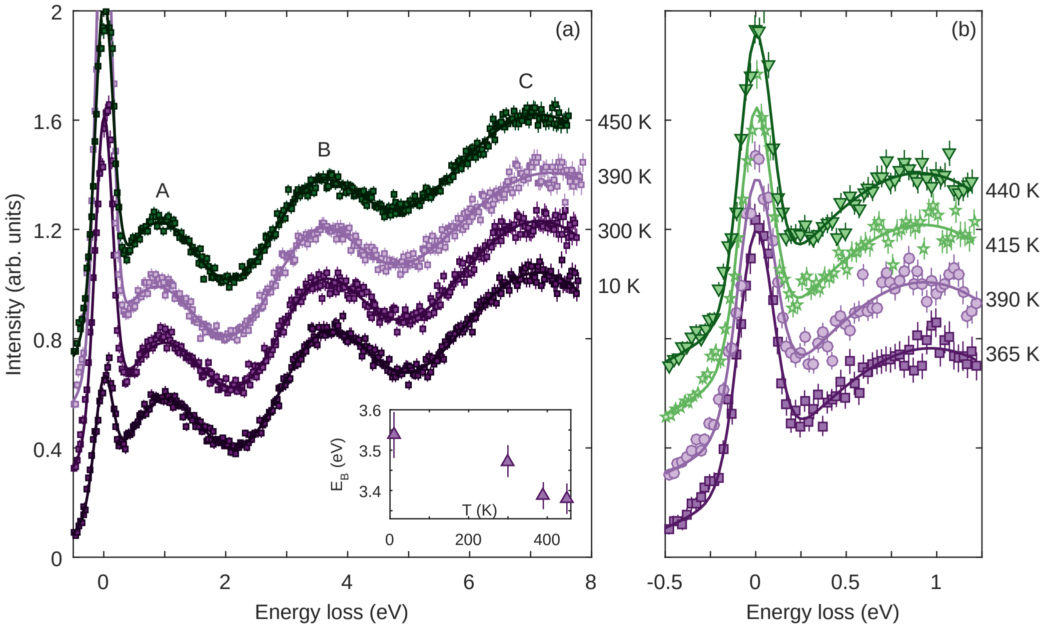

Figure 4.3: Temperature dependence of the orbital excitations (offset for clarity). (a): RIXS spectra out to 8 eV energy loss. Inset shows the fitted energy of peak B as a function of temperature. (b): Spectra focussing on the low energy excitations through the MIT. No significant difference can be seen as a function of temperature.

parametrized by the angle between the ligand-metal bond and the threefold rotation axis. One quantitative measure of the distortion is given by the ratio $D\tau/Dq$ [59, 107, 138]. For $Cd_2Os_2O_7$, one can estimate $D\tau/Dq \approx -0.08$, whilst for $NaOsO_3$, $D\tau/Dq \approx -0.01$. Negative values of $D\tau/Dq$ are indicative of trigonal compression. Consequently in the limit of zero SOC, and for plausible [114] values for the Racah parameters B and C, one finds that the spin-allowed $^4T_1$ multiplet for example is split by 100 meV for $Cd_2Os_2O_7$, whereas it is only split by 10 meV for $NaOsO_3$. The former value is consistent with quantum chemistry calculations [106]. SOC will split these multiplets further (including zero-field splitting of the $^4A_2$ ground state), however the centre of mass should remain constant. Thus it is concluded that other effects must be responsible for the difference between the two compounds, which may include longer-ranged electronic interactions due to itinerancy.

Measurements at the APS revealed no significant variation in the orbital excitations with temperature (Fig. 4.3). This suggests that the coordination environment varies little through the MIT, which agrees with the neutron scattering results [131, 132]. Indeed the only discernible difference between the spectra is the intensity of the quasi-elastic excitations, which increases with increasing temperature. This can be understood in terms of increased phonon population in accordance with the Bose-Einstein distribution. Scattering from phonons is a likely contribution to the quasi-elastic excitations.

4.3 High resolution RIXS measurements

Thus far only electronic excitations have been considered; the energy scale of magnetic excitations is considerably lower. To this end high resolution RIXS measurements were performed at ID20, ESRF, in order to characterise the magnetic Hamiltonian and the relevant interactions.

Experimentally the only difference in the setup to that of the previously presented low-resolution measurements was the use of a Si (6, 6, 4) backscattering channel-cut secondary monochromator. This improved the energy resolution to $\Delta E = 46$ meV, as determined from scattering from a charge peak. The incident photon energy E_i was fixed at 10.880 keV, since this maximized the intensity of the intra-t_{2g} excitations (peak A) in the low-resolution measurements.

4.3.1 Momentum dependence

Insight into the magnetic Hamiltonian can be obtained from the momentum dependence of the low energy RIXS spectra deep in the antiferromagnetic insulating phase. RIXS spectra were collected at 300 K as a function of momentum transfer in the (5, 3, 4) Brillouin zone ($2\theta = 91.1^\circ$). The data are plotted in Fig. 4.4. Two resolution limited peaks can be observed: one corresponding to quasi-elastic excitations, and a dispersive feature at around 100 meV. The intensity variation of the quasielastic line as a function of momentum transfer is almost entirely due to RIXS matrix element effects, which occur away from the ideal $2\theta = 90^\circ$ condition. The second feature appears to be gapped at the Brillouin zone centre (the magnetic and structural Brillouin zones coincide as $\mathbf{k} = 0$), and progressively weakens towards the zone boundary. Furthermore a significant variation of the spectral weight can be observed across the Brillouin zone. It is proposed that this feature is of a magnetic origin, which shall be justified later in this chapter.

In order to quantify these observations, the data (both as a function of momentum transfer and temperature) were fitted with a Pearson VII function for the quasi-elastic line (profile parameter μ fixed to 1.55), and two Gaussians representing the dispersive feature and an intra-t_{2g} excitation background centered at 1.1 eV respectively.

4.3.2 Magnon dispersion

The significant gap for $T < T_\mathrm{N}$ indicates highly anisotropic exchange interactions. Thus the following minimal model for the Hamiltonian was used to describe the data:

$$\mathcal{H} = J_1 \sum_{nn} \mathbf{S}_i \cdot \mathbf{S}_j + J_2 \sum_{nnn} \mathbf{S}_i \cdot \mathbf{S}_j + \mathcal{H}_\mathrm{A}, \tag{4.1}$$

where the first sum is over nearest neighbours (in the a-c plane), the second sum is over next-nearest neighbours (in the b-direction), and the final term represents some degree of anisotropy The nearest-neighbour and next-nearest neighbour distances vary only slightly; the difference between them is due to the weak orthorhombic distortion. Thus Equation 4.1 is in effect an

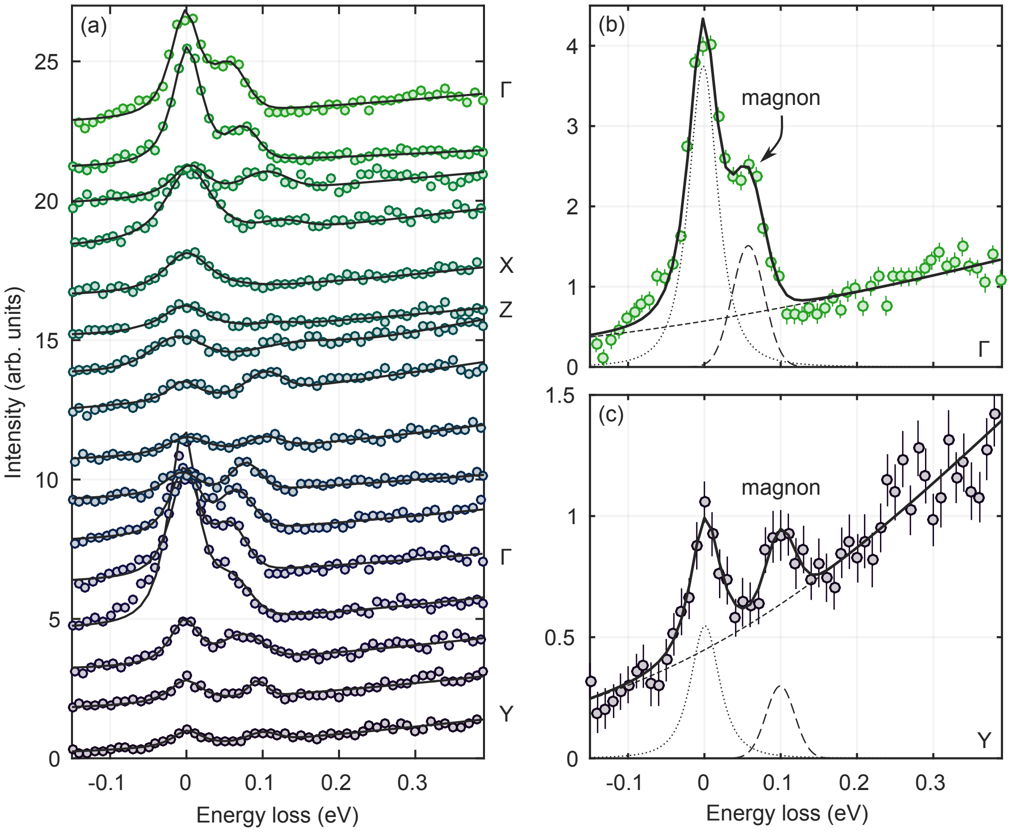

Figure 4.4: (a): Momentum dependence of the RIXS spectra in the (5, 3, 4) Brillouin zone at 300 K. Error bars on individual data points have been omitted for reasons of clarity. There is a strongly momentum dependent feature at ca. 100 meV which corresponds to a spin wave excitation. Solid lines are best fits to the data using the model described in the main text. (b,c): Representative fits at Γ and Y respectively.

anisotropic nearest-neighbour Hamiltonian. Two sources for the observed anisotropy $\mathcal{H}_{\mathrm{A}}$ were considered. These were: (i) single-ion anisotropy (SIA), with $\mathcal{H}_{\mathrm{A}} = \sum_i \mathbf{S}_i \cdot \bar{\mathrm{A}} \cdot \mathbf{S}_i$, and (ii) symmetric anisotropic exchange, where $\mathcal{H}_{\mathrm{A}} = \Gamma \sum_{nn,nnn} S_i^z S_j^z$. The main assumption was that only one of these terms contributed significantly to the Hamiltonian at any one time. Furthermore as the magnetic moments in NaOsO$_3$ rigidly lie along the c-axis (as determined by neutron powder diffraction), the assumption was made that $\bar{\mathrm{A}}$ is dominated by the A_{zz} element and all other elements can be neglected to a first approximation. Hence from now on A represents A_{zz}.

The experimental RIXS data were fitted with Equation 4.1 within a linear spin wave (LSW) approximation. This is expected to be appropriate given a nominal $S = \frac{3}{2}$ model for NaOsO$_3$. Diagonalizing Eqn. 4.1 within a linear spin wave approximation gives the following expression for the spin wave energy ω:

$$\begin{aligned} \omega &= S\sqrt{\eta - X - Y}, \quad \text{with} \\ X &= 4J_1^2 \cos 2\pi h + 2J_2^2 \cos 2\pi k + 4J_1^2 \cos 2\pi l, \\ Y &= 2J_1^2 \cos\left[2\pi(h-l)\right] + 2J_1^2 \cos\left[2\pi(h+l)\right] \\ &\quad + 16 J_1 J_2 \cos \pi h \cos \pi k \cos \pi l. \end{aligned} \tag{4.2}$$

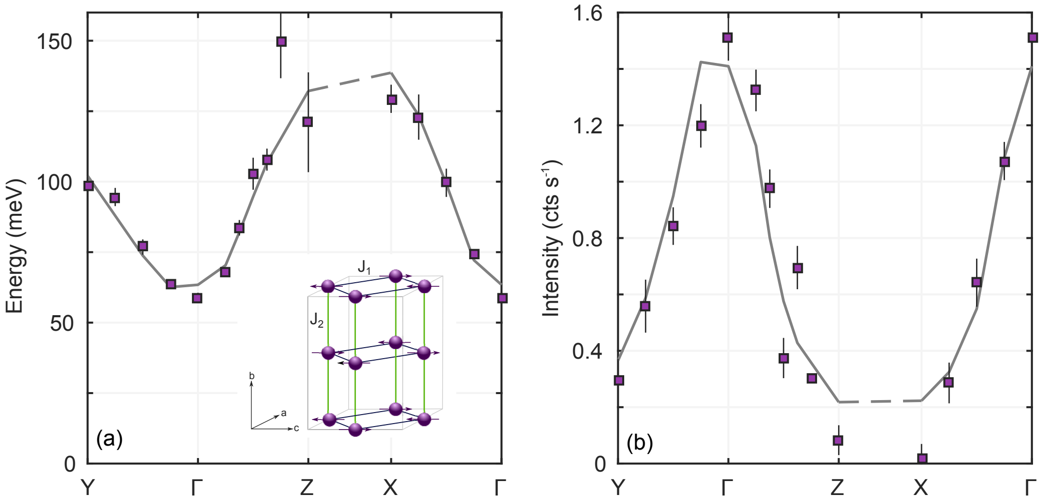

Figure 4.5: Fitted energy (a) and intensity (b) of dispersive feature, along with best fit to spin wave model described in text (solid line). Inset illustrates exchange pathways J_1 and J_2.

The parameter η contains all of the anisotropic contributions to the spin wave dispersion; whilst X and Y are the same for both anisotropy models, η differs. These are given by

$$\begin{aligned} \eta_{\mathrm{aEx}} &= 36A^2 + 48AJ_1 + 24AJ_2 + 12J_1^2 + 2J_2^2 + 16J_1J_2 \\ \eta_{\mathrm{SIA}} &= 4\Gamma^2 + 16\Gamma J_1 + 8\Gamma J_2 + 12J_1^2 + 2J_2^2 + 16J_1J_2, \end{aligned} \tag{4.3}$$

with the relevant spin wave dispersion obtained by simply substituting in the relevant expression for η. In a similar fashion the intensity can be expressed by:

$$S(q,\omega) = F\left[\frac{\eta-(X-Y)}{\eta-(X+Y)}\right]\delta(\omega,\omega_q), \tag{4.4}$$

where F is an arbitrary scale factor.

Neutron powder diffraction measurements [131] revealed that the ordered osmium moment in NaOsO$_3$ is significantly reduced [$S = 1.0(1)\ \mu_\mathrm{B}$] compared the nominal spin only value of $S = 1.5\ \mu_\mathrm{B}$ expected for a d^3 system. Consequently fits to the experimental dispersion and intensity were performed for both values of S, in order to determine whether the reduced moment also extends to the magnetic excitations.

The best fit to the experimental dispersion and intensity is shown in Figure 4.5 for the case of $S = 1.0(1)\ \mu_\mathrm{B}$, with the corresponding fitted parameters given in Table 4.1. Fits to either source of anisotropy or value of S gave fits of identical quality. Furthermore J_2 was fixed to be equal to J_1; allowing both J_1 and J_2 to vary made no improvement in the quality of the fits ($\chi^2 = 1.25$ for $J_1 = J_2$; $\chi^2 = 1.31$ for $J_1 \neq J_2$). This reflects the pseudo-cubic nature of the crystal structure. The analytical model was checked by comparing the result to numerical calculations using the SpinW code [129]; the two approaches gave identical results. The magnon bandwidth and exchange parameters are comparable to those obtained via DFT by Middey *et al.* [137] for small (but non-zero) values of U, consistent with a Slater weak-coupling picture.[2]

---

[2] It should be noted that the dispersion displayed in Ref. [137] is not a true spin wave dispersion, but is an energy minimization of various spin spiral configurations with spin spiral vector q. This explains the lack of a gap in their data.

S (μ_B)	$J_1 = J_2$ (meV)	A (meV)	Γ (meV)	T_N^{MF} (K)
1.5	13.9(4)	4.3(3)	1.4(1)	510(20)
1.0(1)	21(3)	6(1)	2.2(4)	410(40)

Table 4.1: Summary of fitting parameters for $NaOsO_3$, and obtained mean field Néel temperature T_N^{MF}. Note that the fits to the data involved either A or Γ as a free parameter; the other parameter was set to zero. The uncertainties for the $S = 1.0(1)$ μ_B row include both the uncertainty in the moment size and the errors obtained from the least-squares routine.

The results of the fitted intensity to this model are plotted in Fig. 4.5(b), which gives a good description of the data with the scale factor $F = 0.25$. The slight discrepancies between the fitted model and the data can be explained as follows. Firstly the RIXS spectrometer has a finite momentum resolution. Consequently the obtained spectra are an average over a portion of the Brillouin zone. Secondly, unlike neutrons, the RIXS magnetic cross section is only approximately equal to the spin dynamical structure factor $S(\mathbf{q}, \omega)$ [75, 139]. The validity of this approximation however is very good, at least in the localised limit. Finally, strictly speaking, one may have consider contributions from self-absorption in correctly normalising the intensities. The latter contribution is expected to be very small however since the orientation of the crystal varies little for measurements within a single Brillouin zone.

Clearly the minimal model is representative of the observed spin wave dispersion, however there are at present four parameter sets which give apparently identical descriptions of the data. One criterion by which the best parameter set can be identified is the mean field value of the Néel temperature. This simplified picture neglects fluctuations of the moments from their mean value, and T_N can be evaluated using the expression:

$$T_N = \frac{2S(S+1)}{3\mu k_B} \sum_j z_i J_i, \tag{4.5}$$

where $\mu = \Theta_{CW}/T_N^{exp}$ is a mean field constant, and the summation goes over all neighbours with which a given spin interacts. This summation reduces to $6J$ in the case that $J_1 = J_2$. Shi *et al.* [130] determined $\Theta_{CW} = -1949$ K and $T_N^{exp} = 410$ K, thus $\mu = -4.75$ for $NaOsO_3$. In the limit of zero anisotropy, and $J_1 = J_2$, one finds that $T_N^{MF}[S = 1.5\ \mu_B] = 510(20)$ K, whereas $T_N^{MF}[S = 1.0(1)\ \mu_B] = 410(40)$ K. Mean field theory typically overestimates T_N, but there is better agreement between the mean field transition temperature and the experimental one ($T_N = 410$ K) if $S = 1.0(1)$ μ_B, in accordance with the value extracted from neutron powder diffraction [131]. Note that the analysis at present only includes nearest neighbour interactions. Addition of anisotropy would increase T_N^{MF}, whilst the effect of ferromagnetic next-nearest neighbour interactions for example (which would recover the cubic limit) would be to reduce T_N^{MF}.

Furthermore the bandwidth and dispersion displayed in [137] is in units of $J_0 = 6J_1 + 12J_2$. Taking this into account, there is good agreement with the present study.

Source	Scaling	Estimated (meV)	Experiment (meV)
Single-ion anisotropy	$A \sim \frac{\lambda^2}{\delta E}$	8.0	6(1)
Dzyaloshinskii-Moriya (DM)	$\lvert\mathbf{d}\rvert \sim \frac{\lambda}{\delta E} J$	1.0	–
Exchange anisotropy	$\delta J \sim \left(\frac{\lambda}{\delta E}\right)^2 J$	0.05	2.2(4)

Table 4.2: Approximate scaling of various sources of anisotropy (Ref. [65]), assuming a d^3 electronic configuration and that they are the sole source of uniaxial anisotropy. The relative magnitudes for these sources have been estimated using suitable parameters for $NaOsO_3$: $\lambda = \zeta/3 = 0.172$ eV, $\delta E = 3.7$ eV, $J = 21$ meV.

To conclude, one observes coherent spin fluctuations with a reduced local magnetic moment at 300 K. This is consistent with the observation of magnetic long-ranged order in the insulating phase of $NaOsO_3$.

4.3.3 Validity of Hamiltonian

It should be noted at this point that the addition of either a symmetric exchange anisotropy or single ion anisotropy term to the Hamiltonian is a bit of an oversimplification. In reality contributions from symmetric and antisymmetric exchange anisotropy, plus a single-ion anisotropy term would be required to fully describe the magnon dispersion. This results in the following general Hamiltonian of the form:

$$\begin{aligned}\mathcal{H} = &\sum_{i,j} J_{\parallel} S_i^z S_j^z + J_{\perp}\left(S_i^x S_j^x + S_i^y S_j^y\right) + \sum_{i,j} \mathbf{D}_{ij}\cdot(\mathbf{S}_i \times \mathbf{S}_j) \\ &- \mathrm{A}_{zz}\sum_i (S_i^z)^2 ,\end{aligned} \tag{4.6}$$

where the first(second) summation represents (anti)symmetric exchange anisotropy, and the final term represents a single-ion anisotropy. For simplicity summations are restricted to nearest-neighbours, and a uniaxial anisotropy has been assumed. Anisotropy in the magnetic Hamiltonian is driven by spin-orbit coupling. The relative contributions of each of these terms to the magnetic Hamiltonian are discussed below. Note that all scaling relations (as given in Table **??**) stated assume an orbital singlet (quenched orbital angular momentum).

Single-ion anisotropy

Single-ion anisotropy arises due to the non-cubic environment for Os, and scales approximately as $A \sim \lambda^2/\delta E$, where $\delta E = 10\,Dq$ in the case of weak crystal field distortion away from octahedral symmetry. The OsO_6 octahedra are weakly trigonally and tetragonally compressed, both of which would stabilise magnetic order predominantly along the local z-axis. However due to octahedral tilting and rotation resulting from the $GdFeO_3$ type distortion, this does not coincide with the crystallographic c-axis. Using the scaling relation above, one can estimate $A = 8$ meV for $NaOsO_3$, which is in good agreement with the obtained value from the fits to the spin wave dispersion.

However there are a couple of complications with this result. Firstly the above scaling expression assumes uniaxial anisotropy, which given the combined trigonal and tetragonal compression, is not strictly true. Furthermore the almost ideal cubic octahedral environment for the Os ions implies that the magnitude of single-ion anisotropy is small. Finally if single-ion anisotropy were the only contribution to the spin gap, then spin canting and weak ferromagnetism would be expected. A weak ferromagnetic (FM) component has been observed in bulk magnetisation data by Shi [130], with magnitude 0.005 μ_B. This is significantly smaller than the ordered moment size of $\sim$1 μ_B obtained from neutron powder diffraction, and may be evidence for spin canting. The degree of this canting can be estimated from the ratio of the weak FM component to the ordered moment size: $\theta \approx \mathtt{arctan}\,[0.005/\,1.0(1)] = 0.3^\circ$. Such a small canting would not be readily observable with neutron powder diffraction, and further suggests that the effect of the single-ion anisotropy is indeed small.

Dzyaloshinskii-Moriya interaction

In $NaOsO_3$ one would expect a non-zero local Dzyaloshinskii-Moriya (DM) vector, as the oxygen anion mediating the superexchange between the two Os sites does not sit at an inversion centre [66]. This results from rotation of the OsO_6 octahedra in the ac-plane, and concurrent tilting about the b-axis. Both distortions are on the order of 10° away from the cubic $Pm\bar{3}m$ case.

The Dzyaloshinskii-Moriya interaction scales approximately as $|\mathbf{d}| \sim (\lambda/\delta E)\, J$. Evaluating this for $NaOsO_3$, one obtains $|\mathbf{d}| = 1$ meV. Assuming that the DM interaction is the only source for any spin canting, then one can estimate $\theta \approx |\mathbf{d}|/J = 2.7^\circ$. Yet neutron powder diffraction measurements [131] found that the Os magnetic moments are collinear (within resolution), whereas the DM interaction stabilizes a canted ground state. Furthermore the magnitude of the weak FM component observed from the magnetisation data would imply that the DM interaction should be a order of magnitude weaker than the scaling prediction. This suggests that the DM interaction is weak to first order in $NaOsO_3$.

Symmetric anisotropic exchange

Finally consider the effect of symmetric anisotropic exchange. Such a pseudodipolar effect results as a consequence of second-order SOC effects between two neighbouring ions, and hence is generally weaker than both the DM interaction and single-ion anisotropy. This can be shown by the scaling relation $\delta J = J\,(\lambda/\delta E)^2$, which when evaluated for $NaOsO_3$, gives the estimate $\delta J = 0.05$ meV. This alone would imply that symmetric anisotropic exchange does not contribute significantly to the observed anisotropy in the case of a $S = \frac{3}{2}$, d^3 orbital singlet.

It should be noted that exchange anisotropy has been implicated as the source of the spin gap in the d^3 double perovskites Sr_2ScOsO_6 [109] and Ba_2YOsO_6 [140]. However these studies were performed using inelastic neutron scattering on powder samples, leading to the use of a minimal model similar to that which was used earlier for $NaOsO_3$. Furthermore it was found

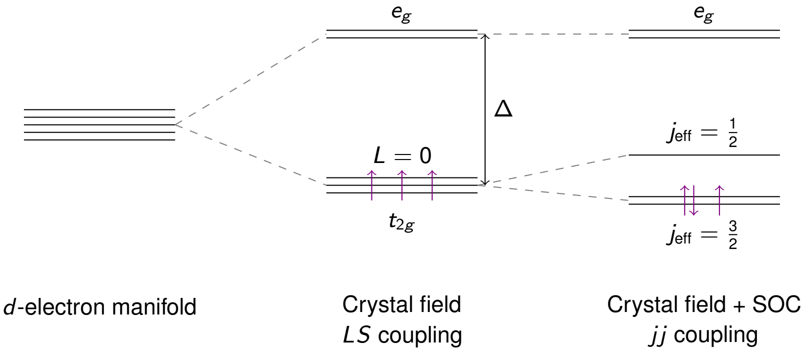

Figure 4.6: Schematic of energy levels in a 5d^3 material. The octahedral crystal field Δ splits the d-electron manifold into states with t_{2g} and e_g symmetry. The t_{2g} manifold is at half-filling, consequently the orbital angular momentum L is quenched in the LS (Russell-Saunders) coupling limit. Strong spin-orbit coupling can split these levels further, leading to $j_{\text{eff}} = \frac{3}{2}$ and $j_{\text{eff}} = \frac{1}{2}$ states. The orbital angular momentum is no longer quenched. Cd$_2$Os$_2$O$_7$ and NaOsO$_3$ are likely intermediate between these coupling schemes.

for Sr$_2$ScOsO$_6$ that the spin wave dispersion could be fit equally well with a model containing a single-ion anisotropy term rather than exchange anisotropy.

Discussion

None of the three anisotropic contributions to the magnetic Hamiltonian are sufficient to explain the observed magnetic ground state and excitations in NaOsO$_3$ on their own. This is exacerbated by the nominally quenched orbital moment for a d^3 electronic configuration in the Russell-Saunders limit, and large crystal field splitting δE which prevents mixing of excited states. However NaOsO$_3$ (and other d^3 osmates) do not lie in the Russell-Saunders limit. Systems with a 5d^3 electronic configuration are believed to be intermediate between the L–S and jj–coupling schemes [115]. In the jj–coupling limit, the ground state is not an orbitally quenched t_{2g}^3 configuration, but rather a partially occupied $j_{\text{eff}} = \frac{3}{2}$ quartet. This leads to a finite value of the orbital magnetization which is anti-parallel to the spin magnetization.[3] Consequently the spin-orbit coupling $\lambda\mathbf{L}\cdot\mathbf{S}$ is larger, which in turn leads to larger anisotropy and a partial breakdown of the previously mentioned scaling relations.

An outstanding question is the observed magnetic ground state. Whilst the microscopic parameters used in the spin wave analysis did reproduce the correct ground state, it was with the assumption that the anisotropy was entirely along the moment direction. This is, as previously mentioned, not strictly correct. One possibility is that the DM interaction and single-ion anisotropy compete with each other, to give rise to an approximately collinear magnetic structure. This is supported by consideration of the direction of the DM vector for a given Os–Os exchange pathway, and the single-ion anisotropy for a given Os site. Combined with a weak symmetric anisotropic exchange term, this would stabilise a collinear antiferromagnetic ground state. One can crudely estimate the magnitude of the Dzyaloshinskii-Moriya interaction required

---

[3] Supported by DFT calculations [135, 136] and RXMS measurements [131, 132].

to compensate for the effect of the single-ion anisotropy as $|\mathbf{d}|/J \approx 0.2$, which is comparable to the value obtained within the quantum chemistry calculations on $Cd_2Os_2O_7$ by Bogdanov and colleagues [106]. Unfortunately the RIXS measurements presented here do not permit straightforward disentanglement of the relative magnitudes of these contributions, as a consequence of the limited energy resolution.

As already discussed in Chapter 1, the valence orbitals in 5*d* TMOs are greatly extended compared to their 3d counterparts. What this means is that one would expect further than nearest-neighbour interactions to be important for $NaOsO_3$, as is the case for Sr_2IrO_4 for example (see later). In a classical J_1–J_2–$J_{\rm nnn}$ model on a cubic lattice (as calculated in Ref. [141]), G-type antiferromagnetic order is stabilised over the stripe ordered phase if $J_1 > 0$ and $J_1 > 2J_{\rm nnn}$. Furthermore for G-type order to occur along the c-axis, there is the additional constraint that $J_2 > 0$. Note that $J_{\rm nnn}$ can have either sign, as long as $J_1 > 2J_{\rm nnn}$ is satisfied. A ferromagnetic (negative) $J_{\rm nnn}$ will stabilise the G-type ground state, and hence enhance T_N; whereas an antiferromagnetic (positive) $J_{\rm nnn}$ will lead to frustration and thus suppress T_N. The fact that further than next-nearest neighbour interactions do not seem to contribute significantly to the magnetic Hamiltonian supports the robustness of the G-type phase for $NaOsO_3$.

Moreover, the result that a LSW theory model works so well for $NaOsO_3$ at 300 K implies comparatively strong correlations and localized magnetic moments. This is unsurprising given that $NaOsO_3$ is well within the insulating regime. Closer to the MIT we would expect LSW theory to fail as a consequence of moving farther from the localized limit.

4.3.4 Temperature dependence

Further insight into the origin of the dispersive feature can be garnered by measuring its dependence on temperature. Preliminary measurements were performed during the same beamtime as the momentum dependence presented in Section 4.3.1, but time constraints meant that it wasn't possible to obtain a full characterisation.

Measurements were performed with a similar setup once again at the ESRF. Two details differ from the previous data: the incident photon energy was set to 10.8765 keV, as this was found to maximise the intensity of the intra-t_{2g} excitations, and the instrumental resolution was 56 meV as determined from elastic scattering from clear adhesive tape. Furthermore the resolution function was found to be clearly asymmetric; this was a consequence of the analyser.

RIXS spectra were collected at three different momentum transfers as a function of temperature: Γ (4.95, 2.95, 3.95),[4] $\Gamma - Y$ (4.75, 3, 4), and Y (4.5, 3, 4). This reflects a progression from the Brillouin zone centre to the zone boundary. Four spectra with count times of 30s/pt were averaged together to obtain the data presented, and normalised to the intensity of the intra-t_{2g} excitations at 1 eV energy loss.

It should be noted that there was a variation in the intensity of the elastic line for successive scans at the same temperature. However this problem only occurred at Γ, which was the first

---

[4] Once more this was to avoid elastic scattering from the weak magnetic Bragg peak at (5, 3, 4).

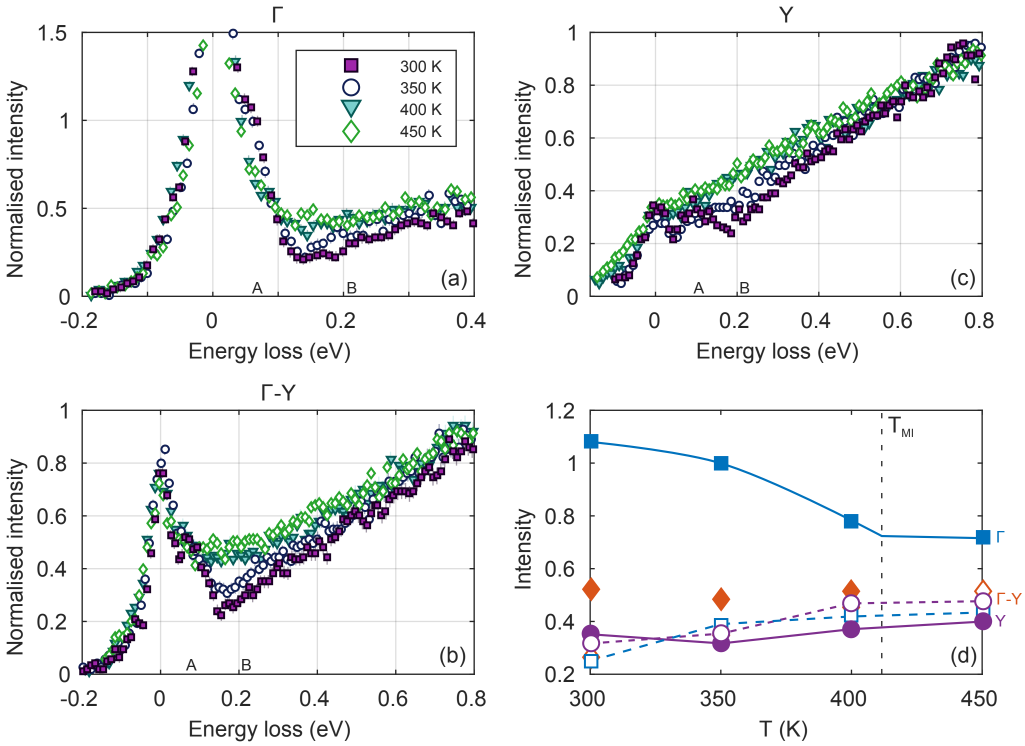

Figure 4.7: RIXS spectra collected at the Γ (a), Γ–Y (b), and Y (c) points of the Brillouin zone for various temperatures (300 K – 450 K). All data has been normalised to the intensity of the d-d excitations at 1 eV energy loss. There is a progressive increase in intensity at 0.2 eV with increasing temperature. (d): Intensity at points A (solid symbols) and B (open symbols) as a function of temperature. A and B correspond to the magnon peak and feature at 0.2 eV energy loss respectively. Solid and dashed lines are guides to the eye.

point measured per temperature step, and only below 400 K. Furthermore the inelastic features remained consistent between scans, which suggests that the observed behaviour may be due to some local surface reconstruction or such like which added extraneous elastic scattering. Selected measurements were repeated over a limited range, which show a much reduced elastic line intensity and aids full characterisation of the salient features. The inelastic features are comparable to those collected in the initial run which allows a comparison to be made.

In summary there is a pronounced anisotropy in the temperature dependence at different momentum transfers. This can be seen in the raw spectra, which are plotted in Figure 4.7. Two main features are apparent. The first is a peak around 100 meV, which is the magnon peak observed earlier. With increasing temperature this feature progressively weakens and broadens. The second observation is that there is a concurrent increase in spectral weight in the region between 0.1 and 0.6 eV with increasing temperature, whilst there is no obvious change in the d-d excitations. These two observations are roughly quantified in Figure 4.7(d), with the solid symbols reflecting the intensity of the magnon peak, and the open symbols showing the intensity at 0.2 eV energy loss.

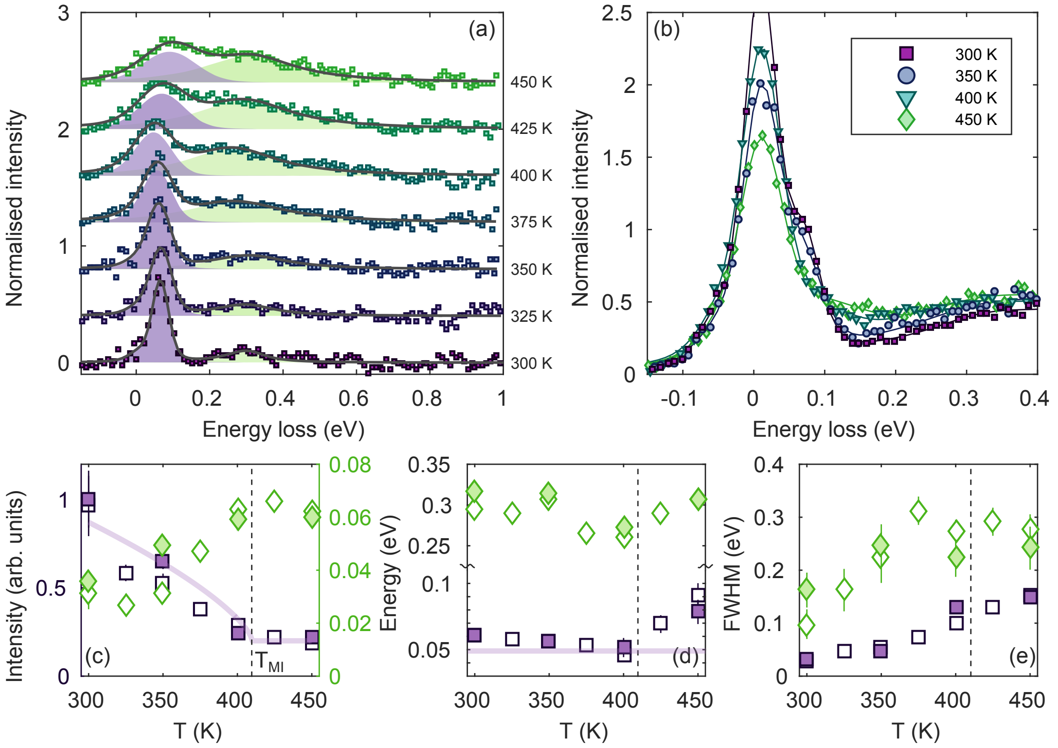

Figure 4.8: Analysis of RIXS spectra collected at Γ. (a): Spectra with elastic line and $d-d$ contributions subtracted. Added are the best fit to the data (black solid line), and relative components of the magnon peak (purple) and particle-hole continuum (green). (b): Spectra from the second run normalised to the intensity of $d-d$ excitations at 1 eV. Fitted peak intensity (c), energy (d) and FWHM (e) of the two components as a function of temperature. The two sets of symbols correspond to the first (open) and second (filled) runs respectively. Dashed lines indicate the metal-insulator transition at 410 K.

In order to quantify these observations further, the data were fitted with the same model used for the momentum dependence, but with two additional constraints. The first is that a Gaussian was added to the fitting model in order to take the increased spectral weight at 200 meV into account. Secondly the fits in the low energy portion of the RIXS spectra were corrected to take the Bose factor into account. All of the features were convoluted with the experimental resolution function. Fits to the data are presented in Figures 4.8 – 4.10.

Magnon peak

In general the magnon peak becomes less intense with increasing temperature (Figures 4.8c – 4.10c), showing order parameter like behaviour with a critical temperature ~400 K. This is consistent with what would be expected for magnetic excitations and is similar to what was observed for $Cd_2Os_2O_7$. At Y the temperature dependence is less clear, however it appears to decay more quickly than at the two other points measured in reciprocal space. Similarly whilst there is a monotonous increase in the peak width (Figures 4.8e – 4.10e) at Γ and $\Gamma - Y$ with increasing temperature, this increase abates above 350 K at Y. Intriguingly the magnons appear to soften along Γ and $\Gamma - Y$ by 10–20 meV below the MIT, with an abrupt hardening above the

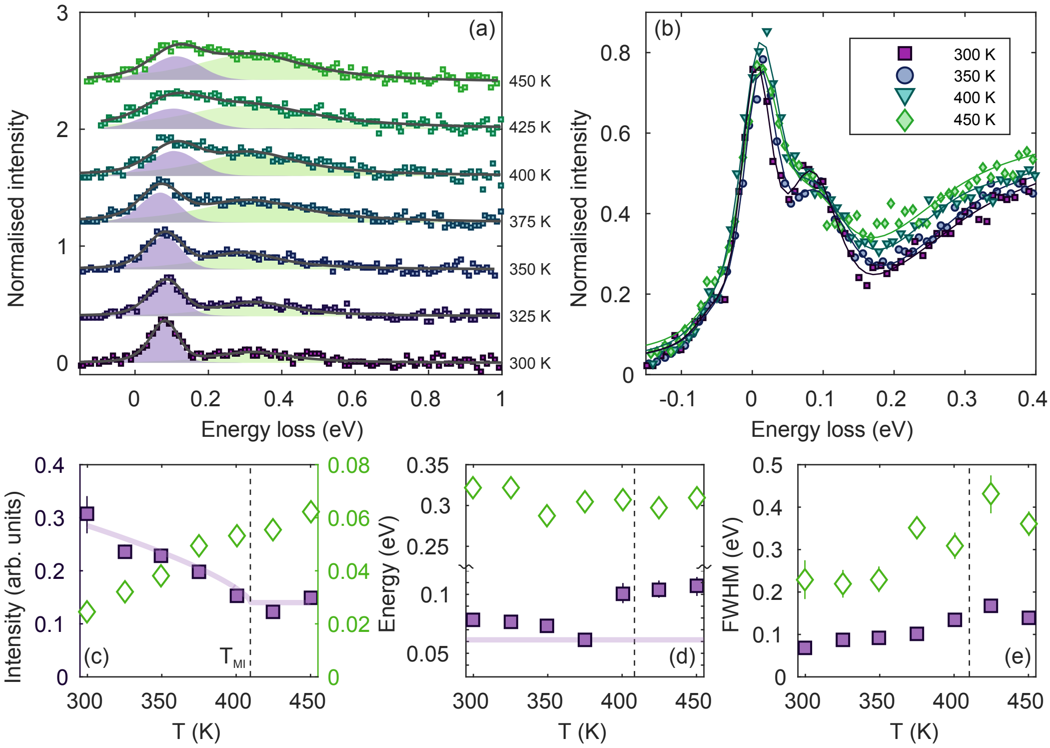

Figure 4.9: Analysis of RIXS spectra collected at $\Gamma - Y$. (a): Spectra with elastic line and $d - d$ contributions subtracted. Added are the best fit to the data (black solid line), and relative components of the magnon peak (purple) and particle-hole continuum (green). (b): Spectra normalised to intensity of $d - d$ excitations at 1 eV. Fitted peak intensity (c), energy (d) and FWHM (e) of the two components as a function of temperature. Solid lines are guides to the eye. Dashed lines indicate the metal-insulator transition at 410 K.

MIT. Conversely for Y, a weak hardening of 20 meV can be observed between the data collected at 300 K and 450 K.

High energy peak

At all reciprocal lattice points there is a increase in intensity of the peak present at 0.3 eV energy loss, coupled with a weak broadening as a function of increasing temperature. However whereas the energy of this peak is relatively constant as a function of temperature at Γ and $\Gamma - Y$, there is a significant hardening at Y.

4.3.5 Discussion

Clearly there is a significant variation of the RIXS spectra through the MIT. The observed behaviour can, at least qualitatively, be explained in terms of a spin-fluctuation model for NaOsO$_3$ [142]. The premise is as follows. Note that for itinerant systems, the concept of a spin wave has no real meaning. Instead one should really think about a statistical fluctuation of the magnetic moment or spin density. The following discussion uses this terminology.

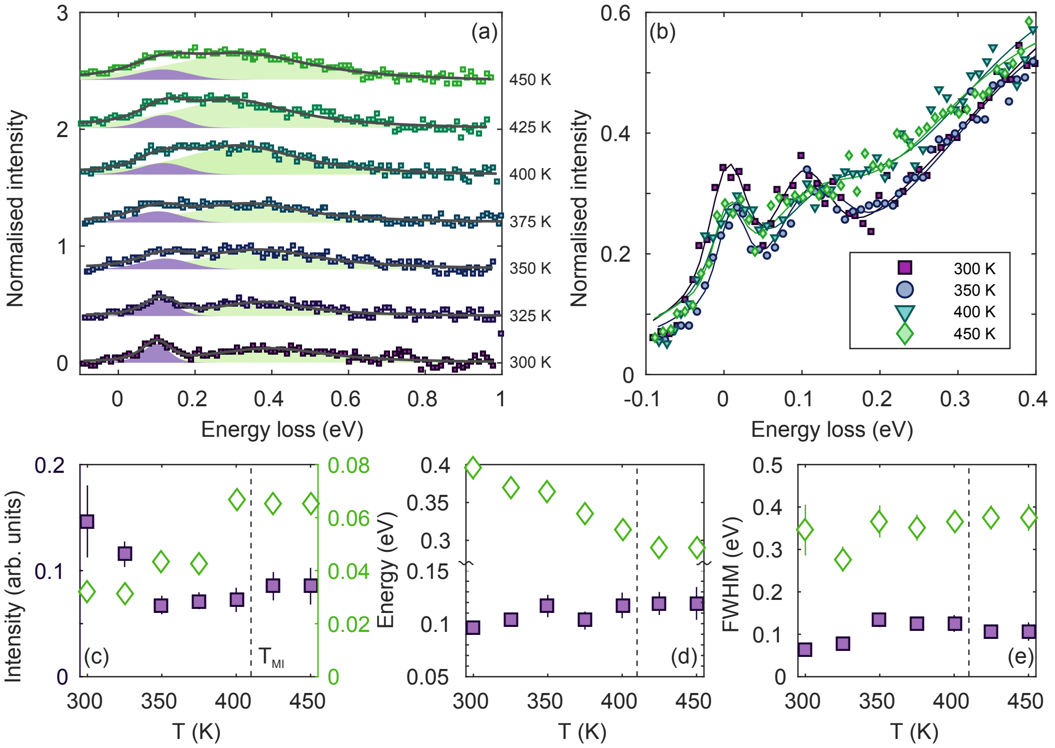

Figure 4.10: Analysis of RIXS spectra collected at Y. (a): Spectra with elastic line and $d-d$ contributions subtracted. Added are the best fit to the data (black solid line), and relative components of the magnon peak (purple) and particle-hole continuum (green). (b): Spectra normalised to intensity of $d-d$ excitations at 1 eV. Fitted peak intensity (c), energy (d) and FWHM (e) of the two components as a function of temperature. Dashed lines indicate the metal-insulator transition at 410 K.

Normally magnetic interactions in materials are defined in terms of one of two limits. In the local moment (Heisenberg) limit, the spin fluctuations – and electrons – are local in real space. At some temperature T (Fig. 4.11b), the orientation of the magnetic moments varies, but their magnitude remains fixed at the $T=0$ value. Consequently only the transverse component of the local spin density fluctuation (LSF) is important. This gives rise to collective spin wave excitations and is generally applicable for magnetic insulators (Fig. 4.11d).

At the other extreme (itinerant or Stoner limit), the electrons and spin fluctuations are extended in real space. Thermodynamic properties of the system are governed by electron-hole pair interactions which have some collective nature. At some temperature T, the orientation of the magnetic moments remains fixed, but their magnitude is reduced from the $T=0$ value (Fig. 4.11c). In this limit, the longitudinal components of the LSF or the temperature variation of the magnitude of LSF are important. The spin-fluctuation model is an intermediate between the Heisenberg and itinerant limits, whereby both the transverse and longitudinal components are important. For $NaOsO_3$, it is proposed that there is a continuous progression from the Heisenberg limit towards the itinerant limit through the MIT.

At 300 K, $NaOsO_3$ is weakly insulating (charge gap ~80 meV) and well-defined collective magnetic excitations (spin waves in the Heisenberg picture) can be observed with a moment

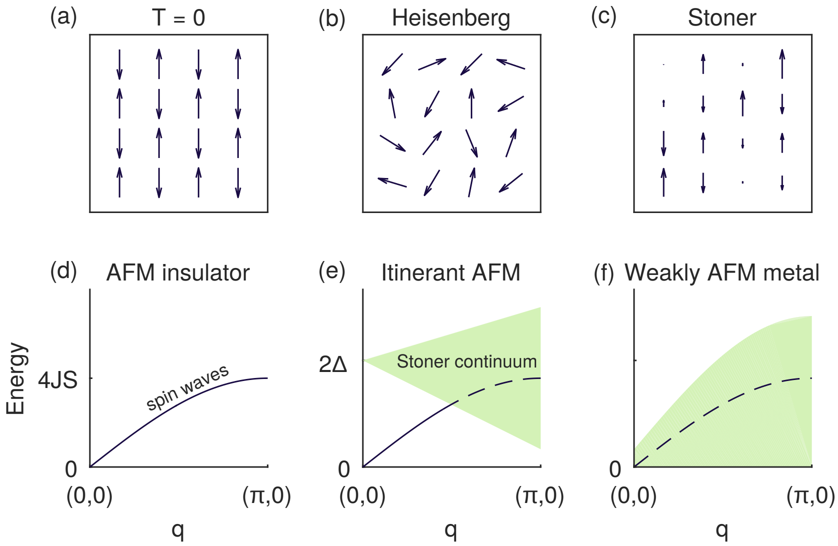

Figure 4.11: Top panels: Schematic of the orientation of antiferromagnetically (AFM) interacting magnetic moments on a square lattice for $T = 0$, and finite temperatures in the Heisenberg or Stoner limits. Bottom panels: Excitation spectra in the Heisenberg limit, for an itinerant AFM (with insulating gap 2Δ), and for a metal with weak AFM correlations. Dashed lines indicate damped excitations.

magnitude of 1 μ_B. Due to the strong Os–O hybridisation, there is a degree of itinerant character which leads to weak scattering from intra-band particle-hole excitations. This is partially the origin for the observed peak at 0.3–0.4 eV. These observations lead to the conclusion that the system is close to the local moment limit, with transverse spin fluctuations dominating.

As the temperature increases, the charge gap continues to close. The system becomes more itinerant, and the transverse fluctuations become more damped due to scattering from the emergent electron-hole (Stoner) continuum (Fig. 4.11e). This effect is largest for larger q as there are a greater number of available states for the magnon to decay into. Longitudinal spin fluctuations become more important, which have two main effects. The first is to effectively reduce the value of S from the ordered value. Evidence of this can be seen for Γ and $\Gamma - Y$, where a weak reduction in the energy of the magnon peak can be observed as a function of increasing temperature (below T_N). This agrees with theoretical calculations by Kim *et al.* [143], which predict a reduction of the magnetic moment from 0.98 μ_B to 0.88 μ_B when going from 300 K to 450 K. The second effect is that two-magnon excitations ($\Delta S = 0{,}2$) become more prominent in the excitation spectra, since the two-magnon scattering cross-section is directly proportional to the longitudinal component of the spin-spin correlation function, $S^{zz}(\mathbf{Q}, E)$. This can be seen through the progressive increase in spectral weight around 0.2 eV energy loss.

Above T_N, NaOsO$_3$ is in the metallic paramagnetic phase. Short-ranged magnetic correlations persist, which gives rise to heavily damped collective paramagnon modes, combined with scattering from an electron-hole continuum. This is consistent with behaviour in the itinerant limit (Fig. 4.11f). Similarities of the behaviour at high temperature can be drawn with neutron scattering[5] measurements on the pnictides [144].

One complication is that RIXS is sensitive to both spin and charge scattering, and it is frequently difficult to disentangle the two components. In particular for $NaOsO_3$, there are issues with resolving the separate contributions of the particle-hole continuum and spin fluctuations, just as for $Cd_2Os_2O_7$. Ideally one would use polarisation analysis of the scattered beam to separate the spin and charge components, however the limited studies of polarisation analysis within RIXS thus far [145, 146] report a factor of 10–100 times less flux. Consequently this shall have to remain a long-term goal.

4.4 Summary and outlook

The magnetic and electronic correlations in $NaOsO_3$ have been probed by resonant inelastic X-ray scattering through the metal-insulator transition. The electronic excitations are consistent with a weak coupling scenario, in which spin-orbit coupling acts as a perturbation to the electronic Hamiltonian, and is similar to that observed for $Cd_2Os_2O_7$.

As a general point, the RIXS spectra of the d^1, d^2, d^3 osmates appear to show a progression from the strong spin-orbit coupling limit (for the d^1 Ba_2LiOsO_6), through to the d^3 osmates which can be adequately described within a weak spin-orbit coupling scenario. In Ba_2LiOsO_6, a sharp, well defined $j_{\text{eff}} = \frac{1}{2} \rightarrow j_{\text{eff}} = \frac{3}{2}$ excitation can be observed [147], which is at noticeably higher energy and broader for Pb_2CaOsO_6. Such behaviour occurs despite a similar local chemical environment, which further demonstrates that the effective magnitude of spin-orbit coupling is dependent on the valence state of the metal cation. This has important ramifications for the electronic and magnetic interactions within 5d TMOs in general.

Well-defined spin excitations were observed at 300 K in $NaOsO_3$, which exhibit an anisotropic gap on the same order as the magnon bandwidth. The magnon dispersion is well described by a minimal anisotropic nearest-neighbour Hamiltonian with a magnetic moment reduced from the nominal spin-only value of 1.5 μ_B. The source of this anisotropy is likely to be a combination of single-ion, anisotropic exchange, and Dzyaloshinskii-Moriya contributions, however it was not possible to disentangle the relative contributions of these interactions within the experimental energy resolution.

Through the MIT the spin excitations show evidence of a continuous progression from localised to itinerant behaviour. Softening of the magnon peak with increasing temperature suggests a reduction of the ordered magnetic moment due to longitudinal spin fluctuations, which is consistent with a spin-fluctuation model for $NaOsO_3$. The presence of longitudinal spin fluctuations, along with a possible Higgs mode in the RIXS spectra, may be indicative of a proximity to a quantum phase transition. Finally Kim *et al.* [143] propose that $NaOsO_3$ is not an example of

---

[5] In $NaOsO_3$, the magnetic propagation vector $\mathbf{q} = 0$, whereas $\mathbf{q} = (\pi, \pi)$ for the pnictides. Due to kinematic constraints, Fe L-edge RIXS on the pnictides can only access the region of reciprocal space around (0,0), whereas neutron scattering can only access the region around (π, π).

a Slater insulator, but instead undergoes a “spin-fluctuation induced Lifshitz MIT”. Consequently it may be possible to suppress T_N by applying pressure and eventually go through the possible quantum critical point.

Summary of contributions

The RIXS measurements were carried out by the author in collaboration with Stuart Calder and Andy Christianson from Oak Ridge National Laboratory, and Christian Donnerer and Davide Pincini from UCL. All analysis and interpretation of the data was performed by the author.

Chapter 5

Magnetic critical scattering measurements on Sr_2IrO_4 and $Sr_3Ir_2O_7$

The perovskite iridates Sr_2IrO_4 and $Sr_3Ir_2O_7$ manifest as examples of materials wherein strong spin-orbit coupling plays a leading role for the electronic and magnetic behaviour. The magnetic ground state in these $j_{\text{eff}} = \frac{1}{2}$ systems is governed by the subtle interplay between the local crystal field environment, spin orbit coupling, and the ratio J_H/U. X-ray magnetic critical scattering was used to probe the spin and lattice dimensionality of the magnetic interactions in Sr_2IrO_4 and $Sr_3Ir_2O_7$. In $Sr_3Ir_2O_7$ the observed behaviour is broadly consistent with 3D Heisenberg interactions, as expected for a bilayer material with significant interlayer correlations previously demonstrated by resonant inelastic X-ray scattering (RIXS). Meanwhile in Sr_2IrO_4 the scattering can be successfully described by a two-dimensional model with appreciable easy-plane anisotropy. The presence of easy-plane anisotropy explains a previously overlooked spin gap present in high-resolution RIXS data, and quantitatively agrees with a number of theoretical predictions, including that presented within the seminal work by Jackeli and Khaliullin [25].

Thus far the discussion has been restricted to osmates (d^3, $S = \frac{3}{2}$ systems), which undergo metal-insulator transitions strongly linked to the onset of magnetic order. From now on the focus shall be on materials which exhibit broadly Mott-insulating behaviour, the perovskite iridates Sr_2IrO_4 and $Sr_3Ir_2O_7$. The term 'broadly' has been used since spin-orbit coupling plays a leading role in the formation of the $j_{\text{eff}} = \frac{1}{2}$ ground state, with insulating behaviour resulting from on-site Coulomb repulsion U within this band. For these reason they are frequently referred to in the literature as 'spin-orbit Mott insulators'. Furthermore there is some evidence of Slater-like phenomena for Sr_2IrO_4 [148–152], and polaronic behaviour for $Sr_3Ir_2O_7$ [153], which means that these materials lie some distance away from the conventional Mott-Heisenberg paradigm.

As discussed by Jackeli and Khaliullin [25], the magnetic exchange parameters in the $j_{\mathrm{eff}} = \frac{1}{2}$ ground state are parameterised by three quantities. The first of these is the ratio of Hund's coupling to the on-site Coulomb repulsion: $\eta = J_{\mathrm{H}}/U$. The second is the *effective* distortion away from the ideal cubic $j_{\mathrm{eff}} = \frac{1}{2}$ state, θ. In the case of weak tetragonal distortion: $\tan(2\theta) = 2\sqrt{2}\lambda/(\lambda - 2\Delta)$, where λ is the many-electron spin-orbit coupling parameter, and Δ reflects the tetragonal crystal field splitting. The final parameter is the rotation angle α of the IrO_6 octahedra within the basal plane.

The dimensionality of magnetic interactions – and hence the magnetic ground state – can be tuned by tuning the effective distortion θ and octahedral rotation within the basal plane. Increasing θ beyond some critical value θ_c induces a spin-flop transition which aligns the $S = \frac{1}{2}$ isospins collinearly along the z-axis. This partly[1] explains the difference in magnetic structure for Sr_2IrO_4 compared to $Sr_3Ir_2O_7$: in Sr_2IrO_4 the magnetic moments lie in the ab-plane, whereas for $Sr_3Ir_2O_7$ the magnetic moments are collinear along the c-axis.

Furthermore Jackeli and Khaliullin hypothesised that the dominant part of the Hamiltonian for Sr_2IrO_4 could be given by:

$$\mathcal{H} = \sum_{ij} \tilde{J}\,\tilde{\mathbf{S}}_i \cdot \tilde{\mathbf{S}}_j - \Gamma_1 \tilde{S}_i^z \tilde{S}_j^z \pm \Gamma_2 \left(\tilde{S}_i^x \tilde{S}_j^y - \tilde{S}_i^y \tilde{S}_j^y \right), \tag{5.1}$$

where the first term reflects effective isotropic exchange, with the second and third terms describing anisotropic exchange. If Γ_1 is positive, then the system exhibits easy-plane anisotropy and the spins lie in the basal plane. The presence of anisotropic exchange means that any spin wave excitations will be gapped; this Hamiltonian predicts the existence of an out-of-plane spin gap with approximate magnitude $\omega_0 \sim \left[\tilde{J}\Gamma_1\right]^{1/2}$.

Given the difference in the magnetic ground state for Sr_2IrO_4 and $Sr_3Ir_2O_7$, one could predict that there would be a corresponding difference in the spin or lattice dimensionality of the magnetic interactions. Normally one attempts to determine the dimensionality of a material by fitting the magnetisation below the critical temperature T_{c} to a power law $M \sim t^{\beta}$, where $t = (T - T_{\mathrm{c}})/T_{\mathrm{c}}$. The obtained value of the critical exponent β can then be compared to the theoretical value for a particular universality class. For a magnetic system these universality classes are governed by the spatial dimensions and spin degrees of freedom. A number of thermodynamic parameters, including the susceptibility, correlation length, and magnetic specific heat, exhibit similar behaviour – with their own critical exponents – in the vicinity of the critical point.

An important point is that the power law dependence is strictly speaking only exact precisely at $T = T_{\mathrm{c}}$; away from T_{c} it is an approximation, albeit rather a good one if t is not too large. Consequently in order to accurately and precisely determine the critical exponents – and corresponding universality class – for a given material, one needs to perform detailed measurements

---

[1] The collinear magnetic moments in $Sr_3Ir_2O_7$ are stabilised as a result of intra-bilayer interactions, which are absent in Sr_2IrO_4.

in the vicinity of T_c. For X-ray or neutron scattering measurements this is given the umbrella term *critical scattering*.

5.1 Critical scattering theory

A brief introduction to critical scattering theory is given here. The reader is referred to Collins [154] for a more detailed discussion.

Consider an antiferromagnet[2] which undergoes a continuous magnetic phase transition at $T = T_N$. At $T = 0$, the system is fully ordered. As temperature increases the spins begin to fluctuate about their mean positions. Near the critical point there are fluctuating microclusters of both the ordered magnetic and paramagnetic phases with mean size ξ, where ξ is known as the correlation length. Furthermore the microclusters have a finite response time $\tau \sim \xi^z$, where z is known as the dynamical critical exponent. As the critical point is reached, both ξ and τ increase dramatically, to the extent that at $T = T_N$, both quantities diverge to infinity: $\xi \sim |t|^{-\nu}$, $\tau \sim |t|^{-z\nu}$. The correlation between the fluctuations of these microclusters can be described in terms of a correlation function $C^{\alpha\beta}$:

$$C^{\alpha\beta}(\mathbf{R}) = \langle \mathbf{S}_i^\alpha \mathbf{S}_j^\beta \rangle - \langle \mathbf{S}_i^\alpha \rangle \langle \mathbf{S}_j^\beta \rangle \tag{5.2}$$

$$= (\mathbf{S}_i^\alpha - \langle \mathbf{S}_i^\alpha \rangle) \left(\mathbf{S}_j^\beta - \langle \mathbf{S}_j^\beta \rangle \right), \tag{5.3}$$

where α and β index the two phases. In magnetic critical scattering one probes the correlation function in reciprocal space [154], so the Fourier transform of the real space correlation function $C^{\alpha\beta}$ is defined as:

$$\hat{C}^{\alpha\beta}(\mathbf{q}, h) = \sum_{\mathbf{R}} e^{i\mathbf{q}\cdot\mathbf{R}} C^{\alpha\beta}(\mathbf{R}) \tag{5.4}$$

$$= \sum_{\mathbf{R}} \left[\langle \mathbf{S_0} \cdot \mathbf{S_R} \rangle - \langle \mathbf{S_0} \rangle \langle \mathbf{S_R} \rangle \right], \tag{5.5}$$

Defining spin variables $\mathbf{S_q}$ as the Fourier transform of $\mathbf{S_R}$, the correlation function reduces to

$$\hat{C}^{\alpha\beta}(\mathbf{q}, h) = \int \langle \mathbf{S_{q'}} \cdot \mathbf{S_q} \rangle \, d\mathbf{q}'.$$

In the zero-field limit this equality can be simplified and expressed in terms of a scaling function, $\hat{f}$:

$$\hat{C}^{\alpha\beta}(\mathbf{q}) = |q|^{\eta-2} \hat{f}(|q|\xi),$$

where η is a critical exponent defined by this equation, and ξ is the correlation length. The scaling function $\hat{f}$ is typically a complicated quantity, however a useful approximation by Ornstein and Zernike [155] sets η equal to zero, an approximation which is not too drastic in three dimensions.[3] Away from the critical point, the generalized form for the correlation function then

---

[2] The following discussion is equally valid for ferromagnets.

[3] Note that different magnetic models have different values for η, and consequently a slightly different shape of the correlation function.

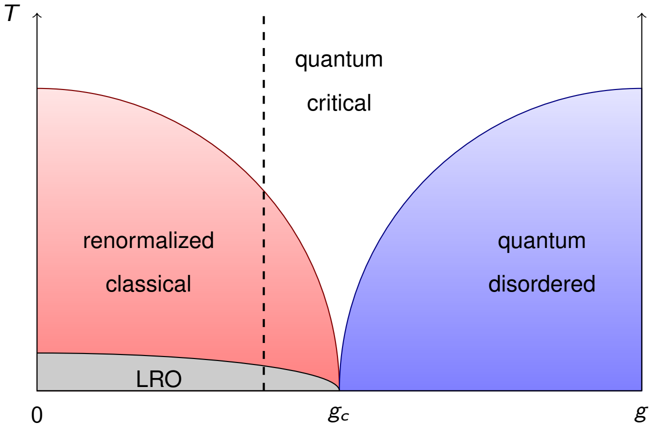

Figure 5.1: Schematic phase diagram of the quantum non-linear sigma model as a function of temperature T and coupling strength g. The renormalized classical phase exhibits Néel long range order (LRO) at $T = 0$. The dashed line represents the 2DQHAFSL.

becomes:

$$\hat{C}^{\alpha\beta}(\mathbf{q}) \sim \frac{1}{\kappa^2 + q^2},$$

or in other words, a Lorentzian function with $\kappa^{-1} = \xi$. More sophisticated expressions [156, 157] for $\hat{C}^{\alpha\beta}(\mathbf{q})$ allow for a non-zero value of η by substituting $\kappa^2 + q^2$ by $(\kappa^2 + \psi q^2)^{1-\eta/2}$, but this is a small correction which is very difficult to resolve experimentally. The physical significance of this is that the critical fluctuations are expected to exhibit a (near) Lorentzian dependence as a function of $\mathbf{q}$, and the half-width at half maximum (HWHM) corresponds to the correlation length ξ. Furthermore for $T > T_\mathrm{c}$, the amplitude of the critical fluctuations is directly proportional to the susceptibility χ.

Motivation

Magnetic critical scattering has been shown to be particularly useful when looking at 2D materials. Mermin and Wagner [158] hypothesised that “at any non-zero temperature, a one- or two-dimensional *isotropic* spin-S Heisenberg model with finite-range exchange interaction can be neither ferromagnetic nor antiferromagnetic”. This concept was found to apply to any system with continuous symmetry. The generalised statement of the Mermin-Wagner theorem states any isotropic system with fewer than three spatial dimensions does not exhibit long-ranged order. Experimental manifestations of a 2D Heisenberg system do however typically have a non-zero magnetic ordering temperature, since real materials are three-dimensional and exhibit some degree of inter-plane coupling or anisotropy.

5.2 2D Heisenberg antiferromagnet on a square lattice (2DQHAFSL)

The 2D Heisenberg antiferromagnet on a square lattice (2DQHAFSL) is one of the simplest, yet most intriguing model systems. It is defined by the Hamiltonian

$$\mathcal{H} = J \sum_{i<j} \mathbf{S}_i \cdot \mathbf{S}_j, \tag{5.6}$$

where the sum is over nearest neighbours. The realization by Chakravarty, Halperin and Nelson (CHN) that the long-wavelength, low-temperature behaviour of the 2DQHAFSL could be mapped onto a (2+1)-dimensional quantum non-linear sigma model is a celebrated piece of theoretical work [159]. The quantum non-linear sigma model exhibits long-ranged order at $T = 0$ provided that the coupling

$$g = \frac{\hbar c \sqrt{2\pi}}{k_B \rho_s a},$$

which expresses the strength of the quantum fluctuations [160], satisfies $g < g_c$. Indeed for the 2DQHAFSL $g/g_c = [1 + Z_\chi Z_c/2]^{-1} = 0.77$, where Z_χ and Z_c are renormalisation parameters. Furthermore for $T > 0$, the correlation length and spin susceptibility could be expressed in terms of a purely classical model, however with the spin-wave stiffness and spin-wave velocity renormalized by quantum fluctuations. This is described as the 'renormalized classical' regime in the literature (and the phase diagram in Fig. 5.1) for this reason. The original work considered a one-loop renormalization group method in the theoretical determination of the structure factor and correlation length; there have been a number of extensions to the model including up to three-loop corrections [161, 162] and prevention of cut-off effects in the quantum Heisenberg model [163]. The cut-off corrections are somewhat difficult to evaluate analytically, thus the model that shall be used for the remainder of this thesis to describe this CHN-type model is the three-loop model given by Hasenfratz and Niedermayer [161], henceforth referred to as CHN-HN. In this model the correlation length ξ^{3l}_{CHN} can be expressed as:

$$\xi^{3l}_{\text{CHN-HN}} = \frac{e}{8} \frac{\hbar c}{2\pi\rho_s} e^{2\pi\rho_s/T} \left[1 - \frac{1}{2}\frac{T}{2\pi\rho_s} + \mathcal{O}\left(\frac{T}{2\pi\rho_s}\right)^2 \right], \tag{5.7}$$

where e is the base of the natural logarithm, $\rho_s = Z_\rho S^2 J = 0.181J$ is the spin-wave stiffness, $c = 2\sqrt{2}\, Z_c S J a = 1.18\sqrt{2} J a$ is the spin-wave velocity, and a is the lattice constant. Strictly speaking the spin-wave stiffness ρ_s and spin-wave velocity c are temperature dependent quantities, the latter of which could be extracted experimentally from the magnon dispersion in the long-wavelength limit. The amplitude of the instantaneous structure factor S_0 can be similarly derived as [164, 165]

$$S_0 \propto N_0^2 \xi^2 \frac{T^2}{(2\pi\rho_s)^2}, \tag{5.8}$$

where $N_0 = 0.307$ is the zero-temperature staggered magnetization, which is reduced to around 61% of its classical value as a result of quantum fluctuations. There are two things to take away from this analysis: firstly the correlation length follows an $\exp(1/T)$ dependence to leading order, and secondly the ratio S_0/ξ^2 should scale as T^2.

Quantum critical regime

The 2DQHAFSL lies close to a quantum critical point at $g = g_c$, and thus it would be expected [162] that there would be evidence of a crossover from the 'renormalized classical' regime to a 'quantum critical' (QC) regime at some finite temperature T. This QC region of the phase diagram as shown in Fig. 5.1 is characterised by a J/T scaling of the correlation length:

$$\xi = \hbar c \left[T\Theta \left(1 + \frac{0.2373}{N} \right) \right]^{-1}, \tag{5.9}$$

where $\Theta = 2\ln\left(\frac{\sqrt{5}+1}{2}\right)$ and $N = 3$ from the mapping to the (2+1)-dimensional quantum non-linear sigma model. Furthermore in the long-wavelength limit ($k \to 0$) the structure factor S_0 can be written as:

$$S_0 = \frac{N_0^2}{\rho_s} \left(\frac{N k_B T}{2\pi\rho_s} \right)^{\eta} \frac{\sqrt{5}}{2} \xi \left(1 - \frac{0.1925}{N} \right), \tag{5.10}$$

where the exponent $\eta = 8/3\pi^2 N$, and ξ is the experimental correlation length. Note that these expressions are valid precisely at the critical point $g = g_c$, and further corrections are likely to be required away from this.

Quantum disordered phase

The quantum disordered phase exists for $g > g_c$, and its behaviour is dictated by a gap between the (non-magnetic) global singlet ground state and the lowest (magnetic) triplet excited states at $T = 0$. In the $N = \infty$ limit, the magnitude of this zero temperature gap is given by $\Delta = 4\pi \left(g_c^{-1} - g^{-1} \right)$, and scales with $\Delta \sim (g - g_c)^{\nu}$ as a function of coupling strength [162]. Consequently the inverse correlation length can be expressed in the form

$$\xi^{-1}(\Delta, T) = \frac{2k_B T}{\hbar c} \operatorname{arcsinh}\left(\frac{e^{\Delta/2T}}{2} \right), \tag{5.11}$$

which in the limit of $\Delta \gg T$ implies a correlation length of the order of Δ^{-1}, that is, independent of temperature.

However the mapping of the 2DQHAFSL to the quantum non-linear sigma model is only valid for $k_B T \ll \rho_s$; there is some question of the validity of this mapping in the high-temperature regime. In particular, there are question marks over the predicted crossover between the RC and QC regimes. Chubukov *et al.* [162] predict a crossover for $T \sim 0.4J$, however the expression used for the quantum critical regime applies in the limit of $g = g_c$. Elstner and colleagues [166] predict some crossover between $0.45J \leq T \leq 0.65J$ for $S = \frac{1}{2}$, based on considerations of the temperature dependence of the spin-wave mass.

It should be noted that there are a number of alternative models which attempt to describe the temperature dependence of the properties for the 2DQHAFSL. These include fitting to quantum Monte Carlo (QMC) [167, 168] simulations, semi-classical approaches (PQSCHA) [169, 170], or series expansions [171]. Each of these models is suited for a particular temperature range T/J or value of S, and there is at present no unified model for the 2DQHAFSL.

Materials exhibiting almost 2DQHAFSL behaviour

As discussed earlier, there are no physical manifestations of a pure 2DQHAFSL, as a consequence of anisotropies, disorder, dipolar interactions etc. which are present in any real system. Most studies looking for 2DQHAFSL-like behaviour focus on $S = \frac{1}{2}$ systems, since these systems offer the greatest departure from classical behaviour and hence better approximate to the quantum non-sigma model limit.

One prototypical example is La_2CuO_4, a perovskite material comprising of 2D layers of CuO_6 octahedra, with Cu in the +2 oxidation state. The electronic configuration of Cu^{2+} is $3d^9$, which leaves a hole in the $d_{x^2-y^2}$ orbital and hence a $S = \frac{1}{2}$ ground state. Doping this material with additional oxygen leads to a high-temperature superconductor, similarly to $YBa_2Cu_3O_{7-\delta}$. Inelastic neutron scattering [172, 173] has revealed that the nearest-neighbour interactions in this material are antiferromagnetic, with significant next-nearest, third-nearest neighbour, and four-spin ring exchange contributions. Above T_N, the correlation length was found to agree very well with the CHN prediction [174, 175], implying that La_2CuO_4 was an example of a 2DQHAFSL.

However one issue with studying the precise temperature dependence of the correlation length (and related thermodynamic parameters) for La_2CuO_4 is the large value of J ($J \sim 1500$ K). Typically these types of materials are studied using neutron scattering, and it is difficult to measure at such high temperatures using this method. This thus limits the range of $\xi(T/J)$ that can be measured. Other examples of 2D Heisenberg antiferromagnets on a square lattice include $Cu(COOH)_2 \cdot 4\,H_2O$ [164, 176–179] (plus its deuterated equivalent, useful for INS measurements) and $Sr_2CuO_2Cl_2$ [180–184]. These materials have much lower values of J and as such have proved more accessible for the study of a potential crossover between the RC and QC regimes and fitting to theoretical models. Additionally these materials exhibit much lower inter-layer anisotropy, thus providing a much closer realisation to a true 2DQHAFSL.

A common theme in all of these materials is that the spin-orbit coupling is a weak perturbation to the electronic and magnetic properties. In $4d$ and $5d$ transition metal oxides, spin-orbit coupling is expected to play a much stronger role. Examples of this are the Ruddlesden-Popper perovskite iridate compounds Sr_2IrO_4, and $Sr_3Ir_2O_7$, where the $j_{\text{eff}} = \frac{1}{2}$ ground state is a direct result of spin-orbit coupling.

5.3 Critical scattering on Sr_2IrO_4

This section has been partly published as J. G. Vale *et al.*, Physical Review B **92**, 020406(R) (2015).

5.3.1 Introduction to physical properties

Sr_2IrO_4 is an example of a Ruddlesden-Popper perovskite[4] material, which comprises of a series of 2D Ir-O layers, interspersed with Sr^{2+} cations. The general formula for these Ruddlesden-Popper phases is $A_{n-1}A'_2B_nX_{3n+1}$, where n is an index which represents the number of layers. So in this interpretation Sr_2IrO_4 can be described as a single-layer compound, and this notation will be used throughout this thesis. Sr_2IrO_4 adopts a tetragonal crystal structure $\big(a = 5.48$ Å, $c = 25.76$ Å, structure shown in Fig. 5.2a$\big)$ with space group $I4_1/acd$, and differs[5] from the ideal $I4/mmm$ space group through a correlated rotation of the IrO_6 octahedra by 12° [188]. In this material iridium is in the 4+ oxidation state, and hence the iridium ions have five d-electrons in a low spin configuration, due to the comparatively large crystal field and extended 5d orbitals. This means that it can be initially considered as a $S = \frac{1}{2}$ system. Strictly speaking however this is incorrect, and the reasons for this shall be detailed later.

Bulk measurements by Cao *et al.* [21] indicated insulating behaviour up to 300 K (Fig. 5.2d), which was unexpected considering the reduced value of U and increased value of the kinetic energy t for 5d systems compared to 3d systems (see Table 1.1). For example, the isostructural cuprate La_2CuO_4 is a Mott insulator and the rhodate Sr_2RhO_4 is metallic at room temperature [189]. The susceptibility was also shown to be strongly anisotropic (Fig. 5.2c), with the susceptibility approximately a factor three larger in the a-direction compared to the c-direction. Furthermore the saturation magnetization revealed an effective paramagnetic moment of 0.50 μ_B per Ir atom, considerably less than the Hund's rule coupling value of 1.7 μ_B per Ir. Cao *et al.* attributed this to hybridisation between the Ir 5d and O 2p orbitals, however in reality the formation of the $j_{\text{eff}} = \frac{1}{2}$ ground state – as described in Chapter 1 – is the origin for the reduced moment.

Kim and colleagues [26] suggested that the Ir magnetic moments resulting from the $j_{\text{eff}} = \frac{1}{2}$ isospins were oriented in the *ab*-plane, based on the existence of allowed reflections at (1, 0, 4n+2) and (0, 1, 4n) positions. This was confirmed by Boseggia *et al.* using XRMS [190], and further measurements showed that the magnetic moments rigidly follow the rotation of the IrO_6 octahedra [191]. Neutron scattering measurements by [185, 186] corroborate this finding,

---

[4] Strictly speaking only the infinite layer member of this series, $SrIrO_3$, is a true perovskite as detailed in Chapter 4. The other members – including Sr_2IrO_4 and $Sr_3Ir_2O_7$ – have layered structures reminiscent of the true perovskites, which gives rise to the misnomer prevalent in the scientific literature.

[5] There is still some controversy over the correct space group, since the assignment is dependent on the positions of oxygen atoms within the crystal structure, which X-rays are not especially sensitive to. Neutron diffraction measurements (both on powders [185] and single crystals [186]) find structural reflections forbidden within $I4_1/acd$, which appear to be consistent with the lower symmetry $I4_1/a$. This is corroborated by recent second and third harmonic generation experiments [187]. Within this thesis however, the $I4_1/acd$ convention shall be used to better compare with literature.

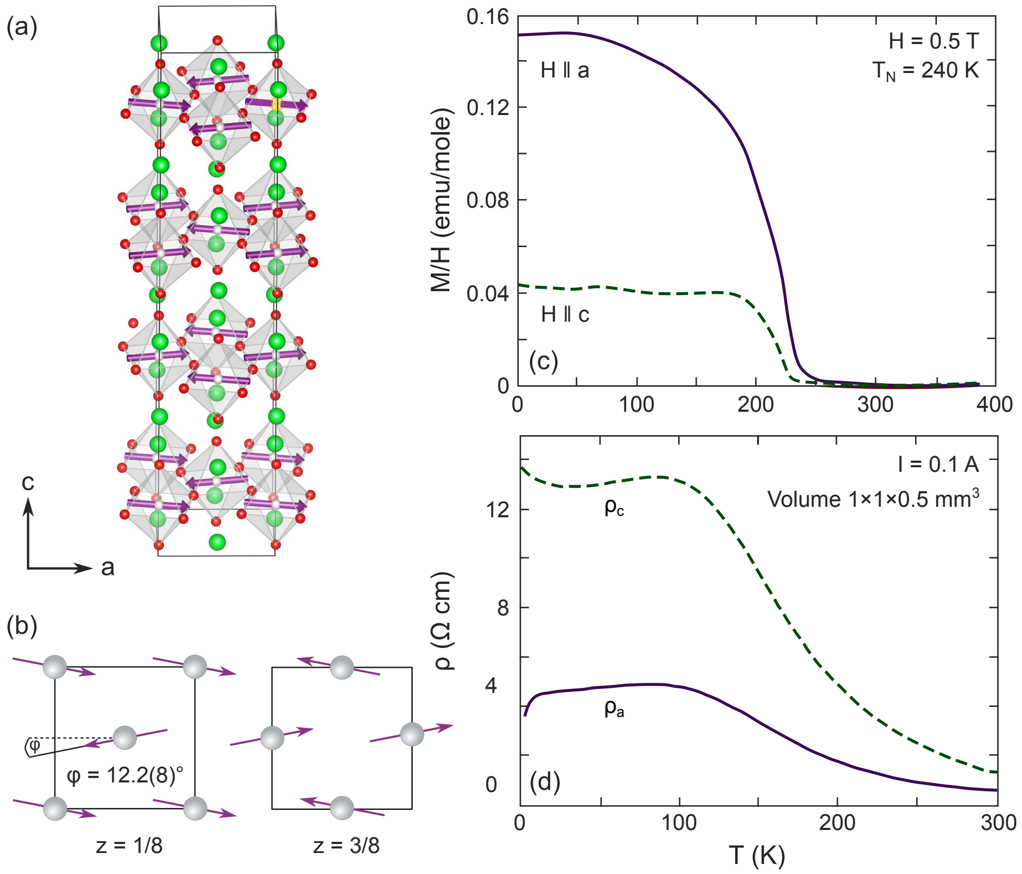

Figure 5.2: (a): Crystal structure of Sr_2IrO_4. The IrO_6 octahedra are rotated by $\pm 12^\circ$ in the *ab*-plane with respect to the ideal $I4/mmm$ structure; alternate layers have the opposite sign of rotation. The magnetic moments rigidly follow this distortion, which is highlighted in (b). (c,d): Magnetization (c) and resistivity (d) measurements by Cao *et al.* [21] on a single crystal of Sr_2IrO_4, which show significant anisotropy in the respective bulk properties.

but as previously mentioned, the observation of weak structural reflections which violate the $I4_1/acd$ space group suggest a reduction of symmetry at high temperature.

Resonant inelastic X-ray scattering measurements (RIXS) have also been performed on Sr_2IrO_4, in order to determine the magnon dispersion, and the origin of the mode at 400 meV as observed by optical spectroscopy. Jungho Kim [37] and colleagues obtained the inelastic spectra for Sr_2IrO_4 for an entire Brillouin zone close to 90 degrees with approximately 130 meV energy resolution. They fitted the experimental magnon dispersion to a $J - J' - J''$ model and obtained a value for the nearest-neighbour exchange constant J of 60 meV. This was consistent with theory predictions made by Jackeli and Khaliulin [25]. Furthermore the inelastic feature at 400 meV energy loss was found to be strongly dispersive – which indicates some propagation mechanism – and was attributed to an excitation of a hole from the $j_{\mathrm{eff}} = \frac{1}{2}$ band to the $j_{\mathrm{eff}} = \frac{3}{2}$ band, coupled with a hopping to an adjacent site. This strongly dispersive mode was dubbed a “spin-orbit exciton”, and is characteristic of the exotic electronic and magnetic behaviour observed in the iridates. Recent measurements obtained by Kim and colleagues [192]

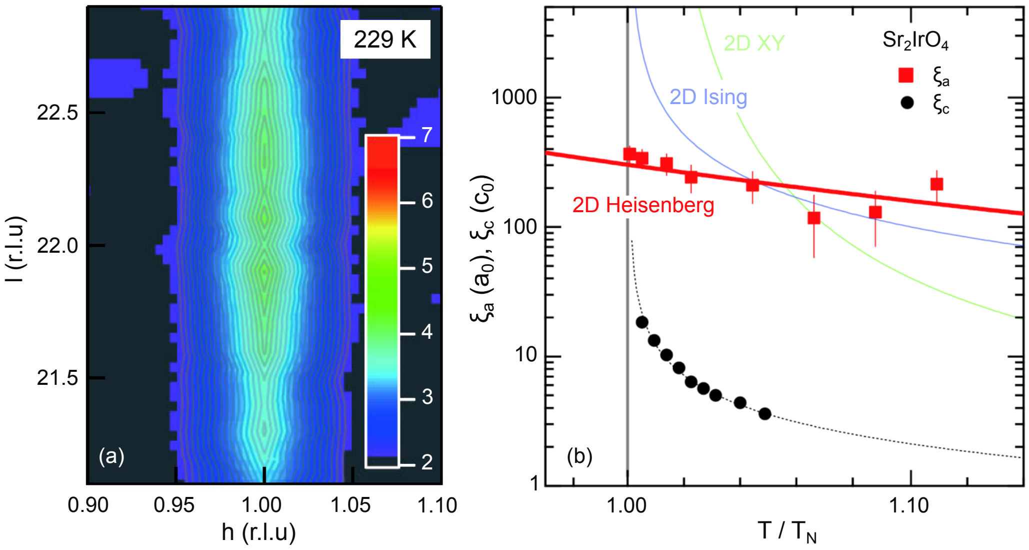

Figure 5.3: Magnetic critical scattering data previously obtained by Fujiyama *et al.* [38]. (a): Intensity map in hl-plane of (1, 0, 22) magnetic Bragg peak at 229 K. (b): In-plane (red squares) and out-of-plane (black circles) correlation length ξ_a above $T_N = 228.5(5)$ K. Overlaid are the theoretical models for the 2DHAFSQL [167] (red), 2D XY model (green), and 2D Ising model (blue). A 2D Heisenberg model with $J = 100(10)$ meV apparently seems to give the best description of the in-plane data, whilst the out-of-plane correlation length ξ_c is best described by a power law with critical exponent $\nu = 0.748$, consistent with 3D interactions.

using a significantly improved energy resolution ($\Delta E = 30$ meV) display a sharp dispersive feature, which is believed to be a quasiparticle peak reminiscent of those observed in the cuprates [193].

This is merely a selection of the literature that has been published for Sr_2IrO_4, however it highlights that Sr_2IrO_4 is not a metal, as would be predicted from trends in the electron correlation and kinetic energy alone. Spin-orbit coupling plays a significant role in the formation of an insulating state with one electron in the uppermost $j_{\text{eff}} = \frac{1}{2}$ band, and hence Sr_2IrO_4 is often referred to as a "$j_{\text{eff}} = \frac{1}{2}$ spin-orbit assisted Mott insulator".

Previous experimental results

Fujiyama *et al.* [38] measured the critical scattering from Sr_2IrO_4 and found that there was persistent intensity for the (1, 0, 22) magnetic Bragg peak up to 254 K, well above the Néel temperature $T_N = 228.5(5)$ K. The temperature dependence of the diffuse scattering (Fig. **??**) revealed a significant dichotomy between the in-plane and out-of-plane directions. Using polarization analysis they were able to conclude that the diffuse scattering was magnetic. Furthermore the in-plane correlation length could be fitted very well to a model [167] consisting of isotropic 2D Heisenberg interactions with a nearest-neighbour exchange of $J = 100(10)$ meV:

$$\xi(T) = 0.276\, a_0 e^{1.25J/k_BT}, \tag{5.12}$$

as obtained from quantum Monte Carlo (QMC) calculations. From this they concluded provided evidence that the type and magnitude of interactions in Sr_2IrO_4 were very similar to those in La_2CuO_4, in spite of the increased spin-orbit coupling and octahedral rotations present for Sr_2IrO_4.

There are however a couple of problems with their interpretation of the data. The first is that close to T_N, the intrinsic resolution of the diffractometer becomes comparable to the width of the intrinsic critical fluctuations in reciprocal space. This means that careful fitting of the data including these resolution effects is required in order to extract the true correlation length. The second is that there appears to be a numerical error in the correlation length data as plotted in the manuscript. The data which have been plotted are too large by a factor of a_0 ($a_0 = 3.9$ Å is the Ir-Ir nearest-neighbour distance) when compared to their raw data. This means that their value of the nearest-neighbour exchange parameter J is too large, which is consistent with other estimates of J that place its value between 45 and 60 meV, depending on the method used.

5.3.2 Experimental setup

Consequently critical scattering experiments were performed at beamline I16, Diamond Light Source, UK, and P09, PETRA III, DESY, Germany. These experiments exploited the large enhancement of the X-ray resonant magnetic scattering cross-section at the Ir L_3 edge. The single crystals of Sr_2IrO_4 used in this study (dimensions $2\times1\times0.05\,\mathrm{mm}^3$) were flux grown from phase-pure polycrystalline Sr_2IrO_4, using techniques described elsewhere [148], and attached to the copper sample mount of a closed-cycle refrigerator. This was in turn mounted on a six-circle diffractometer configured to operate in a vertical scattering geometry. The energy of the incident photon beam was set to 11.218 keV, just below the L_3 edge of iridium, a value found to maximise the intensity of the X-ray resonant magnetic scattering (Fig. 5.4a). The incident beam size was determined to be 200×20 μm^2 (H$\times$V). The polarization of the scattered X-rays was determined by using a Au (3, 3, 3) crystal analyser mounted on the detector arm. The temperature was measured to a precision of ±0.01 K via a thermocouple secured to the sample mount by Teflon tape. The wavevector resolution of the instrument (at FWHM), including the effects of sample mosaic, was determined by mapping Bragg peaks in reciprocal space and was found to be typically 1.7×10^{-3} and 2.0×10^{-3} Å^{-1} perpendicular and parallel to $\mathbf{Q}$ in the scattering plane respectively, and 1.3×10^{-2} Å^{-1} out of the plane (Figs. 5.4b–5.4d).

5.3.3 Order parameter

The first objective was to determine T_N and β, which was achieved by measuring the temperature dependence of the (1, 0, 24) magnetic peak intensity I_M. The results are summarized in Fig. 5.5 for both the in-plane and out-of-plane directions. As can be seen, the scattering is practically isotropic in this temperature range. A fit of the in-plane data to the simple power-law form $I_M \propto [(T_N - T)/T_N]^{2\beta}$ is shown in Fig. 5.5(a) which yields T_N = 226.8(2) K and $\beta = 0.195(4)$.

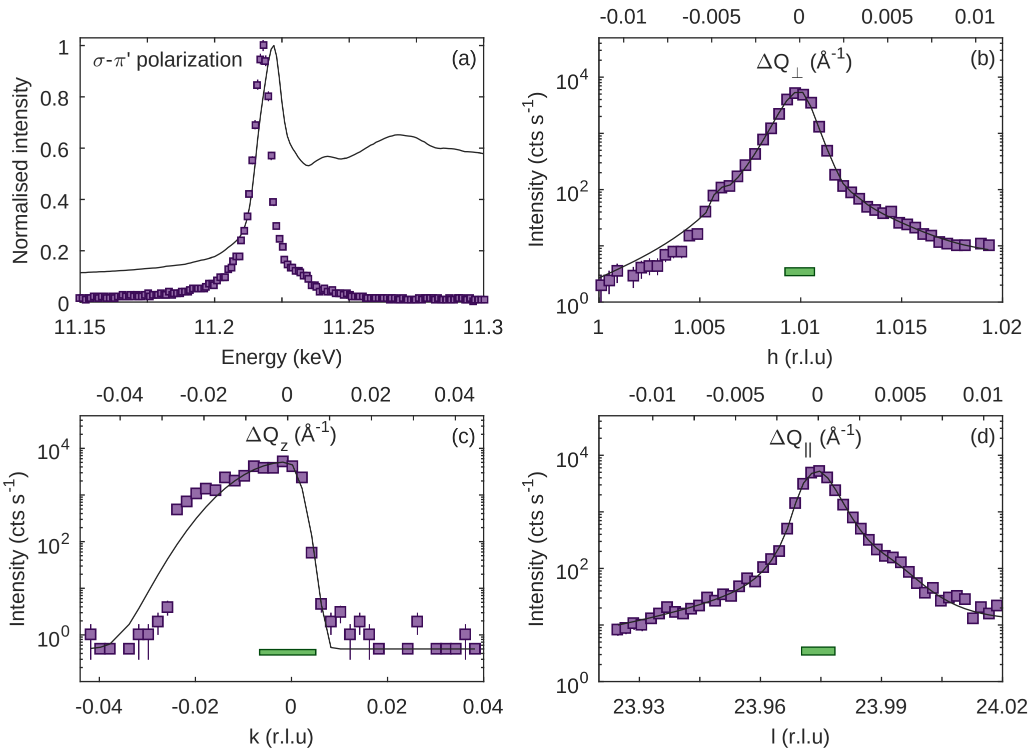

Figure 5.4: (a): Energy scan of the (1, 0, 24) magnetic Bragg peak with σ–π' polarisation (symbols). Overlaid is the total fluorescence yield (TFY) from the sample (solid line). (b)–(d): Reciprocal space scans of the (1, 0, 24) peak at 180 K, which was used to represent the resolution function. Nearby structural peaks exhibited similar behaviour. Added are the best fit (solid lines) of the data to either an asymmetric Lorentzian squared function (b,d) or an asymmetric Gaussian (c). Bars indicate the FWHM of the peak.

These values are consistent with that provided by neutron scattering measurements [185, 186] and muon spin relaxation [194]. The value of β deduced by this analysis deviates significantly from theoretical values for both 2D Ising ($\beta = 1/8$) and 3D systems ($\beta \sim 0.35$), but rather is consistent with the value for the 2D XYh_4 universality class in the strong anisotropy limit [195]. The 2D XYh_4 model shall be discussed later in more detail.

However this is not the full story. There is evidence of a secondary order parameter just above T_N, which appears to have a different critical exponent and transition temperature. This is displayed in Figure 5.6. After fitting this to a power law, one obtains $T_C = 232.3(1)$ K — which corresponds to $T_N + 5.5(2)$ K — and $\beta = 0.32(1)$. The value of the critical exponent β is more consistent with three-dimensional interactions, which implies that it is relevant for the formation of long-ranged antiferromagnetic order. When approaching T_N from above, the interlayer coupling J' causes an antiferromagnetic correlation between adjacent planes.

Yet the presence of 3D critical behaviour in the vicinity of T_N is not unprecedented for layered $S = \frac{1}{2}$ materials. A dimensionality crossover from 2D XY to 3D XY behaviour has been observed in $YBa_2Cu_3O_{7\text{-x}}$ by single crystal neutron diffraction [196] and ^{63,65}Cu NMR [197]. Pozzi *et al.* [197] suggested that the 3D XY fluctuations for $T_N \pm 5$ K result as a consequence of a weak XY anisotropy $J_{xy} \approx 1 \times 10^{-4} J$, which is two orders of magnitude weaker than the intra-

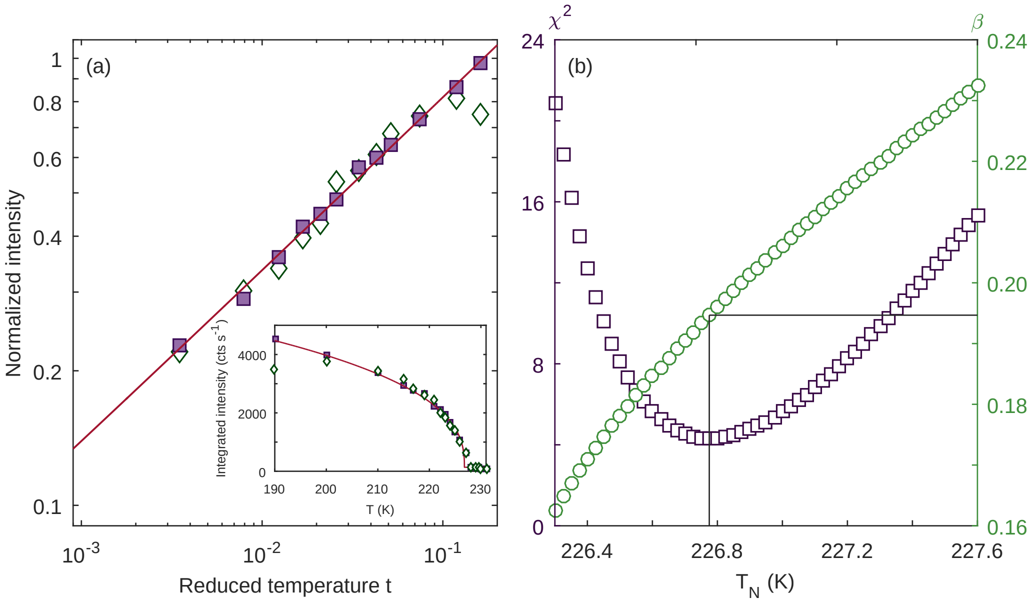

Figure 5.5: (a): Temperature dependence of $(1, 0, 24)$ magnetic Bragg peak for Sr_2IrO_4. Plotted are the integrated intensities for the in-plane (squares) and out-of-plane (diamonds) directions normalised to the in-plane scattering at 180 K. (b): Variation of χ^2 (squares) as a function of fits to $I_M \propto [(T_N - T)/T_N]^{2\beta}$ using fixed values of T_N. The minimum of the χ^2 surface occurs at $T_N = 226.8(2)$ K and $\beta = 0.195(2)$.

bilayer coupling $J' \approx 0.01\ J$. With increasing temperature, there is a continuous crossover from anisotropic to isotropic spin fluctuations on the magnetic Cu(2) site, with 2DQHAFSL behaviour above 500 K ($T_N + 85$ K).

5.3.4 Magnetic scattering above the Néel temperature

The second objective was to investigate the critical scattering above T_N. For these studies the high photon energy and relatively broad energy resolution of X-ray diffractometers ($\gtrsim 1$ eV) offer an advantage over neutrons in that they provide an accurate frequency integration to yield the instantaneous magnetic scattering function $S(\mathbf{Q})$. On the other hand the intrinsic high wavevector resolution of X-ray techniques presents a challenge in terms of following weak critical magnetic scattering to high temperatures as it broadens and weakens further. X-ray experiments to determine the magnetic critical scattering above T_N have revealed that the critical fluctuations just above T_N have two components: a sharp “central” peak, typically with a Lorentzian squared lineshape, believed to be an extrinsic feature due to the presence of defects; and a broader, weaker peak with a Lorentzian line shape arising from intrinsic critical fluctuations [154, 198, 199]. Realisation that the magnetic critical scattering above T_N can have two such components mirrors earlier results for structural phase transitions [200–202].

To summarise, above T_N, scattering in the out-of-plane direction was observed to decay rapidly with increasing temperature, and was practically unobservable at T_N + 7 K. For the in-plane direction however, the critical scattering could be followed out to T_N + 73 K. This is consistent with the previous study by Fujiyama *et al.* [38], roughly trebling the region probed

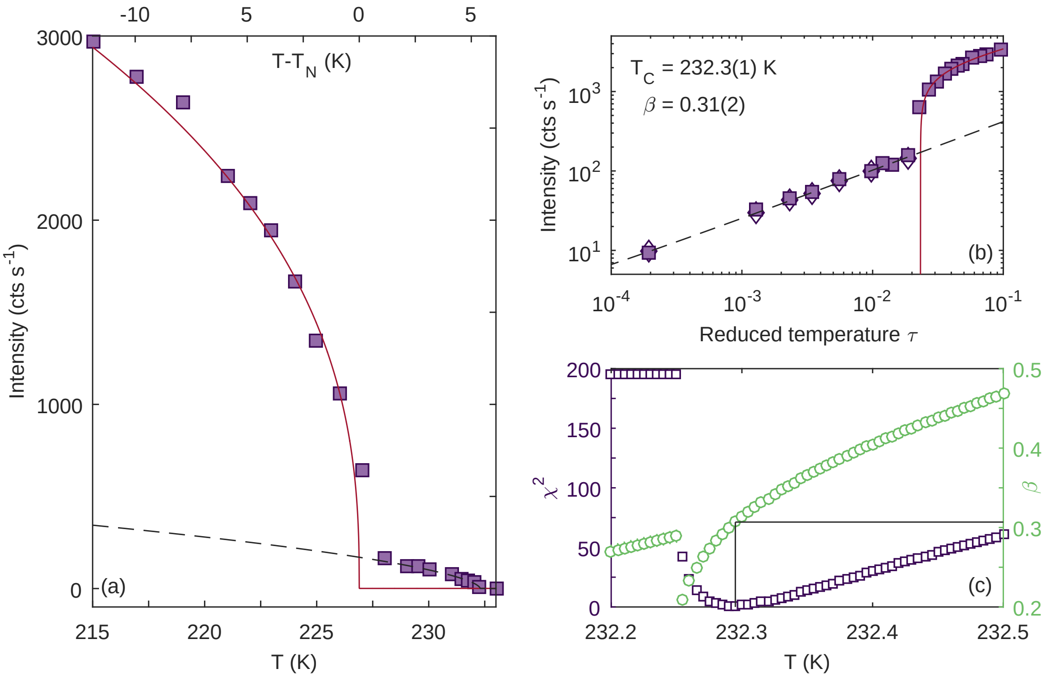

Figure 5.6: (a): Observation of two order parameters for Sr_2IrO_4 as determined from rocking curves (η scans). Red and grey curves are the primary [$T_N = 226.8(2)$ K, $\beta = 0.195(4)$] and secondary [$T_c = 232.3(1)$ K, $\beta = 0.32(1)$] order parameters respectively. (b): Same as (a), but plotted on logarithmic axes and as a function of reduced temperature $\tau = (T_c - T)/T_c$. Open diamonds are Lorentzian squared components of scattering from h-scans. (c): Variation of χ^2 as a function of T_c (squares), with corresponding values of β (circles).

above T_N, which, as shall be shown, places a much tighter constraint on the relevant form of the effective Hamiltonian.

Vicinity of critical temperature

Representative scans of the magnetic critical scattering in the vicinity of T_N are shown in Fig. 5.7. The in-plane scans show two distinct peaks. The first is a sharp peak centred at the Bragg position which weakens considerably with increasing temperature. The second is a broad weaker peak slightly offset in the h-direction, with a smaller dependence on temperature. Meanwhile the out-of-plane scans show a broad diffuse background superimposed on the Bragg peak. Careful examination of the lineshapes of these peaks (convoluted with the instrumental resolution function) found that the sharp component was best fitted to a Lorentzian squared function, whereas the broad component was best fitted to a Lorentzian. This implies that the broader component is indicative of critical fluctuations. The offset in h for the broader peak compared to the Bragg reflection may be due to some weak magnetostriction upon the formation of long-ranged order (corresponding to a change in the lattice parameter on the order of 0.003 Å). Such an observation is corroborated within laboratory powder X-ray diffraction by Bhatti and colleagues [203], who observe that the lattice parameters exhibit a discontinuity of similar magnitude at T_N.

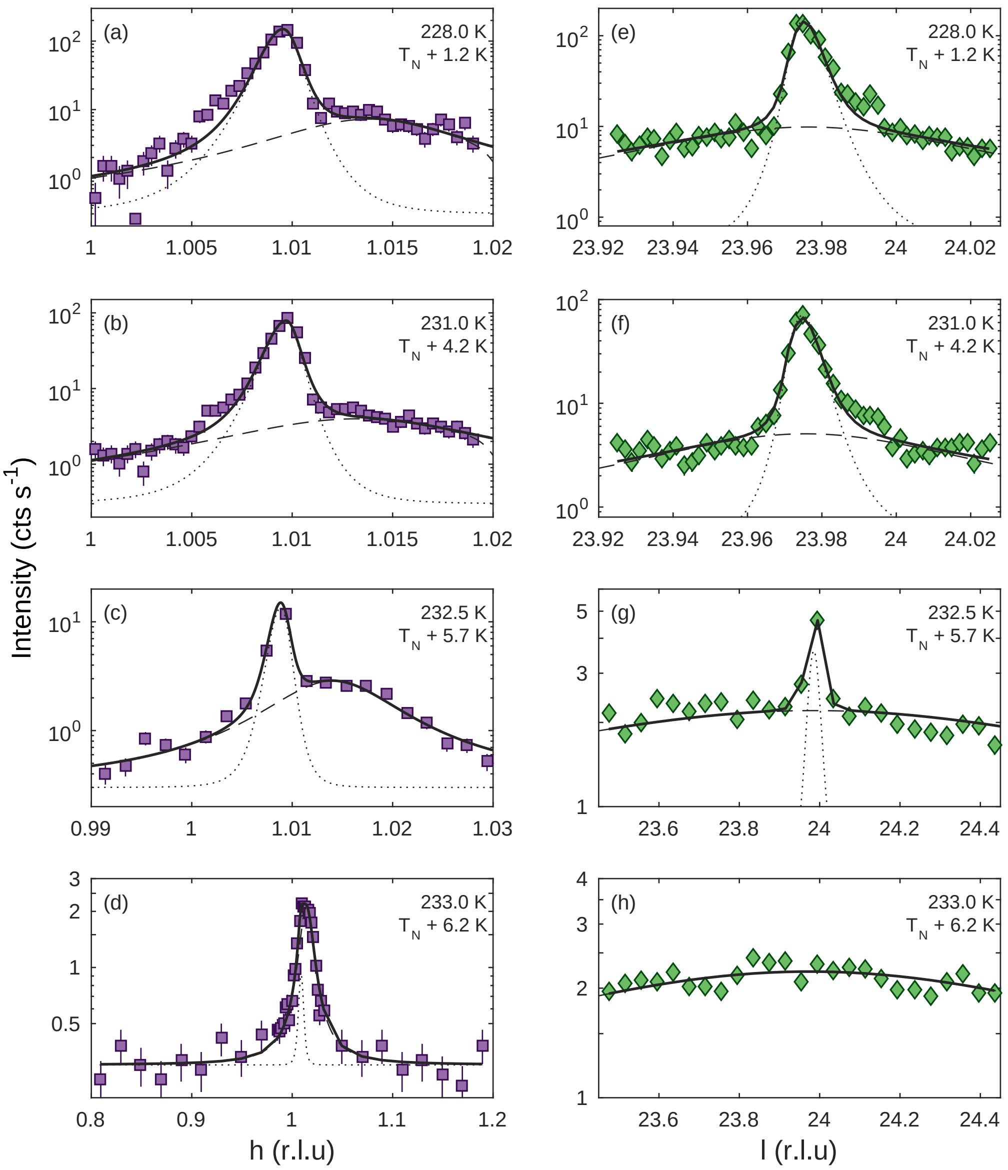

Figure 5.7: Comparison of scattering in-plane [(a)–(d), purple] and out-of-plane [(e)–(h), green], along with best fits to the data using the model described in the main text (solid line). The separate Lorentzian and Lorentzian squared components to the scattering are indicated by dashed and dotted lines respectively. A logarithmic y-axis has been used to highlight the two components.

Quantitative comparisons of the correlation length ξ – inversely proportional to the half-width at half maximum (HWHM) of the Lorentzian critical fluctuations – and the peak amplitude S_0 are displayed in Figure 5.8 as a function of temperature. Only the correlation length of the Lorentzian squared component has been plotted as it was found that the Lorentzian squared component was resolution limited.

First of all there is a clear dichotomy between the behaviour of the in-plane and out-of-plane correlation lengths, in good agreement with the previous study by Fujiyama *et al.* [38]. Above 232.2 K ($T_N + 5.4$ K), the obtained out-of-plane correlation length is sufficiently short such that

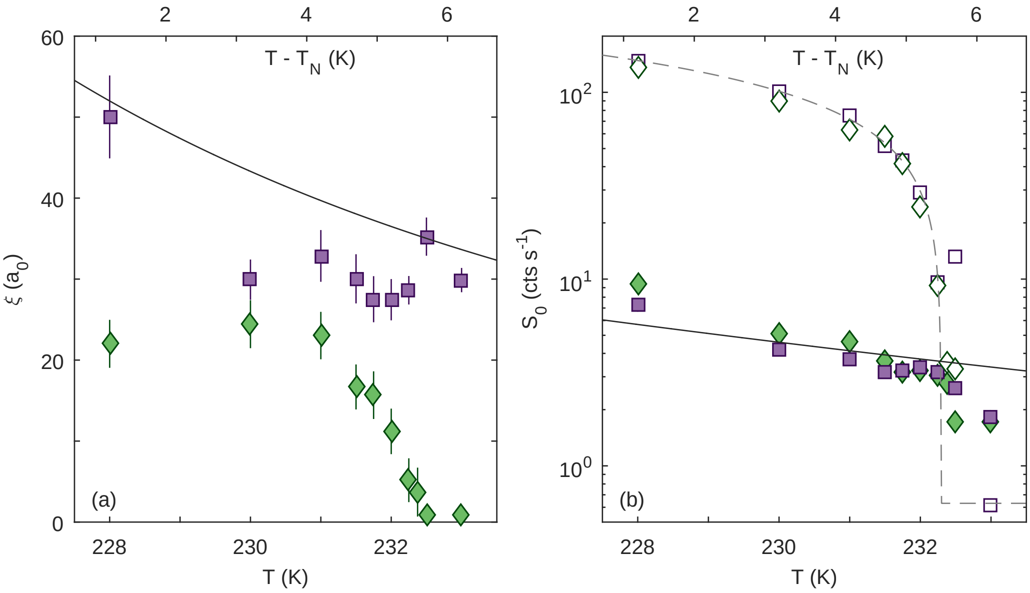

Figure 5.8: (a): Correlation length of Lorentzian component both in-plane (purple squares) and out-of-plane (green diamonds) given in terms of the Ir-Ir distance $a_0 = 3.9$ Å. (b): Amplitude of Lorentzian (filled symbols) and Lorentzian squared (open symbols) components to observed scattering. Dashed line is the same as presented in Figure 5.6. Solid line in (a) and (b) is the best fit to the 2DAH model at high temperatures as plotted in Fig. 5.13.

the interactions can be considered to be confined within in a single Ir-O layer. On the other hand, there are significant in-plane correlations $\xi_a \sim 30$ a_0 indicative of short-ranged magnetic order. Furthermore whilst the Lorentzian squared component exhibits order parameter behaviour, the Lorentzian component decreases much more slowly with increasing temperature. Again the latter is consistent with two-dimensional fluctuations in-plane.

These observations imply that there is simultaneously evidence of two- and three-dimensional behaviour between T_N and $T_N + 6$ K. The former arise from the high temperature in-plane critical fluctuations, whereas the latter are indicative of the transition to three-dimensional Néel order. One possibility is that the sample is weakly inhomogeneous and that different sample domains have slightly varying transition temperatures. Given the size of the incident X-ray beam (200×20 μm^2), then this is not unreasonable. However no obvious rounding of the phase transition can be observed, which suggests that is a minor effect.

Far from T_N

Clearly at higher temperatures, the Lorentzian squared component decays away and only the intrinsic Lorentzian critical fluctuations remain. These critical fluctuations are rather broad in reciprocal space, whilst the momentum resolution of the incident X-rays is extremely good. Consequently one only probes a very small region of momentum space at a time, and thus counting times are correspondingly long. Representative scans of the magnetic critical scattering above T_N are shown in Fig. 5.9. Counting times varied, but at higher temperatures 15 minutes were

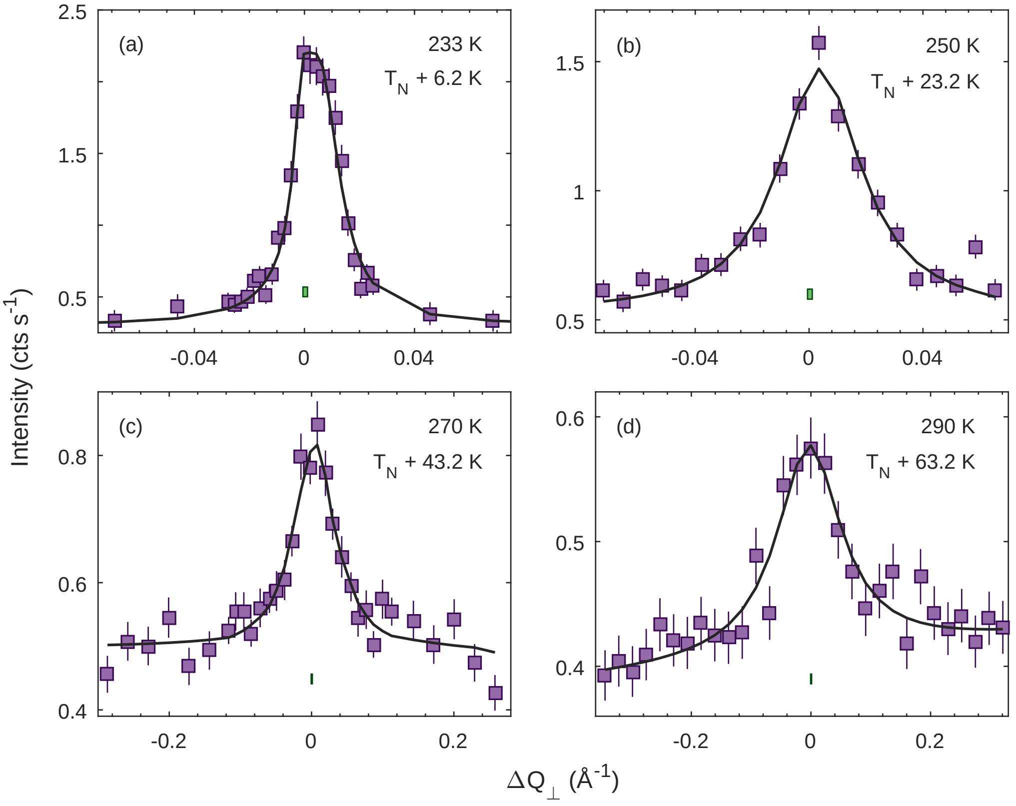

Figure 5.9: Selected in-plane scans of the (1, 0, 24) magnetic Bragg peak above T_{N}. Superimposed are the best fits to a Lorentzian convoluted with the resolution function (full width at half maximum represented by solid bars).

required per data point. As can be seen, there is a progressive weakening and broadening of the magnetic Bragg peak with increasing temperature, which is indicative of a degree of short-ranged correlations in-plane.

The critical scattering above T_{N} was fitted with several different lineshapes convoluted with the instrumental resolution function. The most satisfactory over most of the temperature range was a Lorentzian, as expected for intrinsic magnetic critical scattering. Additionally the width of the diffraction peaks (Fig. 5.10) are comparable to the previous critical scattering study (Ref. [38]). This allows a direct comparison between the two datasets, and confirms the proposition that there was a numerical error in the original manuscript.

The temperature dependence of the correlation length ξ and the peak amplitude S_0 are plotted in Fig. 5.11. Both quantities appear to decay monotonically with increasing temperature, which would be expected for a 2DQHAFSL. Superimposed are a number of theoretical models which attempt to describe the behaviour of a 2DQHAFSL with a nearest-neighbour exchange parameter $J = 60$ meV, chosen to agree with the value obtained from RIXS measurements by Kim and coworkers [37]. The theoretical amplitudes S_0 have been scaled to pass through the point at 300 K to compare their functional forms. However regardless of which model is chosen, or the specific value of J, the 2DQHAFSL is not satisfactory in explaining the observed temper-

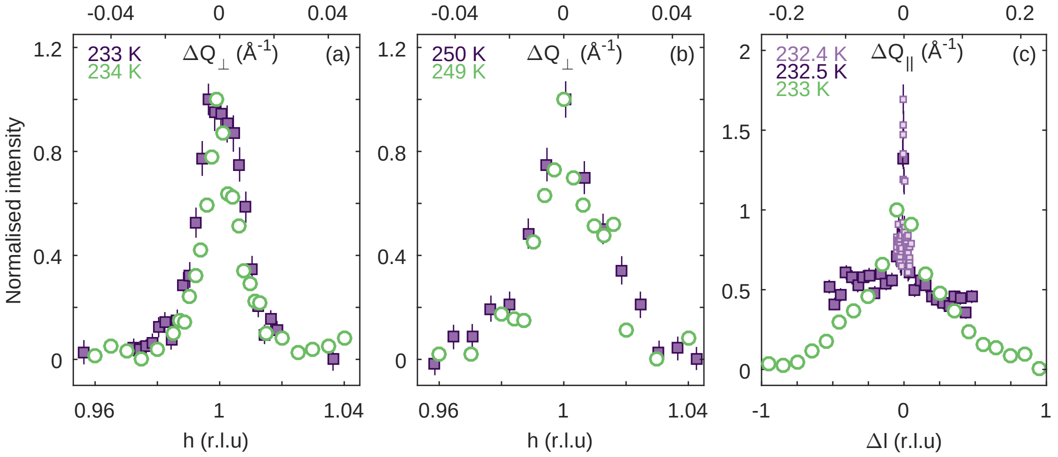

Figure 5.10: Comparison of critical scattering in-plane (a,b) and out-of-plane (c) for the $(1,\ 0,\ 24)$ magnetic Bragg peak (filled squares) with that presented in Ref. [38] for $(1,\ 0,\ 22)$ (open circles). The data have been normalised to fit on the same axes and allow a direct comparison of the lineshapes and peak widths. Note that a sloping background has also been subtracted from the Fujiyama *et al.* [38] data.

ature dependence of the correlation length across the full temperature range studied. This does not preclude the possibility that 2D Heisenberg behaviour is observed at higher temperatures. Indeed this is expected; at high enough temperatures all relevant anisotropies will become insignificant and isotropic behaviour will dominate. It should be noted that Kim *et al.* could not obtain a good fit to the RIXS data without including significant second- and third-nearest interactions ($J' = -20$ meV, $J'' = 15$ meV); these longer-ranged interactions are not included in any of the theoretical models for the 2DQHAFSL given above. In particular a ferromagnetic next-nearest neighbour exchange term J' has the effect of stabilising the Néel ordered state below T_N. On the other hand, Chakravarty, Halperin, and Nelson [159] conjecture that inclusion of antiferromagnetic next-nearest neighbour interactions would have the effect of pushing the system towards the quantum disordered regime ($g > g_c$). This highlights the role that longer ranged interactions may have on the magnetic ground state.

Alternative models were therefore pursued, in particular those which would preserve the two-dimensional nature of the critical scattering. Two possibilities were explored: strong easy-plane anisotropy (2D XYh_4) and weak easy-plane anisotropy (2D anisotropic Heisenberg).

5.4 2D XYh_4 model

The pure 2D XY model has been well described by Berezinskii, Kosterlitz, Thouless (BKT) [204–206], and many others over the years. Inclusion of an additional fourfold anisotropy term in the Hamiltonian (h_4) results in the so-called 2D XYh_4 model. This is distinct from both the 2D Ising and 2D XY models, with its own universality class. In the classical limit, the 2D XYh_4 universality

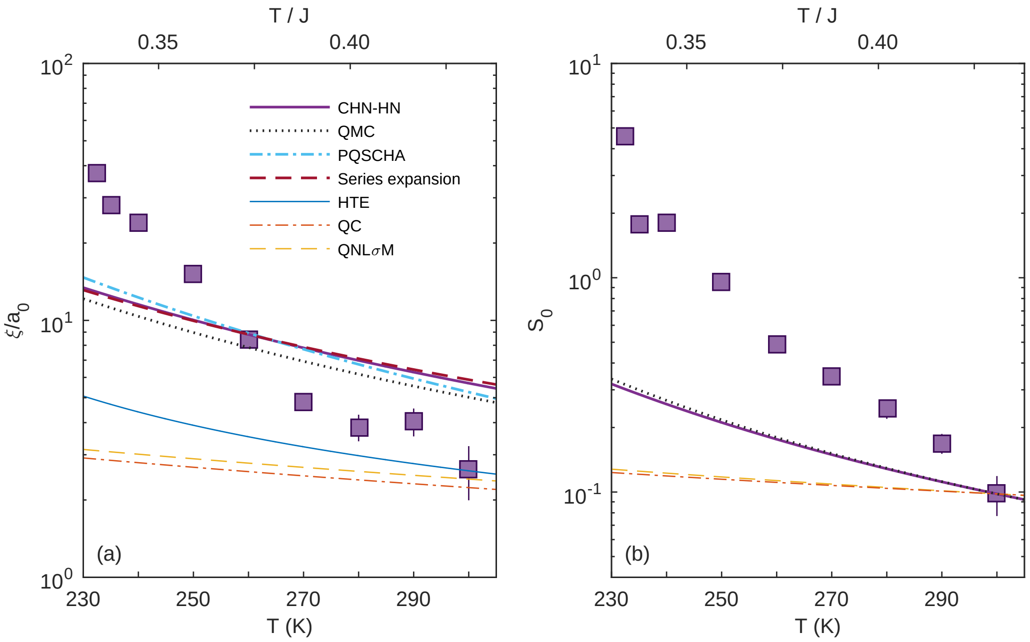

Figure 5.11: Comparison of various models for the 2DQHAFSL to the experimental data. (a): In-plane correlation length ξ. (b): Structure factor S_0. All models are calculated assuming $J = 60$ meV, with the structure factor predictions scaled such that they pass through the data point at 300 K. None of the theoretical models for the 2DQHAFSL are a satisfactory fit to the data for the entire temperature range studied.

class can be described by the following Hamiltonian:

$$\mathcal{H}_4 = -J \sum_{\langle i,j \rangle} \cos(\theta_i - \theta_j) - h_4 \sum_i \cos(4\theta_i), \tag{5.13}$$

where θ_i are the orientations of classical spins on a square lattice and confined to the XY plane and J is the coupling constant. The two limiting cases are $h_4 \to 0$ and $h_4 \to \infty$. As $h_4 \to 0$, the system approaches the pure XY universality class, with behaviour well described by BKT theory. In BKT theory, the critical exponent β has been derived analytically [207, 208] as $\beta = 3\pi^2/128 \sim 0.231$. In the opposite limit $h_4 \to \infty$, XYh_4 crosses over to the four-state clock model, which is equivalent to two perpendicular Ising models, and hence fits into the 2D Ising universality class. This universality class is characterized by $\beta = 0.125$. In between the two limits β varies continuously as a function of h_4. The 2D XYh_4 model is thus predicted to have a range of non-universal critical exponents which depend on the magnitude of h_4 [209]. These exponents exhibit 'weak universality' with both the 2D Ising and 2D XY models,[6] in that the critical exponent $\eta = 1/4$ for all values of h_4. The crossover between XY and Ising behaviours is slow as a function of increasing h_4; this is a direct consequence of η having the same value for the two universality classes. Typically h_4 is a small perturbation for ferromagnets and classical systems; this is demonstrated by the ferromagnet $Rb_2Cu_2Cl_4$ for example which exhibits all of the characteristics of the XY universality class [211]. However there is an argument that antiferromagnets

---

[6] Suzuki [210] proposed that in systems with weak universality, η, δ, and the reduced critical exponents $\hat{\beta} = \beta/\nu'$, $\hat{\gamma} = \gamma/\nu$, $\hat{\phi} = (2/\alpha)/\nu$ were all independent of the system Hamiltonian.

should always be pushed towards the strong h_4 limit, as a result of quantum confinement that forces the spins to lie in the easy plane [195]. This results in a partial breakdown in the scaling for the XY equations, and hence more Ising-like critical behaviour close to T_N.

In real systems exhibiting 2D XYh_4 behaviour, there are two possible sources for h_4 [212]: an in-plane crystal field or an order-by-disorder type mechanism. Additionally three-dimensional order occurs below $\mathrm{T_N} > \mathrm{T_{KT}}$ due to weak interlayer coupling J' amplified by the diverging size of correlated regions $\xi(T)^2$. Here $\mathrm{T_{KT}}$ is the Kosterlitz-Thouless temperature, which is associated with unbinding of vortex-antivortex pairs in the 2D XY model.[7] This model shall now be compared with experiment.

As shown above (Fig. 5.5), the intensity of the $(1, 0, 24)$ magnetic Bragg peak decreases continuously with increasing temperature. These data can be fit to a power law $I = A(T - T_\mathrm{N})^{2\beta}$, where the critical exponent $\beta = 0.195(4)$ and the Néel temperature $T_\mathrm{N} = 226.8(2)$ K. This value of β is intermediate between the 2D Ising ($\beta = 0.125$) and 2D XY limits ($\beta = 0.231$), and hence is consistent with the 2D XYh_4 universality class. Based on this value for β, it is possible to estimate the strength of h_4. Taroni *et al.* [195] performed Monte Carlo simulations on systems of 10^4 spins, and determined the critical exponents β and ν for various values of h_4. They determined β by two different methods: data collapses, or fixing the critical temperature to the maximum in the susceptibility, then deriving β from a log-log plot. The two methods gave somewhat similar results with a linear dependence[8] of β on h_4: $\beta(h_4) = 0.125 + a/h_4$, where $a = 0.04(1)$. From this scaling relation, and the experimentally determined value of β, $h_4 = 0.5(2)$ for Sr_2IrO_4. This comparatively large value of h_4 indicates that in-plane anisotropy is clearly important below T_N, and places Sr_2IrO_4 at the boundary between the weak- and strong-field regimes.

5.4.1 Correlation length and amplitude for 2D XY

As mentioned previously, $\mathrm{T_{KT}}$ is characteristic of the 2D XY universality class. Above $\mathrm{T_{KT}}$, Kosterlitz predicted that the correlation length ξ diverges according to $\xi \sim \exp\left[\pi/\sqrt{c\,(T - T_\mathrm{KT})}\right]$, where c is a constant.[9] This expression for ξ can be rewritten in terms of the dimensionless quantities b and $t = (T - T_\mathrm{KT})/T_\mathrm{KT}$ as:

$$\xi \propto \exp\left(bt^{-1/2}\right), \tag{5.14}$$

which is appropriate since $\mathrm{T_{KT}}$ is a non-universal quantity. Theoretical studies [207] have shown $b \approx 1.9$, and is weakly system dependent. Note that for the 2D XY model the critical exponent ν defined by $\xi \sim t^{\nu}$ does not exist, since the correlation length diverges exponentially and hence faster than any power law [206]. From general scaling relations, the susceptibility χ can be

---

[7] Below $\mathrm{T_{KT}}$, a spin wave peak can be observed. Above $\mathrm{T_{KT}}$, vortex-antivortex pairs unbind, and their diffusion results in a quasielastic peak at $S(\omega, q)$.

[8] There appears to be a typographical error in the original paper; fitting the $1/h_4$ dependence of the 'true' exponents as written gives $a = 0.023(6)$, not 0.032.

[9] The value of c has been somewhat debated, however consensus now puts $c = 2.2\ \mathrm{K}^{-1}$.

determined from the correlation length through $\chi = \xi^{2-\eta}$, where $\eta = \frac{1}{4}$ is a critical exponent derived from the correlation function. For the 2D XY model, this value of η is universal [206]. Since the peak amplitude S_0 is proportional to the dynamical susceptibility at zero wavevector, the amplitude can be written as:

$$S_0 \propto \exp\left[(2-\eta)\, bt^{-1/2}\right]. \tag{5.15}$$

In the 2D XYh$_4$ universality class, the correlation length and amplitude are expected to follow the theoretical expressions for the 2D XY model, provided that h_4 is not too large. This is due to the perturbative effect of h_4 and the partial breakdown of the XY scaling relations.

5.4.2 Comparison to experimental data

The next stage is to compare the 2D XYh$_4$ model with the experimentally obtained temperature dependence of the correlation length ξ and amplitude S_0 for Sr$_2$IrO$_4$. The correlation length and the amplitude were fit simultaneously, and η was fixed to equal 0.25. The best fits of this model to the data for $T > 233$ K are shown in Fig. 5.12. This corresponds to the temperature range where no extrinsic Lorentzian squared component could be observed. At first glance it appears that this model fits the data very well across the whole temperature range studied, which contrasts with the results for the 2DQHAFSL. However extracting the fitted parameters reveals $T_{\mathrm{KT}} = 184(8)$ K and $b = 3.4(8)$; the latter value being significantly larger than the theoretical value for the 2D XY model ($b \approx 1.9$). This can partly be explained by the finite value of h_4, and the breakdown of the XY scaling relations.

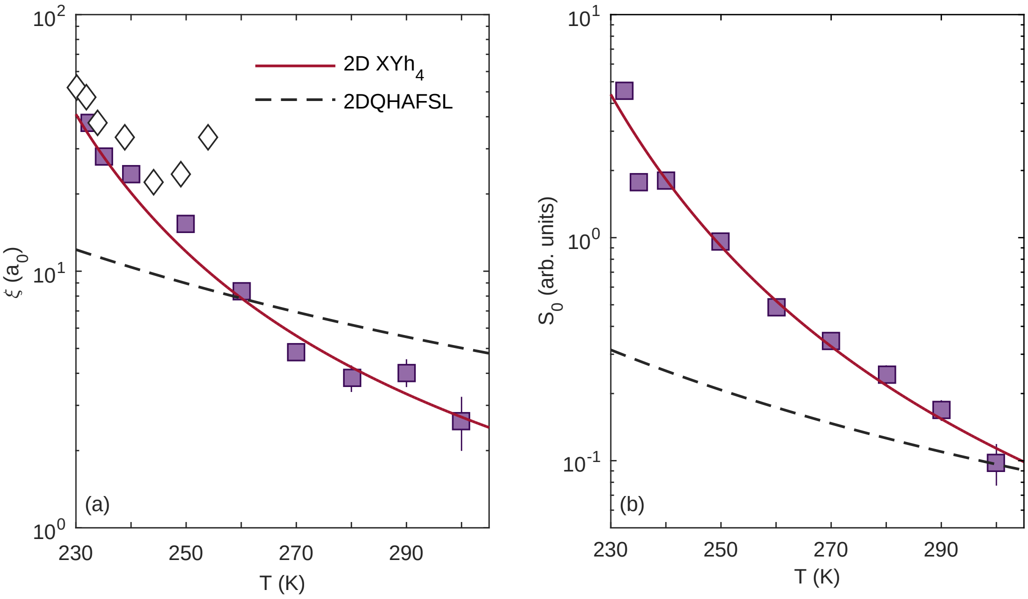

Figure 5.12: (a): Experimentally determined correlation lengths ξ (filled circles) and best fit to 2D XYh$_4$ model (solid red line). The data from Fujiyama *et al.* [38] (open squares) divided by a factor a$_0$ and the QMC result for the 2DQHAFSL [167] with $J = 60$ meV (dashed black line) have been added as a guide. (b): Experimentally obtained amplitudes S_0 (filled circles) and best fit to 2D XYh$_4$ (solid red line).

From these values of T_{KT} and b, it is possible to estimate the ratio between the in-plane and out-of-plane exchange couplings, J and J' respectively. Following the derivation by Als-Nielsen [211], the ratio J'/J is given by $J'/J = \exp\left(-2b/\sqrt{t}\right)$, where $t = \left(T_{\mathrm{N}} - T_{\mathrm{KT}}\right)/T_{\mathrm{KT}}$. Evaluating this ratio gives $J'/J = 8 \times 10^{-7}$, however there is a significant uncertainty in this quantity (approximately two orders of magnitude) as a consequence of the uncertainty in both b and T_{KT}. This value for J'/J is considerably lower than the typical value for the cuprates ($J'/J \sim 5{\times}10^{-5}$) such as La_2CuO_4 [174, 193], and is unphysical for the following reasons. Firstly if one compares the local coordination environment for the metal cations in Sr_2IrO_4 and orthorhombic La_2CuO_4, the in-plane M-O bond lengths are remarkably similar [185, 213] $\left[\mathrm{r}_{\mathrm{Ir\text{–}O}} = 1.981\ \text{Å},\ \mathrm{r}_{\mathrm{Cu\text{–}O}} = 1.9049(1)\ \text{Å}\right]$. The out-of-plane M-O bond lengths differ more strongly $\left[\mathrm{r}_{\mathrm{Ir\text{–}O}} = 2.055\ \text{Å},\ \mathrm{r}_{\mathrm{Cu\text{–}O}} = 2.4210(5)\ \text{Å}\right]$, but can be partly explained by Cu^{2+} being a Jahn-Teller ion and the improved stability associated with a tetragonal distortion along z. Nevertheless the separation between layers of MO_6 octahedra are comparable (Sr_2IrO_4: 6.4575 Å, La_2CuO_4: 6.5716 Å), which implies that in the absence of other contributions, J'/J should be similar for the two compounds.[10] However if one considers the ground state orbitals, then a difference should be observed between the two systems. The ground state for La_2CuO_4 is the $3d_{x^2-y^2}$ orbital – again as a consequence of Jahn-Teller distortion – and lies predominantly in the xy-plane. Yet the ground state in the hole representation for Sr_2IrO_4 is an admixture of $5d$ orbitals with t_{2g} symmetry, which in the limit of zero tetragonal crystal field splitting reduces to the pure $j_{\mathrm{eff}} = \frac{1}{2}$ isospin state [34]. This tetragonal field splitting Δ has been determined by Boseggia [191] to be $-60\ \mathrm{meV} \leq \Delta \leq 35\ \mathrm{meV}$, and hence Sr_2IrO_4 is close to the ideal $j_{\mathrm{eff}} = \frac{1}{2}$ limit. The sign of Δ governs the shape of the ground state wavefunction (and the relative contributions from the ‘spin-up’ and ‘spin-down’ components of the isospin); however the experimental value of Δ is sufficiently close to zero such that the shape of the wavefunction can be assumed to be cubic as a first approximation. A cubic wavefunction naturally has a significant component in the z-direction, and thus one would expect interactions to increase in this direction compared to a wavefunction predominantly polarised in the xy-plane. Based on this argument the ratio J'/J should be *larger* for Sr_2IrO_4 than for La_2CuO_4, which is at odds with the calculated result for the 2D XYh_4 model. An alternative explanation for the observed critical scattering behaviour above T_{N} is required.

5.5 2D anisotropic Heisenberg model (2DAH)

The 2D XYh_4 model is relevant for systems with strong easy-plane anisotropy, and as shown above, does not provide an adequate explanation of the observed critical scattering above T_{N}. Consider what happens when the easy-plane anisotropy is instead treated as a weak perturbation to a nearest neighbour Heisenberg Hamiltonian. A representative Hamiltonian is given

---

[10] Compare this for example with $Sr_2CuO_2Cl_2$, where the increased layer separation results in a much smaller ratio $J'/J \sim 10^{-8}$ [214].

by:

$$\mathcal{H} = J \sum_{\langle nn \rangle} \left[\hat{S}_i^x \hat{S}_j^x + \hat{S}_i^y \hat{S}_j^y + (1 - \Delta_\lambda) \hat{S}_i^z \hat{S}_j^z \right], \tag{5.16}$$

where Δ_λ is the easy-plane anisotropy, and is equal to or smaller than unity. In the limit $\Delta_\lambda = 1$, then there is only exchange coupling in the xy-plane. However there is still the possibility for fluctuations to occur in the z-direction, unlike for the 2D XY model. In the limit $\Delta_\lambda = 0$, then the interactions are isotropic and hence Heisenberg-like.

Cuccoli *et al.* [215, 216] performed quantum Monte Carlo simulations within the 2DAH model, and characterised the behaviour of thermodynamic parameters for small values of Δ. In the limit of long correlation lengths, ξ and S_0 scale the same way as for the pure 2D XY model. However, with increasing temperature there is a crossover towards:

$$\xi(T) \propto \exp(b/t) \tag{5.17}$$

$$S_0 \propto (2 - \eta) \exp(b/t) \tag{5.18}$$

for $\xi \lesssim 100$ a$_0$. The data presented here fall in this regime. The experimental correlation length and amplitude data ($T > 233$ K) were thus fitted simultaneously to Eqns. 5.17 and 5.18, with the results of these fits shown in Fig. 5.13.

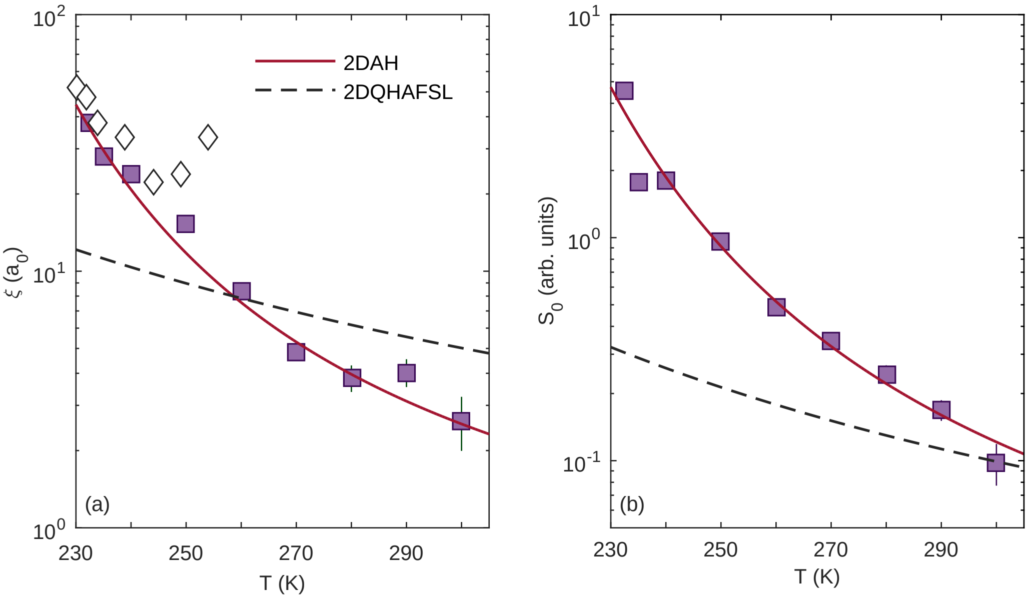

Figure 5.13: (a): Experimentally determined correlation lengths ξ (filled circles) and best fit to 2DAH model (solid red line). The data from Fujiyama *et al.* [38] (open squares) and the QMC result for the 2DQHAFSL [167] with $J = 60$ meV (dashed black line) have been added as a guide. (b): Experimentally obtained amplitudes S_0 (filled circles) and best fit to 2DAH model. Dashed line is 2DQHAFSL model ($J = 60$ meV) scaled to pass through data point at 300 K.

Clearly these fits also provide a good description of the data, with $T_{\mathrm{KT}} = 162(11)$ K and $b = 2.1(7)$, the latter of which is much more consistent with the theoretical value for the 2D XY model. Once again one can estimate the ratio J'/J using the fitted parameters from the

2DAH model, which in this case gives $J'/J = 3\times10^{-5(2)}$. This value is comparable to that obtained for La_2CuO_4, which as mentioned above, is sensible if only structural contributions are considered. However once again there is a significant error in J'/J as a direct result of the inability to constrain the estimates for T_{KT} and b any further.

An alternative method of estimating J'/J is by considering the value of the correlation length at T_N. As T_N is approached from above, the system can be described in terms of an effective length scale L_{eff}, which is of the order $\sqrt{J/J'}$. This length scale can be approximated to be equal to the correlation length, and hence $J'/J \sim \xi(T_N)^{-2}$. Using this expression it is possible to estimate $J'/J \sim 4 \times 10^{-4}$ for Sr_2IrO_4, which assuming an in-plane nearest-neighbour exchange of $J = 60$ meV would imply $J' \sim 0.03$ meV, consistent with the previous estimate. This energy scale is significantly smaller than can be resolved by RIXS for example. What this shows is that magnetic critical scattering is a useful probe of magnetic interactions and weak anisotropies present in a given Hamiltonian.

5.6 RIXS on Sr_2IrO_4

Resonant inelastic X-ray scattering (RIXS) has already been shown to be a useful technique for studying the electronic and magnetic excitations in 5d TMOs. As previously mentioned, Kim and coworkers [37] performed RIXS measurements on Sr_2IrO_4, with a combined energy resolution of $\Delta E = 130$ meV. Their conclusion was that the low temperature magnon dispersion is well described by a phenomenological J–J'–J'' model, with J, J' and J'' representing the exchange between nearest, next-nearest and third nearest neighbours respectively. Fitting this model to the experimental data (Fig. 5.14) revealed $J = 60$ meV, $J' = -20$ meV, and $J'' = 15$ meV, with a ferromagnetic next-nearest neighbour interaction J' required to adequately fit the data between $(\pi/2, \pi/2)$ and $(\pi, 0)$. This helps to stabilise Néel order below T_N. The lack of a gap at $(0, 0)$ and (π, π) is highly suggestive of 2D Heisenberg interactions, which corroborates the conclusions of Fujiyama [38], albeit with a discrepancy in the value of J.

More recent RIXS measurements by the same group [192] however are more suggestive of some degree of intrinsic anisotropy. These measurements were performed with a much better energy resolution ($\Delta E = 30$ meV), and there appears to be a gap in the spin wave dispersion of approximately 30 meV at the structural zone centre $(0, 0)$, which is qualitatively consistent with the existence of XY anisotropy (Fig. 5.14c). The presence of any sort of gap at (π, π) is less clear as the spin-wave intensity diverges due to the magnetic Bragg peak, plus RIXS data is only shown up to $(0.9\pi, 0.9\pi)$. However the possible existence of a gap was not alluded to in the paper in question. Therefore models consistent with easy-plane anisotropy were fitted to the experimental data provided in the paper, in order to ascertain whether this would be responsible for such a gap.

The data was digitised from the paper and the low energy (< 0.4 eV) portion of the spectra were fitted with Gaussians representing the elastic line (and quasi-elastic features), magnons

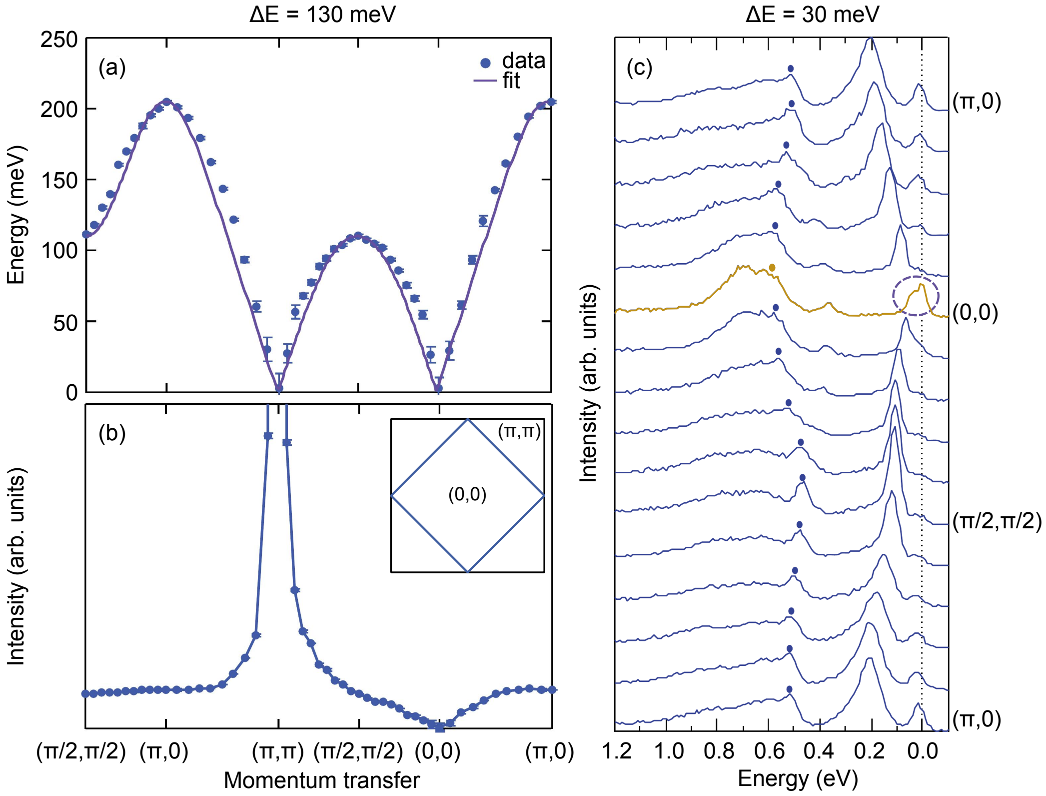

Figure 5.14: (a,b): Magnon dispersion and intensity measured by Kim and colleagues [37] on Sr_2IrO_4. Parameters were obtained from fits to medium resolution data ($\Delta E = 130$ meV). Solid line in (a) is the best fit of the dispersion to a $J - J' - J''$ model with $J = 60$ meV, $J' = -20$ meV and $J'' = 15$ meV. (c): High resolution ($\Delta E = 30$ meV) RIXS data for Sr_2IrO_4 measured by Kim *et al.* [192] at normal incidence. Dots at ca. 0.5 eV indicate the spin-orbit exciton feature. The dispersive feature between 0 and 0.2 eV is the magnon peak. There appears to be a magnon gap of $\sim$30 meV at $(0, 0)$, which has been highlighted.

and bimagnons. The best fits to the data with the 2DAH are shown in Fig. 5.15, along with the extracted momentum dependence of the magnon dispersion and the spectral weight. The fitted data appears consistent with that shown in Fig. 5.14, however there are two key differences. The first is the aforementioned gap at $(0, 0)$ of 38 meV, which is significant compared to $J = 60$ meV. The second difference is a reduction of spectral weight at $(\pi/2, \pi/2)$ compared to $(\pi, 0)$. Closer inspection reveals a distinct variation of lineshape between $(\pi/2, \pi/2)$ and $(\pi, 0)$, with the latter being much broader and showing a pronounced asymmetry[11].

As discussed above, there are two possible scenarios which would explain the existence of such a gap. The first is easy-plane anisotropy caused by a four-fold crystal field (XYh_4), and the second is easy-plane anisotropy as a result of anisotropic exchange (2DAH). Both models shall be considered in turn.

---

[11] Igarashi [217] suggests that this may be evidence of split magnon modes.

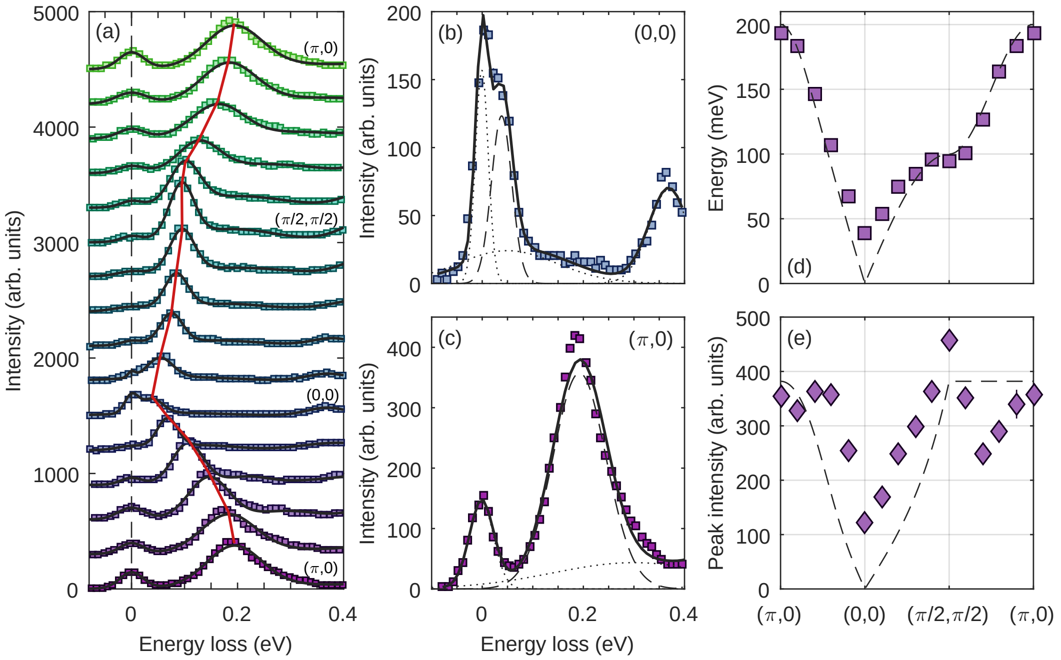

Figure 5.15: (a): Stack plot of the low energy RIXS data from Kim *et al.* [192] fitted to the model described in the text (solid black lines). The fitted position of the magnon peak is shown as the solid red line. (b),(c): Representative RIXS spectra at $(0, 0)$ and $(\pi, 0)$, along with best fits to data and their respective components. The dashed line represents the magnon peak. (d): Magnon dispersion as a function of in-plane momentum transfer. (e): Spectral weight as a function of momentum transfer. Dashed lines in (d,e) represents the fitted model presented in Ref. [37].

2D XYh_4

An alternative formulation of Eqn. 5.13 can be written [195]:

$$\mathcal{H} = J \sum_{\langle i,j \rangle} \mathbf{S}_i \cdot \mathbf{S}_j + D \sum_i \left(S_i^z\right)^2 + \tfrac{1}{2} e \left(S_+^4 + S_-^4\right),$$

where D is a crystal field anisotropy confining the spins to an easy plane, and the four-fold term e breaks symmetry within that plane. In this model inter-plane exchange is ignored, however as demonstrated above, the ratio $J'/J \sim 10^{-4}$ and is hence negligible for our purposes. This Hamiltonian can be diagonalized (through a suitable choice of Bogoliubov transformations if there is antiferromagnetic exchange), leading to a magnon dispersion. Following the reasoning of Thurlings *et al.* [218], the spin-wave dispersion can be written to first order as:

$$\omega_{\mathbf{k}}^{\alpha,\beta} = z|J|S\sqrt{(1+A)^2 - (\gamma_{\mathbf{k}} \pm B)^2}, \tag{5.19}$$

with $A = (D-3E)/z|J|$, $B = (D+E)/z|J|$, $\gamma_{\mathbf{k}} = \frac{1}{2}\left[\cos(q_x) + \cos(q_y)\right]$, $E \approx 6eS^2$, and $z = 4$.

In the antiferromagnetic case, and in the limit $D = e = 0$, this leads to two magnon modes which are gapless at the zone centre (Goldstone modes). These two modes pertain to the degenerate in-plane and out-of-plane spin fluctuations of equal amplitude. If D or e is non-zero, then the degeneracy is lifted and the magnon dispersion is gapped throughout the Brillouin zone.

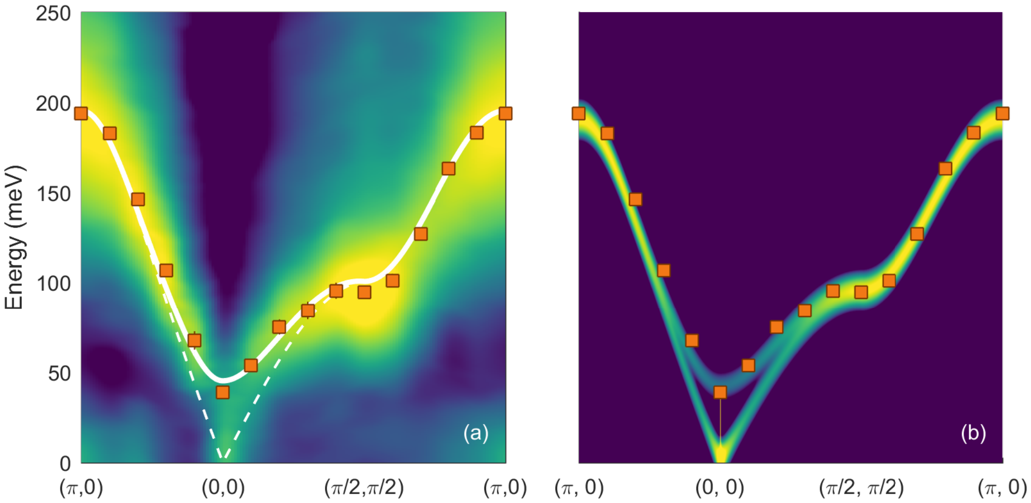

Figure 5.16: (a): Raw RIXS spectra [192] overlaid with the fitted magnon peak energy (orange squares), gapped (solid) and gapless (dashed) modes of the 2D XYh$_4$ model. (b): Spin wave dispersion as simulated in SpinW, which highlights the two distinct magnon modes. The simulated data has been convoluted with a Gaussian of FWHM 10 meV. The colour scale reflects the real part of the spin-spin correlation function components $S^{xx}(\mathbf{Q},\omega) + S^{yy}(\mathbf{Q},\omega) + S^{zz}(\mathbf{Q},\omega)$.

The size of these gaps at the zone centre are given by:

$$\omega_o^{\text{out-of-plane}} \approx 2S\sqrt{Dz|J|} \tag{5.20}$$

$$\omega_o^{\text{in-plane}} \approx 2S\sqrt{2|E|z|J|}. \tag{5.21}$$

It is possible to estimate an upper bound on D for Sr$_2$IrO$_4$ using the experimental gap at zero wavevector; for $\omega_0 = 38$ meV and $J = 60$ meV one obtains $D \leq 6$ meV, which is sizeable compared to J. The in-plane gap is too small to be observed by RIXS; thus an estimate for e cannot be determined. This analysis is complicated somewhat by the strong second- and third-nearest neighbour interactions which are relevant for Sr$_2$IrO$_4$, but were not taken into account in the original theory. Thurlings and colleagues [218] made some headway on the problem, with Eqn. 5.19 now becoming:

$$\omega_{\mathbf{k}} = z|J|S\sqrt{\left[1 + \left(\frac{J_2}{J}\right)\left(\gamma_{\mathbf{k}}^{(2)} - 1\right) + \left(\frac{J_3}{J}\right)\left(\gamma_{\mathbf{k}}^{(3)} - 1\right) + A\right]^2 - (\gamma_{\mathbf{k}} \pm B)^2}, \tag{5.22}$$

where $\gamma_{\mathbf{k}}^{(2)} = \cos q_x \cos q_y$ and $\gamma_{\mathbf{k}}^{(3)} = \frac{1}{2}(\cos 2q_x + \cos 2q_y)$. One finds a good fit to the experimental dispersion using this model, with exchange parameters in good agreement with those obtained originally by Kim *et al.* : $J_1 = 59(7)$ meV, $J_2 = -18(4)$ meV, $J_3 = 15(2)$ meV, $D = 8.7(9)$ meV. The large value of D implies a significant easy-plane anisotropy arising from a in-plane crystal field component. However note that in the Hamiltonian given in Eqn. 5.6, the component arising from h_4 — $D\sum_i (S_i^z)^2 + \frac{1}{2}e\left(S_+^4 + S_-^4\right)$ — is effectively a single-ion anisotropy (SIA). Furthermore remember that SIA vanishes for $S = \frac{1}{2}$ systems as a consequence of Kramers degeneracy (Chapter 1). This would also be expected to apply in the pure $j_{\text{eff}} = \frac{1}{2}$ limit since the ground state can be described by $S = \frac{1}{2}$ isospins $|\uparrow\downarrow\rangle$. Tetragonal or trigonal distortions mix in contributions from $j_{\text{eff}} = \frac{3}{2}$ states [34], which gives rise to non-zero SIA. Consequently one would expect a spin wave gap in the case of distortions away from the ideal $j_{\text{eff}} = \frac{1}{2}$ limit.

Liu and colleagues [219] include an easy-plane SIA term in their spin Hamiltonian, and find that $D = 0.10$ meV. This is considerably smaller than their estimate for the nearest-neighbour exchange $J = 45$ meV, and implies a weak tetragonal distortion. Such an observation is unsurprising [191]. Inserting the theoretical value of D into the expression for the spin wave energy (Eqn. 5.22), one finds a spin gap of ≈ 5 meV, which although sizeable, is significantly smaller than the observed spin wave gap.

This suggests that the experimentally obtained value for D is artificially large. Whilst this can be partly explained by the finite momentum and energy resolution of the RIXS measurements, it is likely that other sources of anisotropy are also relevant for Sr_2IrO_4. Nevertheless, to leading order, XYh_4 interactions appear to be consistent with the observed behaviour in Sr_2IrO_4.

2DAH

Kim and colleagues [37, 192] found that the interactions in Sr_2IrO_4 were Heisenberg-like with significant second and third-nearest neighbour interactions. In order to directly compare the 2DAH with the RIXS data, the Hamiltonian given in Eqn. 5.16 can be extended to include second- and third-nearest neighbour interactions:

$$\begin{aligned}\mathcal{H}_{ab} = &\sum_{\langle i,j\rangle} \tilde{J}\left[S_i^x S_j^x + S_i^y S_j^y + (1-\Delta_\lambda)\, S_i^z S_j^z\right] + \sum_{\langle\langle i,j\rangle\rangle} J_2 \vec{S}_i \cdot \vec{S}_j \\ &+ \sum_{\langle\langle\langle i,j\rangle\rangle\rangle} J_3 \vec{S}_i \cdot \vec{S}_j. \end{aligned} \tag{5.23}$$

Here $\tilde{J} = J_{\text{iso}}/(1-\Delta_\lambda)$ is the effective nearest-neighbour (nn) exchange parameter, J_{iso} is the isotropic Heisenberg nn exchange, and J_2, J_3 symbolizes the exchange between next-nearest and third nearest neighbours respectively. Out-of-plane exchange coupling has been neglected since as demonstrated above, it is a factor of $\sim 10^3$ weaker than the in-plane terms, and thus not resolvable with RIXS at present. The out-of-plane spin gap at the structural zone centre is given to leading order by $\omega_0 = 4JSZ_c\sqrt{2\Delta_\lambda}$ [214], and hence an initial estimate for Δ_λ can be made. Setting $J = 60$ meV, and $\omega_0 = 30$ meV, one obtains $\Delta_\lambda = 0.023$, or in other words, a weak anisotropy in the xy-plane.

This estimate can be improved by fitting the experimental data to a theoretical magnon dispersion. The energy of the two magnon modes is given by:

$$\begin{aligned}\omega_\pm &= 2S\sqrt{A_{\mathbf{q}}^2 - B_{\mathbf{q}}^2}, \\ A_{\mathbf{q}} &= 2\left(\tilde{J} - J_2 - J_3 + J_2 \cos q_x \cos q_y\right) + J_3\left(\cos 2q_x + \cos 2q_y\right) + \Gamma, \\ B_{\mathbf{q}} &= \tilde{J}\left(\cos q_x + \cos q_y\right) \mp \Gamma, \quad \Gamma = \tilde{J}\Delta_\lambda/2. \end{aligned} \tag{5.24}$$

Here the positive sign refers to the gapped mode, and the negative sign to the gapless mode. As the gapless mode could not be unambiguously resolved in the experimental data, only the

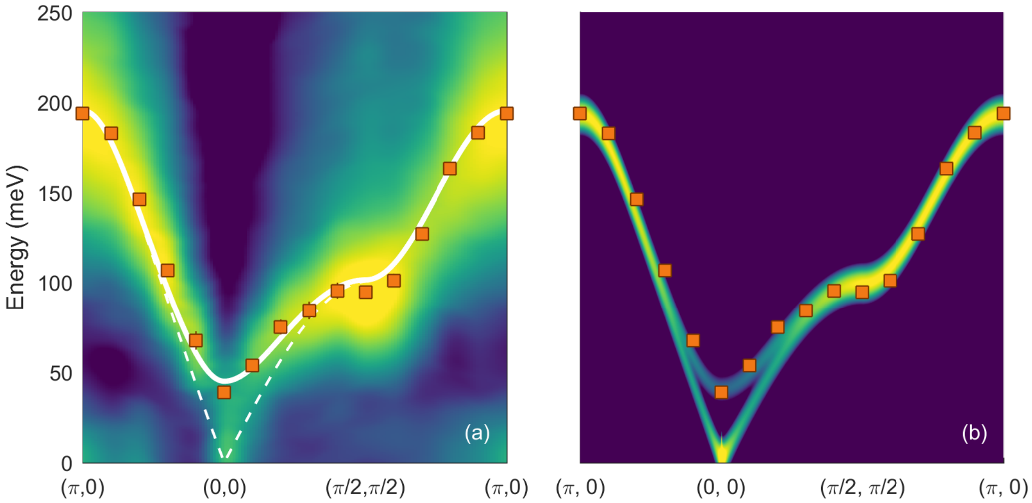

Figure 5.17: (a): Raw RIXS spectra overlaid with the fitted magnon peak energy (orange squares), gapped (solid) and gapless (dashed) modes of the 2DAH. (b): Spin wave dispersion as simulated in SpinW, which highlights the two distinct magnon modes. The simulated data has been convoluted with a Gaussian of FWHM 10 meV. The colour scale reflects the real part of the spin-spin correlation function components $S^{xx}(\mathbf{Q},\omega)+S^{yy}(\mathbf{Q},\omega)+S^{zz}(\mathbf{Q},\omega)$.

gapped mode was fitted with the above model. The best fit to the data was obtained with the following coupling parameters: $\tilde{J} = 59(7)$ meV, $J_2 = -18(4)$ meV, $J_3 = 15(2)$ meV, $\Delta_\lambda = 0.10(2)$. There is good agreement between the experimental dispersion and that calculated from the anisotropic model, with the fitted exchange constants essentially identical to those obtained from the earlier low-resolution study within the statistical error [37]. The agreement for the peak intensity is perhaps less compelling but can be said to be qualitatively reasonable; in particular the model reproduces the non-zero intensity observed at the zone centre. Moreover, it proved difficult to extract the spectral weight from the RIXS data [192] as there appears to be a significant variation of lineshape as a function of momentum transfer, which may be evidence for an additional excitation mode between the single magnon and bi-magnon peaks (the latter was accounted for in the fitting procedure). The easy-plane anisotropy parameter $\Delta_\lambda = 0.10(2)$ determined here should probably be considered as an upper bound to the true anisotropy, since the finite momentum and energy resolution means that the excitation energy at the zone centre cannot be fully resolved. Nevertheless this is significantly larger than that observed for La_2CuO_4 ($\Delta_\lambda = 2.0(5)\times10^{-4}$) [220], which further illustrates the relative importance of XY anisotropy for Sr_2IrO_4.

Fitting the dispersion and intensities to the localized spin model proposed by Igarashi [221, 222] provided similar results, corroborating their prediction of an out-of-plane gap for Sr_2IrO_4. Note that the data plotted in Figure 5.17b shows the sum of spin-spin correlation function components $S^{xx}(\mathbf{Q},\omega)+S^{yy}(\mathbf{Q},\omega)+S^{zz}(\mathbf{Q},\omega)$. Igarashi and Nagao [221, 222] neglect the $S^{xx}(\mathbf{Q},\omega)$ component as they argue that it results purely from two-magnon scattering. The $S^{xx}(\mathbf{Q},\omega)$ component accounts for the finite intensity of the gapless mode at $(0,0)$.

	U	U'	J_{H}	t	ζ_{SO}	J	D	δJ_{xy}	δJ_z
Igarashi *et al.*[12] [221, 222]	3.5	2.6	0.45	0.3	0.4	60	—	1.8	-1.8
Perkins *et al.* [223]	2.4	1.8	0.3	0.13[13]	0.4	59	35	2.2	9.4
Kim *et al.* [224] ($\delta = 0.15$ eV)	1.86	0.86	0.5	0.19[14]	0.4	76.8	-26.2	8.6	5.9
Solovyev *et al.* [225]	3.05	2.09	0.48	0.17	0.43	39.0	3.97	1.2	-2.3

Table 5.1: Comparison of microscopic parameters used in theoretical studies of Sr_2IrO_4. All parameters assume zero tetragonal distortion $\delta = 0$ unless otherwise stated. Definitions used in some of the parameters calculated in this table: $U' = U - 2J_{\text{H}}$, $J = 4t^2/U$, $\delta J_{xy} = J_{xx} - J$, $\delta J_z = J_{zz} - J$.

	This work	Igarashi *et al.* [222]	Perkins *et al.* [223]	Kim *et al.* [224]	Solovyev *et al.* [225]
Δ_λ	0.10(2)	0.058	-0.116	0.039	0.087

Table 5.2: Comparison of anisotropy parameter Δ_λ derived from different theoretical studies and the parameters given in Table 5.1. All models show some degree of weak anisotropy. For reference $\Delta_\lambda = 1 - (J_{zz}/J_{xx}) = (\delta J_{xy} - \delta J_z) / (\delta J_{xy} + J)$.

In fact a number of theoretical studies predict some degree of anisotropy in Sr_2IrO_4. Each of these studies takes a slightly different approach, with varying microscopic parameters, however are all restricted to nearest-neighbour exchange. These are summarised in Table 5.1. The key thing to note is that some of these models include a Dzyaloshinskii-Moriya (DM) term, which arises as a consequence of the finite rotation of the IrO_6 octahedra. This term is frequently considered to be gauged away as a consequence of opposing rotation of IrO_6 octahedra between alternate layers.

It is possible to determine Δ_λ for each of these models, if one carefully considers the differences in the definition of various parameters between studies. These results are summarised in Table 5.2. The calculated anisotropies are of the same magnitude as that obtained from RIXS, with most indicative of easy-plane anisotropy. The one exception [223] is more suggestive of Ising anisotropy, which arises due to the large δJ_z term, and competes with the DM interaction. There is however a strong dependence of the exchange parameters on the magnitudes of the spin-orbit coupling, tetragonal distortion and rotation of the IrO_6 octahedra, along with some inconsistency in the figures in the manuscript. Slightly different values of these leads to a state with weak easy-plane anisotropy; for instance including a tetragonal distortion of 0.15 eV gives $\Delta_\lambda = 0.007$.

ESR measurements

Electron spin resonance (ESR) measurements by Bahr and colleagues [226], and Bogdanov *et al.* [227], also reveal the presence of an out-of-plane spin gap, however the magnitude of said

---

[12] Localised spin picture.

[13] Actually $t_{\text{eff}} = t^2/\Delta_{\text{pd}}$, where Δ_{pd} is the charge-transfer gap. If $\Delta_{\text{pd}} = 3.3$ eV [32], then $t = 0.65$ eV.

[14] Calculated from $J = 4t^2/U$; in manuscript hopping determined in terms of the Slater-Koster parameters $t_{pd\sigma} = -1.8$ eV and $t_{pd\pi} = 0.83$ eV.

gap (0.83 meV and 1.1 meV respectively) is considerably smaller than that observed via RIXS (38 meV). As stated earlier however, the finite energy and momentum resolution means that the true spin gap energy cannot be fully resolved via RIXS, and that it should be treated as an upper estimate. Bogdanov proposed an alternative Hamiltonian which takes the rotation of the iridium octahedra into account via a Dzyaloshinskii-Moriya term $\mathbf{D} \cdot \mathbf{S}_i \times \mathbf{S}_j$, and symmetric anisotropy by a symmetric traceless second-rank tensor $\bar{\Gamma}$, but neglects the effect of second- and third-nearest neighbours. The main reason for the latter is the difficulty of including longer-distance interactions in quantum chemistry calculations. These *ab initio* calculations determined the nearest-neighbour magnetic couplings for a Ir_2O_{11} cluster, obtaining values of $J = 47.8$ meV, $D = \pm 11.9$ meV, $\Gamma_{xx} = \Gamma_{zz} = 0.42$ meV, and $\Gamma_{yy} = -0.84$ meV. If a magnetic field h is applied parallel to the z-direction, then two modes should be observed by ESR: a Goldstone mode and a gapped excitation. Using the Hamiltonian proposed by Bogdanov*et al.* , the frequency of this gapped excitation $\nu_{||}$ is given by

$$\nu^2 = \delta^2 + \frac{2g_{||}^2 h_{||}^2 \tilde{J}}{2\left(J + \Gamma_{zz}\right) + \tilde{J}}, \tag{5.25}$$

where $\delta = \sqrt{2\tilde{J}\left[\tilde{J} - 2\left(J+\Gamma_{zz}\right)\right]}$, $\tilde{J} = \sqrt{4D^2 + \left(2J-\Gamma_{zz}\right)^2}$ and $g_{||} = 2.31$. Consequently in the zero-field limit, and using the values for the couplings given above, the out-of-plane spin gap $\nu_{||} = \delta = 18$ meV, somewhat comparable to that measured by RIXS. However a good fit to experiment ($\nu = 1.1$ meV) could only be achieved if Γ_{zz} were set to 0.98 meV. Nevertheless the ratio $\Gamma_{zz}/\tilde{J}$ – which is approximately equivalent to Δ in the expression for the 2DAH[15] – can be evaluated as $\Gamma_{zz}/\tilde{J} = 0.015(7)$, with the quantum chemistry calculations and experiment taken as the upper and lower limits respectively. This value is of similar magnitude to that obtained for Δ via RIXS, and Igarashi and Nagao's predictions for a localized model, and thus further corroborates the conclusion presented here that easy-plane anisotropy is indeed important for Sr_2IrO_4.

---

[15] From [225], anisotropy $\Delta = 1 - J_{zz}/J_{xx}$.

5.7 Critical scattering from $Sr_3Ir_2O_7$

The single layer compound Sr_2IrO_4 is merely the first in a series of so-called Ruddlesden-Popper perovskite iridates, which follow the progression $Sr_{n+1}Ir_nO_{3n+1}$. The successive compound in the Ruddlesden-Popper series, the bilayer $Sr_3Ir_2O_7$, exhibits considerably different behaviour, despite at first glance appearing to be structurally similar. What follows is a brief précis of the relevant properties of this material.

5.7.1 Synthesis and bulk properties

Subramanian *et al.* [228] first report the synthesis of single crystals[16] of $Sr_3Ir_2O_7$, and via laboratory X-ray diffraction determined the space group to be the tetragonal $I4/mmm$ (lattice parameters $a = 3.896$ Å, $c = 20.879$ Å). In this structure (Fig. 5.18a), the IrO_6 octahedra have a correlated rotation of 12° about the c-axis, but unlike in Sr_2IrO_4, alternate layers have the same rotation.

However there is a degree of controversy over the true space group for $Sr_3Ir_2O_7$. Later X-ray measurements by Cao *et al.* [230] and electron diffraction measurements by Matsuhata *et al.* [231] determined the space group to be $Bbca$ and $Bbcb$ respectively. These space groups were assigned based on the existence of weak oxygen superlattice reflections that cannot easily be observed by laboratory X-ray diffraction, which result due to slight octahedral tilting perpendicular to the c-direction. Recent single crystal neutron diffraction and second harmonic generation (SHG) [232] show further reduction in symmetry to a $C2/c$ space group, caused by an additional octahedral tilt. It should be noted however that these distortions are very small ($< 1^\circ$), and are expected to play little to no significant role for the magnetic correlations and excitations. Consequently the $I4/mmm$ convention shall be used for the remainder of this thesis.

Resistivity measurements by Cao and colleagues [230] revealed that $Sr_3Ir_2O_7$ was insulating (Fig. 5.18d), bordering on semiconducting for all temperatures up to 1000 K. Optical conductivity measurements by Moon *et al.* [32] showed that the optical gap decreases dramatically when moving down the Ruddlesden-Popper series. For $Sr_3Ir_2O_7$, only a very small optical gap could be observed, however no quantitative analysis was performed. Based on DFT calculations, Moon suggested that the increased bandwidth of the $j_{\mathrm{eff}} = \frac{1}{2}$ state for the bilayer was responsible for the reduced optical gap. ARPES measurements by Wojek *et al.* [235] and King *et al.* [153] indicated that the charge gap was on the order of 100 meV, however they noticed that the bandwidth of the $j_{\mathrm{eff}} = \frac{1}{2}$ states was in fact reduced compared to the single layer compound. This implies that $Sr_3Ir_2O_7$ lies close to the metal-insulator boundary, and perturbation of the band structure with pressure may force a metal-insulator transition. However Zocco and colleagues [236] observed no metal-insulator transition in the resistivity, even under 55 GPa of applied pressure.

---

[16] However synthesis of powder samples of $Sr_3Ir_2O_7$ were reported as early as 1972 by Kafalas and Longo. [229]

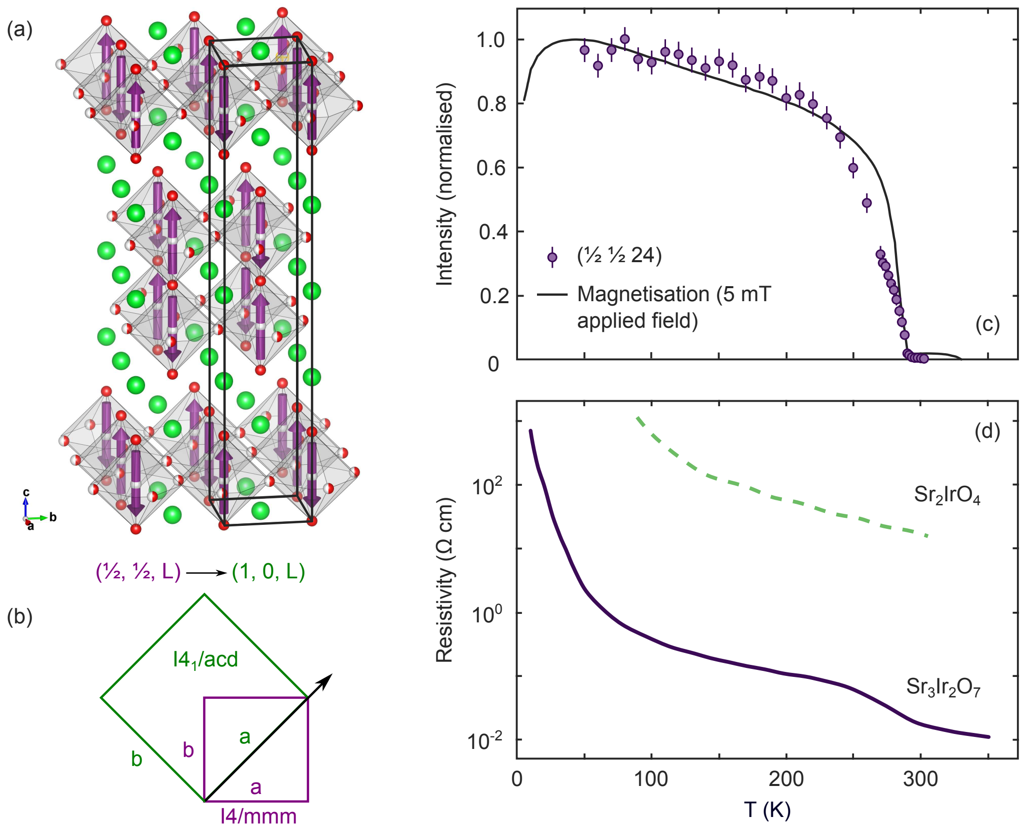

Figure 5.18: (a): Crystal structure of $Sr_3Ir_2O_7$. The material is a G-type antiferromagnet below T_N, as shown by the arrows on each Ir site. (b): Relationship between the $I4/mmm$ space group used for $Sr_3Ir_2O_7$ compared to the $I4_1/acd$ space group used for Sr_2IrO_4. The $I4_1/acd$ unit cell is enlarged by $\sqrt{2}a \times \sqrt{2}b$ and rotated by 45° with respect to the $I4/mmm$ unit cell. (c): Intensity of the $\left(\frac{1}{2}, \frac{1}{2}, 24\right)$ magnetic Bragg peak obtained from XRMS, compared to magnetisation data obtained from a SQUID magnetometer. Adapted from Ref. [233]. (d): In-plane resistivity of Sr_2IrO_4 and $Sr_3Ir_2O_7$. Adapted from Ref. [234].

The initial report by Cao *et al.* [230] suggested that $Sr_3Ir_2O_7$ exhibits weak ferromagnetism below $T_c = 280$ K, with an ordered moment of 0.037 μ_B, considerably below the spin-only value for $S = \frac{1}{2}$ of 1 μ_B. Nagai *et al.* [237] postulated that the weak ferromagnetic moment in the basal plane occurs a result of canted antiferromagnetism arising from the Dzyaloshinskii-Moriya interaction.

In order to determine the true magnetic structure, Boseggia and colleagues [238] performed RXMS measurements and determined propagation vectors of $\mathbf{k} = \left(\frac{1}{2}, \pm\frac{1}{2}, 0\right)$. The two different propagation vectors are due to the presence of two different magnetic domains. Later work by Boseggia *et al.* [239] showed that the magnetic domains had typical dimensions of 100 μm, and the azimuthal dependence of the magnetic scattering revealed a G-type antiferromagnetic ordering (Ir ions coupled antiferromagnetically with all of their nearest neighbours) with the Ir magnetic moments along the *c*-axis.[17] This differs significantly from Sr_2IrO_4, where the

---

[17] According to Hogan *et al.* [232], the magnetic moments likely remain locked to the orientation of the IrO_6 octahedra, and consequently the weak FM component observed by bulk methods is a direct result of the octahedral tilting away

Ir moments are oriented in the *ab*-plane. The $L_3 : L_2$ intensity ratio of the $\left(\frac{1}{2}, \frac{1}{2}, 24\right)$ magnetic reflection was found to be almost 100, and hence $Sr_3Ir_2O_7$ was implicated as a $j_{\text{eff}} = \frac{1}{2}$ system, in a similar fashion as Sr_2IrO_4. Given that the tetragonal distortion in $Sr_3Ir_2O_7$ is smaller than that observed for Sr_2IrO_4 (or Ba_2IrO_4 for that matter), then it can be concluded that $Sr_3Ir_2O_7$ lies close to the ideal $j_{\text{eff}} = \frac{1}{2}$ limit.

RIXS measurements by Jungho Kim *et al.* [35] mapped the magnon dispersion with 30 meV energy resolution (cf. 130 meV for Sr_2IrO_4), and observed rather different behaviour to that observed for the single-layer compound. The most prominent feature was the presence of a magnon gap of ~ 90 meV, which the authors attribute to contributions from anisotropic pseudodipolar and Dzyaloshinskii-Moriya interactions. The former is driven by large Hund's rule exchange ($J_{\text{H}}/U = 0.24$), whilst the latter occurs due to the staggered rotation of IrO_6 octahedra. Moretti Sala *et al.* [36] offer an alternative model in which the magnetic excitations of $Sr_3Ir_2O_7$ exhibit some degree of singlet character. In anisotropic bilayer systems, the quantum critical point, as shown in Figure 5.1, is replaced by a transition between a gapped antiferromagnet and a gapped quantum dimer system. Based on the observation of a longitudinal (Higgs) magnon mode, along with conventional spin wave excitations, it is believed that $Sr_3Ir_2O_7$ is intermediate of these two regimes.

The perovskite iridates Sr_2IrO_4 and $Sr_3Ir_2O_7$ exhibit very different magnetic behaviour, despite both systems being realisations of $j_{\text{eff}} = \frac{1}{2}$ systems. The out-of-plane interaction mediated by an oxygen ion in $Sr_3Ir_2O_7$ results in a reduced electron correlation and hence a reduced charge gap. This mechanism is also responsible for potential superexchange pathways, which may be responsible for some of the observed magnetic behaviour.

Given that the magnetic interactions differ so greatly between the two compounds, one would expect the critical scattering to show some differences as well. To this end critical scattering experiments were performed on $Sr_3Ir_2O_7$. All measurements were indexed in the tetragonal notation, which effectively averages over the two different magnetic domains.

5.7.2 Critical scattering experiment

Experimental setup

The critical scattering experiments were performed on beamline I16, Diamond Light Source. A single crystal of $Sr_3Ir_2O_7$ (dimensions $0.5\times0.5\times0.3$ mm^3) was flux grown from the phase-pure polycrystalline compound using techniques described elsewhere [148]. The experimental setup was identical to that used for the measurements on Sr_2IrO_4, with the exception that a graphite $(0, 0, 8)$ analyser crystal was used to discriminate between the scattered polarization channels. The wavevector resolution of the instrument, including the effects of sample mosaic, was determined by mapping Bragg peaks in reciprocal space and was found to be typically 2.0×10^{-3}

---

from the *c*-axis (in the $I4/mmm$ setting). Such a small canting of the spins would be very difficult to observe with neutron or magnetic X-ray scattering.

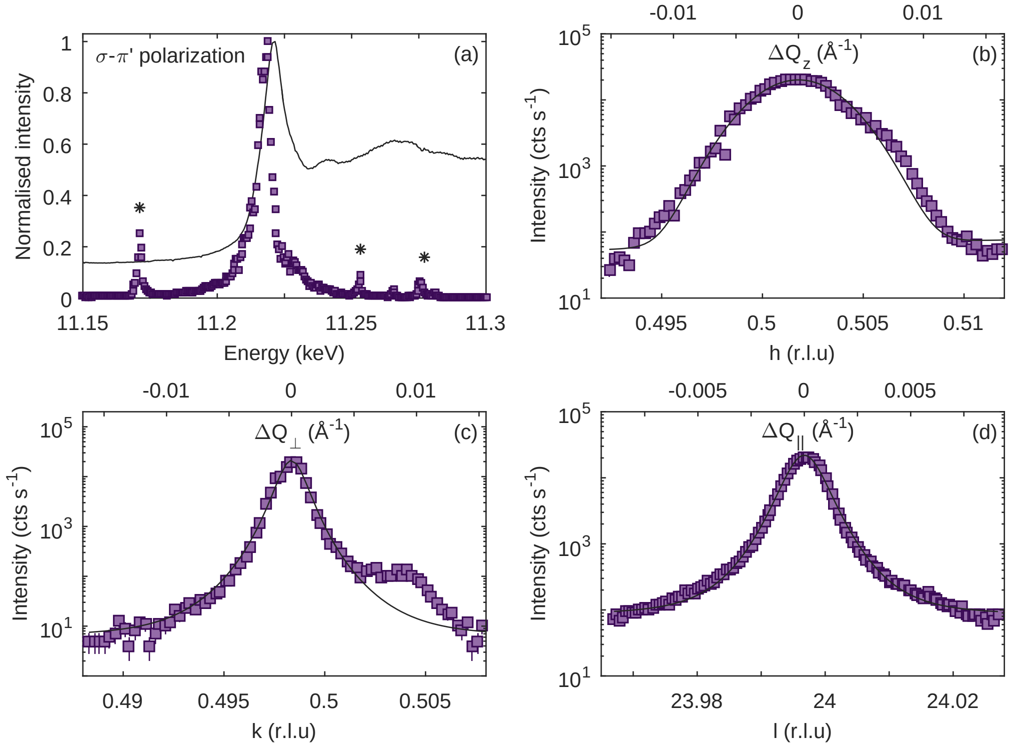

Figure 5.19: (a): Energy scan of the $\left(\frac{1}{2}, \frac{1}{2}, 24\right)$ magnetic Bragg peak with σ–π' polarisation (symbols). Overlaid is the total fluorescence yield (TFY) from the sample (solid line). Peaks marked with asterisks result from multiple scattering. (b)–(d): Reciprocal space scans of the $\left(\frac{1}{2}, \frac{1}{2}, 24\right)$ peak at 200 K, which was used to represent the resolution function. Nearby structural peaks exhibited similar behaviour. Added are the best fit (solid lines) of the data to either a Gaussian function (b) or Lorentzian squared functions (c,d).

Å^{-1} and 1.8×10^{-3} Å^{-1} perpendicular and parallel to $\mathbf{Q}$ in the scattering plane respectively, and 7.4×10^{-3} Å^{-1} out of the plane (Fig. 5.19).

Scattering below T_N

The temperature dependence of the $\left(\frac{1}{2}, \frac{1}{2}, 24\right)$ magnetic Bragg peak was measured in order to determine the value of T_N and the critical exponent β. This is displayed in Fig. 5.20. The intensity decreases continuously as a function of increasing temperature, as would be expected for a second-order magnetic phase transition, going towards zero around 290 K. However unlike a perfect second-order phase transition, the transition is not especially sharp but exhibits some rounding. Rounding of the transition can occur due to sample inhomogeneity or defects for example. Consequently the integrated intensity (as determined from fits to a Lorentzian-squared lineshape) was fitted with a power law: $I_M \propto [(T_N - T)/T_N]^{2\beta}$ convoluted with a Gaussian distribution of transition temperatures of FWHM Γ. The fit shown in Fig. 5.20 was obtained with $T_N = 283.4(2)$ K, $\beta = 0.361(8)$ and $\Gamma = 2.7(1)$ K. The value of T_N is in good agreement with that obtained from bulk magnetisation measurements and neutron powder diffraction [240].

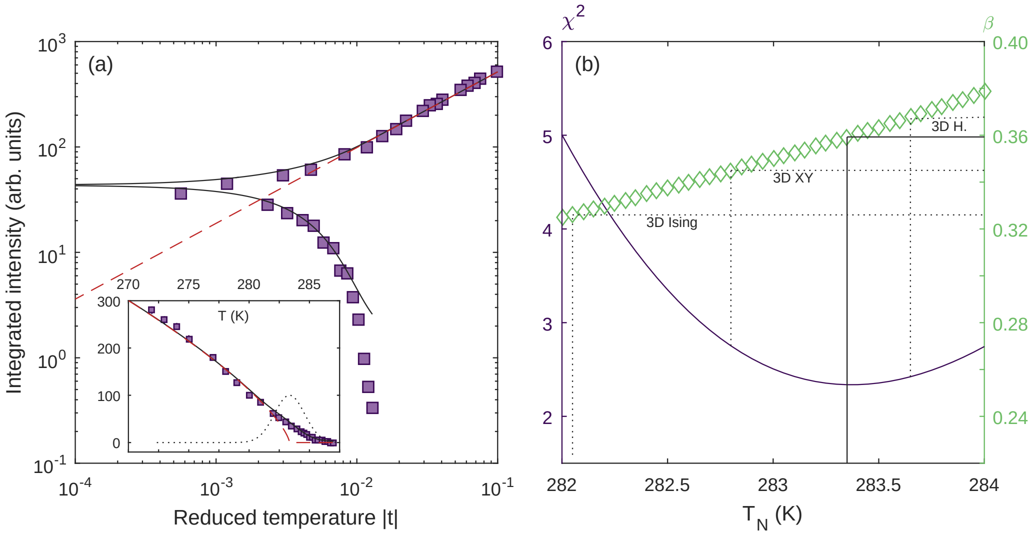

Figure 5.20: (a): Order parameter of $\left(\frac{1}{2}, \frac{1}{2}, 24\right)$ magnetic Bragg peak in terms of the reduced temperature $|t| = |T - T_N|/T_N$, as obtained from θ–2θ scans. Solid line: Best fit to power law convoluted with a Gaussian distribution of T_N with FWHM 2.7(1) K. Dashed line: Corresponding power law assuming single value of T_N. Inset focusses on region around T_N, highlighting the rounding of the transition. Dotted line: Distribution of T_N. (b): Variation of χ^2 (solid line) and β (diamonds) as a function of T_N. The minimum of the χ^2 surface occurs for $T_N = 283.4(2)$ K and $\beta = 0.361(8)$, which is consistent with the theoretical value for 3D Heisenberg interactions.

	β	ν	γ	η	α
3D Ising	0.326	0.6312(3)	1.2378(6)	0.039	0.106
3D XY	0.345	0.669(7)	1.316(9)	0.03	-0.01
3D Heisenberg	0.367	0.707(3)	1.388(3)	0.037	-0.121

Table 5.3: Values of critical exponents for 3D systems as given by Collins [154].

The value of β for $Sr_3Ir_2O_7$ on the other hand differs significantly from previous neutron scattering [$\beta = 0.25$ from [240], revised in [186] as $\beta = 0.20(2)$] and μSR [241] [$\beta = 0.143(3)$] measurements. Discrepancies arise because β was obtained in these studies from power law fits which included a significant number of data points well away from T_N, and hence are somewhat unreliable. The value obtained from critical scattering is representative of 3D magnetic interactions. Comparing it to the theoretical value (Table 5.3), one finds that the magnetic interactions are consistent with a 3D Heisenberg model close to T_N. Given the uniaxial G-type antiferromagnetic structure and excitations, then this is not particularly surprising. The value of β deduced by this analysis establishes the very different critical properties of the single- and bi-layer compounds, and hence the relevant magnetic interactions.

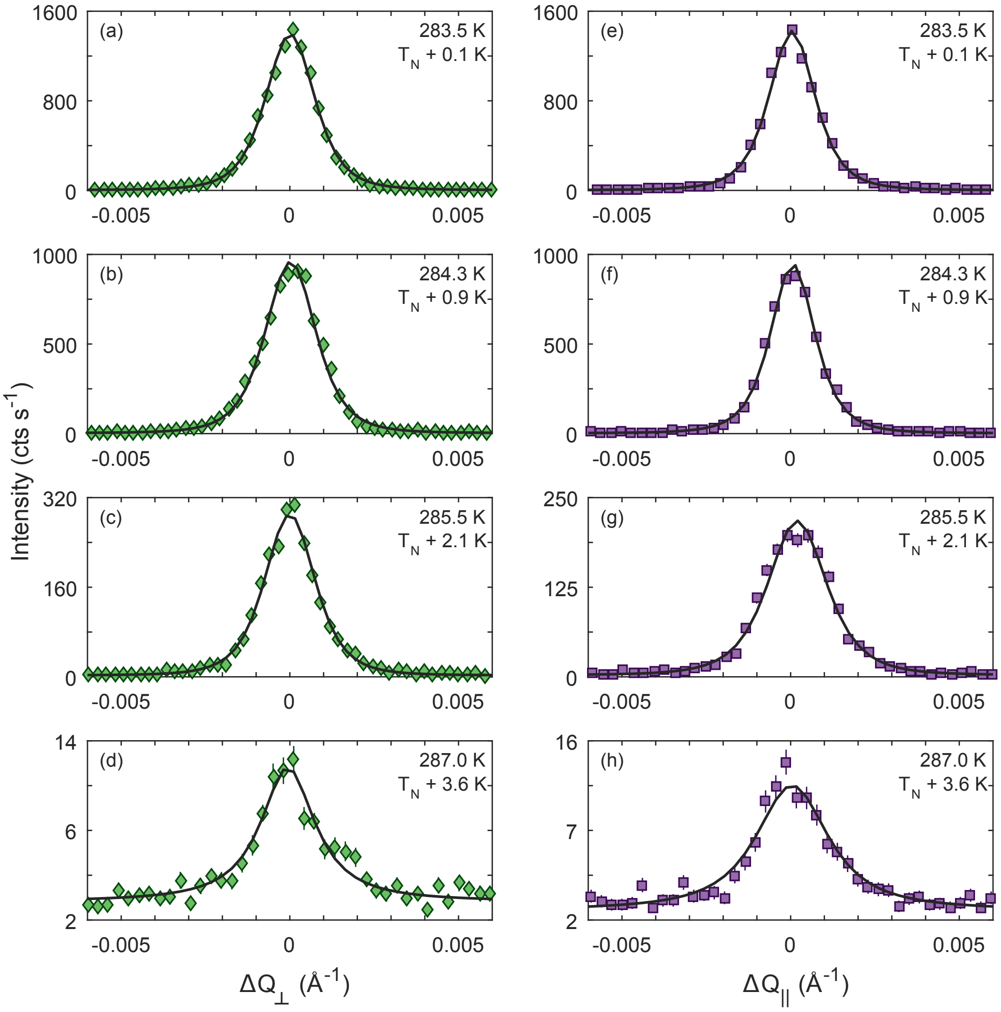

Figure 5.21: Evolution of the $\left(\frac{1}{2}, \frac{1}{2}, 24\right)$ magnetic Bragg peak above T_N in the k- and l-directions (left and right columns respectively). The critical scattering is nearly isotropic. Solid lines are best fit to a Lorentzian-squared function convoluted with the resolution function.

Scattering above T_N

Above T_N, there is some residual intensity, partly resulting from critical scattering, and partly from the rounding of the transition. The magnetic Bragg peak was followed out to 288 K ($T_N + 5.2$ K) for both the in-plane and out-of-plane directions, with a comparison plotted in Fig. 5.21. Compared to Sr_2IrO_4, the critical scattering in $Sr_3Ir_2O_7$ appears isotropic, and decays much more quickly with temperature. This would be expected for systems where 3D interactions are important. Remember that the Néel temperature is associated with the onset of long-ranged three-dimensional antiferromagnetic order. The intensity observed for Sr_2IrO_4 above T_N only arises as a result of dominant 2D correlations in-plane which have a much larger energy scale than those out-of-plane. If the dominant magnetic interactions are three-dimensional, then one would expect both the in-plane and out-of-plane interactions to behave in a similar manner (to first order). In this sense $Sr_3Ir_2O_7$ is more 'conventional'. Consequently the correlation length ξ and intensity S_0 should be expected to follow the simple power laws: $\xi \sim t^{-\nu}$ and $S_0 \sim t^{-\gamma}$.

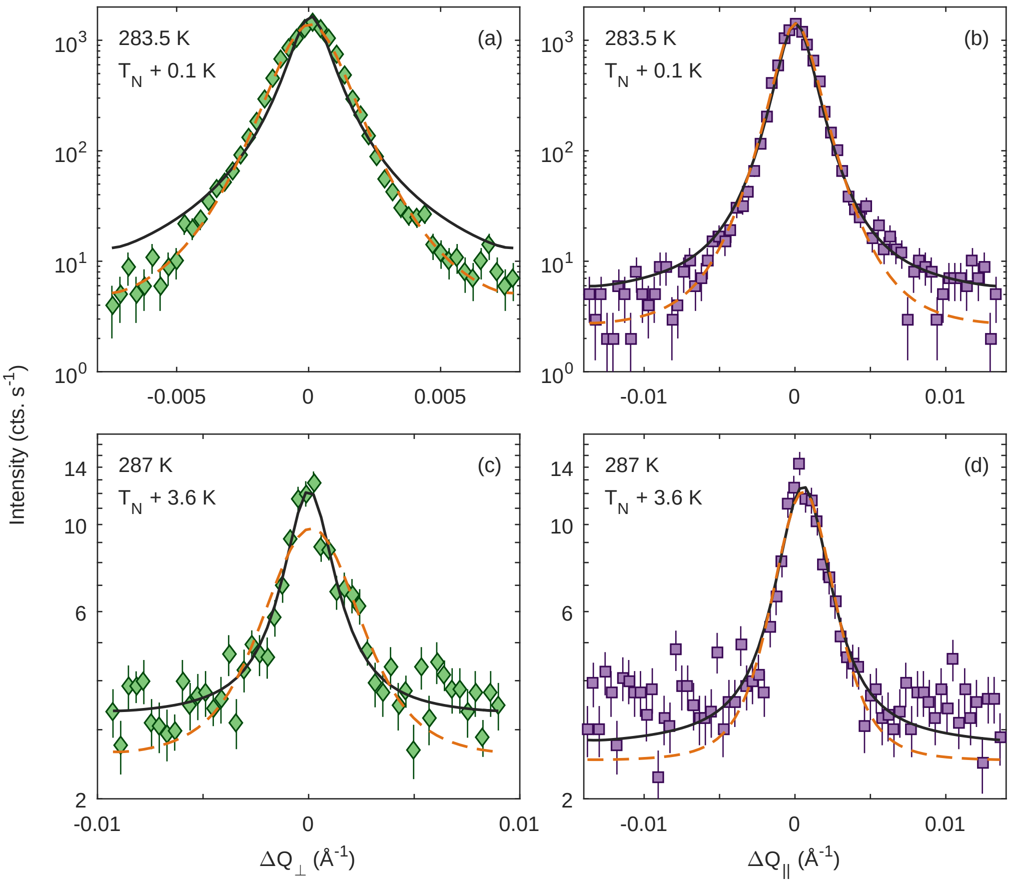

Figure 5.22: Lineshape comparison of fits to critical scattering for the in-plane (a,c) and out-of-plane (b,d) directions. Solid line: Fit to Lorentzian scattering function. Dashed line: Fit to Lorentzian squared scattering function. Results are displayed on a logarithmic scale to highlight differences in the peak tails.

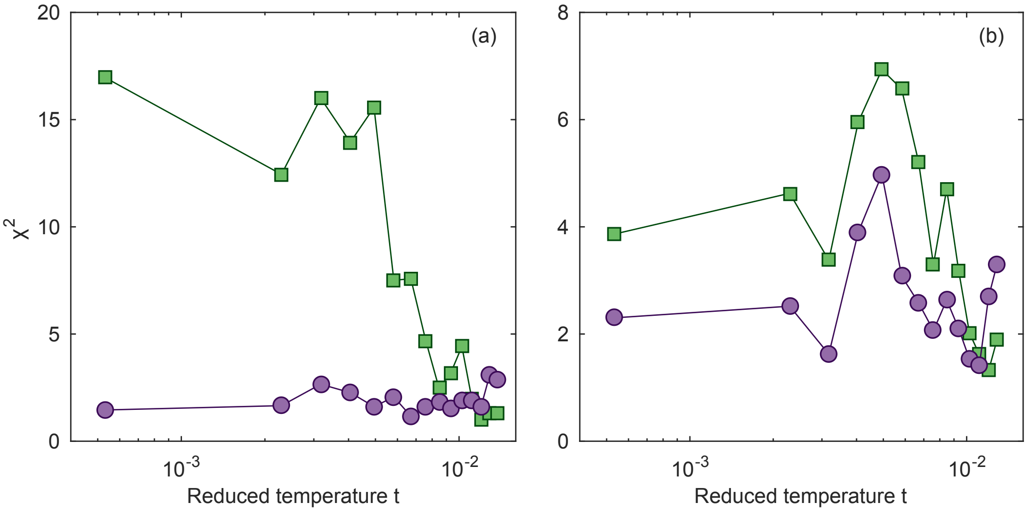

Figure 5.23: Values of χ^2 obtained using either a Lorentzian (squares), or Lorentzian squared (circles) lineshape for the scattering function along $\Delta Q_\perp$ (a) or $\Delta Q_{||}$ (b). A Lorentzian squared function provides the best fit to the data over most of the temperature range.

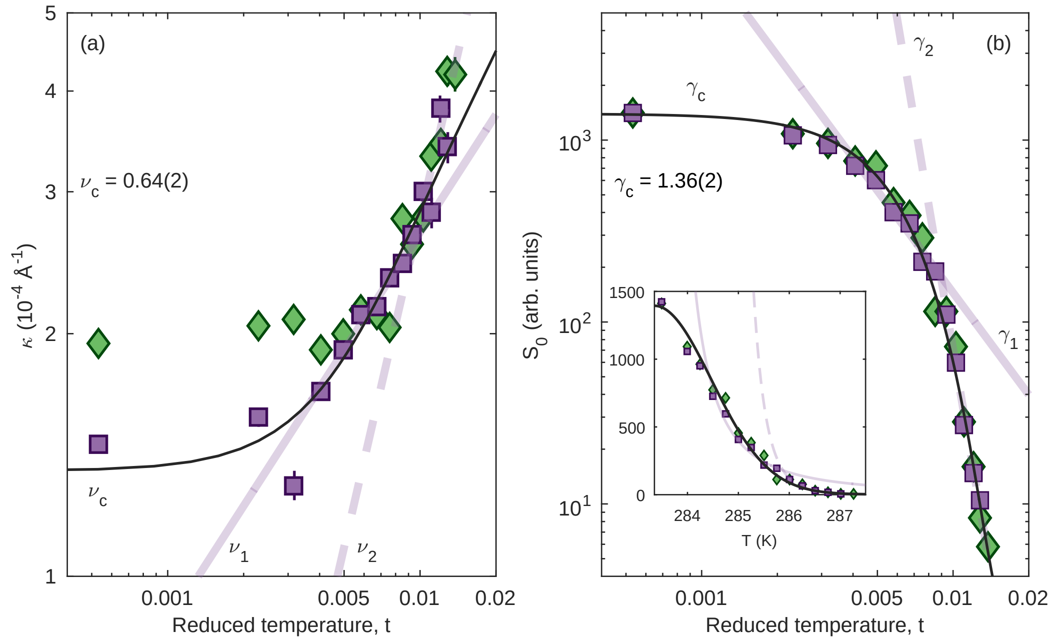

Figure 5.24: Inverse correlation length (a) and intensity (b) of $\left(\frac{1}{2}, \frac{1}{2}, 24\right)$ magnetic Bragg peak as a function of reduced temperature $t = T/T_\mathrm{N} - 1$. Solid and dashed purple lines are fits of the out-of-plane data to the relevant power law for two different temperature regions: $\nu_1 = 0.49(4), \gamma_1 = 1.86(3)$; $\nu_2 = 1.4(1), \gamma_2 = 8.2(3)$. Solid black lines are best fit to a power law convolved with a Gaussian distribution of T_N [FWHM 2.7(1) K]. Inset in (b) is the same as the main panel, only plotted on linear axes.

As stated before, the intrinsic critical fluctuations are expected to have an approximately Lorentzian functional form. Yet upon fitting the lineshapes of the magnetic Bragg peaks above T_N, one finds that a Lorentzian squared function (convoluted with the resolution function) is consistently more representative of the data than a Lorentzian function (Figs. 5.22, 5.23). However the discrepancies in the lineshape are almost entirely in the tails of the peak; the fitted values of the peak width are almost identical for both lineshapes. Furthermore for data collected along $Q_{||}$, the differences between the Lorentzian and Lorentzian squared functional forms are small. Given that a Lorentzian squared form is a better fit to both the $Q_\perp$ and $Q_{||}$ data, this is what has been used in the subsequent analysis. Nevertheless the results can be easily extended to the Lorentzian case.[18]

Critical exponents

The fitted values of the inverse correlation length κ and the peak amplitude S_0 are plotted in Figure 5.24 for data collected along $Q_{||}$ and $Q_\perp$. The two datasets appear isotropic, with the

---

[18] The general formula of a Lorentzian squared function is $I = A/\left[1+\left(\frac{x-x_0}{\Gamma}\right)^2\right]^2$. The half width at half maximum (HWHM) of a Lorentzian squared function with some width parameter Γ_L2 is smaller than that of a Lorentzian with the same Γ_L. Consequently $\kappa = \xi^{-1} = \Gamma_L$ (from the Lorentzian approximation to the Ornstein-Zernike correlation function) is not correct for a Lorentzian squared lineshape. One must multiply Γ_L2 by a conversion factor ζ which relates the two: $\kappa = \zeta\Gamma_\mathrm{L2} \approx 0.645\Gamma_\mathrm{L2}$. All data presented has been corrected in this way.

exception of the correlation length for $t < 0.005$. Some of this discrepancy may be due to the deviation of the observed lineshape from an ideal Lorentzian. The form of the correlation function $\hat{C}(\mathbf{q}, 0)$ is dependent on the critical exponent η, which is defined at $T = T_N$ and becomes increasingly relevant close to that limit. However for three-dimensional systems, $\eta \approx 0$ and so this is likely to be a minor effect. An alternative is that two components may contribute to the observed scattering close to T_N. The second component could, for example, result from defect mediated scattering, which experimentally [198] has been shown to have a Lorentzian squared lineshape. However it was not possible to unambiguously resolve more than one component in the data. As the $Q_{||}$ data shows qualitatively more ideal behaviour, quantitative analysis shall be restricted to this dataset from now on.

The saturation of κ and S_0 for $t < 0.005$ suggests that a single power law is insufficient to fully describe the data. Two distinct temperature regions can be observed in which the data appears linear on logarithmic axes. However upon performing simple power law fits ($\kappa \sim t^{\nu}$, $S_0 \sim t^{-\gamma}$) to the data in these regions, one finds that the critical exponents associated with these fits do not correspond to the theoretical values associated with any conventional universality class. Recall that the order parameter data showed a rounding of the transition, which was best described by the convolution of a power law $I \sim -t^{2\beta}$ with a Gaussian distribution of T_N. Yet the simple power law fits to κ and S_0 assume a single value of T_N. Convolution of a single power law with a Gaussian distribution of T_N (of the same width as that used for the order parameter data) provides a much better description of the temperature dependence of the correlation length and amplitude. The values extracted from these fits are $\nu = 0.64(2)$ and $\gamma = 1.36(2)$.

The critical exponents arising from the order parameter, inverse correlation length, and susceptibility are all consistent with three-dimensional magnetic interactions (Table 5.3). However there is some discrepancy in the spin dimensionality that these exponents represent. Whilst the obtained order parameter exponent $\beta = 0.361(8)$ and susceptibility exponent $\gamma = 1.36(2)$ agree well with the theoretical values for the 3D Heisenberg universality class, the correlation length exponent $\nu = 0.64(2)$ is more comparable to the 3D Ising or 3D XY universality classes. The discrepancy may, at least in part, be down to the complication of the lineshape, especially close to T_N. Calculating the expected values of the critical exponents using various scaling relations (Table 5.4), one generally finds good agreement with the theoretical values for the 3D Heisenberg model. However there is a greater discrepancy from theory for critical exponents for which the relevant scaling relation depends on ν. This leads to the conclusion that ν may have been underestimated slightly experimentally.

One point to note is that the theoretical values of the critical exponents were calculated for an isotropic 3D Heisenberg Hamiltonian. Yet a significant spin wave gap can be observed for $Sr_3Ir_2O_7$, which implies a degree of anisotropy. There is however a renormalisation group argument [243] which follows that even if the effects are relevant perturbations of the Heisenberg fixed point, the difference in critical exponent is sufficiently small such that it is experimentally indistinguishable from the isotropic case.

Scaling relation	Expected value	Theoretical value	Experiment
$\nu = (\gamma + 2\beta)/d$	0.69(1)	0.705(5)	0.64(2)
$\beta = \frac{3}{2}\nu - \frac{1}{2}\gamma$	0.28(5)	0.361(8)	0.362(2)
$\eta = 2 - \gamma/\nu$	-0.1(1)	0.033(4)	–
$\alpha = 2 - 2\beta - \gamma$	-0.08(3)	-0.11(2)	–
$\delta = 1 + \gamma/\beta$	4.8(1)	4.837(7)	–

Table 5.4: Scaling relations. Expected values are calculated from experimental values. Theoretical values for 3D Heisenberg model are obtained from Holm and Janke [242].

5.7.3 Summary

Magnetic critical scattering highlights the significant differences in the dimensionality of the magnetic interactions for Sr_2IrO_4 and $Sr_3Ir_2O_7$. For Sr_2IrO_4, analysis of the order parameter below the Néel temperature reveals that the magnetic interactions are predominantly two-dimensional, in agreement with previous results. However the critical exponent was found to be consistent with the 2D XYh_4 universality class, which implies the presence of significant anisotropy. Furthermore the temperature dependence of the correlation length and amplitude could not be fitted to any previously assumed 2DHAFSQL model, but was consistent with a model including some degree of easy-plane anisotropy. The magnitude of this anisotropy was estimated via the spin gap observed by recent high-resolution RIXS measurements, and found to be in quantitative agreement with a number of theoretical predictions, including the seminal work by Jackeli and Khaliullin [25]. This demonstrates that Sr_2IrO_4 exhibits significant departures from an ideal 2DHAFSQL, and highlights the effect that spin-orbit coupling plays within the magnetic Hamiltonian.

On the other hand, $Sr_3Ir_2O_7$ is a more three-dimensional system, as evidenced by practically isotropic critical scattering. Despite a rounding of the transition and some complications with the scattering lineshape, critical exponents could be extracted which are broadly consistent with a 3D Heisenberg model. This is consistent with a picture where significant intra-bilayer interactions are present.

Summary of contributions

The critical scattering data (Sr_2IrO_4 and $Sr_3Ir_2O_7$) were collected with the assistance of Stefano Boseggia and Zhuo Feng from UCL, Helen Walker from DESY, and Ross Springell from the University of Bristol. All data analysis was performed by the author. Modelling of the Sr_2IrO_4 critical scattering data was aided by theoretical discussions with Steve Bramwell from UCL (2D XYh_4), and Henrik Rønnow from EPFL (2DAH). These discussions were limited to the choice of model, and expected scaling of the thermodynamic parameters with temperature. The Sr_2IrO_4 RIXS data was extracted from Ref. [192], modelled, and fitted by the author.

Chapter 6

Time-resolved resonant X-ray scattering measurements on Sr_2IrO_4

Transition metal oxides can be driven out of equilibrium using an optical pulse which couples to a specific degree of freedom of the system. This includes the manipulation of charge and spin gaps, which evolve on an ultrafast timescale (10^{-15} – 10^{-12}s). The transient behaviour of the system can only be measured by a probe which acts on the same timescale. Fortunately state of the art X-ray free-electron laser (XFEL) facilities provide such capabilities.

Proof-of-principle experiments were performed on Sr_2IrO_4, in order to determine whether resonant (in)elastic X-ray scattering on 5d TMOs could be extended to the time-resolved domain. Excitation of electrons across the charge gap through photo-doping resulted in the partial melting of long-ranged magnetic order. This recovered on a timescale proportional to the pump fluence. Time-resolved RIXS measurements (using custom-built instrumentation) determined that two-dimensional correlations recovered much more quickly, with some differences between the behaviour at (π, π) and $(\pi, 0)$. This is what would be expected for a system where the magnetic interactions are predominantly two-dimensional. Moreover the relevant timescales are in quantitative agreement with the various interactions present, and the results can be directly compared to observations for the bulk electron doped system $Sr_{2-x}La_xIrO_4$.

It is well known that introducing dopant ions or oxygen vacancies into layered copper oxides leads to a number of exotic electronic and magnetic ground states. The most famous example is $YBa_2Cu_3O_{7-x}$, which exhibits high temperature superconductivity for a narrow range of hole doping x. Another well characterised example is hole-doped $La_{2-x}Sr_xCuO_4$, which for small x is an antiferromagnetic Mott insulator, whereas at higher x the behaviour is rich and diverse (Figure 6.1).

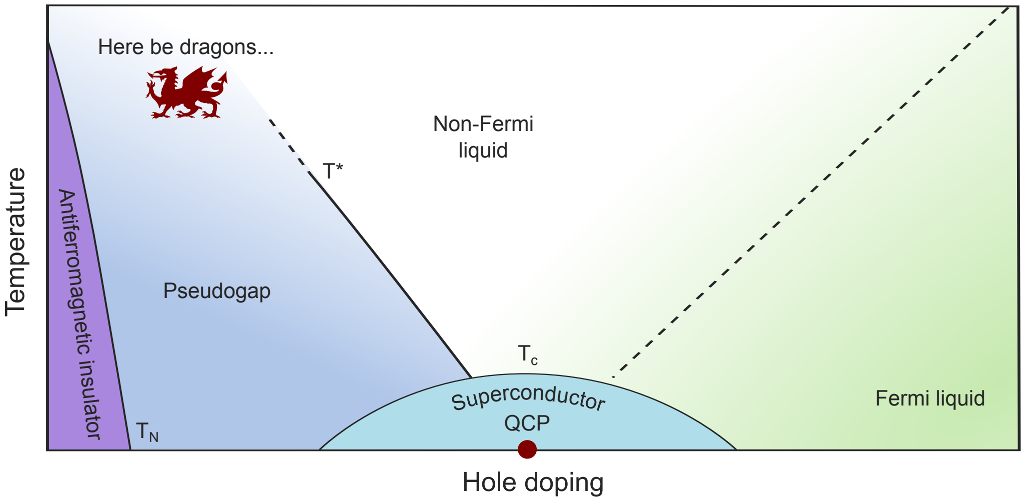

Figure 6.1: Phase diagram for the hole-doped cuprates. There are expected to be a number of similarities between this phase diagram and that for the electron-doped iridates. Crossovers are indicated by dashed lines. There is a quantum critical point (QCP) situated underneath the superconducting dome.

A number of theoretical predictions and experimental studies find similarities between the hole-doped cuprates and the electron-doped iridates. These include a metal-insulator transition as a function of carrier doping, pseudogap phases, Fermi arcs[1], and suppression of long-ranged antiferromagnetic order. The holy grail is superconductivity, which has not been observed at the time of writing. Chemical doping suffers from a number of problems, including homogeneity within the sample, phase separation, discrepancies between the surface and bulk doping, and knowing the precise quantity of dopant ion which has incorporated.

One alternative is photodoping, whereby the normally insulating system is excited by some optical pulse. An electron in the valence band is excited across the charge (Mott-Hubbard) gap and populates the conduction band (Fig. 6.2). This excited electron hops to a neighbouring site, leading to the formation of a doublon-hole pair. After some time τ_c these doublon-hole pairs recombine, leading to a recovery of the insulating state.

The formation of doublon-hole pairs perturbs the local magnetic correlations, resulting in the destruction of long-ranged magnetic order above some critical concentration of doublon-hole pairs. However the magnetic interactions may have a lower energy than the doublon-hole pair energy, and consequently take a longer time to recover. The interactions in the transient state can be directly related to those in the bulk chemically doped state. A *pump-probe* experiment can be performed so that the dynamics of these interactions can be measured.

---

[1] Note that these were observed in a system which was extrinsically doped on the surface with potassium ions, and hence may not be representative of the bulk phase.

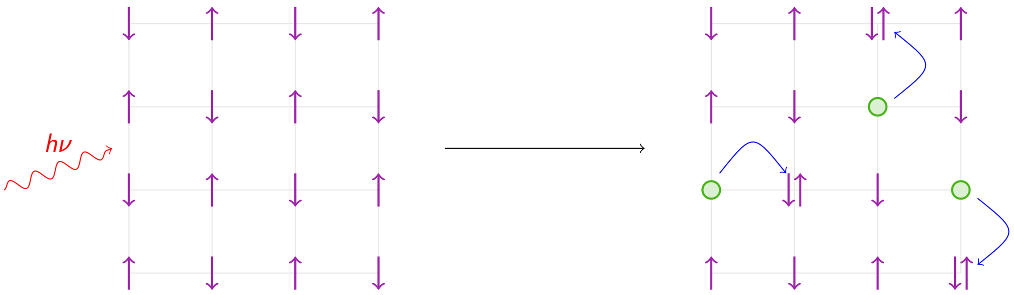

Figure 6.2: Formation of doublon-hole pairs upon excitation with some pump pulse. Left panel: An electron is excited across the charge gap and populates the valence band. Right panel: This excited electron hops to a neighbouring site, leading to the formation a doublon-hole pair. These doublon-hole pairs then recombine on some ultrafast timescale (∼ picoseconds) which depends on their energy of formation and their separation.

Outline of a pump-probe experiment

The principle behind a pump-probe experiment is very simple. An optical pulse (the pump) shines on the sample and perturbs the system in some way. Depending on the energy of the pump pulse, a rotational, vibrational, electronic transition or another type of excitation may be induced. Some time t later, a probe pulse hits the sample and interacts with it in some way, for example scattering or absorption. The scattered, diffracted or transmitted probe is measured by a detector and by varying the time delay between the pump and the probe, the temporal dependence of the transition can be determined. If both the pump and the probe are optical, then varying the time delay is simply a case of varying their relative path lengths (since they travel at the speed of light in free space). For example, a time delay of 1 ps would correspond to a path difference of 0.3 mm. Measurement of shorter timescales involves a significant amount of precision engineering and/or electronic control of the delay time.

Ultrafast optical techniques have been used to probe reaction dynamics since the 1950s, with Eiger, Norrish and Porter independently developing the flash photolysis method to look at radical formation and their kinetics. With the development of the laser, these techniques have pushed further towards probing samples with atomic resolution and sub-femtosecond timescales. Using ultrafast lasers to pump magnetic systems and study their dynamics is a relatively recent progression [244, 245]. In essence one probes the time dependence of the magnetisation as a function of pump time delay and fluence.

The choice of pump and probe pulse used strongly depends on the specifics of the system to be measured, in particular the relative energy scales of the magnetic interactions and of any relevant perturbations. Using an X-ray source (such as a synchrotron) as the probe enables atomic resolution of the structure and magnetic behaviour both before and after the pump.

6.1 X-ray free electron lasers (XFELs)

However as mentioned previously (Chapter 2), a synchrotron suffers from the fundamental limitation that the electron bunch length is considerably longer than many electronic and magnetic timescales. Free electron lasers (FELs) on the other hand have much shorter bunch lengths on the order of 100 fs. Furthermore the intense coherent radiation generated (peak brightness orders of magnitude greater than at a synchrotron) allows ultrafast imaging of atomic and molecular states.

A FEL is characterised by two main properties: high transverse coherence of the generated radiation, and a gain process that is based on stimulated emission. In these regards an FEL really does behave like a laser. There are some differences however which shall be detailed below.

Low gain FEL

The first of these is that in a conventional laser (IR or visible), the light is generated by stimulated emission and reflected within an optical cavity by two mirrors. One of these mirrors allows a small proportion of the light to be emitted. A free-electron laser in the infrared and optical regime broadly follows the same principle, and is referred to as a low gain FEL. A low gain FEL consists of three components. The first of these is a circulating electron beam, produced for example in a synchrotron. This electron beam passes through an undulator which generates a light pulse. Thus far the principle is the same for conventional synchrotron radiation. The difference is that this light is reflected between two mirrors (one is semi-permeable to allow a small amount to be emitted), and is amplified by a few percent in each turn. Coherent emission of radiation is achieved by energy transfer between the electron and light wave to obtain the correct phase of the light wave.

However this technique is very difficult to implement in the UV and X-ray regimes as no suitable mirrors are available (reflectivity very small). Therefore the FEL gain must be achieved in a single pass through a very long undulator. This is known as a high gain FEL.

High gain FEL

In a high gain FEL, a large number of electrons have to radiate coherently. The radiation emitted from a high gain FEL grows quadratically with the number of electrons in the bunch. However Coulomb repulsion between electrons means that maintaining a single bunch is very difficult.

A high gain FEL is started up by some seed signal which co-propagates with the electron beam in the undulator. Depending on the relative phase of the electrons compared to the seed signal, some electrons gain energy from the radiation whilst others lose energy as they pass through the undulator. As faster electrons begin to catch up with slower electrons, density modulations occur in the electron bunch (microbunching). If the conditions are favourable, then the microbunched electron beam emits coherent radiation at the expense of the beam kinetic en-

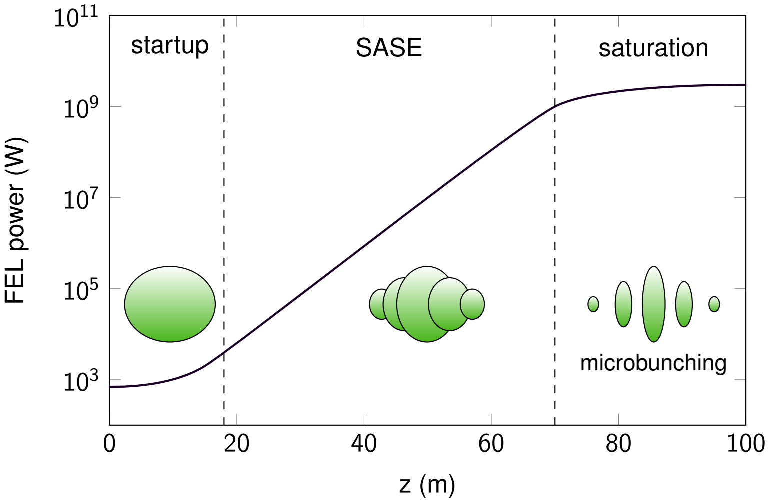

Figure 6.3: Power gain $P(z)$ as a function of undulator distance z for a high-gain XFEL. Labelled are the startup, self-amplified spontaneous emission (SASE) and saturation regions. The SASE region is characterised by an exponential gain in the FEL power as a function of z. After a critical distance $\sim 18L_{g0}$, the FEL power saturates as the electron beam begins to take energy away from the generated light wave.

ergy. Thus the electromagnetic wave gains energy and FEL amplification is achieved. This amplification is characterised by an exponential gain in the FEL power P as a function of undulator distance z (Fig. 6.3).

Solution of the 1D FEL equations (higher dimensions require consideration of many-body effects) gives:

$$P(z) = \exp\left(z/L_{g0}\right), \tag{6.1}$$

with the gain length

$$L_{g0} = \frac{\lambda_u}{4\pi\sqrt{3}\rho},$$

where λ_u is the undulator period, and ρ is the Pierce FEL parameter. Typically $\rho \sim 5 \times 10^{-4}$ in the hard X-ray regime, however the exact value depends on a number of parameters including the wavelength, peak current, undulator parameter K and horizontal emittance. Experimentally this exponential gain region occurs after some initial stabilisation period (approximately $4L_{g0}$, and the FEL power reaches saturation at $\sim 18L_{g0}$ since if the undulator is longer than this, then the electron beam starts to take energy away from the light wave.

Usually the seed signal is provided by the spontaneous undulator radiation which arises from the electron shot noise. This method is called self-amplified spontaneous emission (SASE), and is used in the majority of XFELs in some form. The SASE FEL exhibits excellent transverse coherence as a consequence of a feature called optical guiding, in which a Gaussian fundamental mode starts to dominate over all other fluctuations after a few L_{g0}. On the other hand, the longitudinal coherence is relatively poor, as a consequence of the noisy startup. The fluctuations of the shot-to-shot pulse energy follows a Gaussian distribution (Fig. 6.4), with the root mean

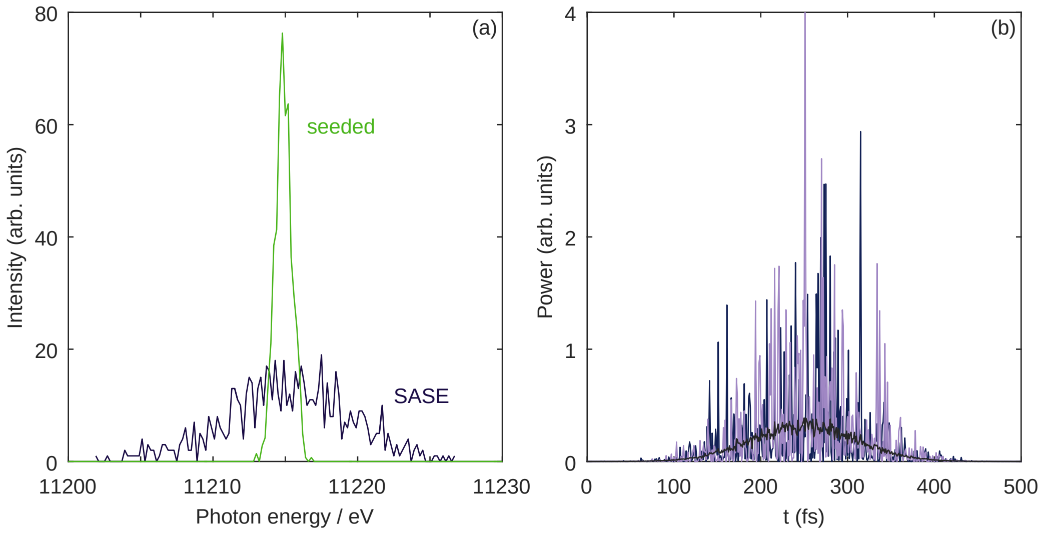

Figure 6.4: (a): Comparison of the spectra of a single FEL pulse using a SASE or a seeded mode. (b): Temporal profile of two FEL pulses (different shades of purple), along with average over 120 pulses (black). FEL parameters used were obtained from Huang [246].

squared fluctuation given by $1/\sqrt{M}$. The parameter M in this case characterises the number of temporal degrees of freedom,[2] which for a FEL in the hard X-ray regime is typically $\sim 10^3$.

In the frequency domain, the full SASE spectral width is approximately $2\sqrt{\pi}\sigma_\omega$, which consists of M individual modes. This bandwidth is typically tens of eV in the hard X-ray regime when averaged over a number of pulses, and also follows a Gaussian distribution. Using a monochromator to select a small bandwidth of the pulse (and hence a small number of spectral modes) will improve the longitudinal coherence, however the pulse power will be subsequently decreased. An additional problem is that the statistical fluctuations from pulse to pulse will increase as a consequence of the $1/\sqrt{M}$ dependence. To summarise, the normalised frequency bandwidth $\Delta\omega/\omega \sim \rho$ for a SASE FEL, where ρ is the Pierce FEL parameter. Furthermore the temporal profile of the radiation generated by the SASE process exhibits considerable fluctuations as a consequence of the initial noisy startup.

These deficiencies can be ameliorated somewhat by using an external seed signal instead of electron shot noise to startup the FEL. In the XUV and soft X-ray regimes, it is possible to use a laser to directly seed the electron beam via high-gain harmonic generation (HGHG). However this technique does not extend easily to the hard X-ray regime. An alternative is to use X-rays from one part of the undulator to seed a subsequent part. This is known as self-seeding [247, 248].

In the hard X-ray regime, the principle is as follows. SASE radiation is generated by a sufficiently long portion of the undulator, such that the exponential gain region is reached. Empirically the peak power of this radiation should be $\sim$1 GW to act as an effective seed. As before, this

---

[2] The critical quantities are the coherence time t_c and the pulse duration T. The coherence time t_c is defined as $t_c = \sqrt{\pi}/\sigma_\omega$, where $\sigma_\omega = \omega_1 \left[\frac{3\sqrt{3}\rho}{k_u z}\right]^{1/2}$ and ω_1 is the fundamental undulator frequency. For a photon energy of 11 keV, $t_c \approx 300$ attoseconds at saturation. If $T \gg t_c$, then $M \sim T/t_c$, which for a pulse length of 300 fs implies $M \sim 10^3$.

SASE radiation has an intrinsic bandwidth of tens of eV. A crystal monochromator then selects a portion of the SASE radiation, which is then used as a seed for the electron beam for the second part of the undulator. However the monochromatic X-rays will be delayed with respect to the initial X-ray beam, in accordance with the dynamical theory of diffraction. Thus the electron beam must also be delayed in order for it to be seeded effectively. This is done by the addition of a magnetic chicane. A typical two-bounce monochromator would delay the incoming X-rays by 5-10 ps, which would require an inordinately long chicane and suppression of the FEL gain. Utilising a forward Bragg diffraction (FBD) geometry enables a much shorter chicane to be used, that is one which can be easily fitted in place of one or two short undulator segments[3] (a couple of metres long).

For these reasons a seeded X-ray beam is ideal for measuring time-resolved resonant magnetic X-ray scattering. However difficulties in engineering a suitable setup – especially at high energies where longer chicanes and higher order Bragg reflections are required – mean that it was not possible to use a seeded beam for the measurements presented here. Nevertheless, it remains a future opportunity.

6.2 System dynamics

Pump-probe experiments at an XFEL examine the transient dynamics of a material on an ultrafast timescale (femtoseconds–picoseconds). How the system behaves upon excitation is dependent on the strength and type of interactions inherent to that system. In general interactions in a system can be qualitatively described by a single model which contains three separate, yet mutually interacting reservoirs [245]. These are namely the carriers (electrons/holes), the lattice, and the atomic spins. Each of these baths can be ascribed an effective temperature, which is possible if some equilibrium between the baths is assumed. The relative magnitude of coupling between these baths dictates the relevant timescales in the system.

Upon excitation with some optical pulse, a series of sequential phenomena occur (Fig. 6.5). Firstly electron-hole pairs are generated on a timescale of $\sim$1 fs. This extremely fast timescale results from either interband transitions in metals, or the charge transfer gap in insulators, and frequently leads to a dramatic increase in the effective electron temperature T_e of a few thousand Kelvin. Such a large increase is a consequence of the electronic heat capacity ($\sim T/T_\mathrm{F}$) being significantly smaller than the lattice heat capacity for instance ($\sim T^3$). The excited electronic system then equilibrates at some elevated temperature $\mathrm{T_{el}}$ within a time period of 10–500 fs by electron-electron interactions. Recombination of the electron-hole pairs occurs either by phonon

---

[3] Further details are given in the studies by Geloni *et al.* [249], Lindberg and Shvyd'ko [248, 250], but the basic principle is as follows. Forward Bragg diffraction smears out the exiting X-rays temporally, giving rise to a monochromatic tail (wakefield) with a series of Bessel oscillations characteristic to the specifics of the system – including the crystal thickness. The period of these oscillations is on the order of tens of fs for typical crystal thicknesses and energies. The monochromatic portion is also separated spatially from the SASE background. By introducing a delay in the electron beam equal to this period, the same effect of self-seeding occurs.

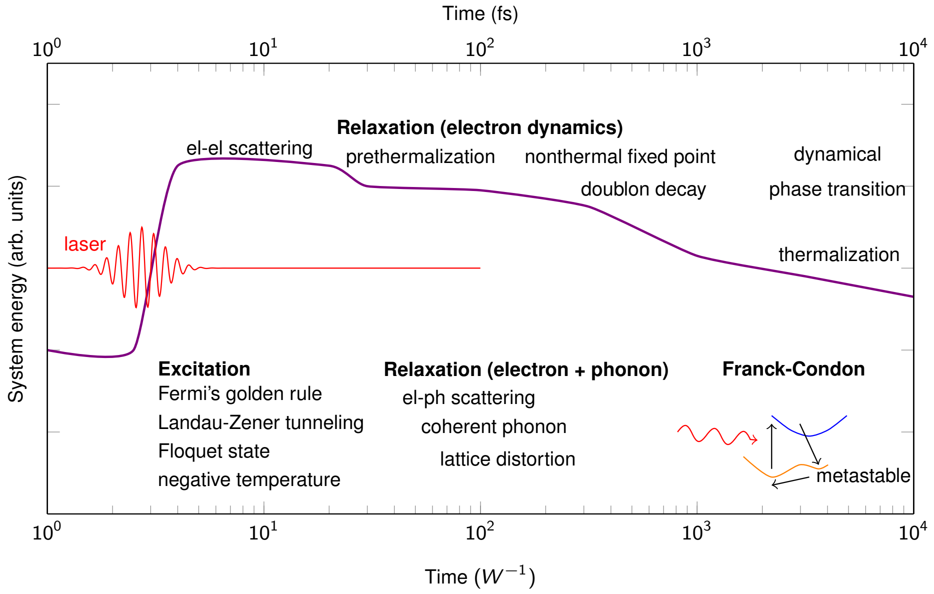

Figure 6.5: Schematic time evolution of a system in a pump-probe experiment, with various physical processes labelled. The time scale of the various phenomena are dictated by the electronic bandwidth W, with the actual time in femtoseconds given as a ballpark figure. Adapted from [251].

cascades due to the electron-phonon interaction, or in insulators, by doublon decay.[4] Finally thermalisation of the system occurs through dissipation of the deposited energy by low-energy interactions such as phonon-phonon scattering.

Often the altered density of the electron-hole carriers leads to a change in the optical properties of the material after excitation. For example, the transient change in the reflectivity can be interpreted as [252]

$$\frac{\Delta R}{R}(t) = \frac{\partial \ln R}{\partial \varepsilon_1}\Delta\varepsilon_1(t) + \frac{\partial \ln R}{\partial \varepsilon_2}\Delta\varepsilon_2(t), \tag{6.2}$$

where R is the reflectivity, and $\Delta\varepsilon_1$, $\Delta\varepsilon_2$ are the induced changes in the real and imaginary parts of the dielectric function respectively. These two latter parameters can be directly related to the optical conductivity and other optical parameters via Kramers-Kronig analysis. A similar effect can be observed in magnetic systems, where the perturbation of long-ranged magnetic order from its equilibrium state can be observed through the temporal dependence of the magnetisation.

6.3 Time-resolved RXMS measurements on Sr_2IrO_4

Hsieh and colleagues [151] performed pump-probe optical spectroscopy on Sr_2IrO_4 in order to determine the effect of magnetic order on the $j_{\mathrm{eff}} = \frac{1}{2}$ ground state. Upon excitation of the sample with a 800 nm pump pulse, the electron temperature increased dramatically from the equilibrium level within 50 fs. This gave rise to a photo-induced MIT, characterised by a reduction in the

---

[4] The relaxation time of doublons in a gapped system scales as $\tau \propto W^{-1}\exp[\alpha(U/W)\ln(U/W)]$, where $\alpha \sim \mathcal{O}(1)$ is a dimensionless constant [251]. Consequently in the limit $U/W = 1$, $\tau \propto W^{-1}$.

optical reflectivity by around 0.1%. Recombination of the generated electron-hole pairs occurred on a slower timescale ($\sim$ 500 fs), which was weakly dependent on temperature. The authors proposed that this behaviour was a signature of coexisting Slater- and Mott-type behaviour for the photo-induced MIT. Such an experiment showed that it was possible to probe the transient dynamics of 5d TMOs using pump-probe spectroscopy. If the transient optical properties could be measured, then presumably the transient magnetic properties could also be explored. To this end time-resolved XRMS experiments were performed on Sr_2IrO_4 at the Spring-8 Angstrom Compact Linear Accelerator (SACLA) XFEL, in collaboration with others from Brookhaven National Laboratory, the Paul Scherrer Institute, ICFO Barcelona, and the Centre for Free Electron Laser Science, Hamburg.

Sections of the remainder of this chapter have been published as M. P. M. Dean *et al.*, Nature Materials **16**, 601 (2016) [253].

6.3.1 Experimental procedure

Sample mount

Time-resolved RXMS measurements were performed on a 200 nm (h, h, l) thin film of Sr_2IrO_4 epitaxially grown on a substrate of $SrTiO_3$. A thin film was used to maximise the pump-probe volume (see later for a more detailed explanation). Two additional materials were placed on the same sample mount (Fig. 6.6): a piece of GaAs and a thin film of Bi, the latter oriented such that the (1, 1, 1) direction is normal to the sample surface. The reasons are as follows. GaAs is a semiconductor, and fluoresces both upon excitation by X-rays, and in the mid-IR range. This enables rough spatial and temporal overlap of the pump and probe pulses. Bismuth acts as a fine-timing tool, and has a well characterised response in the infra-red region. Bismuth is a semi-metal; electrons are excited from bonding to antibonding orbitals upon excitation by the pump. This weakens the interatomic potential, and induces a transient structural distortion. As a consequence the structure factor of the excited state is smaller than at equilibrium, leading to a weakening of the Bi (1, 1, 1) structural Bragg peak. It is then possible to define time zero based on the temporal dependence of the bismuth peak.

Laser

The optical laser system used was based on a commercial Ti:sapphire laser comprising a mode-locked oscillator and chirped pulse amplifier. This delivers 800 nm pulses at 1 kHz with a pulse duration of around 100 fs. Frequency conversion of this light is required in order to generate ultrafast light pulses in the mid-IR range, which can be done through the use of non-linear optics. In particular, the technique known as optical parametric amplification (OPA) was used. The basic principle [254] is as follows, with a schematic given in Fig. 6.7. Light from a high intensity and high frequency laser source is split into two diverging beams with the aid of a partially reflective

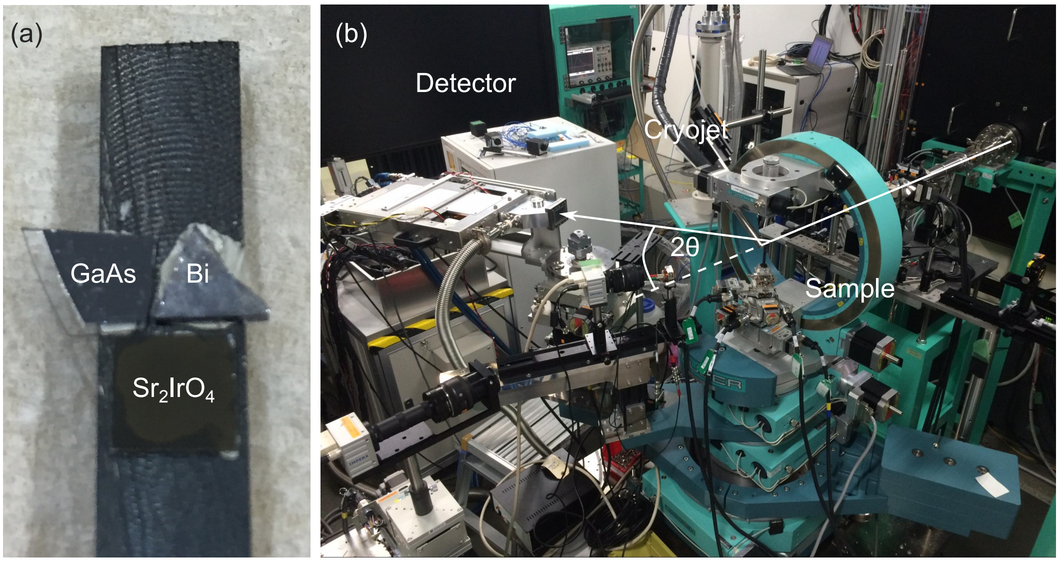

Figure 6.6: (a): Sample mount as used at SACLA. Labelled are the GaAs, Bi (1, 1, 1) single crystals, and Sr_2IrO_4 thin film. (b): Experimental setup.

mirror. One of these beams is focussed into a sapphire crystal, which spectrally broadens the pulse producing a quasi-white light continuum. This is henceforth known as the *seed* or *signal*. It is then combined with the other diverging beam – somewhat confusingly called the *pump* – in a suitable non-linear crystal such as barium borate ($Ba_2B_2O_4$) or $KTiOPO_4$. The choice of crystal used depends on the eventual desired wavelength. An optical delay line may be required to ensure that the two pulses arrive at the crystal at the same time. The angle between the pump and the seed is chosen such that a third beam fulfils the phase and frequency matching condition for so-called three-wave mixing. In this case the seed pulse is amplified by the pump pulse, also producing the *idler* pulse (at the expense of the pump pulse energy) with frequency ω_{idler} and wavevector $\mathbf{k}_{\text{idler}}$. The principles of conservation of momentum and conservation of energy require that $\omega_{\text{pump}} = \omega_{\text{seed}} + \omega_{\text{idler}}$ and $\mathbf{k}_{\text{pump}} = \mathbf{k}_{\text{seed}} + \mathbf{k}_{\text{idler}}$, with $\omega_{\text{idler}} < \omega_{\text{seed}} < \omega_{\text{pump}}$. A number of these amplification stages can be used in series if desired to further amplify the seed pulse. Finally the pump, seed and idler beams are all separated from each other by the use of dichroic filters, which have different optical properties depending on the wavelength of incident light. Remember that the desired infrared source is the seed or idler beam, which is the pump in a pump-probe experiment. Lenses and mirrors focus the laser spot size down and guide the infrared beam towards the sample.

In the present experiment, infrared pump pulses of 100 fs duration were generated at a wavelength of 2 μm (620 meV), and derived from the idler beam of a single stage OPA. This energy corresponds to an excitation between the lower and upper Hubbard bands, that is, across the charge gap, and is consistent with previous optical conductivity measurements [32].

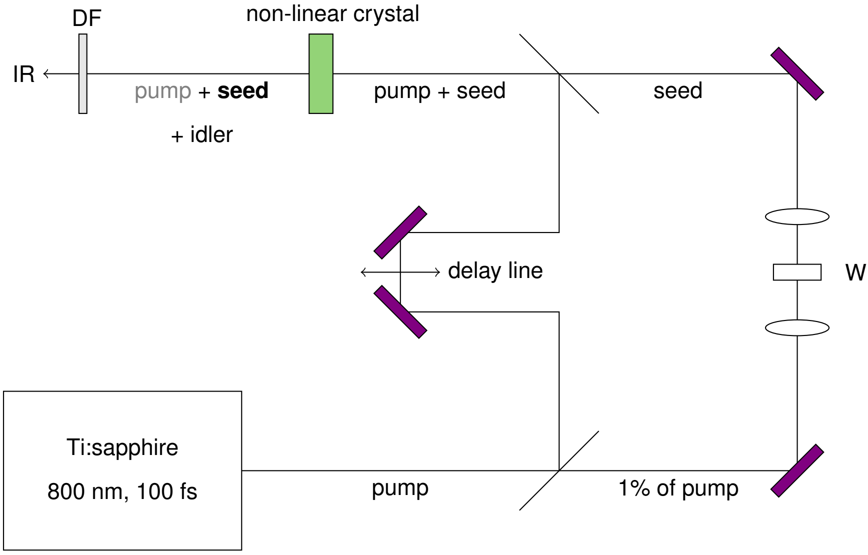

Figure 6.7: Schematic of a single-stage optical parametric amplifier (OPA) as described in the main text. WL stands for white light generator, DF for dichroic filter. The greyed out or bold type font after the non-linear crystal represents the attenuation of the pump and amplification of the seed respectively.

XFEL setup

The incident energy of the XFEL pulses was tuned to the Ir L_3 resonance at 11.215 keV, with a repetition rate of 30 Hz. This is 3 eV below the maximum of the obtained white line (Figure 6.8c). A horizontal scattering geometry was adopted. In-plane polarized X-rays hit the sample at almost grazing incidence ($\sim 1^\circ$), with the pump polarized vertically in the ab-plane of the sample and incident at 13° with respect to the sample surface. This geometry was chosen in order to match the penetration depths of the incident X-rays (10 μm at 11.215 keV, normal incidence) and the pump laser ($\sim$0.8 μm, normal incidence). The sample was cooled to around 110 K by a liquid nitrogen cryojet; this temperature is far below $T_\mathrm{N} \approx 230$ K. The sample was aligned using the $(0, 0, 28)$ and $(-2, -2, 24)$ structural reflections; Figs 6.8a,b show the rocking curves obtained with a photodiode.

For the time-resolved measurements, a multi port charge coupled device (MPCCD) detector was placed at $2\theta = 88.7^\circ$, which corresponds to the magnetic $(-3, -2, 28)$ Bragg reflection. This reflection was chosen in order to optimise the XRMS cross-section, and suppress charge scattering without the need for a polarization analyser. The detector was read out shot-by-shot, with the signal from each image thresholded to remove background resulting from fluorescence and electrical noise. The peak intensity was determined by summing 1000–4000 shots (with each shot normalized to the pulse energy) and binning the 2D detector data into a 1D spectrum. The resultant spectrum was then fitted to a Lorentzian squared lineshape with a constant background. This functional form was found to consistently give the best fit to the data.

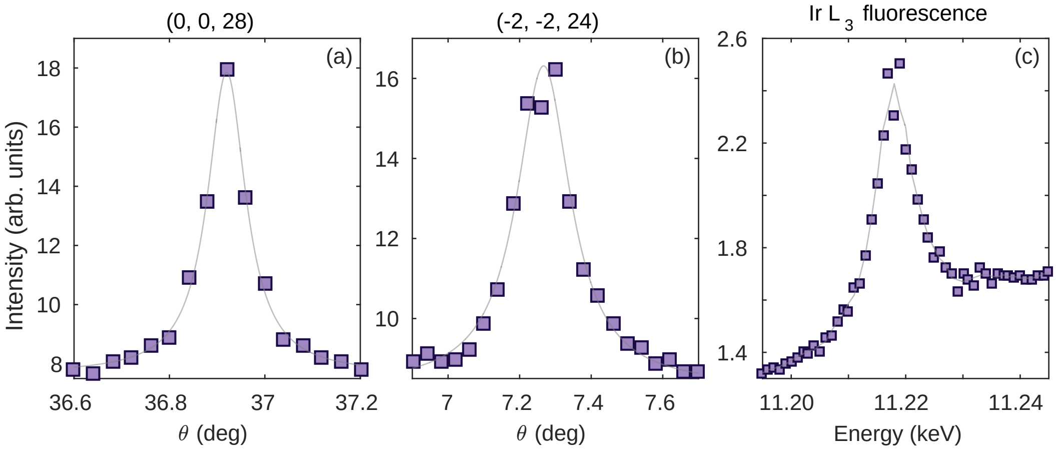

Figure 6.8: Rocking curves of $(0,\ 0,\ 28)$ (a) and $(-2,\ -2,\ 24)$ (b) structural Bragg reflections collected at SACLA. Solid lines are fits to Lorentzian functions. Also plotted is the fluorescence obtained at the Ir L_3 edge (c).

6.3.2 Results

The energy of the pump laser per pulse was calibrated prior to the experiment. In practice the pump energy is varied by placing a diffuser in front of the beam which attenuates some of the pulse intensity. The pump fluence can be calculated from this by considering the spot size of the laser, angle of incidence and reflectivity of the sample.

The intensity of the $(-3,\ -2,\ 28)$ magnetic Bragg peak is plotted in Fig. 6.9 for two delay times: -1 ps and 1 ps. For negative delay times there is a well-defined Bragg peak. However a clear reduction in intensity can be seen after the pump hits the sample; this corresponds to a melting of three-dimensional magnetic order. At small pump fluences (0.4 mJ cm^{-2}), approximately 70% of the peak intensity remains. However for larger pump fluences (6.8 mJ cm^{-2}), the peak is melted away further and only 17% remains.

A detailed dependence of the magnetic peak intensity as a function of delay time and pump fluence was carried out, with the results plotted in Figure 6.10. The peak intensity has been normalised to that obtained for negative delay times. For small pump fluences there is a partial melting of magnetic order, with full recovery to the unperturbed state occurring on a timescale on the order of 100–1000 ps.

In order to gather a quantitative description of the observed behaviour, the data were fitted with the following minimal model:

$$\begin{aligned} I(t) = I_0 \{ & \exp(-t/\tau_{\text{decay}}) + C\,[1-\exp(-t/\tau_{\text{r1}})] \\ & + (1-C)\,[1-\exp(-t/\tau_{\text{r2}})] \} \end{aligned} \tag{6.3}$$

In this model, I_0 is the initial intensity, τ_{decay} corresponds to the initial decay timescale, whereas τ_{r1} and τ_{r2} relate to two separate processes which contribute fractions C and $(1-C)$ to the overall recovery respectively. All of these timescales reflect the time required for the intensity to decay by a factor of $1/e$ or recover by a factor e. The minimal model was convoluted

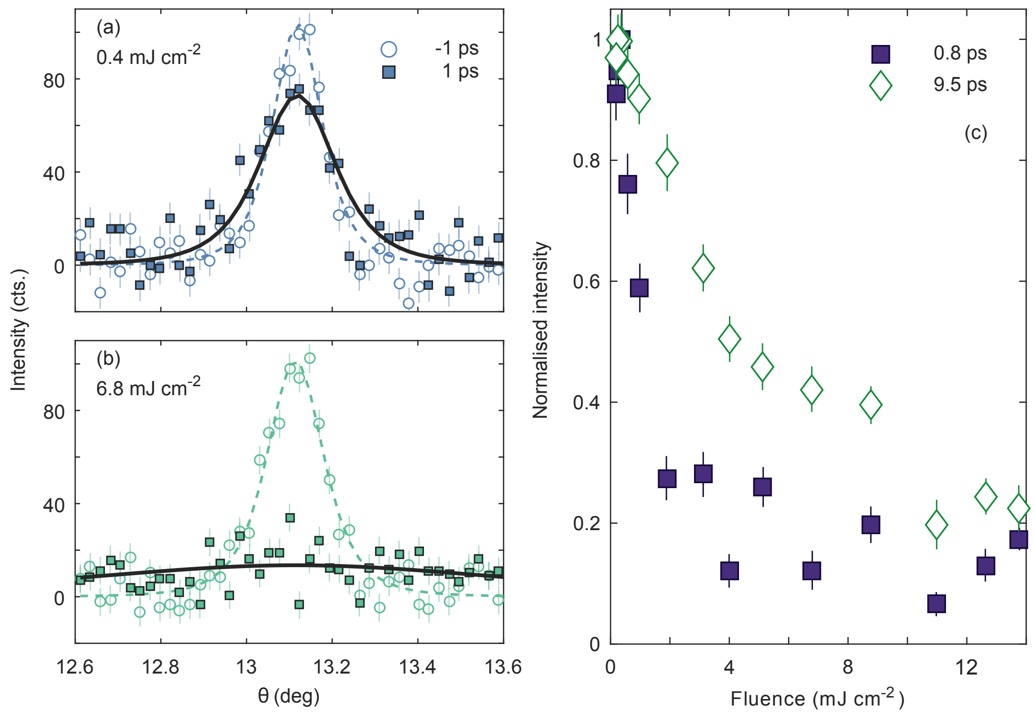

Figure 6.9: (a,b): Rocking curves about the $(-3, -2, 28)$ magnetic Bragg peak for delay times of -1 ps (open circles) and 1 ps (filled squares) collected at SACLA. The best Lorentzian squared fits to the data are given by the solid and dashed lines respectively. The pump fluences used were (a): 0.4 mJ cm^{-2} and (b): 6.8 mJ cm^{-2} respectively. Long-ranged magnetic order has been melted within this timescale at high pump fluences. (c): Intensity of the magnetic Bragg peak as a function of pump fluence, normalised to the intensity with the pump laser off.

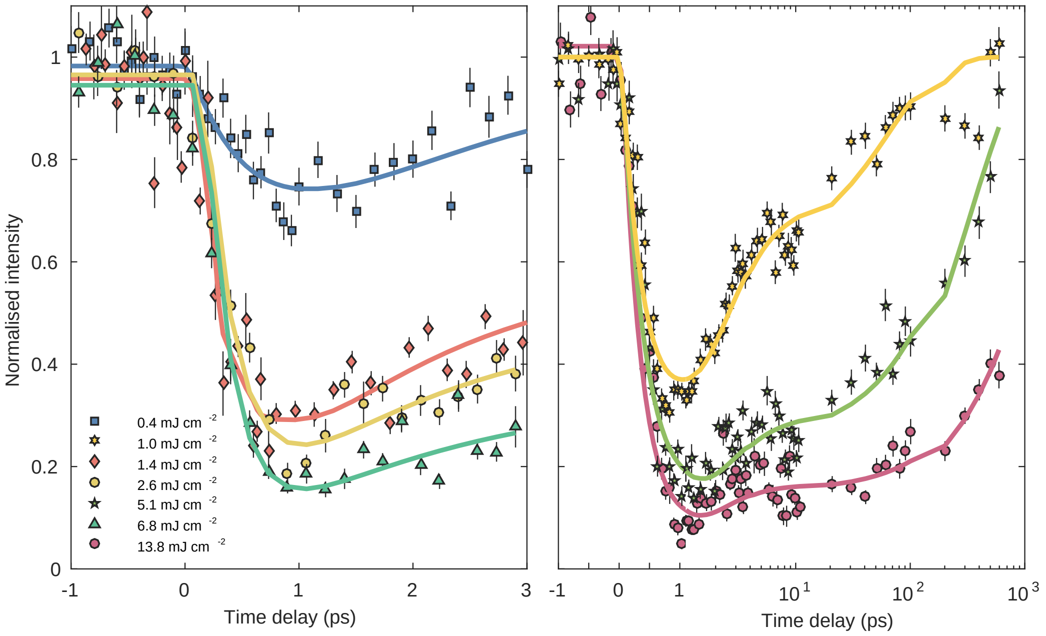

Figure 6.10: Intensity of the $(-3, -2, 28)$ magnetic Bragg peak as a function of time delay focussing on short (left panel) and long (right panel) timescales. Different symbols correspond to different incident pump fluences. Two recovery timescales are apparent from the data out to long time delays.

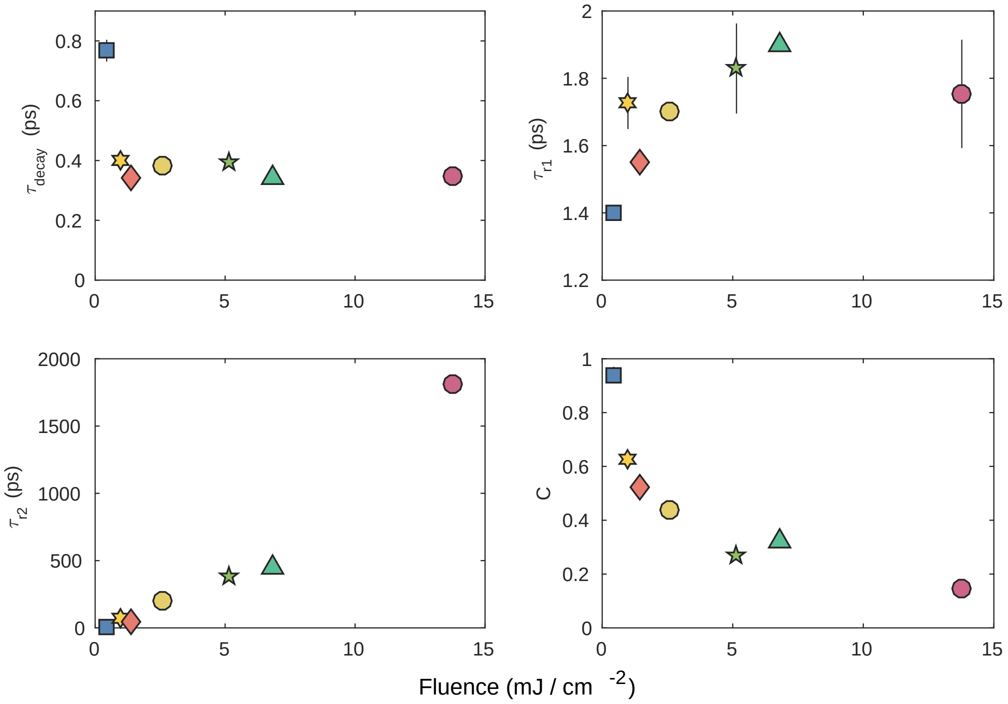

Figure 6.11: Fitted parameters for Eqn. 6.3 as a function of pump fluence. Symbols and colours correspond to those plotted in Fig. 6.10.

with a Gaussian of width 100 fs to represent the pump pulse width, and fitted to the magnetic peak intensity in Fig. 6.10. For fits to those scans performed out to 3 ps delay time, τ_{r2} was constrained by assuming a linear variation in τ_{r2} as a function of pump fluence (as suggested by the data), and interpolating to sensible values. Extracted parameters from these fits are plotted in Fig. 6.11.

A number of observations can be made from the fluence dependence of the fitted parameters. The first is that τ_{decay} is approximately independent of the pump fluence, with a value (350 ± 50 fs) which is comparable to the jitter-limited time resolution of the experiment. This sets an upper limit on the timescale for the melting of long-ranged magnetic order. Note that the discrepancy for a pump fluence of 0.4 mJ cm^{-2} is likely due to an uncertainty in the determination of t_0. The second observation is that there is a slow increase in τ_{r1} with increasing fluence, which appears to abate around $\sim$10 mJ cm^{-2}. On the other hand, the second recovery timescale τ_{r2} varies approximately linearly with fluence. At higher fluences this second timescale dominates the recovery, as demonstrated by the variation of C. The linear dependence of τ_{r2} implies that the recovery of the long-ranged magnetic order relies crucially on the dissipation of energy in the material.

The energy E and characteristic time scale τ of an excitation are directly related by $\tau \sim h/E$. Consequently extrapolating τ_{r1} to zero fluence gives an estimate for the magnon energy at (π, π). Doing this for $\tau_{r1} = 1.4$ ps gives an energy scale of 3 meV, comparable to the antiferromagnetic spin-gap determined by Bahr [226] and Bogdanov [227] from electron spin resonance measurements, and values estimated in the previous chapter. For higher pump fluences τ_{r1} increases slightly, which implies a reduction of the spin gap. On the other hand, the energy scale of the process governing τ_{r2} varies from 0.1–10 μeV as a function of fluence. This is considerably weaker than the in-plane exchange, however it is comparable to estimates of the inter-layer exchange. One can then make the supposition that τ_{r1} is related to the easy-plane anisotropy, whereas τ_{r2} is related to interlayer correlations.

6.4 Time-resolved RIXS (tr-RIXS)

RIXS is one of the few techniques which enables measurement of both the energy and momentum dependences of the photon scattering cross-section. Furthermore RIXS directly probes both the temporal and spatial Fourier transforms of the spin-spin correlation function as a function of time and space. This function contains all of the interactions present in the magnetic Hamiltonian, enabling magnetic excitations to be measured.

Extending this technique to include time resolution (tr-RIXS) provides an unrivalled method of probing orbital and magnetic excitations and their dynamics. The inherent link between time and energy – as demonstrated by the Heisenberg uncertainty principle – means that weak interactions out of the reach of other probes can be resolved by moving into the time domain [255].

Sr_2IrO_4 is an almost ideal system with which to develop the technique of tr-RIXS, given that the unperturbed system has already been well characterised. Furthermore well defined spin waves exist up to 200 meV at the zone boundaries, coupled with spin-orbit exciton modes at 0.6 eV. These energy scales are well within reach, even with a medium-resolution RIXS setup.

6.5 tr-RIXS measurements

Time-resolved RIXS measurements were performed on a bulk crystal of Sr_2IrO_4 at XPP, Linac Coherent Light Source (LCLS). Infrared pump pulses were generated in the same way as for the elastic experiment at SACLA.

The incident energy of the X-ray pulses was tuned to the Ir L_3 resonance at 11.215 keV, with a repetition rate of 120 Hz. This photon energy was at the limit of the capabilities of the LCLS; initial measurements were limited to using the third harmonic. A Si (3, 3, 3) double-bounce monochromator provided an incident energy bandpass of 50 meV, at the expense of shot-to-shot intensity fluctuations of a factor of 2 as discussed above.

The sample geometry was such that horizontally polarized X-rays hit the sample at almost grazing incidence ($\sim 1^\circ$), with the pump polarized vertically in the *ab*-plane of the sample and incident at 13° with respect to the sample surface. This geometry was chosen in order to match the penetration depths of the incident X-rays (10 μm at 11.215 keV) and the pump laser ($\sim$0.8 μm).

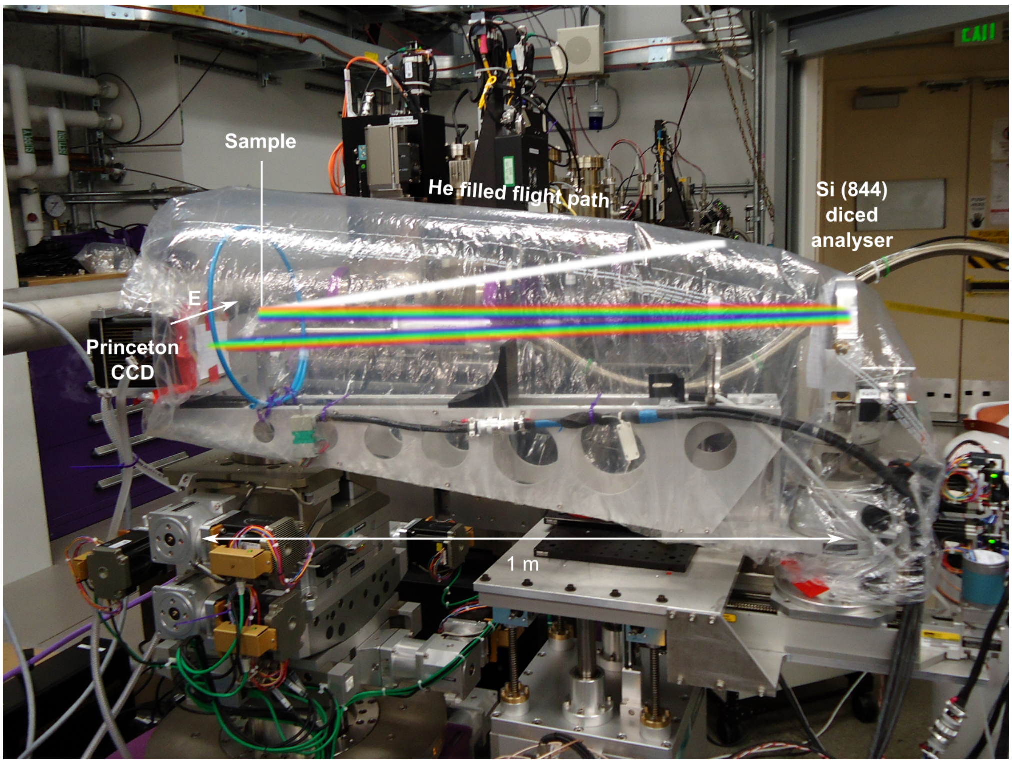

Figure 6.12: Photograph of RIXS spectrometer constructed at the LCLS. The photograph has been annotated with the locations of key components and X-ray beam path. The helium flight path is in fact a dry cleaning garment bag obtained nearby, with any holes taped up to prevent leakage of gas.

The design of the RIXS spectrometer itself was based on MERIX at the APS. Parts were made at Brookhaven, then shipped to the LCLS where it was constructed in a few days. The main difference between the spectrometer used and the design of MERIX is the length of the spectrometer arm (and corresponding analyser radius), which was only 1 m due to space constraints.

Scattered photons from the sample were reflected by a Si (8, 4, 4) diced analyser crystal with block size 1.5 mm. These photons were collected by a Princeton Instruments LCX CCD detector with pixel size 20 μm. The main reasons for using this detector were the small pixel size (which directly affects the energy resolution) and sensitivity to single photons. However one limitation is that the CCD was not capable of reading out individual shots; for this reason 1800 shots were accumulated before the CCD was read out. RIXS spectra were collected in a stationary mode without moving the spectrometer because space constraints meant that it was not possible to fit a counterweight to the spectrometer arm.

6.5.1 Spectrometer calibration

An important part of any RIXS experiment is the initial calibration of the spectrometer. It also provides a useful estimate for the intrinsic energy resolution. Typically calibration is performed with an amorphous material which only scatters diffusely; this also allows for focussing of the

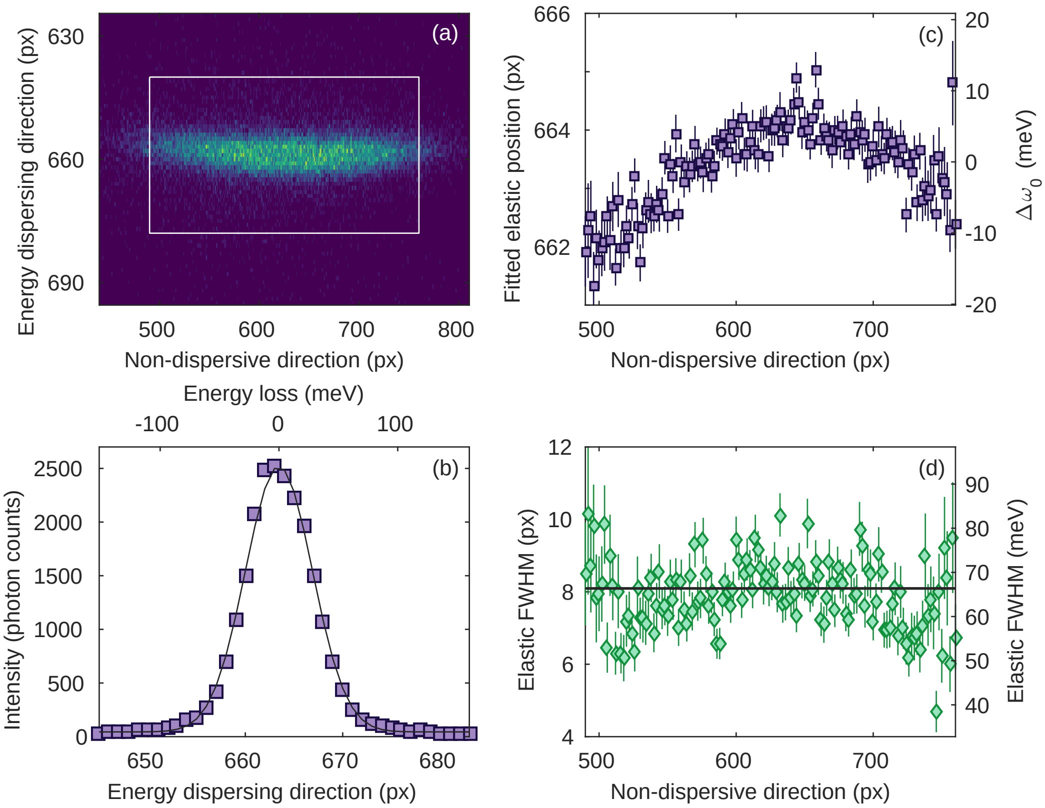

Figure 6.13: Determination of the instrumental resolution. (a): CCD image of elastic line obtained from scattering off transparent adhesive tape (after thresholding). White box indicates region of interest used for subsequent plots. (b): CCD image summed over the non-dispersive direction. Solid line is a fit to a Gaussian with FWHM 8.09(5) px, equivalent to an instrumental resolution of 66.4(4) meV. (c): Peak position extracted from fits of single cuts through the elastic peak. Neighbouring pixels have been binned together to ensure a reliable fit. (d): Width of elastic line (symbols), with width extracted from fit shown in (b) added as a comparison (solid line).

analyser image onto the detector. In this case transparent adhesive tape (Scotch tape) was used.

The CCD image of the elastic scattering is displayed in Figure 6.13(a). The vertical direction as shown corresponds to the energy dispersive direction. If one simply sums over the non-dispersing (horizontal) direction, then one obtains the elastic peak shown in Figure 6.13(b). The elastic peak is described well by a Gaussian of FWHM 8.09(5) px, which gives the first estimate of the instrumental energy resolution.

However there is one complication of note. Ideally the elastic line would lie perfectly horizontal on the detector, which leads to a direct pixel-to-energy mapping. Yet in Figure 6.13(a), a slight curvature can be seen which should be corrected for. The source of this curvature may arise from a slight misalignment of the detector or analyser. Quantitative results are plotted in Figure 6.13(c), in which the fitted position of the elastic line drifts by up to 2 pixels from its nominal value as you move from one side of the detector to the other. Yet the fitted width of the elastic line remains fairly constant as a function of pixel position (Figure 6.13(d)); and compares well with the result obtained simply by summing over the non-dispersive direction (Figure 6.13(b)). The reason for this is that the intrinsic energy resolution is relatively broad as a consequence of the optical setup upstream of the sample. This means that the curvature of the image on the detector is only a minor contribution to the total resolution. Consequently one can neglect it to a first approximation.

Pixel-to-energy conversion

A RIXS spectrum in pixels is not particularly useful however, since one would ideally convert it into energy to aid comparison with physical models. Fortunately in a Rowland geometry, the distance along the detector in the energy dispersive direction is directly proportional to energy. For given change in photon energy δE, the change in position of the elastic peak δd is given by

$$\delta d = \frac{2R_A \cos^3 \vartheta}{\sin \vartheta} \frac{\delta E}{E_H}, \tag{6.4}$$

where R_A is the analyser radius, $E_H = hc/2d_A$ is the photon energy required to satisfy $2\theta_A = 90^\circ$, and $\vartheta = 90^\circ - 2\theta_A(E)$. It should be stated at this point that the above equation and subsequent calculations are appropriate for a static collection scheme. To clarify, this is a method where no physical motors are scanned, with the energy collection window limited by the physical size of the analyser ($\sim$1 eV). This contrasts with the collection method performed in Chapters 3 and 4, where both the analyser theta angle and detector position are moved concurrently to keep the elastic line on the same pixel. This allows for collection windows much larger than those available for the static setup.

Consequently one can calculate the pixel-to-energy conversion for the instrument described above. For a Si (8, 4, 4) diced spherical analyser with $R_A = 1$ m, $E_H = 11.186$ keV. It follows for an incident photon energy of 11.215 keV (corresponding to the Ir L_3 edge) that $\vartheta = 4.123^\circ$, and hence for a change in photon energy $\delta E = 1$ eV, $\delta d = 2.47$ mm. Now the Princeton CCD has pixel dimensions of 20×20 μm, which means that $\delta E = 1$ eV is equivalent to $\delta d = 123.4$ px. This gives the final result of a calibration factor of 8.1 meV/px. This factor shall be used throughout this chapter.

Image processing

One important reason for using a position sensitive detector is that photons can be collected over a comparatively large solid angle. This ensures that the majority of the RIXS signal emanating from the sample can be obtained, minimising collection times and facilitating easy alignment of the sample/spectrometer. However the required signal is usually only located in a small region of the CCD – a direct effect of the finite size of analyser used. Furthermore the CCD does not directly discriminate the energy of the scattered photons; the raw signal obtained contains contributions from a number of processes, mainly fluorescence and dark current due to shot noise. Figure 6.14(b) shows a portion of one typical CCD image integrated over 1800×20 shots

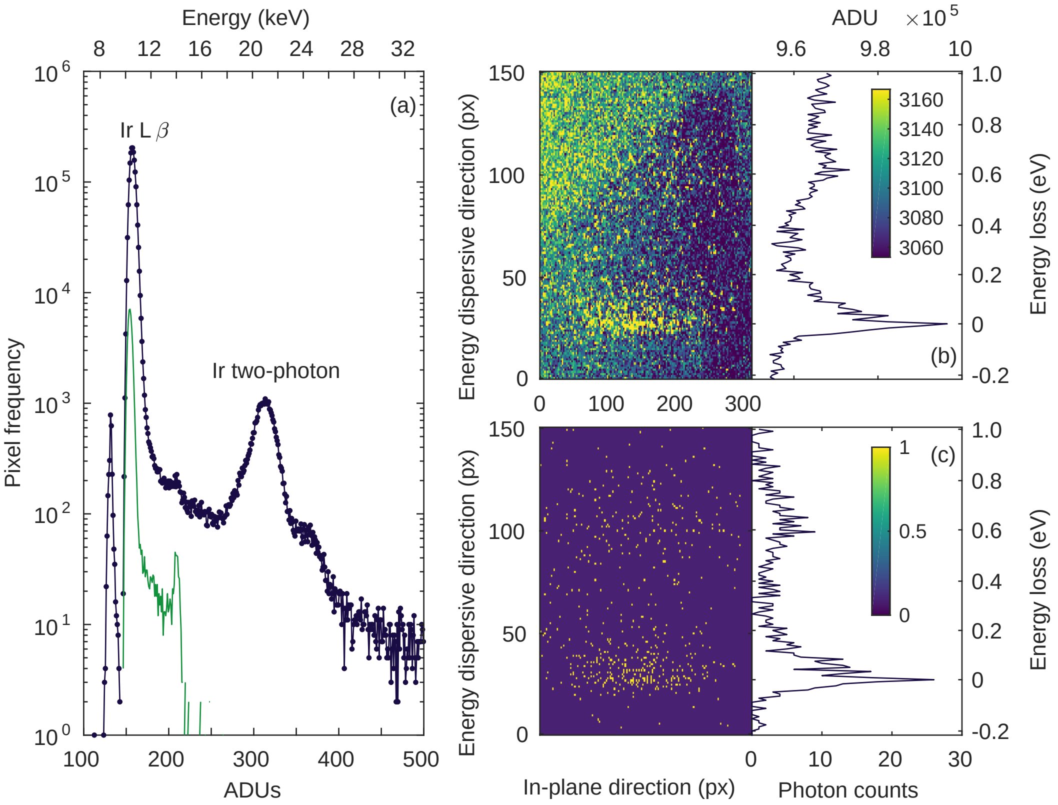

Figure 6.14: (a): Histograms of the entire CCD (purple), and a 310×150 px region of interest (green), each summed over 1800×20 shots and before thresholding. (b): Raw CCD image (within the aforementioned region of interest) and lineplot of the sum in the non-dispersive direction resulting from a single run of 1800×20 shots. (c): Same as for (b), but with dark image subtracted and lower threshold of 160 ADUs applied. In (b) and (c), the extremes of the colorscale reflect the 5% and 95% confidence limits. Additionally neighbouring pixels have been binned together in the in-plane direction for clarity.

(five minutes accumulation time). The desired RIXS signal is in the bottom portion of the image; however there is a significant non-linear background present.

Fortunately it is possible to subtract off these extraneous contributions by performing two steps. The first is to collect a “dark image”, which is a CCD image with no X-ray or pump laser impingent on the sample. This should be collected for the same amount of time as a normal run, and characterises the intrinsic noise of the detector. The second involves thresholding off the fluorescent (and very high energy) contribution. A CCD works by the conversion of photons to electric charges, and conversion to a voltage. The absorption of an X-ray photon ejects a free, energetic photoelectron. As this electron moves through the silicon lattice, it generates a measurable number of electron-hole pairs, each with energy 3.65 eV. After some period of time, the number of electron-hole pairs collected by each pixel is read out, amplified, measured as a voltage, and converted into a output digital number (analogue-to-digital units or ADUs, always an integer). The number of electron-hole pairs required to generate a single ADU is defined as the gain of the CCD, G. Consequently a number of photons N_{ph} with energy E_{ph} will generate a number of ADUs: $S_{\mathrm{ADU}} = N_{\mathrm{ph}} E_{\mathrm{ph}}/(3.65G)$.

A histogram of the entire CCD (1300 × 1340 px) is plotted in Figure 6.14a, integrated over 1800×20 shots. Three clear peaks can be seen. The first sharp peak at 130 ADUs is the Ir Lα emission line. The second broader peak at 155 ADUs comprises the set of Ir Lβ emission lines at $\sim$10.8 keV, whereas the broad peak at 320 ADUs incorporates all Ir two-photon events. Consequently all events which correspond to less than 160 ADUs were thresholded off. This somewhat conservative estimate was used to ensure no photon events contributing to the RIXS signal were missed; effects such as the quantum efficiency of the CCD mean that the conversion from ADUs to photon energy is only approximate. An example image and associated lineplot are displayed in Figure 6.14(c). The signal appears much more like a typical RIXS spectrum, with good statistics given that the total accumulation time is only five minutes.

6.5.2 Measurements at (π, π)

Time-resolved RIXS (tr-RIXS) measurements were first performed at $(-4, -3, 23.9)$, which corresponds to the magnetic Brillouin zone centre at (π, π). A non-integer value of L was used to ensure that $2\theta = 90^\circ$. Remember there are three main features in the previously observed RIXS spectra as presented in Chapter 5: an elastic line (which also contains quasielastic features within the instrumental resolution), dispersive and weakly gapped spin wave excitations which emanate out of the magnetic Bragg peak at (π, π), and a "spin-orbit exciton" deriving ultimately from a transition between the $j_{\mathrm{eff}} = \frac{3}{2}$ and $j_{\mathrm{eff}} = \frac{1}{2}$ states.

RIXS spectra were obtained by collecting seven runs together, each comprising 40 accumulations of 1800 shots each. Alternate sets of 1800 shots were obtained with the pump laser on or off (-50 ps delay) to allow direct comparison between datasets obtained at similar times. So each spectrum corresponds to a total accumulation time of $(7 \times 20 \times 1800\,\text{shots})/120\,\text{Hz} = 35$ min.

Time-resolved RIXS (tr-RIXS) spectra at (π, π) are plotted in Figure 6.15a,b for various delays. At first glance, they look similar to those obtained at conventional synchrotron facilities, with the same well-defined inelastic features. The large elastic line is a consequence of the magnetic Bragg peak situated at (π, π); the $2\theta = 90^\circ$ condition cannot be fully satisfied and some finite elastic contribution makes its way through. A well defined magnetic contribution can also be observed, albeit with some asymmetry as a consequence of the finite momentum resolution.[5]

However when the pump laser is switched on, there is only a weak change in the RIXS spectra. Well defined magnons can still be seen 2 ps after the pump, albeit with a reduction in intensity of around 12 ± 10 % compared to before the pump. This contrasts with the elastic case where long-ranged Néel order is heavily suppressed for this value of the pump fluence and optical delay. On the other hand, there is an increase in intensity below the elastic line which suggests some redistribution of spectral weight around the Fermi level.

---

[5] A large proportion of the dispersion surface is sampled – all the way to the zone boundary in the present case.

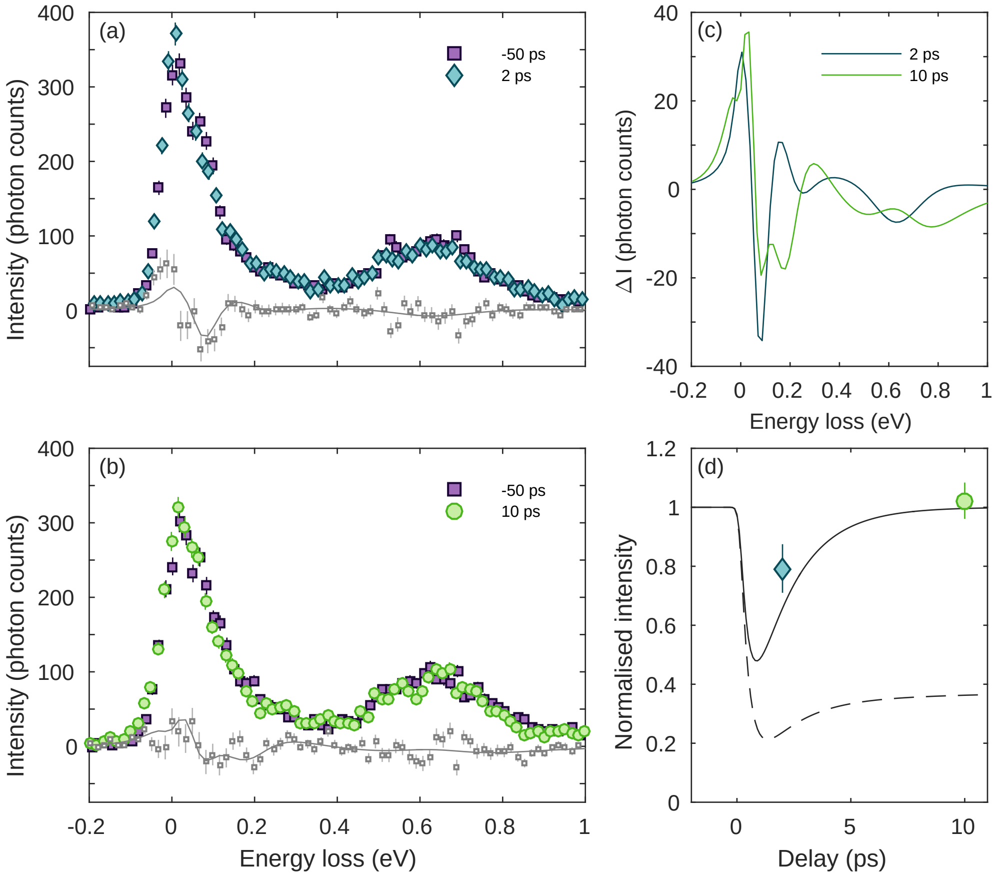

Figure 6.15: (a,b) Pump-probe RIXS spectra at (π, π) along with difference spectra $I_{\text{on}} - I_{\text{off}}$ (open symbols) for different optical delays. (c): Overlay of difference spectra for optical delays of 2 ps and 10 ps. Error bars have been omitted for clarity. (d): Fitted intensity of magnon peak normalised to intensity with no pump laser (symbols). Overlaid are models comprising Equation 6.3 with parameters interpolated from the elastic data for a pump fluence of 6 mJ cm^{-2} and convoluted with a Gaussian of FWHM 300 fs. The two models are identical apart from the value of C: $C = 1$ (solid), $C = 0.35$ (dashed).

A weak suppression of the spin-orbit exciton can also be observed. At longer delay times (10 ps), there is a further partial recovery of the magnon and spin-orbit exciton intensities. It should be noted at this point that the overall intensity of the RIXS spectra for 10 ps/$-$50 ps runs are a factor of two lower than that for the 2 ps/$-$50 ps runs; this is due to an issue with the alignment of the spectrometer which has been accounted for in the above figures.

Recall from Chapter 5 that for Sr_2IrO_4, Néel order occurs below T_N as a result of out-of-plane correlations. Consequently the melting of magnetic order seen in the tr-RXMS corresponds to the destruction of correlations out-of-plane. In this geometry, the RIXS cross-section is dominated by correlations within the ab-plane. Thus the fact that well-defined spin wave excitations persist for 2 ps delay implies two things. Firstly, long-ranged magnetic correlations are present in-plane, whereas we already know that the elastic data implies that three-dimensional order has been all but destroyed for this pump fluence. This is consistent with a scenario of two-dimensional magnetic order. Additionally these correlations must be of a sufficiently high energy to have practically recovered by 2 ps. This makes sense given that the nearest-neighbour exchange $J \approx 60$ meV.

Further evidence for 2D behaviour can be gathered by considering the temporal dependence of the magnon intensity. The dependence of the RXMS intensity upon optical delay could be described by Equation 6.3, with the parameter $(1 - C)$ proportional to the degree of melting of three-dimensional magnetic order. Extrapolating from the calculated values of C presented in Figure 6.11, one finds $C = 0.35$ for a pump fluence of 6 mJ cm^{-2}. The corresponding theoretical delay curve (convoluted with a Gaussian of FWHM 300 fs to take the jitter of the FEL into account[6]) is plotted in Figure 6.15d as a dashed line. Contrast this with the scenario of $C = 0$, which represents the limit of zero correlations out of plane (solid line). Such a description fits the RIXS data more convincingly for optical delays of 2 and 10 ps, which thus suggests the dominance of 2D in-plane correlations.

6.5.3 Measurements at $(\pi, 0)$

The advantage of RIXS over Raman scattering for example lies in the ability to measure non-zero momentum transfers. What this means is that one can not only measure the excitations at the Brillouin zone centre, but also at the zone boundary. In Sr_2IrO_4 the magnons disperse up to 200 meV at the zone boundary; consequently they are well separated from the elastic line and any other inelastic features. This means that unlike at (π, π), the width and energy of the magnon peak can be well characterised as a function of optical delay.

To this end pump-probe RIXS spectra were collected at $(-3.5, -3.5, 24.1)$, which corresponds to the $(\pi, 0)$ point. Two optical delays were chosen: -50 ps and 2 ps, which enables a direct comparison with the zone centre data. The resulting spectra are plotted in Figure 6.16, and are each the sum of four consecutive runs of 1800×20 shots. Just as for the data collected at (π, π), neighbouring pixels in the energy-dispersing direction were binned together for a total bin-width of 8.2×2 meV$\,=16.4$ meV.

Upon photo-doping the intensity of both the magnon peak and spin-orbit exciton are weakly suppressed, just as at the magnetic zone centre (π,π). Furthermore the general form of the RIXS spectra remain comparable. In order to quantify these observations, the RIXS spectra were fitted with a sum of four Lorentzian squared functions. The results of these fits lead to the following conclusions.

Firstly the intensity of the magnon peak is suppressed by 10% upon photo-doping; this is comparable to the observation at (π, π). However whilst at (π, π) there is a shift of spectral weight towards the elastic line, at $(\pi, 0)$ the peak suppression is more uniform as a function of energy (Figure 6.16(b). The fact that the magnon peak intensity at $(\pi, 0)$ is so similar to that at (π, π) is somewhat surprising, given that one would expect higher energy excitations to decay more quickly as there are a greater number of lower energy, multi-particle decay pathways.

---

[6] Note that this does not assume any long-term drift of time zero; the true jitter is likely to be on the order of 1 ps.

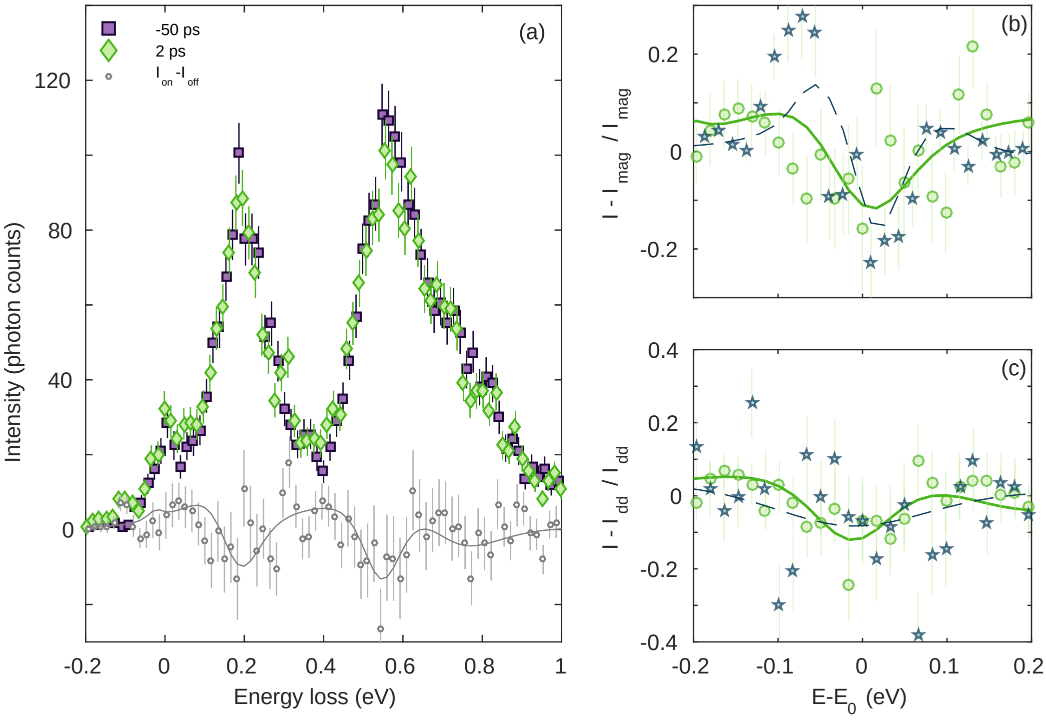

Figure 6.16: (a): RIXS spectra at $(\pi, 0)$ before (purple squares) and after (green diamonds) the pump, along with their difference $I_{on} - I_{off}$ (open circles). The solid grey line is the difference between the best fits to the two RIXS spectra. (b): Enlarged view of the difference spectra at (π, π) (blue stars, dashed) and $(\pi, 0)$ (green circles, solid), each normalised to the fitted maximum of the magnon peak at E_0. (c): Same as (b), except normalised to fitted maximum of SO-exciton at $E_0 \sim 0.6$ eV. Again the dashed (solid) lines in (b,c) reflect the normalised difference between the best fits to the RIXS spectra at (π, π) and $(\pi, 0)$ respectively.

However one possible explanation is that the data may simply be temporally resolution-limited due to a gradual shift of time zero during the measurement time.

The intensity of the spin-orbit exciton mode at ~0.6 eV decreases by a similar amount upon photo-doping, again comparable to (π, π). Furthermore one finds that the energy of the magnon peak does not shift appreciably with the onset of the pump [196(5) meV with pump off, 188(5) meV with pump on]. This indicates the strength of the magnetic correlations – in terms of J – remains comparable upon photo-doping. The width of the magnon peak on the other hand does increase slightly with the onset of the pump [156(7) meV pump off, 180(10) meV pump on, all FWHM], which implies that there is a weak variation in magnon damping. Deconvolution of the resolution function leads to magnon linewidths of 134(8) meV and 160(10) meV. However it should be noted that these values are likely to be overestimates of the true magnon linewidths due to the finite momentum resolution. To summarise, the apparent effect of the pump at some given optical delay is to uniformly suppress the magnetic spectral weight across the Brillouin zone, with some evidence for increased damping at the zone boundary.

6.5.4 Comparison with chemical doping

However there is a caveat with this conclusion. The present measurements only reflect the magnon dispersion at (π, π) and $(\pi, 0)$ in the photo-doped compound. It is instructive to compare these results with RIXS measurements on chemically doped Sr_2IrO_4.

RIXS measurements have recently been performed by Liu *et al.* [256] and Gretarsson *et al.* [257] on bulk electron-doped $(Sr_{1\text{-}x}La_x)_2IrO_4$. These measurements show strongly anisotropic behaviour; the magnon energy for $x = 0.03$ is similar to that for the undoped compound at (π, π) and $(\pi, 0)$, whereas there is a pronounced softening at $(\pi/2, \pi/2)$ of $\sim$20 meV. Furthermore the magnons along the nodal direction $(0, 0)$–(π, π) are considerably damped compared to the undoped case, whereas those along $(0, 0)$–$(\pi, 0)$ are comparable. Thus the conclusion that the magnons remain relatively robust at (π, π) and $(\pi, 0)$ upon photo-doping is not that surprising.

One can go further and attempt quantitative comparisons between the two datasets. To this end RIXS spectra were collected on cleaved single crystals of $Sr_{2\text{-}x}La_xIrO_4$ at ID20, ESRF, for three doping levels: $x = 0, 0.01, 0.035$. Doping levels were characterised after cleavage by energy-dispersive X-ray spectroscopy (EDX). All spectra were collected at 20 K and in an identical configuration ($\Delta E = 22$ meV). The data at $(\pi, 0)$ are plotted in Figure 6.17a, and normalised to the $d - d$ excitation intensity at 1 eV to facilitate comparison. However, due to a transient technical issue, the raw intensity for the undoped compound is a factor of three weaker than expected. Furthermore only one usable scan could be collected, as opposed to two for the other doping levels. This explains the increased scatter in the plotted spectra, and greater uncertainty in extracted fitting parameters for $x = 0$. Nevertheless the results obtained compare well with those previously published in Refs. [256] and [257]. Remembering that the true magnon linewidth is likely narrower than that extracted from the tr-RIXS data, one can estimate that 2 μm photo-doping with a pump fluence of 6 mJ cm^{-2} is approximately equivalent to 2% electron doping with La.

One may think that you can increase the pump fluence indefinitely, and eventually move to a region of the magnetic phase diagram that has not yet been probed by chemical doping.[7] However by increasing the pump fluence the heat load on the sample also increases. An increased heat load can give rise to surface reconstruction and eventually to sample damage. Evidence of localised sample damage could be seen even with the pump fluences used for the measurements presented here, however it is not entirely clear whether this is a result of the pump or the XFEL probe pulse. It thus seems like there is an ultimate limit to the degree of photo-doping that can be achieved, which is likely similar to that obtainable with lanthanum doping.

---

[7] It proves relatively difficult to introduce dopant cations into Sr_2IrO_4. Unlike the cuprates, only a maximum of 10% La can be introduced into the structure, even when a surplus of lanthanum oxide is added into the reaction mixture. The reasons for this are presently unclear. Additionally there are frequently issues with differences between doping levels in the bulk and at the surface. All RIXS measurements presented here were performed on cleaved samples to ensure that the results are representative of the bulk crystal.

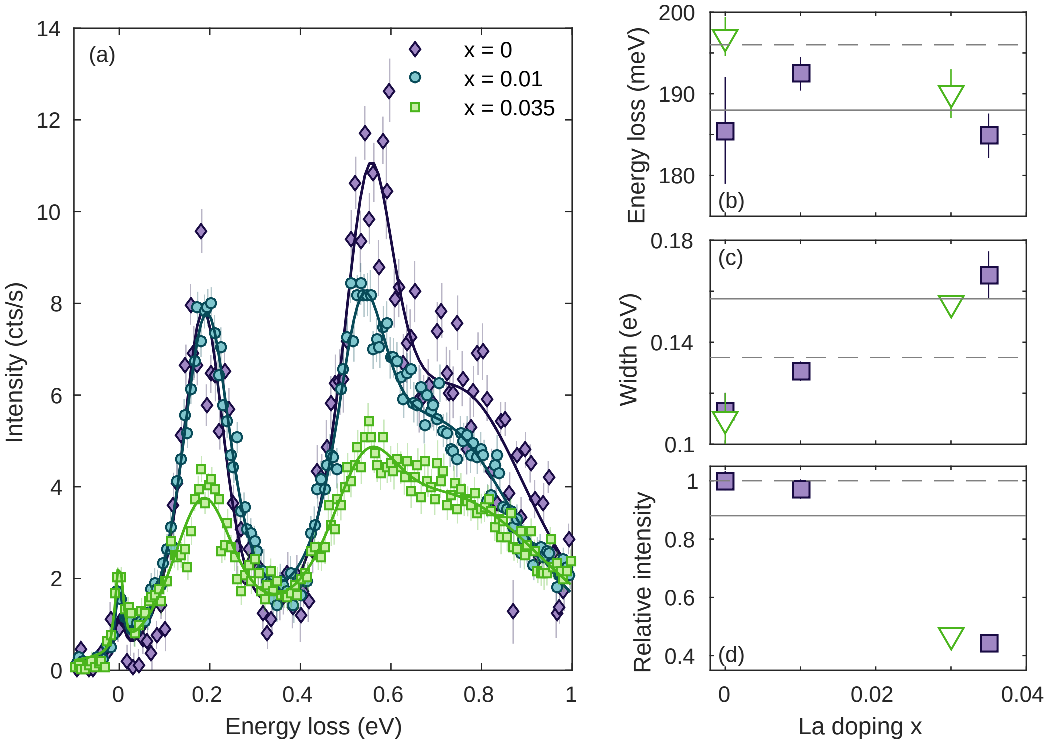

Figure 6.17: (a): RIXS spectra of $(Sr_{1\text{-}x}La_x)_2IrO_4$ at $(\pi, 0)$, collected for three doping levels $x = 0$, 0.01, 0.035. Solid lines are the best fit to a sum of four Lorentzian squared functions. The spectra have been offset vertically to aid comparison. Right panels reflect the magnon peak position (b), FWHM (c) and intensity (d) relative to the value for $x = 0$. Squares: values extracted from fits to data in (a). Triangles: data extracted from Ref. [256]. The solid(dashed) line on each of the plots represents the fitted value from the tr-RIXS data with pump laser on(off).

6.5.5 Summary

To summarise, time-resolved resonant magnetic X-ray scattering (tr-RXMS) and time-resolved resonant inelastic X-ray scattering (tr-RIXS) measurements were performed on Sr_2IrO_4, in order to determine the short timescale dynamics of the instantaneously photo-doped state. Time-resolved XRMS measurements revealed that long-ranged antiferromagnetic order was suppressed upon excitation across the charge gap, only to recover with two characteristic timescales. The shortest timescale likely corresponds to the recovery of the magnetic spin gap, which results from in-plane exchange anisotropy as demonstrated in Chapter 5. The second, longer, timescale is heavily dependent on the magnitude of the incident pump fluence and is associated with the recovery of 3D Néel order. Notably the former timescale is similar to that observed in optical reflectivity measurements, which suggests that the magnetic and electronic behaviour are related in some way. This links back to the optical conductivity measurements by Hsieh *et al.* [151], which finds evidence of simultaneous Mott and Slater-type characteristics for the photo=induced metal-insulator transition.

Time-resolved RIXS allows the measurement of the excitations as a function of momentum transfer. What these measurements show for Sr_2IrO_4 is that in-plane magnetic excitations persist at 2 ps delay, even though long-ranged magnetic order is all but destroyed for a pump fluence of 6 mJ cm^{-2}. Furthermore increased magnon damping can be observed at the zone boundary after the onset of the pump. This behaviour is consistent with that observed for electron-doped $(Sr_{1\text{-}x}La_x)_2IrO_4$, and implies some degree of similarity between photo-doping and bulk carrier doping.

Summary of contributions

As mentioned previously, the time-resolved resonant X-ray scattering experiments were a collaborative effort between a large number of people from different groups. The author's contribution during the experiments was predominantly limited to assistance with the initial diffractometer/spectrometer setup, software development, data processing and analysis. All data presented in this thesis was generated with the author's own data processing and analysis codes written in MATLAB; this explains some of the minor quantitative differences with the data presented in Ref. [253].

The RIXS measurements on electron-doped $(Sr_{1\text{-}x}La_x)_2IrO_4$ were performed with the assistance of Christian Donnerer and Davide Pincini from UCL, and Alberto de la Torre from Caltech. All analysis presented here was performed by the author.

Chapter 7

Conclusions and future perspectives

In this thesis, the electronic and magnetic correlations within four 5d transition metal oxides have been studied using resonant X-ray scattering techniques. The advantages of resonant X-ray scattering mean that it is possible to probe the magnetic and electronic degrees of freedom simultaneously over a large parameter space. Consequently it has been possible to explore the role of spin-orbit coupling in determining the electronic and magnetic properties of these materials.

However, a number of unanswered questions remain. For the osmates, these questions are predominantly orientated towards experimental observation of the band structure variation through the MIT, and the robustness of the MIT to applied physical or chemical pressure. For the iridates, the focus is on the effect of carrier doping (both bulk and photo-doping), with the eventual long-term aim of perhaps observing unconventional superconductivity. A more detailed discussion follows.

7.1 $Cd_2Os_2O_7$

7.1.1 ARPES

A number of experiments are proposed which would shed further light into the nature of the MIT for $Cd_2Os_2O_7$. Angle-resolved photoemission (ARPES) measurements would provide definitive proof of a change of topology at the Fermi surface. ARPES is a complementary technique to RIXS since it directly probes the occupied valence states as a function of momentum transfer, whereas RIXS examines excitations from the electronic ground state. Similar measurements have already been performed on the isostructural $Nd_2Ir_2O_7$ ($T_{MI} = 40$ K), where a clear evolution of the electronic gap can be observed as a function of temperature [258]. However performing such an experiment would certainly require the use of synchrotron sources, and even so, be rather challenging for three reasons.

The first is the issue of thermal broadening. At $T = 0$, the Fermi surface is sharp and well defined. However at elevated temperatures a number of the electrons can gain energy in accordance with the Fermi-Dirac distribution. This leads to smearing of the Fermi surface and hence features close to the Fermi energy become less well-defined. What this means is that it will likely prove more difficult to gain quantitative estimates of the gap magnitude (and any related quasiparticles) for $Cd_2Os_2O_7$ compared to $Nd_2Ir_2O_7$.

Secondly within the ARPES technique photo-electrons are excited from a material by an optical probe. This generally requires metallic (or semi-metallic) samples, whereas at low temperature $Cd_2Os_2O_7$ is certainly within an insulating regime. Thus sample charging occurs when removing photo-electrons, which cannot be compensated for by addition of a conducting electronic contact. This is a constraint because if too much sample charging occurs, then it may not be possible to obtain a satisfactory ARPES signal due to a paucity of available photoelectrons.

Finally ARPES is predominantly a surface-sensitive technique, and samples are typically cleaved *in-situ* within an ultra-high vacuum prior to measurement. The three-dimensional nature of the $Cd_2Os_2O_7$ crystals means that cleaving is difficult, and even then, may only produce small homogeneous surfaces. This could be mediated somewhat by the use of soft X-ray ARPES, which is more bulk-sensitive and has the advantage of better k_z resolution. However this comes at the expense of energy resolution ($\Delta E \sim 100$ meV).

7.1.2 Resistivity under pressure

Another potential study involves resistivity measurements of $Cd_2Os_2O_7$ under applied external pressure. Remember that a Lifshitz transition is an example of a QCP at $T = 0$. Instead of inducing Lifshitz-like behaviour by varying the temperature, a similar effect could be gained by varying the pressure. This would be accompanied by a decrease in T_{MI}, eventually reaching $T = 0$ at some critical pressure P_c. Mandrus *et al.* [94] performed preliminary measurements and found that T_{MI} decreases linearly by around 4 K per GPa increase in pressure. Assuming the linear pressure dependence in T_{MI}, then one can estimate the QCP will occur at 50–60 GPa. There is also the intriguing possibility of observing some quantum critical or non-Fermi liquid behaviour which would be associated with the metallic phase at high pressure. However this does assume that there is no high-pressure structural distortion such as that undergone by the isostructural $Cd_2Re_2O_7$ [259].

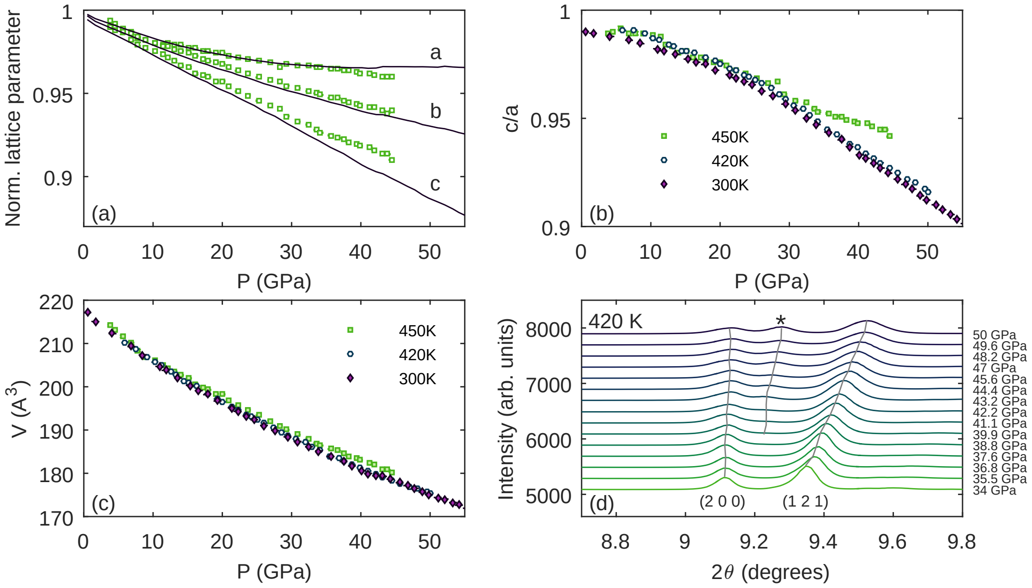

Figure 7.1: Pressure dependence of structural parameters for $NaOsO_3$. (a): Lattice parameters normalised to the zero pressure values at 300 K (lines) and 450 K (symbols). (b): c/a ratio at 300, 420 and 450 K. (c): Equation of state at 300, 420 and 450 K show minimal volume change as a function of temperature, with no obvious anomalies characteristic of a first-order phase transition. (d): Above the MIT an additional peak appears above 40 GPa which is consistent with a continuous monoclinic distortion.

7.2 $NaOsO_3$

7.2.1 Resistivity/magnetisation measurements as a function of applied pressure

One possible future experiment is the resistivity and magnetisation of $NaOsO_3$ as a function of applied external pressure. Remember that the structure of $NaOsO_3$ is pseudo-cubic, with the orthorhombic distortion arising as a result of a concerted rotation of the OsO_6 octahedra in the *a*–*c* plane, coupled with a tilting about the *b*-axis. The Os–O–Os bond angle decreases continuously as a function of decreasing temperature in order that the octahedra better align with the unit cell at low temperature. When sufficiently close, the Os ions interact and form the magnetically ordered phase. Calder *et al.* [131] proposed that there may be a magnetostriction control parameter in which it may be able to control the onset of antiferromagnetic order by applying external pressure.

Characterisation of the structure of $NaOsO_3$ as a function of applied pressure was performed at ID09, ESRF. A small quantity of powder was placed into a diamond anvil cell (DAC) and diffraction patterns obtained in a transmission geometry. Preliminary analysis reveals a continuous phase transition to a monoclinic phase above 40 GPa, which likely results from a tilting of the OsO_6 octahedra. The pressure dependence of the unit cell volume was fitted to a

Rose-Vinet equation of state:

$$P = 3B_0 \frac{1-\eta}{\eta^2} \exp\left[\frac{3}{2}\left(B_0' - 1\right)\left(1-\eta\right)\right], \tag{7.1}$$

where $\eta = (V/V_0)^{1/3}$. The parameters V_0, B_0 and B_0' refer to the unit cell volume at $P = 0$, the isothermal bulk modulus, and $\mathrm{d}B_0/\mathrm{d}P$ respectively. V_0 was fixed to the values obtained from neutron powder diffraction at ambient pressure for 300, 420 and 450 K. The parameters extracted from these fits reveal a weak temperature dependence [300 K: $B_0 = 149.03(2)$ GPa, $B_0' = 3.784(2)$; 450 K: $B_0 = 147.4(5)$ GPa, $B_0' = 4.38(4)$], however the important point is that the structure is fairly robust as a function of applied pressure.

It is presently unclear whether the observed structural phase transition also drives a metal-to-insulator transition above T_N. If so, this would be the opposite of a typical pressure-driven insulator-to-metal transition, since usually materials have a tendency to metallic behaviour at high pressures due to the electronic bands being pushed closer together. Such a MIT may or may not induce magnetic long-ranged order as well through magnetostriction. Another intriguing possibility is that the structural phase transition also induces a Lifshitz transition in the metallic phase and a corresponding change of topology in the Fermi surface. As discussed earlier for $Cd_2Os_2O_7$, such a transition may push the system towards a quantum critical point.

7.2.2 Non-resonant magnetic X-ray diffraction (nRXMS)

Recall the discussion in Chapter 3. In most materials, both the spin and orbital components are important to fully explain the observed behaviour. For d^3 systems in the Russell-Saunders limit (weak spin-orbit coupling), the orbital component is quenched as the t_{2g} manifold is half-filled. Consequently one would expect a spin-only magnetic moment of 1.5 μ_B. A reduced magnetic moment of 1.0(1) μ_B has been observed for $NaOsO_3$, which has been ascribed to significant hybridisation between the Os 5d and O 2p states and weak spin-orbit coupling. Such behaviour has been proposed as direct evidence for Slater insulating behaviour in $NaOsO_3$.

However there is an alternative scenario. Spin-orbit coupling entangles the spin and orbital components of the magnetisation such that it can no longer be considered as quenched for 5d TMOs. The hypothesis is that in the *strong* spin-orbit coupling limit, the spin and orbital components of the magnetisation oppose each other and result in a reduced moment that way. It has already been shown that spin-orbit coupling is relevant for the magnetic behaviour of $Cd_2Os_2O_7$ and $NaOsO_3$, as shown by the significant anisotropies observed in the excitation spectra. Consequently one would expect a non-zero orbital component to the magnetisation for $NaOsO_3$, just like that seen for $Cd_2Os_2O_7$ using XMCD [100].

The magnitude of the orbital component allows quantitative determination of the departure from the Slater (and Russell-Saunders) limit. Two techniques allow the measurement of this orbital component: X-ray magnetic circular dichroism (XMCD) and non-resonant magnetic X-ray diffraction (nRXMS). However only the latter technique is suitable to look at $NaOsO_3$ for the following reason. XMCD is sensitive to the ferromagnetic component of the magnetisation, yet

$NaOsO_3$ is a G-type antiferromagnet below T_N with an almost zero canting angle (see Chapter 4). Consequently the XMCD signal is likely to be vanishingly small. Whilst the non-resonant signal is approximately two orders of magnitude weaker than the resonant magnetic signal, it should still be possible to at least determine the ratio $\langle \mathbf{L} \rangle / \langle \mathbf{S} \rangle$ by measuring the azimuthal dependence of a series of related reflections. One can then compare the experimentally obtained behaviour with DFT calculations [115, 135, 136] to examine whether spin-orbit coupling does indeed induce a significant orbital component for $NaOsO_3$.

7.2.3 Probing the band structure

The most direct evidence of Slater or Lifshitz like behaviour can be garnered from experimental measurements of the electronic band structure. Density functional theory (DFT) calculations, whilst useful for qualitative comparisons, frequently have quantitative disagreements with experiment as a result of the inherent approximations used. Furthermore the results obtained are highly dependent on the initial starting parameters used, including the choice of pseudopotentials, the magnitude of the electron correlation U, and inclusion of spin-orbit coupling.

Ideally one would perform ARPES measurements on $NaOsO_3$. However the same limitations as those relevant for $Cd_2Os_2O_7$ apply, only more stringent as a consequence of the higher T_{MI}. One possibility is to lightly dope $NaOsO_3$ and attempt to suppress T_{MI} (and perhaps T_N) through the introduction of additional charge carriers. Unfortunately this would also likely perturb the band structure, the extent of which is presently unclear. DFT calculations are proposed to study this in more detail.

7.2.4 Itinerant model for magnetic excitations

Thus far the magnetic and electronic excitations have only been examined in terms of a localised (Heisenberg) model. From the RIXS data we know that this seems to work well at 300 K, deep within the insulating antiferromagnetic regime. However with increasing temperature the localised model gives a poorer description of the data, with the spin waves becoming significantly more damped and less well-defined. Furthermore the valence 5d-orbitals are extended in real space for $NaOsO_3$, which leads to large hybridisation (as determined from DFT calculations). Both of these points lead to itinerant behaviour.

Calculation of the excitation spectrum from an itinerant starting point may prove insightful. To do this one typically uses the random-phase approximation (RPA) to simplify the calculations. RPA neglects the temporal fluctuations of the local exchange about its mean value. One example is the concurrent simulation of magnons in Sr_2IrO_4 by Igarashi [217] from both a localised and itinerant perspective.

7.3 Sr_2IrO_4

7.3.1 Crossover phenomena

Easy-plane anisotropy seems to be important for Sr_2IrO_4 between T_{KT} and T_N. Yet there are a number of outstanding questions pertaining to the quasi-2D behaviour. The first of these is whether there is any evidence of a crossover in the magnetization at T_{KT}. From muon spin relaxation (μSR) data [194], it does not appear like there is any sort of transition at T_{KT}. However μSR probes long time-scale dynamics (microsecond); there may be shorter time-scale dynamics that may be relevant and can be probed by X-rays for instance.

7.3.2 Sample dependence of magnetic properties

A recent study [260] examined how the magnetic properties vary for Sr_2IrO_4 when the synthesis conditions are changed. What they found was a significant variation in the magnetic susceptibility, transition temperature, and Raman scattering response for seemingly minor alterations in the method. Energy dispersive X-ray spectroscopy (EDX) measurements – which should be noted is not especially sensitive to oxygen – did determine that samples with reduced transition temperatures suffered from oxygen deficiency. Raman scattering also determined that oxygen deficient samples exhibited additional peaks characteristic of an in-plane distortion. This would likely increase the in-plane anisotropy compared to stoichiometric samples. Further examination of this point would prove insightful, especially using a probe that is more sensitive to the oxygen content of a material.

7.3.3 Imaging the Griffiths phase

Recent work by Rathi *et al.* [261] suggests the presence of a Griffiths phase in Sr_2IrO_4. In the simplest case [262]: “A dilute ferromagnet is in the Griffiths phase if its temperature T is between the critical temperature $T_c(p)$ for the onset of magnetic long-range order and the critical temperature $T_c(1)$ of the pure (i.e., non-dilute) system.” More specifically, the phase comprises a number of localised ferromagnetic clusters which do not exhibit long-ranged magnetic order, but do have short-ranged magnetic correlations.

Rathi and colleagues performed bulk magnetisation measurements on a single crystal of Sr_2IrO_4. Remember that Sr_2IrO_4 is a weak ferromagnet due to the magnetic moments locking to the correlated in-plane rotation of IrO_6 octahedra [191]. This leads to a positive Curie-Weiss temperature $\theta_{CW} \sim 200$ K. The magnetisation below $T_C = 221.5$ K was to be consistent with the behaviour expected for a second-order phase transition [$\beta = 0.19(1)$]. This agrees with the value for β obtained from the critical scattering measurements presented in Chapter 5. The susceptibility above T_C was measured at low field (100 Oe), and was found to exhibit a downturn above 280 K, a feature that was proposed to be a signature of the Griffiths phase. Further quantitative analysis determined that the Griffiths phase was extant between $T_C^R = 234.0(7)$ K and $T_G = 279.0(5)$ K. This temperature range is comparable to that studied by magnetic critical scattering. Further studies are proposed to examine the extent/validity of this Griffiths phase scenario.

7.3.4 Effect of carrier doping

Finally as discussed in Chapter 6, it is possible to chemically dope Sr_2IrO_4, in an analogous fashion to the cuprates. Pseudo-gap behaviour, Fermi arcs, and perhaps even superconductivity have been observed in these materials. Lanthanum doping Sr_2IrO_4 by as little as 5% suppresses long-ranged magnetic order, and induces a metallic state. One argument is that doping Sr_2IrO_4 will push the system closer towards the quantum critical point g_c as shown in Fig. 5.1. This implies that (if the theoretical predictions for a 2DHAFSQL hold) close to g_c there would be $1/T$ scaling of the correlation length in the paramagnetic metal phase, which would be representative of the quantum critical regime. This is still an open question however and would be intriguing for further study.

7.4 $Sr_3Ir_2O_7$

The critical scattering measurements on $Sr_3Ir_2O_7$ presented in Chapter 5 were characterised by a degree of defect mediated behaviour which obscured the true critical behaviour. These defects may arise either from surface strain, or oxygen vacancies close to the surface. One proposal is to measure the critical scattering from a cleaved sample, which would likely show behaviour more representative of the bulk. Consequently a more accurate determination of the critical exponents – and hence dimensionality of the magnetic interactions – can be made.

A further proposition is the study of photodoped $Sr_3Ir_2O_7$ by time-resolved resonant X-ray scattering. The charge gap has a magnitude of around 100 meV; consequently one would need a pump pulse with wavelength 12 μm to induce the transient metallic state. Such a wavelength is certainly attainable as shown by the data obtained for Sr_2IrO_4. The hypothesis is that there would be a suppression of long-ranged antiferromagnetic order upon photo-doping, albeit with a much faster recovery timescale compared to Sr_2IrO_4. This is due to the three-dimensional nature of the magnetic correlations.

7.5 Summary

To summarise, the metal-insulator transitions in 5d transition metal oxides occur as a consequence of a number of competing energy scales. This has profound effects on the magnetic interactions, which can be directly probed using resonant X-ray scattering techniques. Whilst the iridates have narrow electronic bands and undergo MITs with pressure, bulk- or photo-doping (albeit with a degree of Slater character), the osmates are more itinerant. What has been demonstrated in this thesis is that the apparent discrepancy is a direct result of spin-orbit coupling playing a reduced role for the osmates compared to the iridates. This has important consequences for the mechanism of the MIT, which show some degree of coupling to the onset of magnetic order. However the magnitude of spin-orbit coupling is still sufficient to induce significant anisotropic gaps in the spin wave dispersion for the osmates.

Furthermore tr-RIXS has been shown to be a viable technique with which to study the magnetic and electronic excitations in 5d TMOs. With time and expertise, the proof-of-principle experiments detailed in this thesis will become more routine and accessible to the general user. The same progression has occurred at synchrotron sources. Fifteen years ago RIXS was a niche and under-developed technique; whereas today it is mature, with RIXS spectrometers well over-subscribed and facilitating the construction of state-of-the-art instrumentation to fulfil this demand. With the construction of new XFEL facilities around the world (EU-XFEL, SwissFEL, LCLS-II to name but a few), then capabilities and possibilities for tr-RIXS can only increase. This paves the way for a series of new experiments and novel scientific directions to look forward to for years to come.

Appendices

A Energy resolution of RIXS instruments

There are three main contributions to the energy resolution of RIXS instruments: the monochromator setup, the spot size incident on the sample, and the energy analyser. The Darwin width is a measure of the intrinsic reflectivity of a crystal, and in particular its angular acceptance. The Darwin width is given by [71]:

$$\zeta_D = \frac{4}{\pi}\left(\frac{d}{m}\right)^2 \frac{r_0\,|F|}{v_c}, \tag{A.1}$$

where m is the order of diffraction, r_0 is the classical electron radius, $|F|$ is the structure factor of the unit cell, and v_c is the volume of the unit cell. As $h^2 + k^2 + l^2$ increases, d decreases[1] and $|F|$ decreases (as a consequence of the Debye-Waller factor), and hence the Darwin width also decreases.

The energy resolution of a monochromator setup ΔE_m is given by:

$$\Delta E_m = E_i \cot\theta_B \sqrt{\Omega^2 + \Delta\theta_{DW}^2}, \tag{A.2}$$

where E_i is the incident angle, θ_B is the Bragg angle of the monochromator, Ω is the source divergence, and $\Delta\theta_{DW}$ is the angular Darwin width. Thus a better energy resolution can be achieved by using monochromator crystals with θ_B closer to 90°, a smaller Darwin width and a source with a smaller angular divergence.

The energy resolution of the analyser crystal is comprised of two components. The first of these comes from the intrinsic Darwin width of the crystal:

$$\Delta E_\mathrm{A} = E_i \cot\theta_B\, \Delta\theta_{DW}. \tag{A.3}$$

The second contribution arises from the dicing of the crystal. As discussed above, dicing the analyser crystal reduces spherical distortions, at the expense of adding a geometrical broadening term to the energy resolution, due to each individual crystal focussing onto a different point on the detector. It can be derived [263] that the pixel size on the position-sensitive detector is the limiting factor for the geometrical broadening, with

$$\Delta E_\mathrm{g} = E_i \frac{\Delta d_D}{2R_A \tan\theta_A}, \tag{A.4}$$

---

[1] In general $\frac{1}{d^2_\mathrm{hkl}} = h^2a^2 + k^2b^2 + l^2c^2 + 2kl\,bc\cos\alpha + 2hl\,ac\cos\beta + 2hk\,ab\cos\gamma$, however this expression simplifies for more symmetrical Bravais lattices.

where Δd_D is the pixel size of the detector, R_A is the analyser radius, and θ_A is the Bragg angle of the analyser.

Combining all of these terms in quadrature (including a contribution ΔE_s from the finite spot size of the sample) gives an expression for the total instrumental energy resolution:

$$\Delta E_{\text{tot}} = \sqrt{\Delta E_{\text{M}}^2 + \Delta E_{\text{A}}^2 + \Delta E_{\text{g}}^2 + \Delta E_s^2}. \tag{A.5}$$

It is instructive to calculate the instrumental resolution at MERIX for the measurements on $Cd_2Os_2O_7$ described in Chapter 3. Using the tables in Ref. [264], and assuming the incident energy $E_i = 10.871$ keV the energy resolution for a Si$\,(1,\ 1,\ 1)$ primary and Si$\,(4,\ 4,\ 4)$ secondary monochromator setup $\Delta E_M = 144.57$ meV. The intrinsic analyser contribution for a Si$\,(6,\ 4,\ 4)$ crystal $\Delta E_A = 16.93$ meV, and the geometrical contribution $E_g = 23.2$ meV, assuming a 2 m analyser radius and pixel size of 50 μm from the micro-strip detector. The vertical spot size is 10 μm, which means that $E_s \approx 5$ meV. Thus:

$$\begin{aligned}\Delta E_{\text{tot}} &= \sqrt{144.57^2 + 16.93^2 + 23.2^2 + 5^2}\ \text{meV} \\ &= 147\ \text{meV}\end{aligned}$$

This agrees reasonably well with the experimental energy resolution, however the experimental energy resolution was in fact slightly lower [$\Delta E_{\text{tot}} \sim 130$ meV]. One possible explanation for this is that since the monochromator resolution is dependent on the source divergence, then a smaller source divergence than calculated would improve the monochromator bandpass. Clearly the monochromator setup is the dominant contribution to the experimental energy resolution here, and future high-resolution experiments would benefit from utilising a higher-order secondary monochromator.

B Linear spin wave theory applied to $NaOsO_3$

In this section a detailed derivation of the linear spin wave theory method shall be given and applied to $NaOsO_3$.

The starting point is the trial Hamiltonian presented earlier for a Heisenberg model with anisotropic exchange:

$$\mathcal{H} = J_1 \sum_{\mathrm{nn}} \mathbf{S}_i \cdot \mathbf{S}_j + J_2 \sum_{\mathrm{nnn}} \mathbf{S}_i \cdot \mathbf{S}_j + \Gamma \sum_{\mathrm{nn,nnn}} \mathbf{S}_i^z \mathbf{S}_j^z + \sum_i \mathbf{S}_i \cdot \bar{\mathrm{D}} \cdot \mathbf{S}_i \tag{B.1}$$

$$= \mathcal{H}_{\mathrm{NN}} + \mathcal{H}_{\mathrm{NNN}} + \mathcal{H}_{\mathrm{A}} + \mathcal{H}_{\mathrm{SIA}}, \tag{B.2}$$

where $\mathcal{H}_{\mathrm{NN}}$, $\mathcal{H}_{\mathrm{NNN}}$, $\mathcal{H}_{\mathrm{A}}$ and $\mathcal{H}_{\mathrm{SIA}}$ stand for the nearest neighbour, next-nearest-neighbour, anisotropic exchange, and single-ion anisotropy (SIA) contributions to the Hamiltonian respectively. Note that in principle a Dzyaloshinskii-Moriya term should also included within this Hamiltonian, however this has been neglected for reasons of simplicity.

One can rewrite these individual contributions in terms of raising and lowering operators $\mathbf{S}_j^{\pm} = \mathbf{S}_j^x \pm i\mathbf{S}_j^y$. The effect of these operators is to increase or decrease the z-component of the spin angular momentum. Consider some arbitrary state with angular momentum $|m\rangle$. If $|m\rangle$ is an eigenstate of $\mathbf{S}_j^z$ and $\mathbf{S}_j^2$, then $\mathbf{S}_j^{\pm} = \hbar\sqrt{s\,(s+1) - m\,(m \pm 1)}\,|m \pm 1\rangle$.

Consequently $\mathbf{S}_i \cdot \mathbf{S}_j = \mathbf{S}_i^z \mathbf{S}_j^z + \frac{1}{2}\left(\mathbf{S}_i^+ \mathbf{S}_j^- + \mathbf{S}_i^- \mathbf{S}_j^+\right)$. The ground state of $NaOsO_3$ is a G-type antiferromagnet. Assume a perfectly ordered Neel state at $T = 0$. The spins are divided into two sublattices A and B, which point along the positive and negative z-directions respectively. This is defined to coincide with the c-axis for $NaOsO_3$.

In the Holstein-Primakoff transformation, the spin raising and lowering operators are rewritten in terms of boson creation and annihilation operators:

$$\begin{aligned}
\mathbf{S}_i^+ &= \sqrt{2S\left(1 - \tfrac{a_i^\dagger a_i}{2S}\right)}\,a_i & \mathbf{S}_j^+ &= b_j^\dagger \sqrt{2S\left(1 - \tfrac{b_i^\dagger b_i}{2S}\right)} \\
\mathbf{S}_i^- &= a_i^\dagger \sqrt{2S\left(1 - \tfrac{a_i^\dagger a_i}{2S}\right)} & \mathbf{S}_j^- &= \sqrt{2S\left(1 - \tfrac{b_j^\dagger b_j}{2S}\right)}\,b_j \\
\mathbf{S}_i^z &= S - a_i^\dagger a_i & \mathbf{S}_j^z &= -S + b_i^\dagger b_i
\end{aligned}$$

In the Holstein-Primakoff *approximation*, the square root within the spin operators is formally expanded as a Taylor series into powers of $(a_i^\dagger a_i/2S)$ and $(b_i^\dagger b_i/2S)$. Expanding to zeroth order, one obtains the linear spin wave theory (LSWT) expression. Interactions between spin waves are neglected within the LSWT. Furthermore inclusion of the higher order terms results in a renormalisation of the dispersion compared to the linear spin wave case.

In the LSWT, the spin operators are approximated as:

$$\begin{aligned}
\mathbf{S}_i^+ &\simeq \sqrt{2S}\,a_i & \mathbf{S}_j^+ &\simeq \sqrt{2S}\,b_j^\dagger \\
\mathbf{S}_i^- &\simeq \sqrt{2S}\,a_i^\dagger & \mathbf{S}_j^- &\simeq \sqrt{2S}\,b_j \\
\mathbf{S}_i^z &= S - a_i^\dagger a_i & \mathbf{S}_j^z &= -S + b_j^\dagger b_j
\end{aligned}$$

There are four Os atoms ($N = 4$) in one unit cell of $\mathrm{NaOsO_3}$, located at lattice positions $\mathbf{r} = (\frac{1}{2}, 0, 0)$, $(0, \frac{1}{2}, 0)$, $(\frac{1}{2}, 0, \frac{1}{2})$ and $(0, \frac{1}{2}, \frac{1}{2})$. Rewriting $\mathbf{S}_i \cdot \mathbf{S}_j$ and $\mathbf{S}_i^z \mathbf{S}_j^z$ in terms of the spin operators, and inserting them into Eqn. B.1, one obtains for $\mathcal{H}_{\mathrm{NN}}$:

$$\begin{aligned}\mathcal{H}_{\mathrm{NN}} = J \sum_{\mathbf{r}\in A} & \left(S - a_{\mathbf{r}}^{\dagger} a_{\mathbf{r}}\right)\left(-S + b_{\mathbf{r+m}}^{\dagger} b_{\mathbf{r+m}}\right) + S\left(a_{\mathbf{r}} b_{\mathbf{r+m}} + a_{\mathbf{r}}^{\dagger} b_{\mathbf{r+m}}^{\dagger}\right) \\ + & \left(S - a_{\mathbf{r}}^{\dagger} a_{\mathbf{r}}\right)\left(-S + b_{\mathbf{r-m}}^{\dagger} b_{\mathbf{r-m}}\right) + S\left(a_{\mathbf{r}} b_{\mathbf{r-m}} + a_{\mathbf{r}}^{\dagger} b_{\mathbf{r-m}}^{\dagger}\right) \\ + & \left(S - a_{\mathbf{r}}^{\dagger} a_{\mathbf{r}}\right)\left(-S + b_{\mathbf{r+n}}^{\dagger} b_{\mathbf{r+n}}\right) + S\left(a_{\mathbf{r}} b_{\mathbf{r+n}} + a_{\mathbf{r}}^{\dagger} b_{\mathbf{r+n}}^{\dagger}\right) \\ + & \left(S - a_{\mathbf{r}}^{\dagger} a_{\mathbf{r}}\right)\left(-S + b_{\mathbf{r-n}}^{\dagger} b_{\mathbf{r-n}}\right) + S\left(a_{\mathbf{r}} b_{\mathbf{r-n}} + a_{\mathbf{r}}^{\dagger} b_{\mathbf{r-n}}^{\dagger}\right), \end{aligned} \tag{B.3}$$

where the summation is over all A sublattice sites, and $\mathbf{m} = (\frac{1}{2}, 0, 0)$, $\mathbf{n} = (0, 0, \frac{1}{2})$. Neglecting terms higher than second order in $a^{(\dagger)}$, $b^{(\dagger)}$:

$$\begin{aligned}\mathcal{H}_{\mathrm{NN}} = -8JS^2 + JS \sum_{\mathbf{r}\in A} & \left(4a_{\mathbf{r}}^{\dagger} a_{\mathbf{r}} + b_{\mathbf{r+m}}^{\dagger} b_{\mathbf{r+m}} + b_{\mathbf{r-m}}^{\dagger} b_{\mathbf{r-m}} + b_{\mathbf{r+n}}^{\dagger} b_{\mathbf{r+n}} + b_{\mathbf{r-n}}^{\dagger} b_{\mathbf{r-n}}\right) \\ & + a_{\mathbf{r}} b_{\mathbf{r+m}} + a_{\mathbf{r}}^{\dagger} b_{\mathbf{r+m}}^{\dagger} + a_{\mathbf{r}} b_{\mathbf{r-m}} + a_{\mathbf{r}}^{\dagger} b_{\mathbf{r-m}}^{\dagger} \\ & + a_{\mathbf{r}} b_{\mathbf{r+n}} + a_{\mathbf{r}}^{\dagger} b_{\mathbf{r+n}}^{\dagger} + a_{\mathbf{r}} b_{\mathbf{r-n}} + a_{\mathbf{r}}^{\dagger} b_{\mathbf{r-n}}^{\dagger}, \end{aligned} \tag{B.4}$$

where $-8JS^2 = -2NJS^2$ is the classical ground state energy for $\mathcal{H}_{\mathrm{NN}}$.

In a similar fashion:

$$\begin{aligned}\mathcal{H}_{\mathrm{NNN}} = -4J_2S^2 + J_2S \sum_{\mathbf{r}\in A} & \left(2a_{\mathbf{r}}^{\dagger} a_{\mathbf{r}} + b_{\mathbf{r+o}}^{\dagger} b_{\mathbf{r+o}} + b_{\mathbf{r-o}}^{\dagger} b_{\mathbf{r-o}}\right) \\ & + a_{\mathbf{r}} b_{\mathbf{r+o}} + a_{\mathbf{r}}^{\dagger} b_{\mathbf{r+o}}^{\dagger} + a_{\mathbf{r}} b_{\mathbf{r-o}} + a_{\mathbf{r}}^{\dagger} b_{\mathbf{r-o}}^{\dagger} \end{aligned} \tag{B.5}$$

with $\mathbf{o} = (0, \frac{1}{2}, 0)$.

$$\begin{aligned}\mathcal{H}_{\mathrm{A}} = & -8\Gamma_1S^2 + \Gamma_1S \sum_{\mathbf{r}\in A} \left(4a_{\mathbf{r}}^{\dagger} a_{\mathbf{r}} + b_{\mathbf{r+m}}^{\dagger} b_{\mathbf{r+m}} + b_{\mathbf{r-m}}^{\dagger} b_{\mathbf{r-m}} + b_{\mathbf{r+n}}^{\dagger} b_{\mathbf{r+n}} + b_{\mathbf{r-n}}^{\dagger} b_{\mathbf{r-n}}\right) \\ & -4\Gamma_2S^2 + \Gamma_2S \sum_{\mathbf{r}\in A} \left(2a_{\mathbf{r}}^{\dagger} a_{\mathbf{r}} + b_{\mathbf{r+o}}^{\dagger} b_{\mathbf{r+o}} + b_{\mathbf{r-o}}^{\dagger} b_{\mathbf{r-o}}\right), \end{aligned} \tag{B.6}$$

where the first and second lines refer to summations over nearest and next-nearest neighbours respectively. In the limit $\Gamma_1 \equiv \Gamma_2$ this reduces to:

$$\begin{aligned}\mathcal{H}_{\mathrm{A}} = -12\Gamma S^2 + \Gamma S \sum_{\mathbf{r}\in A} & \left(6a_{\mathbf{r}}^{\dagger} a_{\mathbf{r}} + b_{\mathbf{r+m}}^{\dagger} b_{\mathbf{r+m}} + b_{\mathbf{r-m}}^{\dagger} b_{\mathbf{r-m}} \right. \\ & \left. + b_{\mathbf{r+n}}^{\dagger} b_{\mathbf{r+n}} + b_{\mathbf{r-n}}^{\dagger} b_{\mathbf{r-n}} + b_{\mathbf{r+o}}^{\dagger} b_{\mathbf{r+o}} + b_{\mathbf{r-o}}^{\dagger} b_{\mathbf{r-o}}\right). \end{aligned} \tag{B.7}$$

Single-ion anisotropy

For $\mathrm{NaOsO_3}$, the Os (4b) site only possesses inversion symmetry [265]. Consequently the rhombic zero-field splitting parameter E is in principle non-zero, and two acoustic magnon branches should be observable. However given that the distortion away from the ideal octahedral case is small (especially in terms of bond angles), then one can assume that $E \approx 0$ as a first approximation. This implies $D_{\mathrm{XX}} \approx D_{\mathrm{YY}}$.

One finds:

$$\begin{aligned}\mathcal{H}_{\mathrm{SIA}} = 4DS^2 - 2DS\sum_{\mathbf{r}\in A} a_{\mathbf{r}}^{\dagger}a_{\mathbf{r}} + ES\sum_{\mathbf{r}\in A}\left(a_{\mathbf{r}}a_{\mathbf{r}} + a_{\mathbf{r}}^{\dagger}a_{\mathbf{r}}^{\dagger}\right)\\ - 2DS\sum_{\mathbf{r}\in B} b_{\mathbf{r}}^{\dagger}b_{\mathbf{r}} + ES\sum_{\mathbf{r}\in B}\left(b_{\mathbf{r}}b_{\mathbf{r}} + b_{\mathbf{r}}^{\dagger}b_{\mathbf{r}}^{\dagger}\right)\end{aligned} \tag{B.8}$$

Fourier transform into reciprocal space

It is convenient to convert into reciprocal space by Fourier transforming the spin operators:

$$\begin{aligned} a_q^{\dagger} &= \sqrt{\frac{2}{N}}\sum_{\mathbf{r}\in A} e^{i\mathbf{q}\cdot\mathbf{r}}a_r^{\dagger} \qquad & b_q^{\dagger} &= \sqrt{\frac{2}{N}}\sum_{\mathbf{r}\in B} e^{-i\mathbf{q}\cdot\mathbf{r}}b_r^{\dagger}\\ a_q &= \sqrt{\frac{2}{N}}\sum_{\mathbf{r}\in A} e^{-i\mathbf{q}\cdot\mathbf{r}}a_r \qquad & b_q &= \sqrt{\frac{2}{N}}\sum_{\mathbf{r}\in B} e^{i\mathbf{q}\cdot\mathbf{r}}b_r, \end{aligned} \tag{B.9}$$

with the inverse transforms given by:

$$\begin{aligned} a_r^{\dagger} &= \sqrt{\frac{2}{N}}\sum_{\mathbf{q}} e^{-i\mathbf{q}\cdot\mathbf{r}}a_q^{\dagger} \qquad & b_r^{\dagger} &= \sqrt{\frac{2}{N}}\sum_{\mathbf{q}} e^{i\mathbf{q}\cdot\mathbf{r}}b_q^{\dagger}\\ a_r &= \sqrt{\frac{2}{N}}\sum_{\mathbf{q}} e^{i\mathbf{q}\cdot\mathbf{r}}a_q \qquad & b_r &= \sqrt{\frac{2}{N}}\sum_{\mathbf{q}} e^{-i\mathbf{q}\cdot\mathbf{r}}b_q \end{aligned} \tag{B.10}$$

The summations over $\mathbf{q}$ run over $N/2$ wavevectors in the first Brillouin zone. We wish to substitute the Fourier transformed spin operators into Eqn. B.4. A useful relation is the Fourier transform of the delta function:

$$\delta_{\mathbf{q}+\mathbf{q}',0} = \frac{1}{N}\sum_{j=1}^{N} e^{i(\mathbf{q}+\mathbf{q}')\cdot\mathbf{r}_j} = \begin{cases} 1 \text{ iff } \mathbf{q}-\mathbf{q}'=0\\ 0 \text{ iff } \mathbf{q}-\mathbf{q}'\neq 0\end{cases} \tag{B.11}$$

A useful table summarising the relevant Fourier transform identities is given in Peter Babkevich's thesis [266]. These identities simplify the equations dramatically, leading to:

$$\begin{aligned}\mathcal{H}_{\mathrm{NN}} &= -8J_1S^2 + J_1S\left[4\sum_{\mathbf{q}} a_q^{\dagger}a_q + 4\sum_{\mathbf{q}} b_q^{\dagger}b_q + 2\left(\sum_{\mathbf{q}} e^{-i\mathbf{q}\cdot\mathbf{m}}a_qb_{-q} + \sum_{\mathbf{q}} e^{i\mathbf{q}\cdot\mathbf{m}}a_q^{\dagger}b_{-q}^{\dagger}\right)\right.\\ &\left.+ 2\left(\sum_{\mathbf{q}} e^{-i\mathbf{q}\cdot\mathbf{n}}a_qb_{-q} + \sum_{\mathbf{q}} e^{i\mathbf{q}\cdot\mathbf{n}}a_q^{\dagger}b_{-q}^{\dagger}\right)\right]\\ &= 4J_1S\sum_{\mathbf{q}}\left(a_q^{\dagger}a_q + b_q^{\dagger}b_q\right) + 2J_1S\sum_{\mathbf{q}}\left[\cos\pi(h+l) + \cos\pi(h-l)\right]\left(a_qb_{-q} + a_q^{\dagger}b_{-q}^{\dagger}\right)\end{aligned} \tag{B.12}$$

assuming that independent operators commute, i. e. $\left[a_q^{\dagger}, b_q\right] = 0$. Similarly for $\mathcal{H}_{\mathrm{NNN}}$ and the anisotropic terms $\mathcal{H}_{\mathrm{A}}$ and $\mathcal{H}_{\mathrm{SIA}}$:

$$\mathcal{H}_{\mathrm{NNN}} = -4J_2S^2 + 2J_2S\sum_{\mathbf{q}}\left(a_q^{\dagger}a_q + b_q^{\dagger}b_q\right) + 2J_2S\sum_{\mathbf{q}}\cos(\pi k)\left(a_qb_{-q} + a_q^{\dagger}b_{-q}^{\dagger}\right) \tag{B.13}$$

$$\mathcal{H}_{\mathrm{A}} = -12\Gamma S^2 + 6\Gamma S\sum_{\mathbf{q}}\left(a_q^{\dagger}a_q + b_q^{\dagger}b_q\right) \tag{B.14}$$

$$\mathcal{H}_{\text{SIA}} = 4DS^2 - 2DS\sum_{\mathbf{q}}\left(a_q^\dagger a_q + b_q^\dagger b_q\right) + ES\sum_{\mathbf{q}}\left(a_q a_{-q} + a_q^\dagger a_{-q}^\dagger + b_q b_{-q} + b_q^\dagger b_{-q}^\dagger\right), \tag{B.15}$$

with the summations in the single-ion contribution divided by two to avoid double counting.

Diagonalisation of Hamiltonian

However this form of the Hamiltonian still cannot be diagonalised for two reasons. The first is that there are terms which do not conserve the number of bosons (for example $a_q^\dagger a_q^\dagger$). The second is there is a coupling between the q and $-q$ spin waves. Fortunately there are techniques one can employ to resolve this issue.

The total Hamiltonian $\mathcal{H}$ (Eqn. B.1) can be expressed in the following form:

$$\mathcal{H} = \mathcal{H}_0 + \frac{1}{2}\sum_{\mathbf{q}} x_{\mathbf{q}}^\dagger H_{\mathbf{q}} x_{\mathbf{q}} \tag{B.16}$$

where

$$x_{\mathbf{q}} = \begin{pmatrix} a_q \\ b_q \\ a_{-q}^\dagger \\ b_{-q}^\dagger \end{pmatrix}, \qquad H_{\mathbf{q}} = \begin{pmatrix} A_{\mathbf{q}} & B_{\mathbf{q}} & C_{\mathbf{q}} & D_{\mathbf{q}} \\ B_{\mathbf{q}} & A_{\mathbf{q}} & D_{\mathbf{q}} & C_{\mathbf{q}} \\ C_{\mathbf{q}} & D_{\mathbf{q}} & A_{\mathbf{q}} & B_{\mathbf{q}} \\ D_{\mathbf{q}} & C_{\mathbf{q}} & B_{\mathbf{q}} & A_{\mathbf{q}} \end{pmatrix} \tag{B.17}$$

The elements in $H_{\mathbf{q}}$ are generated as follows. If one multiplies out $x_{\mathbf{q}}^\dagger H_{\mathbf{q}} x_{\mathbf{q}}$, then the result is a sum of product of ladder operators and an associated coefficient $X_{\mathbf{q}} \in H_{\mathbf{q}}$:

$$x_{\mathbf{q}}^\dagger H_{\mathbf{q}} x_{\mathbf{q}} = \sum X_{\mathbf{q}} \alpha_k^\alpha \beta_k^\alpha$$

In the case of NaOsO$_3$, one can rewrite $\mathcal{H}$ using Equations B.12–B.15, with the resulting ground state energy $\mathcal{H}_0$ and coefficients $X_{\mathbf{q}}$ given by:

$$\begin{aligned} \mathcal{H}_0 &= -8J_1S^2 - 4J_2S^2 - 12\Gamma S^2 + 4DS^2 \\ A_{\mathbf{q}} &= 2S\left(2J_1 + J_2 + 3\Gamma - D\right) \\ B_{\mathbf{q}} &= 0 \\ C_{\mathbf{q}} &= 2SE \\ D_{\mathbf{q}} &= 2S\left[J_1\left(\cos\pi\left(h+l\right) + \cos\pi\left(h-l\right)\right) + J_2\cos\pi k\right] \end{aligned} \tag{B.18}$$

This Hamiltonian can now be diagonalised via a Bogoliubov transformation in the method described by White [267], leading to two magnon branches $\hbar\omega_\pm$ (which are degenerate in the limit $E \to 0$), with dispersion relations given by:

$$\hbar\omega_\pm = \left[\left(A_{\mathbf{q}} \pm B_{\mathbf{q}}\right)^2 - \left(C_{\mathbf{q}} \pm D_{\mathbf{q}}\right)^2\right]^{1/2}. \tag{B.19}$$

Bibliography

[1] M. Z. Hasan and C. L. Kane, Rev. Mod. Phys. **82**, 3045 (2010).

[2] D. Pesin and L. Balents, Nature Physics **6**, 376 (2010).

[3] X.-L. Qi and S.-C. Zhang, Rev. Mod. Phys. **83**, 1057 (2011).

[4] A. Bansil, H. Lin, and T. Das, Rev. Mod. Phys. **88**, 021004 (2016).

[5] W. Witczak-Krempa, G. Chen, Y. B. Kim, and L. Balents, Ann. Rev. Cond. Mat. Phys. **5**, 57 (2014).

[6] H. Weyl, Zeitschrift für Physik **56**, 330 (1929).

[7] X. Wan, A. M. Turner, A. Vishwanath, and S. Y. Savrasov, Phys. Rev. B **83**, 205101 (2011).

[8] A. A. Burkov and L. Balents, Phys. Rev. Lett. **107**, 127205 (2011).

[9] B. Q. Lv, H. M. Weng, B. B. Fu, X. P. Wang, H. Miao, J. Ma, P. Richard, X. C. Huang, L. X. Zhao, G. F. Chen, Z. Fang, X. Dai, T. Qian, and H. Ding, Phys. Rev. X **5**, 031013 (2015).

[10] S.-Y. Xu, I. Belopolski, N. Alidoust, M. Neupane, G. Bian, C. Zhang, R. Sankar, G. Chang, Z. Yuan, C.-C. Lee, S.-M. Huang, H. Zheng, J. Ma, D. S. Sanchez, B. Wang, A. Bansil, F. Chou, P. P. Shibayev, H. Lin, S. Jia, and M. Z. Hasan, Science **349**, 613 (2015).

[11] S. Rao, J. Indian Inst. Sci **96**, 145 (2016).

[12] B. Canals and C. Lacroix, Phys. Rev. Lett. **80**, 2933 (1998).

[13] B. Canals and C. Lacroix, Phys. Rev. B **61**, 1149 (2000).

[14] Z. Meng, T. Lang, S. Wessel, F. Assaad, and A. Muramatsu, Nature **464**, 847 (2010).

[15] J. S. Gardner, B. D. Gaulin, C. Lhuillier, P. Mendels, G. Misguich, and A. S. Wills, in *Introduction to Frustrated Magnetism: Materials, Experiments, Theory*, edited by C. Lacroix, P. Mendels, and F. Mila (Springer, London, 2011).

[16] L. Savary and L. Balents, arXiv:1601.03742 (2016).

[17] R. Perry, F. Baumberger, L. Balicas, N. Kikugawa, N. Ingle, A. Rost, J. Mercure, Y. Maeno, Z. Shen, and A. Mackenzie, New J. Phys. **8**, 175 (2006).

[18] F. Baumberger, N. J. C. Ingle, W. Meevasana, K. M. Shen, D. H. Lu, R. S. Perry, A. P. Mackenzie, Z. Hussain, D. J. Singh, and Z.-X. Shen, Phys. Rev. Lett. **96**, 246402 (2006).

[19] M. W. Haverkort, I. S. Elfimov, L. H. Tjeng, G. A. Sawatzky, and A. Damascelli, Phys. Rev. Lett. **101**, 026406 (2008).

[20] S. J. Moon, M. W. Kim, K. W. Kim, Y. S. Lee, J.-Y. Kim, J.-H. Park, B. J. Kim, S.-J. Oh, S. Nakatsuji, Y. Maeno, I. Nagai, S. I. Ikeda, G. Cao, and T. W. Noh, Phys. Rev. B **74**, 113104 (2006).

[21] G. Cao, J. Bolivar, S. McCall, J. E. Crow, and R. P. Guertin, Phys. Rev. B **57**, R11039 (1998).

[22] N. Kini, A. Strydom, H. Jeevan, C. Geibel, and S. Ramakrishnan, J. Phys.: Condens. Matter **18**, 8205 (2006).

[23] S. Chikara, O. Korneta, W. Crummett, L. DeLong, P. Schlottmann, and G. Cao, Phys. Rev. B **80**, 140407 (2009).

[24] B. J. Kim, H. Jin, S. J. Moon, J.-Y. Kim, B.-G. Park, C. S. Leem, J. Yu, T. W. Noh, C. Kim, S.-J. Oh, J.-H. Park, V. Durairaj, G. Cao, and E. Rotenberg, Phys. Rev. Lett. **101**, 076402 (2008).

[25] G. Jackeli and G. Khaliullin, Phys. Rev. Lett. **102**, 017205 (2009).

[26] B. J. Kim, H. Ohsumi, T. Komesu, S. Sakai, T. Morita, H. Takagi, and T. Arima, Science **323**, 1329 (2009).

[27] S. J. Moon, H. Jin, W. S. Choi, J. S. Lee, S. S. A. Seo, J. Yu, G. Cao, T. W. Noh, and Y. S. Lee, Phys. Rev. B **80**, 195110 (2009).

[28] J. Chaloupka, G. Jackeli, and G. Khaliullin, Phys. Rev. Lett. **105**, 027204 (2010).

[29] I. Kimchi and Y.-Z. You, Phys. Rev. B **84**, 180407 (2011).

[30] V. M. Katukuri, S. Nishimoto, V. Yushankhai, A. Stoyanova, H. Kandpal, S. Choi, R. Coldea, I. Rousochatzakis, L. Hozoi, and J. van den Brink, New J. Phys. **16**, 013056 (2014).

[31] S. H. Chun, J.-W. Kim, J. Kim, H. Zheng, C. C. Stoumpos, C. D. Malliakas, J. F. Mitchell, K. Mehlawat, Y. Singh, Y. Choi, T. Gog, A. Al-Zein, M. M. Sala, M. Krisch, J. Chaloupka, G. Jackeli, G. Khaliullin, and B. J. Kim, Nature Physics **11**, 462 (2015).

[32] S. J. Moon, H. Jin, K. W. Kim, W. S. Choi, Y. S. Lee, J. Yu, G. Cao, A. Sumi, H. Funakubo, C. Bernhard, and T. W. Noh, Phys. Rev. Lett. **101**, 226402 (2008).

[33] M. Blume and D. Gibbs, Phys. Rev. B **37**, 1779 (1988).

[34] M. Moretti Sala, S. Boseggia, D. F. McMorrow, and G. Monaco, Phys. Rev. Lett. **112**, 026403 (2014).

[35] J. Kim, A. H. Said, D. Casa, M. H. Upton, T. Gog, M. Daghofer, G. Jackeli, J. van den Brink, G. Khaliullin, and B. J. Kim, Phys. Rev. Lett. **109**, 157402 (2012).

[36] M. Moretti Sala, V. Schnells, S. Boseggia, L. Simonelli, A. Al-Zein, J. G. Vale, L. Paolasini, E. C. Hunter, R. S. Perry, D. Prabhakaran, A. T. Boothroyd, M. Krisch, G. Monaco, H. M. Rønnow, D. F. McMorrow, and F. Mila, Phys. Rev. B **92**, 024405 (2015).

[37] J. Kim, D. Casa, M. H. Upton, T. Gog, Y.-J. Kim, J. F. Mitchell, M. van Veenendaal, M. Daghofer, J. van den Brink, G. Khaliullin, and B. J. Kim, Phys. Rev. Lett. **108**, 177003 (2012).

[38] S. Fujiyama, H. Ohsumi, T. Komesu, J. Matsuno, B. J. Kim, M. Takata, T. Arima, and H. Takagi, Phys. Rev. Lett. **108**, 247212 (2012).

[39] D. Khomskii, *Basic Aspects of the Quantum Theory of Solids: Order and Elementary Excitations* (Cambridge University Press, Cambridge, 2010).

[40] P. Fazekas, *Lecture Notes on Electron Correlation and Magnetism*, Series in Modern Condensed Matter Physics (World Scientific, Singapore, 1999).

[41] M. H. Upton, Y. Choi, H. Park, J. Liu, D. Meyers, J. Chakhalian, S. Middey, J.-W. Kim, and P. J. Ryan, Phys. Rev. Lett. **115**, 036401 (2015).

[42] I. M. Lifshitz, Sov. Phys. JETP **11**, 1130 (1960).

[43] I. M. Lifshitz and M. I. Kaganov, Sov. Phys. Usp. **5**, 878 (1963).

[44] Y. M. Blanter, M. I. Kaganov, A. V. Pantsulaya, and A. A. Varlamov, Physics Reports **245**, 159 (1994).

[45] V. I. Makarov and V. G. Bar'yakhtar, Sov. Phys. JETP **21**, 1151 (1965).

[46] C. Liu, T. Kondo, R. M. Fernandes, A. D. Palczewski, E. D. Mun, N. Ni, A. N. Thaler, A. Bostwick, E. Rotenberg, J. Schmalian, S. L. BudâĂŹko, P. C. Canfield, and A. Kaminski, Nature Physics **6**, 419 (2010).

[47] E. Yelland, J. Barraclough, W. Wang, K. Kamenev, and A. Huxley, Nature Physics **7**, 890 (2011).

[48] Y. Wu, N. H. Jo, M. Ochi, L. Huang, D. Mou, S. L. Bud'ko, P. C. Canfield, N. Trivedi, R. Arita, and A. Kaminski, Phys. Rev. Lett. **115**, 166602 (2015).

[49] H. v. Löhneysen, A. Rosch, M. Vojta, and P. Wölfle, Rev. Mod. Phys. **79**, 1015 (2007).

[50] S. T. Carr, J. Quintanilla, and J. J. Betouras, Phys. Rev. B **82**, 045110 (2010).

[51] Y. Okamoto, A. Nishio, and Z. Hiroi, Phys. Rev. B **81**, 121102 (2010).

[52] S. Slizovskiy, J. J. Betouras, S. T. Carr, and J. Quintanilla, Phys. Rev. B **90**, 165110 (2014).

[53] S. Slizovskiy, A. V. Chubukov, and J. J. Betouras, Phys. Rev. Lett. **114**, 066403 (2015).

[54] Y. Yanagi and K. Ueda, Phys. Rev. B **90**, 085113 (2014).

[55] J. C. Slater, Phys. Rev. **82**, 538 (1951).

[56] J. D. Cloizeaux, J. Phys. Radium **20**, 606 (1959).

[57] I. L. Vecchio, A. Perucchi, P. Di Pietro, O. Limaj, U. Schade, Y. Sun, M. Arai, K. Yamaura, and S. Lupi, Scientific Reports **3**, 2990 (2013).

[58] M. T. Hutchings, Solid State Physics **16**, 227 (1964).

[59] J. R. Perumareddi, J. Phys. Chem. **71**, 3144 (1967).

[60] C. J. Ballhausen, *Introduction to Ligand Field Theory*, McGraw-Hill Series in Advanced Chemistry (McGraw-Hill, New York, 1962).

[61] V. M. Katukuri, *Quantum chemical approach to spin-orbit excitations and magnetic interactions in iridium oxides*, Ph.D. thesis, Technische Universität Dresden (2014).

[62] B. Tsukerblat, *Group Theory in Chemistry and Spectroscopy: A Simple Guide to Advanced Usage*, Dover Books on Chemistry (Dover Publications, Mineola, New York, 2006).

[63] A. Georges, L. de' Medici, and J. Mravlje, Ann. Rev. Cond. Mat. Phys. **4**, 137 (2013).

[64] D. van der Marel and G. A. Sawatzky, Phys. Rev. B **37**, 1067 (1988).

[65] D. I. Khomskii, *Transition Metal Compounds* (Cambridge University Press, Cambridge, 2014).

[66] T. Moriya, Phys. Rev. **120**, 91 (1960).

[67] J. H. Van Vleck, J. Phys. Radium **12**, 262 (1951).

[68] R. Maurice, P. Verma, J. M. Zadrozny, S. Luo, J. Borycz, J. R. Long, D. G. Truhlar, and L. Gagliardi, Inorg. Chem. **52**, 9379 (2013).

[69] J. Liu, H.-J. Koo, H. Xiang, R. K. Kremer, and M.-H. Whangbo, J. Chem. Phys. **141**, 124113 (2014).

[70] F. De Bergevin and M. Brunel, Acta Cryst. A **37**, 314 (1981).

[71] J. Als-Nielsen and D. McMorrow, *Elements of Modern X-ray Physics* (Wiley-Blackwell, 2009).

[72] D. Gibbs, D. R. Harshman, E. D. Isaacs, D. B. McWhan, D. Mills, and C. Vettier, Phys. Rev. Lett. **61**, 1241 (1988).

[73] J. P. Hannon, G. T. Trammell, M. Blume, and D. Gibbs, Phys. Rev. Lett. **61**, 1245 (1988).

[74] L. Paolasini, "Magnetism in condensed matter: Resonant and magnetic scattering by synchrotron radiation," (2012), italian School on Magnetism, Pavla, Italy.

[75] L. J. P. Ament, M. van Veenendaal, T. P. Deveraux, J. P. Hill, and J. van den Brink, Rev. Mod. Phys. **83**, 705 (2011).

[76] F. Fabrizi, H. C. Walker, L. Paolasini, F. de Bergevin, A. T. Boothroyd, D. Prabhakaran, and D. F. McMorrow, Phys. Rev. Lett. **106**, 239902 (2011).

[77] S. Grenier and Y. Joly, Journal of Physics: Conference Series **519**, 012001 (2014).

[78] J. P. Hill and D. F. McMorrow, Acta Cryst. A **52**, 236 (1996).

[79] R. D. Johnson, S. R. Bland, C. Mazzoli, T. A. W. Beale, C.-H. Du, C. Detlefs, S. B. Wilkins, and P. D. Hatton, Phys. Rev. B **78**, 104407 (2008).

[80] F. Fabrizi, H. C. Walker, L. Paolasini, F. de Bergevin, A. T. Boothroyd, D. Prabhakaran, and D. F. McMorrow, Phys. Rev. Lett. **102**, 237205 (2009).

[81] H. C. Walker, F. Fabrizi, L. Paolasini, F. de Bergevin, J. Herrero-Martin, A. T. Boothroyd, D. Prabhakaran, and D. F. McMorrow, Science **333**, 1273 (2011).

[82] X. Liu, M. P. M. Dean, J. Liu, S. G. Chiuzbăian, N. Jaouen, A. Nicolaou, W. G. Yin, C. R. Serrao, R. Ramesh, H. Ding, and J. P. Hill, J. Phys. Condens. Matter **27**, 202202 (2015).

[83] P. Olalde-Velasco, Y. Huang, V. Bisogni, J. Pelliciari, M. Dantz, S. Fatale, J. Vale, J. Miyawaki, Y. Harada, A. Nicolaou, S. Chiuzbăian, D. McMorrow, D. Prabhakaran, A. Boothroyd, J. Chang, H. Rønnow, V. Strokov, and T. Schmitt, "Oxygen K-edge RIXS on insulating and correlated metallic iridates," Unpublished.

[84] B. H. Kim and J. van den Brink, Phys. Rev. B **92**, 081105 (2015).

[85] Y. V. Shvyd'ko, J. Hill, C. Burns, D. Coburn, B. Brajuskovic, D. Casa, K. Goetze, T. Gog, R. Khachatryan, J.-H. Kim, C. Kodituwakku, M. Ramanathan, T. Roberts, A. Said, H. Sinn, D. Shu, S. Stoupin, M. Upton, M. Wieczorek, and H. Yavas, J. Electron Spectrosc. **188**, 140 (2013).

[86] L. Hozoi, H. Gretarsson, J. P. Clancy, B.-G. Jeon, B. Lee, K. H. Kim, V. Yushankhai, P. Fulde, D. Casa, T. Gog, J. Kim, A. H. Said, M. H. Upton, Y.-J. Kim, and J. van den Brink, Phys. Rev. B **89**, 115111 (2014).

[87] D. Uematsu, H. Sagayama, T.-h. Arima, J. J. Ishikawa, S. Nakatsuji, H. Takagi, M. Yoshida, J. Mizuki, and K. Ishii, Phys. Rev. B **92**, 094405 (2015).

[88] J. P. Clancy, H. Gretarsson, E. K. H. Lee, D. Tian, J. Kim, M. H. Upton, D. Casa, T. Gog, Z. Islam, B.-G. Jeon, K. H. Kim, S. Desgreniers, Y. B. Kim, S. J. Julian, and Y.-J. Kim, Phys. Rev. B **94**, 024408 (2016).

[89] C. Donnerer, M. C. Rahn, M. M. Sala, J. G. Vale, D. Pincini, J. Strempfer, M. Krisch, D. Prabhakaran, A. T. Boothroyd, and D. F. McMorrow, Phys. Rev. Lett. **117**, 037201 (2016).

[90] E. K.-H. Lee, S. Bhattacharjee, and Y. B. Kim, Phys. Rev. B **87**, 214416 (2013).

[91] J. S. Gardner, M. J. P. Gingras, and J. E. Greedan, Rev. Mod. Phys. **82**, 53 (2010).

[92] L. Balents, Nature **464**, 199 (2010).

[93] A. Sleight, J. Gillson, J. Weiher, and W. Bindloss, Solid State Commun. **14**, 357 (1974).

[94] D. Mandrus, J. Thompson, R. Gaal, L. Forro, J. Bryan, B. Chakoumakos, L. Woods, B. Sales, R. Fishman, and V. Keppens, Phys. Rev. B **63**, 195104 (2001).

[95] J. Yamaura, K. Ohgushi, H. Ohsumi, T. Hasegawa, I. Yamauchi, K. Sugimoto, S. Takeshita, A. Tokuda, M. Takata, M. Udagawa, M. Takigawa, H. Harima, T. Arima, and Z. Hiroi, Phys. Rev. Lett. **108**, 247205 (2012).

[96] J. Reading and M. T. Weller, J. Mater. Chem. **11**, 2373 (2001).

[97] Z. Hiroi, J. Yamaura, T. Hirose, I. Nagashima, and Y. Okamoto, APL Materials **3**, 041501 (2015).

[98] W. Padilla, D. Mandrus, and D. Basov, Phys. Rev. B **66**, 035120 (2002).

[99] C. H. Sohn, H. Jeong, H. Jin, S. Kim, L. J. Sandilands, H. J. Park, K. W. Kim, S. J. Moon, D.-Y. Cho, J. Yamaura, Z. Hiroi, and T. W. Noh, Phys. Rev. Lett. **115**, 266402 (2015).

[100] Y. Matsuda, J. Her, S. Michimura, T. Inami, M. Suzuki, N. Kawamura, M. Mizumaki, K. Kindo, J. Yamaura, and Z. Hiroi, Phys. Rev. B **84**, 174431 (2011).

[101] A. Koda, R. Kadono, K. Ohishi, S. R. Saha, W. Higemoto, S. Yonezawa, Y. Muraoka, and Z. Hiroi, J. Phys. Soc. Jpn. **76**, 063703 (2007).

[102] A. Koda, M. Miyazaki, M. Hiraishi, I. Yamauchi, K. M. Kojima, R. Kadono, J. Yamaura, and Z. Hiroi, *CMRC Annual Report 2012*, Tech. Rep. 1 (High Energy Accelerator Research Organisation (KEK), 2012).

[103] D. J. Singh, P. Blaha, K. Schwarz, and J. O. Sofo, Phys. Rev. B **65**, 155109 (2002).

[104] H. Shinaoka, T. Miyake, and S. Ishibashi, Phys. Rev. Lett. **108**, 247204 (2012).

[105] A. Uehara, H. Shinaoka, and Y. Motome, Physics Procedia **75**, 495 (2015).

[106] N. A. Bogdanov, R. Maurice, I. Rousochatzakis, J. van den Brink, and L. Hozoi, Phys. Rev. Lett. **110**, 127206 (2013).

[107] S. Sugano, Y. Tanabe, and H. Kamimura, *Multiplets of Transition-Metal Ions in Crystals*, Pure and Applied Physics (Academic Press, New York, 1970).

[108] J.-H. Choy, D.-K. Kim, and J.-Y. Kim, Solid State Ionics **108**, 159 (1998).

[109] A. E. Taylor, R. Morrow, D. J. Singh, S. Calder, M. D. Lumsden, P. M. Woodward, and A. D. Christianson, Phys. Rev. B **91**, 100406 (2015).

[110] M. C. Shapiro, S. C. Riggs, M. B. Stone, C. R. de la Cruz, S. Chi, A. A. Podlesnyak, and I. R. Fisher, Phys. Rev. B **85**, 214434 (2012).

[111] J. N. Millican, R. T. Macaluso, S. Nakatsuji, Y. Machida, Y. Maeno, and J. Y. Chan, Mat. Res. Bull. **42**, 928 (2007).

[112] Y. Tanabe and S. Sugano, J. Phys. Soc. Jpn. **9**, 753 (1954).

[113] W. Runciman and K. Schroeder, Proc. R. Soc. A **265**, 489 (1962).

[114] P. A. Reynolds, C. D. Delfs, B. N. Figgis, M. J. Henderson, B. Moubaraki, and K. S. Murray, J. Chem. Soc., Dalton Trans. **15**, 2309 (1992).

[115] H. Matsuura and K. Miyake, J. Phys. Soc. Jpn. **82**, 073703 (2013).

[116] J. N. Reimers, J. E. Greedan, and M. Björgvinsson, Phys. Rev. B **45**, 7295 (1992).

[117] A. Sadeghi, M. Alaei, F. Shahbazi, and M. J. P. Gingras, Phys. Rev. B **91**, 140407 (2015).

[118] S. Calder, J. G. Vale, N. A. Bogdanov, X. Liu, C. Donnerer, M. H. Upton, D. Casa, A. H. Said, M. D. Lumsden, Z. Zhao, *et al.*, Nature Communications **7**, 11651 (2016).

[119] H. Gretarsson, J. P. Clancy, X. Liu, J. P. Hill, E. Bozin, Y. Singh, S. Manni, P. Gegenwart, J. Kim, A. H. Said, D. Casa, T. Gog, M. H. Upton, H.-S. Kim, J. Yu, V. M. Katukuri, L. Hozoi, J. van den Brink, and Y.-J. Kim, Phys. Rev. Lett. **110**, 076402 (2013).

[120] M. Georgiev and L. Mihailov, Molecular Engineering **7**, 263 (1997).

[121] U. Fano, Phys. Rev. **124**, 1866 (1961).

[122] A. E. Miroshnichenko, S. Flach, and Y. S. Kivshar, Rev. Mod. Phys. **82**, 2257 (2010).

[123] D. Pröpper, A. N. Yaresko, T. I. Larkin, T. N. Stanislavchuk, A. A. Sirenko, T. Takayama, A. Matsumoto, H. Takagi, B. Keimer, and A. V. Boris, Phys. Rev. Lett. **112**, 087401 (2014).

[124] H. Gretarsson, N. H. Sung, M. Höppner, B. J. Kim, B. Keimer, and M. Le Tacon, Phys. Rev. Lett. **116**, 136401 (2016).

[125] K. Kobayashi, H. Aikawa, S. Katsumoto, and Y. Iye, Phys. Rev. B **68**, 235304 (2003).

[126] M. Elhajal, B. Canals, R. Sunyer, and C. Lacroix, Phys. Rev. B **71**, 094420 (2005).

[127] J. D. M. Champion, M. J. Harris, P. C. W. Holdsworth, A. S. Wills, G. Balakrishnan, S. T. Bramwell, E. Čižmár, T. Fennell, J. S. Gardner, J. Lago, D. F. McMorrow, M. Orendáč, A. Orendáčová, D. M. Paul, R. I. Smith, M. T. F. Telling, and A. Wildes, Phys. Rev. B **68**, 020401 (2003).

[128] S. Petit, J. Robert, S. Guitteny, P. Bonville, C. Decorse, J. Ollivier, H. Mutka, M. J. P. Gingras, and I. Mirebeau, Phys. Rev. B **90**, 060410 (2014).

[129] S. Toth and B. Lake, J. Phys.: Condens. Matter **27**, 166002 (2015).

[130] Y. G. Shi, Y. F. Guo, S. Yu, M. Arai, A. A. Belik, A. Sato, K. Yamaura, E. Takayama-Muromachi, H. F. Tian, H. X. Yang, J. Q. Li, T. Varga, J. F. Mitchell, and S. Okamoto, Phys. Rev. B **80**, 161104 (2009).

[131] S. Calder, V. Garlea, D. McMorrow, M. Lumsden, M. B. Stone, J. Lang, J.-W. Kim, J. Schlueter, Y. Shi, K. Yamaura, Y. S. Sun, Y. Tsujimoto, and A. D. Christianson, Phys. Rev. Lett **108**, 257209 (2012).

[132] S. Calder, J. H. Lee, M. B. Stone, M. D. Lumsden, J. C. Lang, M. Feygenson, Z. Zhao, J.-Q. Yan, Y. G. Shi, Y. S. Sun, Y. Tsujimoto, K. Yamaura, and A. D. Christianson, Nature Communications **6**, 9916 (2015).

[133] O. Bunău and Y. Joly, J. Phys.: Condens. Matter **21**, 345501 (2009).

[134] L. S. I. Veiga, G. Fabbris, M. van Veenendaal, N. M. Souza-Neto, H. L. Feng, K. Yamaura, and D. Haskel, Phys. Rev. B **91**, 235135 (2015).

[135] Y. Du, X. Wan, L. Sheng, J. Dong, and S. Y. Savrasov, Phys. Rev. B **85**, 174424 (2012).

[136] M.-C. Jung, Y.-J. Song, K.-W. Lee, and W. E. Pickett, Phys. Rev. B **87**, 115119 (2013).

[137] S. Middey, S. Debnath, P. Mahadevan, and D. D. Sarma, Phys. Rev. B **89**, 134416 (2014).

[138] J. C. Hempel, J. Chem. Phys. **64**, 4307 (1976).

[139] C. Jia, E. Nowadnick, K. Wohlfeld, Y. Kung, C. C. Chen, S. Johnston, T. Tohyama, B. Moritz, and T. Devereaux, Nature Communications **5**, 3314 (2014).

[140] E. Kermarrec, C. A. Marjerrison, C. M. Thompson, D. D. Maharaj, K. Levin, S. Kroeker, G. E. Granroth, R. Flacau, Z. Yamani, J. E. Greedan, and B. D. Gaulin, Phys. Rev. B **91**, 075133 (2015).

[141] D. C. Johnston, R. J. McQueeney, B. Lake, A. Honecker, M. E. Zhitomirsky, R. Nath, Y. Furukawa, V. P. Antropov, and Y. Singh, Phys. Rev. B **84**, 094445 (2011).

[142] T. Moriya, *Spin fluctuations in itinerant electron magnetism*, Springer Series in Solid-State Sciences (Springer-Verlag Berlin Heidelberg, 1985).

[143] B. Kim, P. Liu, Z. Ergönenc, A. Toschi, S. Khmelevskyi, and C. Franchini, arXiv:1601.03310 (2016).

[144] Q. Wang, Y. Cao, J. A. Waugh, S. R. Park, T. F. Qi, O. B. Korneta, G. Cao, and D. S. Dessau, Phys. Rev. B **87**, 245109 (2013).

[145] X. Gao, C. Burns, D. Casa, M. Upton, T. Gog, J. Kim, and C. Li, Rev. Sci. Instrum. **82**, 113108 (2011).

[146] X. Gao, D. Casa, J. Kim, T. Gog, C. Li, and C. Burns, Rev. Sci. Instrum. **87**, 083107 (2016).

[147] A. J. Princep, "Origin of the metal insulator transition in Pb_2CaOsO_6," (2016), ESRF Experimental Report.

[148] Q. Li, G. Cao, S. Okamoto, J. Yi, W. Lin, B. Sales, J. Yan, R. Arita, J. Kuneš, A. Kozhevnikov, A. Eguiluz, M. Imada, Z. Gai, M. Pan, and D. Mandrus, Sci. Rep. **3**, 3073 (2013).

[149] R. Arita, J. Kuneš, A. V. Kozhevnikov, A. G. Eguiluz, and M. Imada, Phys. Rev. Lett. **108**, 086403 (2012).

[150] A. Yamasaki, S. Tachibana, H. Fujiwara, A. Higashiya, A. Irizawa, O. Kirilmaz, F. Pfaff, P. Scheiderer, J. Gabel, M. Sing, T. Muro, M. Yabashi, K. Tamasaku, H. Sato, H. Namatame, M. Taniguchi, A. Hloskovskyy, H. Yoshida, H. Okabe, M. Isobe, J. Akimitsu, W. Drube, R. Claessen, T. Ishikawa, S. Imada, A. Sekiyama, and S. Suga, Phys. Rev. B **89**, 121111 (2014).

[151] D. Hsieh, F. Mahmood, D. H. Torchinsky, G. Cao, and N. Gedik, Phys. Rev. B **86**, 035128 (2012).

[152] H. Watanabe, T. Shirakawa, and S. Yunoki, Phys. Rev. B **89**, 165115 (2014).

[153] P. D. C. King, T. Takayama, A. Tamai, E. Rozbicki, S. M. Walker, M. Shi, L. Patthey, R. G. Moore, D. Lu, K. M. Shen, H. Takagi, and F. Baumberger, Phys. Rev. B **87**, 241106 (2013).

[154] M. F. Collins, *Magnetic Critical Scattering* (Oxford University Press, New York, 1989).

[155] L. S. Ornstein and F. Zernike, Proc. K. Ned. Akad. Wetensc. **17**, 793 (1914).

[156] M. E. Fisher, J. Math. Phys. **5**, 944 (1964).

[157] M. E. Fisher and R. J. Burford, Phys. Rev. **156**, 583 (1967).

[158] N. D. Mermin and H. Wagner, Phys. Rev. Lett. **11**, 1133 (1966).

[159] S. Chakravarty, B. I. Halperin, and D. R. Nelson, Phys. Rev. Lett. **60**, 1057 (1988).

[160] A. Rigamonti and P. Carretta, *Structure of Matter: An Introductory Course with Problems and Solutions* (Springer, Switzerland, 2015).

[161] P. Hasenfratz and F. Niedermayer, Phys. Lett. B **268**, 231 (1991).

[162] A. V. Chubukov, S. Sachdev, and J. Ye, Phys. Rev. B **49**, 11919 (1994).

[163] P. Hasenfratz, Eur. Phys. J. B **13**, 11 (2000).

[164] H. M. Rønnow, D. F. McMorrow, and A. Harrison, Phys. Rev. Lett. **82**, 3152 (1999).

[165] A. V. Chubukov and O. A. Starykh, J. Phys.: Condens. Matter **11**, L169 (1999).

[166] N. Elstner, R. L. Glenister, R. R. P. Singh, and A. Sokol, Phys. Rev. B **51**, 8984 (1995).

[167] M. S. Makivić and H.-Q. Ding, Phys. Rev. B **43**, 3562 (1991).

[168] J.-K. Kim and M. Troyer, Phys. Rev. Lett. **80**, 2705 (1998).

[169] A. Cuccoli, V. Tognetti, P. Verrucchi, and R. Vaia, Phys. Rev. B **58**, 14151 (1998).

[170] B. B. Beard, A. Cuccoli, R. Vaia, and P. Verrucchi, Phys. Rev. B **68**, 104406 (2003).

[171] N. Elstner, A. Sokol, R. R. P. Singh, M. Greven, and R. J. Birgeneau, Phys. Rev. Lett. **75**, 938 (1995).

[172] R. Coldea, S. M. Hayden, G. Aeppli, T. G. Perring, C. D. Frost, T. E. Mason, S.-W. Cheong, and Z. Fisk, Phys. Rev. Lett. **86**, 5377 (2001).

[173] N. S. Headings, S. M. Hayden, R. Coldea, and T. G. Perring, Phys. Rev. Lett. **105**, 247001 (2010).

[174] B. Keimer, N. Belk, R. J. Birgeneau, A. Cassanho, C. Y. Chen, M. Greven, M. A. Kastner, A. Aharony, Y. Endoh, R. W. Erwin, and G. Shirane, Phys. Rev. B **46**, 14034 (1992).

[175] R. J. Birgeneau, M. Greven, M. A. Kastner, Y. S. Lee, B. O. Wells, Y. Endoh, K. Yamada, and G. Shirane, Phys. Rev. B **59**, 13788 (1999).

[176] S. J. Clarke, A. Harrison, T. E. Mason, and D. Visser, Solid State Commun. **112**, 561 (1999).

[177] P. Carretta, T. Ciabattoni, A. Cuccoli, E. Mognaschi, A. Rigamonti, V. Tognetti, and P. Verrucchi, Phys. Rev. Lett. **84**, 366 (2000).

[178] H. M. Rønnow, D. F. McMorrow, A. Harrison, I. D. Youngson, R. Coldea, T. G. Perring, G. Aeppli, and O. Syljuåsen, J. Magn. Magn. Mater. **236**, 4 (2001).

[179] H. M. Rønnow, D. F. McMorrow, R. Coldea, A. Harrison, I. D. Youngson, T. G. Perring, G. Aeppli, O. Syljuåsen, K. Lefmann, and C. Rischel, Phys. Rev. Lett. **87**, 037202 (2001).

[180] L. L. Miller, X. L. Wang, S. X. Wang, C. Stassis, D. C. Johnston, J. Faber, and C.-K. Loong, Phys. Rev. B **41**, 1921 (1990).

[181] M. Greven, R. J. Birgeneau, Y. Endoh, M. A. Kastner, B. Keimer, M. Matsuda, G. Shirane, and T. R. Thurston, Phys. Rev. Lett. **72**, 1096 (1994).

[182] Y. J. Kim, R. J. Birgeneau, F. C. Chou, R. W. Erwin, and M. A. Kastner, Phys. Rev. Lett. **86**, 3144 (2001).

[183] M. Guarise, B. Dalla Piazza, M. Moretti Sala, G. Ghiringhelli, L. Braicovich, H. Berger, J. N. Hancock, D. van der Marel, T. Schmitt, V. N. Strocov, L. J. P. Ament, J. van den Brink, P.-H. Lin, P. Xu, H. M. Rønnow, and M. Grioni, Phys. Rev. Lett. **105**, 157006 (2010).

[184] K. W. Plumb, A. T. Savici, G. E. Granroth, F. C. Chou, and Y.-J. Kim, Phys. Rev. B **89**, 180410 (2014).

[185] F. Ye, S. Chi, B. C. Chakoumakos, J. A. Fernandez-Baca, T. Qi, and G. Cao, Phys. Rev. B **87**, 140406 (2013).

[186] C. Dhital, T. Hogan, Z. Yamani, C. de la Cruz, X. Chen, S. Khadka, Z. Ren, and S. D. Wilson, Phys. Rev. B **87**, 144405 (2013).

[187] D. H. Torchinsky, H. Chu, L. Zhao, N. B. Perkins, Y. Sizyuk, T. Qi, G. Cao, and D. Hsieh, Phys. Rev. Lett. **114**, 096404 (2015).

[188] M. K. Crawford, M. A. Subramanian, R. L. Harlow, J. A. Fernandez-Baca, Z. R. Wang, and D. C. Johnston, Phys. Rev. B **49**, 9198 (1994).

[189] T. Shimura, M. Itoh, and T. Nakamura, J. Solid State Chem. **98**, 198 (1992).

[190] S. Boseggia, R. Springell, H. C. Walker, H. M. Rønnow, C. Rüegg, H. Okabe, M. Isobe, R. S. Perry, S. P. Collins, and D. F. McMorrow, Phys. Rev. Lett. **110**, 117207 (2013).

[191] S. Boseggia, H. C. Walker, J. Vale, R. Springell, Z. Feng, R. S. Perry, M. M. Sala, H. M. Rønnow, S. P. Collins, and D. F. McMorrow, J. Phys. Condens. Matter **25**, 422202 (2013).

[192] J. Kim, M. Daghofer, A. H. Said, T. Gog, J. van den Brink, G. Khaliullin, and B. J. Kim, Nature Communications **5**, 4453 (2014).

[193] E. Manousakis, Rev. Mod. Phys. **63**, 1 (1991).

[194] I. Franke, P. J. Baker, S. J. Blundell, T. Lancaster, W. Hayes, F. L. Pratt, and G. Cao, Phys. Rev. B **83**, 094416 (2011).

[195] A. Taroni, S. T. Bramwell, and P. C. W. Holdsworth, J. Phys.: Condens. Matter **20**, 275233 (2008).

[196] W. Montfrooij, H. Casalta, P. Schleger, N. Andersen, A. Zhokov, and A. Christensen, Physica B **241**, 848 (1997).

[197] R. Pozzi, M. Mali, D. Brinkmann, and A. Erb, Phys. Rev. B **60**, 9650 (1999).

[198] T. R. Thurston, G. Helgesen, J. P. Hill, D. Gibbs, B. D. Gaulin, and P. J. Simpson, Phys. Rev. B **49**, 15730 (1994).

[199] M. Altarelli, M. D. Núñez-Regueiro, and M. Papoular, Phys. Rev. Lett. **74**, 3840 (1995).

[200] S. R. Andrews, J. Phys. C: Solid State Physics **19**, 3721 (1986).

[201] D. F. McMorrow, N. Hamaya, S. Shimomura, Y. Fujii, S. Kishimoto, and H. Iwasaki, Solid State Commun. **76**, 443 (1990).

[202] H. Hünnefeld, T. Niemöller, J. R. Schneider, U. Rütt, S. Rodewald, J. Fleig, and G. Shirane, Phys. Rev. B **66**, 014113 (2002).

[203] I. N. Bhatti, R. Rawat, A. Banerjee, and A. Pramanik, J. Phys.: Condens Matter **27**, 016005 (2014).

[204] V. L. Berezinskii, Sov. Phys. JETP **32**, 493 (1971).

[205] J. M. Kosterlitz and D. J. Thouless, J. Phys. C: Solid State Phys. **6**, 1181 (1973).

[206] J. M. Kosterlitz, J. Phys. C: Solid State Phys. **7**, 1046 (1974).

[207] S. T. Bramwell and P. C. W. Holdsworth, J. Phys.: Condens. Matter **5**, L53 (1993).

[208] S. T. Bramwell and P. C. W. Holdsworth, Phys. Rev. B **49**, 8811 (1994).

[209] J. V. José, L. P. Kadanoff, S. Kirkpatrick, and D. R. Nelson, Phys. Rev. B **16**, 1217 (1977).

[210] M. Suzuki, Prog. Theor. Phys. **51**, 1992 (1974).

[211] J. Als-Nielsen, S. T. Bramwell, M. T. Hutchings, G. J. McIntyre, and D. Visser, J. Phys. Condens. Matter **5**, 7871 (1993).

[212] C. Kraemer, N. Nikseresht, J. O. Piatek, N. Tsyrulin, B. D. Piazza, K. Kiefer, B. Klemke, T. F. Rosenbaum, G. Aeppli, C. Gannarelli, K. Prokes, A. Podlesnyak, T. Straessle, L. Keller, O. Zaharko, K. W. Krämer, and H. M. Rønnow, Science **336**, 1416 (2012).

[213] M. Reehuis, C. Ulrich, K. Prokeš, A. Gozar, G. Blumberg, S. Komiya, Y. Ando, P. Pattison, and B. Keimer, Phys. Rev. B **73**, 144513 (2006).

[214] M. Greven, R. Birgeneau, Y. Endoh, M. Kastner, M. Matsuda, and G. Shirane, Z. Phys. B **96**, 465 (1995).

[215] A. Cuccoli, T. Roscilde, V. Tognetti, R. Vaia, and P. Verrucchi, Phys. Rev. B **67**, 104414 (2003).

[216] A. Cuccoli, T. Roscilde, R. Vaia, and P. Verrucchi, Phys. Rev. Lett. **90**, 167205 (2003).

[217] J. Igarashi and T. Nagao, Phys. Rev. B **90**, 064402 (2014).

[218] M. P. H. Thurlings, E. Frikkee, and H. W. de Wijn, Phys. Rev. B **25**, 4750 (1982).

[219] P. Liu, S. Khmelevskyi, B. Kim, M. Marsman, D. Li, X.-Q. Chen, D. D. Sarma, G. Kresse, and C. Franchini, Phys. Rev. B **92**, 054428 (2015).

[220] B. Keimer, R. Birgeneau, A. Cassanho, Y. Endoh, M. Greven, M. Kastner, and G. Shirane, Z. Phys. B **91**, 373 (1993).

[221] J. Igarashi and T. Nagao, Phys. Rev. B **88**, 104406 (2013).

[222] J. Igarashi and T. Nagao, Phys. Rev. B **89**, 064410 (2014).

[223] N. B. Perkins, Y. Sizyuk, and P. Wölfle, Phys. Rev. B **89**, 035143 (2014).

[224] B. H. Kim, G. Khaliullin, and B. I. Min, Phys. Rev. Lett. **109**, 167205 (2012).

[225] I. V. Solovyev, V. V. Mazurenko, and A. A. Katanin, Phys. Rev. B **92**, 235109 (2015).

[226] S. Bahr, A. Alfonsov, G. Jackeli, G. Khaliullin, A. Matsumoto, T. Takayama, H. Takagi, B. Büchner, and V. Kataev, Phys. Rev. B **89**, 180401 (2014).

[227] N. A. Bogdanov, V. M. Katukuri, J. Romhányi, V. Yushankhai, V. Kataev, B. Büchner, J. van den Brink, and L. Hozoi, Nature Communications **6**, 7306 (2015).

[228] M. Subramanian, M. Crawford, and R. Harlow, Mat. Res. Bull. **29**, 645 (1994).

[229] J. Kafalas and J. Longo, J. Solid State Chem. **4**, 55 (1972).

[230] G. Cao, Y. Xin, C. S. Alexander, J. E. Crow, P. Schlottmann, M. K. Crawford, R. L. Harlow, and W. Marshall, Phys. Rev. B **66**, 214412 (2002).

[231] H. Matsuhata, I. Nagai, Y. Yoshida, S. Hara, S. Ikeda, and N. Shirakawa, J. Solid State Chem. **177**, 3776 (2004).

[232] T. Hogan, L. Bjaalie, L. Zhao, C. Belvin, X. Wang, C. G. Van de Walle, D. Hsieh, and S. D. Wilson, Phys. Rev. B **93**, 134110 (2016).

[233] S. Boseggia, *Magnetic order and excitations in perovskite iridates studied with resonant X-ray scattering techniques*, Ph.D. thesis, University College London (2014).

[234] S. Fujiyama, K. Ohashi, H. Ohsumi, K. Sugimoto, T. Takayama, T. Komesu, M. Takata, T. Arima, and H. Takagi, Phys. Rev. B **86**, 174414 (2012).

[235] B. M. Wojek, M. H. Berntsen, S. Boseggia, A. T. Boothroyd, D. Prabhakaran, D. F. McMorrow, H. M. Rønnow, J. Chang, and O. Tjernberg, J. Phys.: Condens. Matter **24**, 415602 (2012).

[236] D. A. Zocco, J. J. Hamlin, B. D. White, B. J. Kim, J. R. Jeffries, S. T. Weir, Y. K. Vohra, J. W. Allen, and M. B. Maple, J. Phys.: Condens. Matter **26**, 255603 (2014).

[237] I. Nagai, Y. Yoshida, S. I. Ikeda, H. Matsuhata, H. Kito, and M. Kosaka, J. Phys.: Condens. Matter **19**, 136214 (2007).

[238] S. Boseggia, R. Springell, H. C. Walker, A. T. Boothroyd, D. Prabhakaran, D. Wermeille, L. Bouchenoire, S. P. Collins, and D. F. McMorrow, Phys. Rev. B **85**, 184432 (2012).

[239] S. Boseggia, R. Springell, H. C. Walker, A. T. Boothroyd, D. Prabhakaran, S. P. Collins, and D. F. McMorrow, J. Phys.: Condens. Matter **24**, 312202 (2012).

[240] C. Dhital, S. Khadka, Z. Yamani, C. de la Cruz, T. C. Hogan, S. M. Disseler, M. Pokharel, K. C. Lukas, W. Tian, C. P. Opeil, Z. Wang, and S. D. Wilson, Phys. Rev. B **86**, 100401 (2012).

[241] M. Miyazaki, R. Kadono, M. Hiraishi, A. Koda, K. M. Kojima, K. Ohashi, T. Takayama, and H. Takagi, Phys. Rev. B **91**, 155113 (2015).

[242] C. Holm and W. Janke, Phys. Rev. B **48**, 936 (1993).

[243] A. Pelissetto and E. Vicari, Physics Reports **368**, 549 (2002).

[244] E. Beaurepaire, J.-C. Merle, A. Daunois, and J.-Y. Bigot, Phys. Rev. Lett. **76**, 4250 (1996).

[245] A. Kirilyuk, A. V. Kimel, and T. Rasing, Rev. Mod. Phys. **82**, 2731 (2010).

[246] Z. Huang and K.-J. Kim, Phys. Rev. ST Accel. Beams **10**, 034801 (2007).

[247] E. Saldin, E. Schneidmiller, Y. Shvyd'ko, and M. Yurkov, Nucl. Instr. Meth. Phys. Res. A **475**, 357 (2001).

[248] R. R. Lindberg and Y. V. Shvyd'ko, Phys. Rev. ST Accel. Beams **15**, 050706 (2012).

[249] G. Geloni, V. Kocharyan, and E. Saldin, Journal of Modern Optics **58**, 1391 (2011).

[250] Y. Shvyd'ko and R. Lindberg, Phys. Rev. ST Accel. Beams **15**, 100702 (2012).

[251] H. Aoki, N. Tsuji, M. Eckstein, M. Kollar, T. Oka, and P. Werner, Rev. Mod. Phys. **86**, 779 (2014).

[252] D. N. Basov, R. D. Averitt, D. van der Marel, M. Dressel, and K. Haule, Rev. Mod. Phys. **83**, 471 (2011).

[253] M. P. M. Dean, Y. Cao, X. Liu, S. Wall, D. Zhu, R. Mankowsky, V. Thampy, X. M. Chen, J. G. Vale, D. Casa, J. Kim, A. H. Said, P. Juhas, R. Alonso-Mori, J. M. Glownia, A. Robert, J. Robinson, M. Sikorski, S. Song, M. Kozina, H. Lemke, L. Patthey, S. Owada, T. Katayama, M. Yabashi, Y. Tanaka, T. Togashi, J. Liu, C. R. Serrao, B. J. Kim, L. Huber, C. L. Chang, D. F. McMorrow, M. Först, and J. P. Hill, Nature Materials **16**, 601 (2016).

[254] G. Cerullo and S. De Silvestri, Rev. Sci. Instr. **74**, 1 (2003).

[255] D. Zhu, A. Robert, T. Henighan, H. T. Lemke, M. Chollet, J. M. Glownia, D. A. Reis, and M. Trigo, Phys. Rev. B **92**, 054303 (2015).

[256] X. Liu, M. P. M. Dean, Z. Y. Meng, M. H. Upton, T. Qi, T. Gog, Y. Cao, J. Q. Lin, D. Meyers, H. Ding, G. Cao, and J. P. Hill, Phys. Rev. B **93**, 241102 (2016).

[257] H. Gretarsson, N. H. Sung, J. Porras, J. Bertinshaw, C. Dietl, J. A. N. Bruin, A. F. Bangura, Y. K. Kim, R. Dinnebier, J. Kim, A. Al-Zein, M. Moretti Sala, M. Krisch, M. Le Tacon, B. Keimer, and B. J. Kim, Phys. Rev. Lett. **117**, 107001 (2016).

[258] M. Nakayama, T. Kondo, Z. Tian, J. J. Ishikawa, M. Halim, C. Bareille, W. Malaeb, K. Kuroda, T. Tomita, S. Ideta, K. Tanaka, M. Matsunami, S. Kimura, N. Inami, K. Ono, H. Kumigashira, L. Balents, S. Nakatsuji, and S. Shin, Phys. Rev. Lett. **117**, 056403 (2016).

[259] P. S. Malavi, S. Karmakar, and S. M. Sharma, Phys. Rev. B **93**, 035139 (2016).

[260] N. H. Sung, H. Gretarsson, D. Proepper, J. Porras, M. L. Tacon, A. V. Boris, B. Keimer, and B. J. Kim, Philosophical Magazine **96**, 413 (2016).

[261] A. Rathi, S. Perween, P. Rout, R. Singh, A. Gupta, S. Singh, B. Gahtori, B. Sivaiah, A. Dhar, A. Shukla, R. Rakshit, R. Pant, and G. Basheed, arXiv:1608.02726 (2016).

[262] A. J. Bray, Phys. Rev. Lett. **59**, 586 (1987).

[263] S. Huotari, G. Vankó, F. Albergamo, C. Ponchut, H. Graafsma, C. Henriquet, R. Verbeni, and G. Monaco, J. Synch. Rad. **12**, 467 (2005).

[264] T. Gog, D. Casa, A. Said, M. Upton, J. H. Kim, I. Kuzmenko, X. Huang, and R. Khachatryan, "Analyser and monochromator atlas," `http://www.aps.anl.gov/Sectors/Sector30/Useful.html`.

[265] T. Hahn, ed., *International Tables for Crystallography Volume A: Space-Group Symmetry*, 5th ed. (Springer, 2005).

[266] P. Babkevich, *Quantum materials explored by neutron scattering*, Ph.D. thesis, University of Oxford (2012).

[267] R. M. White, M. Sparks, and I. Ortenburger, Phys. Rev. **139**, A450 (1965).

Acknowledgements

Finally, after 120,000 miles, a couple of thousand cups of coffee, and more than a few bags of Haribo later, I have this thesis to show for it. Over the past four years I've had the opportunity and pleasure to work with a large number of people, too numerous to offer my gratitude to individually. There are, however, a few that I must mention.

Firstly I'd like to thank Des for being such a supportive and insightful supervisor. Des has shown me the importance of always being critical of the data and making any results tell a captivating story. It has been a pleasure working with him through my PhD.

Secondly I'd like to thank Henrik and the group at EPFL, especially with regards to financial support through a UCL Impact Studentship, and the interpretation of the critical scattering data. Everywhere I go I seem to bump into more people affiliated with EPFL in some way, and it feels reassuring to be part of that welcoming wider community.

Helen, Ross, and Stefano, I have you to thank for teaching me the ropes of resonant X-ray scattering as it were, and making long beamtimes genuinely enjoyable experiences. I've definitely gotten better at the Guardian cryptic crosswords whilst waiting for scans to finish!

Stuart and Andy, for the collaboration that led to the studies on the osmates. I'll always remember that icy trip to the APS in December, and the ridiculously big sandwich...

Steve and Marco, a number of the experiments presented here would not have been possible without your knowledge and expertise. It's always a pleasure to go to I16 and ID20. I also have Marco to thank for showing me where to get the best pizza in Grenoble.

Many thanks to Aymeric, Diling, Makina, and the staff at Ako General Hospital, for being lovely people, and looking after me in the immediate aftermath of my bike accident in Japan.

To my friends Andy, Anna, Ben, Francis, Hannah, Kathryn, and Zarrin. Thank you for putting up with me continually having to rearrange plans and being there to share the trials and tribulations of doing our PhDs. Plus feeding my caffeine addiction!

Eloise, thank you for being my best friend and supporting me through all this. I'll especially miss the long lunch breaks when we did get a chance to meet up at UCL, and trips to come and visit you in Russia and Finland.

Finally Amy, I give you my greatest thanks and adoration. Without your love, support, and encouragement, none of this would have been possible. Thank you for putting up with me being away from London for at least three months a year, and looking after me when I needed it most. We will get to have our holiday in Japan soon, I promise.